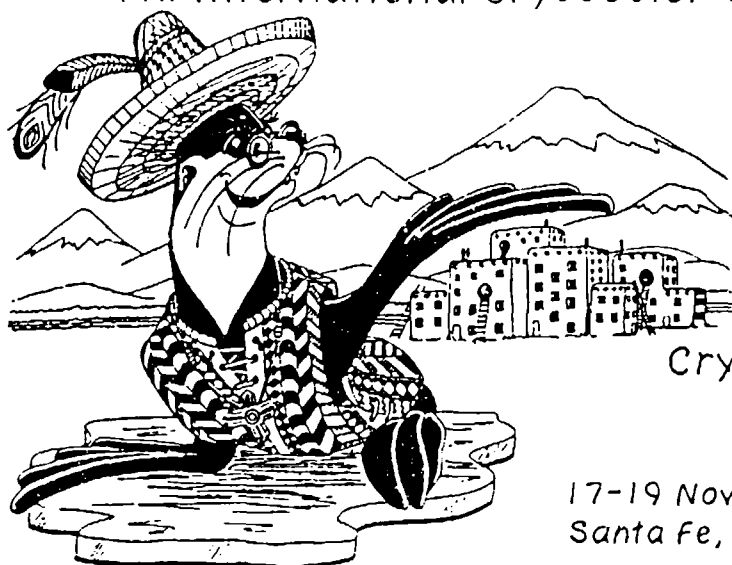


(2)



7th International Cryocooler Conference



Cryocoolers 7

17-19 November 1992
Santa Fe, New Mexico

Part 2 of 4

April 1993

DTIC
ELECTE
AUG 09 1993
S A D

Conference Proceeding

93-18248



APPROVED FOR PUBLIC RELEASE; DISTRIBUTION IS UNLIMITED.



PHILLIPS LABORATORY
Directorate of Space and Missiles Technology
AIR FORCE MATERIEL COMMAND
KIRTLAND AIR FORCE BASE, NM 87117-5776

This final report was prepared by the Phillips Laboratory, Kirtland Air Force Base, New Mexico, under Job Order 11050502. The Laboratory Project Officer-in-Charge was Marko M. Stoyanof (VTPT).

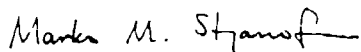
When Government drawings, specifications, or other data are used for any purpose other than in connection with a definitely Government-related procurement, the United States Government incurs no responsibility or any obligation whatsoever. The fact that the Government may have formulated or in any way supplied the said drawings, specifications, or other data, is not to be regarded by implication, or otherwise in any manner construed, as licensing the holder, or any other person or corporation; or as conveying any rights or permission to manufacture, use, or sell any patented invention that may in any way be related thereto.

This report has been authored by employees and contractors of the United States Government and Foreign Governments. Accordingly, the United States Government retains a nonexclusive royalty-free license to publish or reproduce the material contained herein, or allow others to do so, for the United States Government purposes.

This report has been reviewed by the Public Affairs Office and is releasable to the National Technical Information Service (NTIS). At NTIS, it will be available to the general public, including foreign nationals.

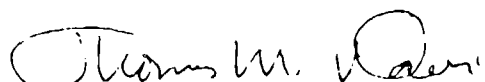
If your address has changed, or if your organization no longer employs the addressee, please notify PL/VTPT, Kirtland AFB, NM 87117-5776 to help maintain a current mailing list.

This conference proceeding has been reviewed and is approved for publication.


MARKO M. STOYANOF
Project Officer

FOR THE COMMANDER


ROBERT M. VACEK, GM-14, DAF
Chief, Thermal Management Br


THOMAS M. DAVIS, Lt Col, USAF
Acting Director of Space & Missile
Technology

DO NOT RETURN COPIES OF THIS REPORT UNLESS CONTRACTUAL
OBLIGATIONS OR NOTICE ON A SPECIFIC DOCUMENT REQUIRES THAT
IT BE RETURNED.

REPORT DOCUMENTATION PAGE			Form Approved OMB No. 0704-0188	
<small>Public reporting burden for this collection of information is estimated to average 1 hour per response, including the time for reviewing instructions, searching existing data sources, gathering and maintaining the data needed, and completing and reviewing the collection of information. Send comments regarding this burden estimate or any other aspect of this collection of information, including suggestions for reducing this burden, to Washington Headquarters Services, Directorate for Information Operations and Reports, 1215 Jefferson Davis Highway, Suite 1204, Arlington, VA 22202-4302, and to the Office of Management and Budget, Paperwork Reduction Project (0704-0188), Washington, DC 20503.</small>				
1. AGENCY USE ONLY (Leave blank)		2. REPORT DATE April 1993		3. REPORT TYPE AND DATES COVERED 17-19 Nov 92, Conference Proceeding
4. TITLE AND SUBTITLE 7th International Cryocooler Conference Part 2 of 4			5. FUNDING NUMBERS PE: 62601F PR: 1105 TA: 05 WU: 02	
6. AUTHOR(S) Several authors				
7. PERFORMING ORGANIZATION NAME(S) AND ADDRESS(ES) Phillips Laboratory Kirtland AFB, NM 87117-5776			8. PERFORMING ORGANIZATION REPORT NUMBER PL-CP--93-1001	
9. SPONSORING MONITORING AGENCY NAME(S) AND ADDRESS(ES)			10. SPONSORING MONITORING AGENCY REPORT NUMBER	
11. SUPPLEMENTARY NOTES Publication of this report does not constitute approval or disapproval of the ideas or findings. It is published in the interest of scientific and technical information exchange. The established procedures for editing reports were not followed for this report.				
12a. DISTRIBUTION AVAILABILITY STATEMENT Approved for public release; distribution is unlimited.			12b. DISTRIBUTION CODE	
13. ABSTRACT (Maximum 200 words) The 7th International Cryocooler Conference was held in Santa Fe, New Mexico, on 17-19 November, 1992. Jiri L. Ludwigsen of Nichols Research was the conference chairperson; Capt William Wyche and Marko Stoyanof of Phillips Laboratory served as the program committee chairmen. The topics included Cryocooler Testing and Modeling, Space and Long Life Applications, Stirling Cryocoolers, Pulse Tube Refrigerators, Novel Concepts and Component Development, Low Temperature Regenerator Development, and J-T and Absorption Coolers.				
14. SUBJECT TERMS Absorption, Cryocoolers, Cryogenic, Low Temperature Heat Exchanger, Pulse Tube Refrigerators, Regenerative, Recuperative, Stirling, Thermal Modeling			15. NUMBER OF PAGES 306	
			16. PRICE CODE	
17. SECURITY CLASSIFICATION OF REPORT Unclassified	18. SECURITY CLASSIFICATION OF THIS PAGE Unclassified	19. SECURITY CLASSIFICATION OF ABSTRACT Unclassified	20. LIMITATION OF ABSTRACT SAR	

Chairman

Jill Ludwigsen
 Nichols Research Corporation
 2201 Buena Vista, S.E. #203
 Albuquerque, NM 87106
 (505) 843-7364

Program Committee

Capt. Bill Wyche, Co-Chairman
 Marko Stoyanof, Co-Chairman
 Air Force Phillips Laboratory

Ronald White, WRDC/FIVE

Dodd Stacy, Creare

Ron Ross, Jet Propulsion Lab

Al Johnson, Aerospace Corp.

Peter Gifford, Cryomech

Local Arrangements

Peter Jones, Aerospace Corp.

Advisory Board

John Barclay
 University of Victoria

Joseph Smith
 MIT

DTIC QUALITY INSPECTED 3

Stephen Castles
 NASA/GSFC

Michael Superczynski
 DTRC

Ray Radebaugh
 NIST

Klaus Timmerhaus
 University of Colorado

Hiroshi Nagano
 Toyama University, Japan

Paul Sheihing
 DOE

Ralph Longworth
 APD Cryogenics

Peter Kerney
 Janis Research

Martin Nisenoff
 NRL

George Robinson
 Nichols Research Corp.

Accession For	
NTIS	CEARI <input checked="" type="checkbox"/>
DTIC	TAU <input type="checkbox"/>
Unpublished	<input type="checkbox"/>
J. A. F. Jones	
By	
Distribution	
Availability Codes	
Dist	Availability or Special
A-1	

FOREWORD

This report contains the proceedings of the Seventh International Cryocooler Conference, held in Santa Fe, New Mexico, on 17-19 November, 1992. Jiri L. Ludwigsen of Nichols Research was the conference chairperson; Capt William Wyche and Marko Stoyanof of Phillips Laboratory served as the program committee chairmen.

The first cryocooler conference held in 1980 was designed to stimulate interest and discussion in the scientific and engineering community about the latest developments and advances in refrigeration for cryogenic sensors and electronic systems. The conference is held every even numbered year and this year over 300 participants attended representing 11 countries.

The technical program consisted of over 100 unrestricted oral and poster presentations. The topics included Cryocooler Testing and Modeling, Space and Long Life Applications, Stirling Cryocoolers, Pulse Tube Refrigerators, Novel Concepts and Component Development, Low Temperature Regenerator Development, and J-T and Absorption Coolers. The proceedings show significant progress in the field of cryocooler technology.

ACKNOWLEDGEMENTS

The Seventh International Cryocooler Conference Board would like to thank the Air Force Phillips Laboratory for sponsoring the conference and publishing these proceedings. The generous supply of manpower and dedication contributed by Phillips Laboratory was key to the success of the 1992 conference.

The Conference Chairperson would like to express her appreciation to Nichols Research Corporation for providing the support, assets and time required for this effort.

CONTENTS

TUESDAY SESSION	1
SDIO AND AIR FORCE CRYOCOOLER TECHNOLOGY DEVELOPMENTS AT USAF PHILLIPS LABORATORY	
....P. J. Thomas	3
JPL CRYOCOOLER DEVELOPMENT AND TEST PROGRAM OVERVIEW	
....R. G. Ross, Jr.	14
NASA/GSFC CRYOCOOLER DEVELOPMENT PROGRAM	
....S. Castles, T. Cygnarowicz, R. Boyle, L. Sparr, R. Cory, F. ConnorsE. James, R. Fink, V. Arillo, J. Marketon, C. Lee, and D. Bugby	26
DEVELOPMENT AND DEMONSTRATION OF A DIAPHRAGM STIRLING 65 K STANDARD SPACECRAFT CRYOCOOLER	
....D. Stacy, J. McCormick, and J. Valenzuela	40
STIRLING SPACE COOLER	
....C. K. Chan, M. Lopez, J. Raab, E. Tward, and G. Davey	50
THERMAL, VIBRATION, AND RELIABILITY TEST RESULTS FOR A BALANCED 80 K CRYOCOOLER	
....R. Boyle, L. Sparr, T. Cygnarowicz, S. Castles,R. G. Fink, and E. F. James	57
SPACECRAFT COOLER CHARACTERIZATION	
....D. L. Johnson, G. R. Mon, and R. G. Ross, Jr.	73
PERFORMANCE OF A LONG LIFE REVERSE BRAYTON CRYOCOOLER	
....W. Swift and H. Sixsmith	84
SDI CRYOCOOLER PRODUCIBILITY PROGRAM	
....J. Bruning	98
MINIATURES PULSE TUBE COOLER	
....C. K. Chan, C. B. Jaco, J. Raab, E. Tward, and M. Waterman	113
FLOW PATTERNS INTRINSIC TO THE PULSE TUBE REFRIGERATOR	
....J. M. Lee, P. Kittel, K. D. Timmerhaus, and R. Radebaugh	125
EXPERIMENTAL PERFORMANCE OF MODIFIED PULSE TUBE REFRIGERATOR BELOW 80 K DOWN 23 K	
....Y. Ishizaki and E. Ishizaki	140

CONTENTS (Continued)

PULSE TUBE REFRIGERATOR RESEARCH

....Y. Zhou and Y. J. Han 147

DEVELOPMENT OF PULSE TUBE REFRIGERATOR WITH LINEAR-MOTOR DRIVE COMPRESSOR

....T. Kuriyama, H. Hatakeyama, Y. Ohtani, H. Nakagome, Y. Matsubara,
....H. Okuda, and H. Murakami 157

AN EXPERIMENTAL AND ANALYTICAL INVESTIGATION OF 4 K PULSE TUBE REFRIGERATOR

....Y. Matsubara, J. L. Gao, K. Tanida, Y. Hiresaki, M. Kaneko 166

A NEW CONFIGURATION FOR SMALL-CAPACITY, LIQUID-HELIUM-TEMPERATURE CRYOCOOLER

....J. A. Crunkleton 187

ANALYSIS OF A MINIATURE TWO-STAGE CRYOCOOLER

....E. B. Ratts, Dr J. L. Smith, Jr., and Dr Y. Iwasa 197

POWER, EFFICIENCY, AND OPTIMUM DESIGN OF ELECTROCHEMICAL REFRIGERATORS

....R. T. Ruggeri 213

LINEARIZED PULSE TUBE CRYOCOOLER THEORY

....H. Mirels 221

VIBROIMPACT RESONANCE APPLICATION FOR THE DISPLACER MOTION PASSIVE CONTROL IN THE SPLIT CRYOGENIC COOLER

....A. Veprik and N. Pundak 233

A HIGHLY RELIABLE, MINIATURE STIRLING-CYCLE CRYOCOOLER

....C. S. Keung and G. Esposito 247

PERFORMANCE TEST RESULTS ON A MINIATURE STIRLING CRYOCOOLER FOR USE IN INTEGRATED DEWAR DETECTOR ASSEMBLIES

....P. Ab-der-Halden 257

VALIDATION OF THE STIRLING REFRIGERATOR PERFORMANCE MODEL AGAINST THE PHILLIPS/NASA MAGNETIC BEARING REFRIGERATOR

....S. W. K. Yuan and I. E. Spradley 280

THE MS*2 STIRLING CYCLE CODE

....M. P. Mitchell 290

CONTENTS (Continued)

AN INTRODUCTION TO THE LUCAS AEROSPACE THERMODYNAMIC COMPUTER MODEL CMOD	
....C. S. Brice.	294
THERMOACOUSTIC THEORY FOR REGENERATIVE CRYOCOOLERS: A CASE STUDY FOR A PULSE TUBE REFRIGERATOR	
....J. H. Xiao	305
SOME PRELIMINARY EXPERIMENTAL RESULTS ON OSCILLATORY HEAT TRANSFER IN A PERIODICALLY REVERSING PIPE FLOW	
....X. Tang and P. Cheng	321
THERMOELECTRIC COOLERS FOR THE TWS, SFW, WAM AND SADARM PROGRAMS, AND ASSOCIATED MANTECH PROGRAM OBJECTIVES	
....W. L. Kolander, B. Morrison, J. Bierschenk,J. Fuhrer, and T. Kottak	332
CRYOGENIC ATTACHMENT FIXTURE WITH HIGH STRENGTH AND LOW THERMAL CONDUCTION	
....P. R. Roach	349
HELIUM LIQUID- AND GAS-GAP HEAT SWITCHES	
....A. Kashani, B. P. M. Helvensteijn,F. J. McCormack, and A. L. Spivak	355
A RADIATIVE COOLING SYSTEM FOR THE EOS STRATOSPHERIC WIND INFRARED LIMB SOUNDER	
....D. J. Kuiper	371
NEW MAGNETIC REFRIGERANTS FOR THE LOW TEMPERATURES REGION	
....M. D. Kuz'min, A. M. Tishin, and S. Y. Dan'kov	385
WEDNESDAY SESSION	
387	
EXPERIMENTAL INVESTIGATION OF THE REGENERATIVE MAGNETIC REFRIGERATOR OPERATING BETWEEN 4.2 K AND 1.8 K	
....S. Jeong, J. L. Smith, Jr., Y. Iwasa, and T. Numazawa	389
A 4 K GIFFORD-McMAHON REFRIGERATOR FOR RADIO ASTRONOMY	
....R. Plambeck, N. Thatte, and P. Sykes	401

CONTENTS (Continued)

DYNAMIC CHARACTERISTICS OF REGENERATORS USED IN CRYOCOOLERS	
....B. J. Huang and C. W. Lu	416

REGENERATOR PERFORMANCE AND REFRIGERATION MECHANISM FOR 4 K GM REFRIGERATOR USING RARE EARTH COMPOUND REGENERATOR MATERIALS	
....T. Kuriyama, M. Takahashi, H. Nakagome, T. Hashimoto,	
....T. Eda, and M. Yabuki	429

A STIRLING CYCLE CRYOCOOLER FOR 4 K APPLICATIONS	
....D. Stacy, J. McCormick, and P. Wallis	444

SUPERFLUID STIRLING REFRIGERATOR WITH A COUNTERFLOW REGENERATOR	
....J. G. Brisson and G. W. Swift	460

GRADED AND NONGRADED REGENERATOR PERFORMANCE	
....W. Rawlins, K. D. Timmerhaus, R. Radebaugh,	
....J. Gary, and P. Bradley	471

SPECIFIC HEAT DESIGN AND PROPOSAL OF A NEW CUBIC TYPE MAGNETIC MATERIAL FOR A REGENERATOR MATRIX	
....Y. Tokai, A. Takahasi, M. Sahashi, and T. Hashimoto	484

A COMPACT 150 GHz SIS RECEIVER COOLED BY 4 K GM REFRIGERATOR	
....M. Takahasi, H. Hatakeyama, T. Kuriyama, H. Nakagome, R. Kawabe,	
....H. Iwashita, G. McCulloch, K. Shibata, and S. Ukita	495

DEVELOPMENT OF A PRECISION, SIX-AXIS LABORATORY DYNAMOMETER	
....P. J. Champagne, S. A. Cordova, M. S. Jacoby, and K. R. Lorell	508

DEVELOPMENT AND DEMONSTRATION OF AN ELECTRONIC CONTROLLER FOR A DOUBLE-ACTING DIAPHRAGM CRYOCOOLER	
....C. Konkel, T. Gibboney, L. Van Allen, K. Ha, and R. Boyle	526

MAGNETIC NOISE PRODUCED BY GM CRYOCOOLERS	
....S. Fujimoto, H. Ogata, and H. Kado	560

REGENERATOR TWO-PHASE "SINGLE-BLOW" FOR PERFORMANCE EVALUATION AT SMALL VELOCITIES: ORIENTATION INFLUENCE AT "1g"	
....K. V. Ravikumar, R. M. Carandang, T. H. K. Frederking,	
....R. Confair, W. Hong, F. Sherman, and C. Toribio	569

CONTENTS (Continued)

OPTIMIZATION ANALYSIS ON A TWO-STAGE AMR HYDROGEN LIQUEFIERL. Zhang, A. J. DeGregoria, S. A. Sherif, and T. N. Veziroglu	586
SUBMILLIMETER SPACE ASTRONOMY WITHOUT LIQUID HELIUM?C. Hagmann and P. L. Richards	595
RECENT PROGRESS ON APPLICATION OF HIGH ENTROPY MAGNETIC MATERIAL TO THE REGENERATOR IN HELIUM TEMPERATURE RANGET. Hashimoto, T. Eda, M. Yabuki, T. Kuriyama, and H. Nakagome	605
THE EFFECTS OF A LAYERED BED ON ACTIVE MAGNETIC REGENERATOR PERFORMANCES. R. Schuricht, A. J. DeGregoria, and C. B. Zimm	614
LONG LIFE STIRLING CYCLE COOLER DEVELOPMENTS FOR THE SPACE APPLICATION RANGE OF 20 K TO 80 KB. G. Jones and R. C. Peddle	621
STIRLING CRYOCOOLER WITH DUAL OPPOSED DISPLACERS FOR SPACE APPLICATIONSP. Arter, D. Berry, W. Gully, and C. Varner	644
DEVELOPMENT AND SPACE QUALIFICATION TESTING OF A RANGE OF MECHANICAL CRYOCOOLERSC. Weir	656
NOVEL LINEAR FLEXURE BEARINGI. E. Wong, R. B. Pan, and A. L. Johnson	675
NASA/GSFC CRYOCOOLER TEST PROGRAM RESULTSL. Sparr, R. Boyle, R. Cory, F. Connors, E. James,R. Fink, V. Arillo, and J. Marketon	699
PERFORMANCE OF THE SIGNAAL USFA STIRLING COOLING ENGINESD. Verbeek, H. Helmonds, and P. Roos	728
PRESENT LIFE-TESTING STATUS OF "OXFORD TYPE" CRYOCOOLERS FOR SPACE APPLICATIONSC. Jewell, T. Bradshaw, A. Orlowska, and B. Jones	738

CONTENTS (Continued)

DESIGN AND TEST OF A COMPREHENSIVE FACILITY FOR LIFE-TESTING SPACE CRYOCOOLERS ...R. G. Ross, Jr. and D. L. Johnson	748
SIMULATION PROGRAM FOR MULTIPLE EXPANSION STIRLING MACHINES ...G. Walker, M. Weiss, R. Fauvel, G. Reader, and E. R. Bingham	759
COMPUTER MODELING OF STIRLING CYCLE COOLERS ...T. W. Bradshaw, A. H. Orlowska, and J. Hieatt	772
DESIGN EQUATIONS AND SCALING LAWS FOR LINEAR COMPRESSORS WITH FLEXURE SPRINGS ...E. Marquardt, R. Radebaugh, and P. Kittel	783
NON-REAL TIME, FEED FORWARD VIBRATION CONTROL SYSTEM DEVELOPMENT AND TEST RESULTS ...R. Boyle, F. Connors, J. Marketon, V. Arillo, ...E. James, and R. Fink	805
DEMONSTRATION OF ACTIVE VIBRATION REDUCTION ON A STIRLING- CYCLE CRYOCOOLER TESTBED ...B. G. Johnson, D. B. Eisenhaure, F. J. Flynn, M. S. Gaffney, ...R. L. Hockney, D. L. Johnson, and R. G. Ross, Jr.	820
THURSDAY SESSION	829
EVOLUTION OF THE 10 K PERIODIC SORPTION REFRIGERATOR CONCEPT ...A. L. Johnson and J. A. Jones	831
DEVELOPMENT OF A PERIODIC 10 K SORPTION CRYOCOOLER ...S. Bard, T. Fujita, L. Wade, J. Rodriguez, and J. J. Wu	854
EVALUATION OF A PROTOTYPE HYDRIDE COMPRESSOR FOR PERIODIC HYDROGEN SORPTION CRYOCOOLERS ...R. C. Bowman, Jr., B. D. Freeman, D. Labor, F. E. Lynch, ...R. W. Marmaro, and L. A. Wade	867
ASSESSMENT OF A HYDROGEN JOULE-THOMSON EXPANDER AND VANADIUM HYDRIDE SORPTION BEDS FOR 20 K CRYOCOOLERS ...E. L. Ryba, B. D. Freeman, R. C. Bowman, Jr., R. E. Spjut, ...E. A. Liu, P. Budic, and C. Okado	880

CONTENTS (Continued)

DESIGN OF A METAL HYDRIDE SORPTION CRYOCOOLER SYSTEMH. J. Strumpf and R. H. Norman	898
LINEAR COMPRESSOR FOR JT CRYOCOOLERD. T. Kuo	921
PROGRESS REPORT ON THE DEVELOPMENT OF THE BALL J-T CRYOCOOLERR. Levenduski and R. Scarlotti	931
JT CRYOSTAT WITH LIQUID-SOLID CRYOGEN RESERVOIRR. C. Longworth	958
DESIGN AND OPERATION OF A 30 K TWO-STAGE NITROGEN-NEON J-T COOLERW. A. Little, R. Yaron, and C. Fuentes	971
DESIGN CONCEPTS FOR A 10 K SOLID HYDROGEN SORPTION REFRIGERATORJ. R. Phillips, B. D. Freeman, and R. C. Bowman, Jr.	978
EXPERIMENTAL VERIFICATION OF JOULE-THOMSON CRYOCOOLER COOLDOWN PERIOD SIMILARITY RATIOSB-Z. Maytal	996
BI-MATERIAL CONTROLLED DEMAND FLOW JOULE-THOMSON COOLERSG. E. Bonney	1003
CONTAMINATION CONTROL IN CLOSED CYCLE JOULE-THOMSON CRYOCOOLERS AND A NEW J-T VALVE ... * Lester and S. Nieczkoski	1012
PHASE EQUILIBRIA IN CRYOGENIC MIXTURESL. B. Robinson	1025
INCORPORATING A MECHANICAL REFRIGERATOR WITH A REFREEZABLE CRYOGEN IN SPACE APPLICATIONSB. G. Williams and J. C. Batty	1043
APPLICATIONS AND PACKAGING OF SEMICONDUCTOR DEVICES FOR USE AT CRYOGENIC TEMPERATURESK. P. Hyde, J. R. McCoy, and C. S. Naiman	1064

CONTENTS (Concluded)

A METHOD TO ESTIMATE THE PULSE TUBE REFRIGERATOR PERFORMANCES	
....M. David, J. Marechal, and Y. Simon	1078
CRYOCOOLER TIP MOTION SUPPRESSION USING ACTIVE CONTROL OF PIEZOELECTRIC ACTUATORS	
....R. J. Glaser, R. G. Ross, Jr., and D. L. Johnson	1086
HIGH TEMPERATURE SUPERCONDUCTING SPACE EXPERIMENT CRYOGENIC SYSTEM OVERVIEW	
....T. Kawecki	1098
10 K SORPTION CRYOCOOLER FLIGHT EXPERIMENT (BETSCE)	
....S. Bard, P. Cowgill, J. Rodriguez, L. Wade, J. J. Wu,	
....M. Gehrlein, and W. Von Der Ohe	1107
GAS ATOMIZED E₃Ni POWDER FOR CRYOCOOLER APPLICATIONS	
....I. E. Anderson, M. G. Osborne, H. Takeya,	
....and K. A. Gschneidner, Jr.	1120
MAGNETIC NANOCOMPOSITES AS MAGNETIC REFRIGERANTS	
....R. D. Shull, R. D. McMichael, J. J. Ritter,	
....L. J. Swartzendruber, and L. H. Bennett	1133
ENTHALPY FLOW TRANSITION LOSSES IN REGENERATIVE CRYOCOOLERS	
....P. Kittel	1145
NEODYMIUM REGENERATOR TEST RESULTS IN A STANDARD GIFFORD-McMAHON REFRIGERATOR	
....J. Chafe, G. Green, and R. C. Riedy	1157
SOLVAY REFRIGERATOR OPERATING AT HELIUM TEMPERATURES	
....G. Chen, J. Zheng, F. Zhang, J. Yu, and T. Sun	1165

THERMOACOUSTIC THEORY FOR REGENERATIVE CRYOCOOLERS: A CASE STUDY FOR A PULSE TUBE REFRIGERATOR

J. H. Xiao

Cryogenic Laboratory, Academia Sinica
PO Box 2711, Beijing 100080, P.R. China

ABSTRACT

A thermoacoustic theory is established for analysis of gas oscillations and time averaged energy fluxes in regenerative cryocoolers. In regenerative cryocoolers, the oscillatory motions of the gaseous medium are longitudinally transmitted in the form of acoustic wave motion, which is governed by the wave equations. The thermoacoustic effects, i.e., time averaged energy effects is caused by thermal interaction of oscillatory gaseous fluid and solid mediums, which could be described by the energy-temperature equations. With these equations and other thermoacoustic relations, one can perform systematic evaluation for the dynamics and thermal characteristics of a regenerative cryocooler. The paper gives a brief introduction to the basics of the thermoacoustic approach for regenerative cryocoolers analysis. Then it present a case study for a orifice pulse tube refrigerator in terms of the thermoacoustic theory. The calculated results, including the gas fluctuations, energy fluxes, and the system performance, is presented. The analytical overall performance is well comparable to experimental results.

INTRODUCTION

It is commonly known that there is still a lot to do with working processes analysis and dynamic modeling of regenerative cryocoolers, for this problem is

considerably complicated. Many theories based on regenerative thermodynamic cycle analysis have been established to analyze the thermal performance of regenerative cryocoolers¹². These theories usually make quasi-steady assumptions and do not consider the interaction between flow characteristics and thermal characteristics, they use steady flow thermodynamics and heat transfer analysis methods to evaluate the ideal performance and heat transfer efficiency of the coolers, then by separately calculating of various losses (pressure-drop loss, heat conduction loss, *etc.*), they could find out the overall performance.

To have a more realistic model of regenerative cryocoolers, it is necessary to model the irreversibility that may occur during the cycle more accurately. Therefore, one must solve all the fundamental transport equations simultaneously: continuity, momentum, energy and the equation of state (gas laws). In addition, the problem can not be simplified into steady flow or incompressible. In order to deal with this problem analytically, we suggest investigating this problem in Eulerian point of view rather than in Lagrangian point of view of fluid dynamics. It is well known that the oscillations of compressible fluid is sound (acoustic oscillations). Reminding this, one can realize that regenerative cryocoolers work rely on time averaged energy effects caused by the thermal interaction of oscillatory gaseous fluid medium and solid medium, i.e., rely on thermoacoustic effects. The thermoacoustic approach for regenerative cryocoolers analysis mainly deals with two problems: first, the wave propagation in the cryocoolers, second, the time averaged energy flow (thermoacoustic effects) of the cryocoolers.

The most noticeable works on thermoacoustics in recent times were carried out by Rott, Merkli and Thomann, Wheatley and Swift *etc.*. In 1970's, Rott and his co-workers established a sound theoretical foundation to describe how the acoustic energy and heat energy is mutually transformed in tubes with adiabatic walls where acoustic standing waves impose¹³. Merkli and Thomann studied the thermoacoustic effects in a resonant tube with isothermal wall, i.e., forced acoustic oscillations induced time averaged heat flow in the tube and heat exchange of the

tube with its environment both theoretically and experimentally". Based on Rott's theoretical work, in 1980's, Wheatley and Swift *et al.* developed the standing wave "thermoacoustic engines", and extended Rott's theory applicable to both standing wave thermoacoustic refrigerators and prime movers^{4,5}. All above thermoacoustic theory is successful, but they limited their study to acoustic standing waves, we can not apply their theory to regenerative cryocoolers.

This paper will briefly describe the basic equations of the thermoacoustic approach for regenerative cryocoolers analysis, and present a case study for a orifice pulse tube refrigerator using the thermoacoustic theory.

THERMOACOUSTIC EQUATIONS

BASIC ASSUMPTIONS

The basic assumptions for the theoretical analysis are: (1) the solid materials (solid outer walls and porous solid matrices) are stationary and rigid. (2) the fluid medium is a simple compressible fluid, mechanical energy and heat energy are the only two active work forms involved. (3) the cryocooler are under periodically stationary working condition, and the mean fluid velocity is zero. (4) the dimension of the regenerator gaps in porous matrix and the dimension of porous solid matrix are smaller than the thermal penetration depth of the fluid δ_a ,

$\delta_a = \left(\frac{2K_o}{\rho_o C_{po} \omega} \right)^{\frac{1}{2}}$, and the thermal penetration depth of the solid matrix material δ_s ,

$\delta_s = \left(\frac{2K_{so}}{\rho_{so} C_{so} \omega} \right)^{\frac{1}{2}}$, respectively, so we can use volume averaging method to average

the states variables to describe the flow and thermal characteristics of the regenerators. (5) the acoustic amplitudes are low enough to avoid turbulence, so

that $\frac{\rho_o |u| \delta_\mu}{\mu_o} < 500$, $\delta_\mu = \left(\frac{2\mu_o}{\rho_o \omega} \right)^{\frac{1}{2}}$. (6) let $\epsilon = \frac{|u|}{2\pi a_o}$, which represents the ratio of

particle displacement to the wave length. Finally, it is assumed that $\epsilon \ll 1$, so that

we can assume complete linearization, with nonlinear effects neglected.

WAVE EQUATIONS

Using pressure, volume velocity, gas and solid temperature fluctuations as state variables and also using complex notation of fluctuation quantities, the cross section averaged longitudinal wave equations for regenerative cryocoolers, under the above assumptions, could be written as^{11,12}:

$$\begin{aligned}\frac{d\tilde{p}}{dx} &= -z_f \tilde{U} \\ \frac{d\tilde{U}}{dx} &= -\frac{1}{z_c} \tilde{p} + f_{\text{MT}} \beta_o \frac{dT_o}{dx} \tilde{U}\end{aligned}\quad (1)$$

where z_f is the flow inductive impedance, z_c is the flow capacitive impedance, f_{MT} is a complex acoustic factor.

Eqs.(1) are the longitudinal wave equations for regenerative cryocoolers, it express the relationship between pressure and velocity fluctuations, from which acoustic attenuation and phase shift of pressure and velocity fluctuations could be predicted.

THERMOACOUSTIC EFFECTS

Thermoacoustic effects are time averaged energy effects caused by interaction of the gas working medium and the solid working medium. The time averaged energy effects concerned are: acoustic work flux, heat flux, and total energy flux, etc.. We just write out equations for base waves (first harmonic). High order harmonics can be treated easily on the basis of superposition principle.

ACOUSTIC WORK FLUX

The longitudinal acoustic work flux is:

$$w_x = \frac{1}{2} \operatorname{Re} [\dot{U} \dot{P}^*] \quad (2)$$

The transverse work flux is zero because the solid wall is rigid.

HEAT FLUX

Heat flux is caused by the hydrodynamic transportation of entropy (carried by the oscillatory velocity) and heat conduction of gas and solid.

The entropy transportation caused longitudinal heat flux is:

$$\begin{aligned} Q_x^s &= \frac{1}{2} \operatorname{Re} [\rho_o T_o \int S \dot{U}^* dA] = \frac{1}{2} \operatorname{Re} [\int (\rho_o C_{p0} \dot{T} \dot{U}^* - T_o \beta_o \dot{P} \dot{U}^*) dA] \\ &= -\frac{1}{2} T_o \beta_o \operatorname{Re} [\dot{U} \dot{P}^* \epsilon_{qx}] - \frac{1}{2} \rho_o C_{p0} \frac{|\dot{U}|^2}{A_f^2 \omega} g_{qx} \frac{dT_o}{dx} \end{aligned} \quad (3)$$

where ϵ_{qx} and g_{qx} is a complex and a real acoustic factor, respectively.

The first term in Eq. (3) is caused by sound oscillations, it can be positive or negative, depend upon the sound field. The second term is caused by irreversibility of heat exchange between the gas and solid mediums, and it is proportional to the temperature gradient, its direction is always opposite to that of the temperature gradient, which means that it always flow from hot end to cold end. It is convenient to introduce an "effective" coefficient of heat conduction by

$$K_{ef}^s = \frac{1}{2} \rho_o C_{p0} \frac{|\dot{U}|^2}{A_f^2 \omega} g_{qx} \quad (4)$$

The longitudinal conductive heat flux is:

$$Q_x^c = -A_f K_o \frac{dT_o}{dx} - A_s K_{so} \frac{dT_o}{dx} \quad (5)$$

where the first and second terms are contributions of gas and solid, respectively.

Combining Eqs. (3) and (5), the total longitudinal heat flux write:

$$Q_x = Q_x' + Q_x'' = -\frac{1}{2} T_o \beta_o \operatorname{Re} [\tilde{U} \tilde{p}^* f_{qx}] - A_f K_o \frac{dT_o}{dx} \quad (6)$$

where K_o is the total effective coefficient of heat conductivity

$$K_o = K_o' + K_o'' + \frac{A_s}{A_f} K_{so} \quad (7)$$

The transverse heat flux is caused by heat exchange between walls of the cryocooler and its environments. It is reasonable to suppose the transverse heat flux is proportional to the temperature difference of the solid wall and its environment, so that the transverse heat flux per unit length reads:

$$Q_b' = h_w U_w (T_o - T_s) \quad (8)$$

where we choose the direction of heat flow from the cryocooler solid walls to its environment as positive direction.

TOTAL ENERGY FLUX

The total energy flux of regenerative cryocoolers is caused by the hydrodynamic transportation of enthalpy (carried by the oscillatory velocity) and heat conduction of gas and solid, it is equal to the sum of acoustic energy and heat energy.

The longitudinal total energy flux reads:

$$E_x = W_x + Q_x = \frac{1}{2} \operatorname{Re} [\tilde{U} \tilde{p}^* (1 - T_o \beta_o f_{qx})] - A_f K_o \frac{dT_o}{dx} \quad (9)$$

where the first term can be positive or negative, depend upon the sound field; the sign of the second term is always opposite to that of the temperature gradient.

The transverse total energy flux is equal to transverse heat flux. For the total energy is conservatory, it can not be produced nor absorbed. The increase of longitudinal total energy flux per unit length should be equal to the heat absorbed from the environment, so that:

$$\frac{dE_x}{dx} = -Q'_b = h_w U_w (T_o - T_e) \quad (10)$$

Eqs. (9) and (10) express the relationship which the longitudinal total energy flux E_x and temperature distribution T_o should be satisfied, we can rewrite them as:

$$\frac{dT_o}{dx} = -\frac{\frac{1}{2} Re [\bar{U} \bar{p}^* (1 - T_o \beta_o f_{qx})] - E_x}{A_f K_o}$$

$$\frac{dE_x}{dx} = h_w U_w (T_o - T_e) \quad (11)$$

We call Eqs.(11) the energy-temperature equations, from which the mean temperature and total energy flux fields could be predicted.

The wave equations (1) and energy-temperature equations (11) form a close, complete thermoacoustic longitudinal equation group. Once we know the geometrical configurations, thermo-physical properties of the materials and longitudinal boundary conditions of a regenerative cryocooler, the above equations could be solved. With their solutions, and other thermoacoustic relations, one can find out the performance of the cryocooler.

CASE STUDY FOR A PULSE TUBE REFRIGERATOR

ORIFICE PULSE TUBE CONFIGURATION

The one-stage orifice pulse tube refrigerator configuration includes a wave generator, a connecting pipe, a hot end heat exchanger, a regenerator, a cold end heat exchanger, a pulse

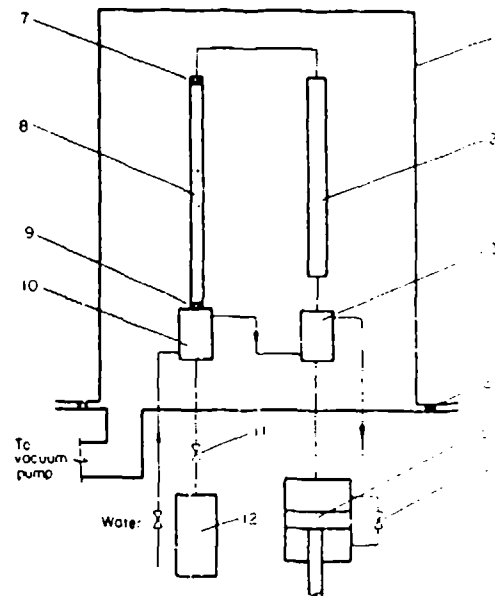


Figure 1 Experimental set-up 1. Vacuum vessel 2. regenerator 3. heat exchanger 4. sealing ring 5. compressor 6. by-pass valve 7. flow straightener 8. pulse tube 9. flow straightener 10. heat exchanger 11. orifice 12. gas reservoir

tube, a pulse tube hot end heat exchange, a orifice and a reservoir", see Fig.1.

TREATMENT OF COMPONENTS

WAVE GENERATOR

The wave generator is considered as a segment of tube with the length of half the piston stroke. The volume velocity of the piston at its equilibrium position is given by $\dot{V}_c = \frac{1}{2} \omega v_c \exp(j\omega t)$, where v_c is the swept volume of the piston. Here it is assumed the piston velocity is much slow than that of the sound velocity of the working fluid.

TUBES

The connecting tube is assumed to have nature heat convection with room air. The pulse tube is assumed to have ideal thermal insulation with its surroundings, i.e., the heat transfer coefficient of the pulse tube wall with its environment is set to be zero.

HEAT EXCHANGERS

All room temperature heat exchangers of this orifice pulse tube is forced water cooled, so the heat transfer coefficient is determined from forced heat convection. For we hope to obtain the system performance of the refrigerator with a fixed cold-end temperature, the heat transfer coefficient of the cold-end heat exchanger is set to be a very large number, such that the temperature difference could be very small to satisfy our requirements.

REGENERATOR

The regenerator is assumed to have ideal thermal insulation with its surroundings, i.e., the heat transfer coefficient of the regenerator wall with its environment is set to zero. The heat exchange coefficient of the working fluid and porous matrix is simply determined by $N_o=4.36$.

ORIFICE(VALVE) AND RESERVOIR

The orifice and reservoir construction is called Helmholtz resonator in acoustics. It is a forced acoustic oscillation structure. It dissipate acoustic energy into heat at the orifice or valve. We have assumed to simplify the flow pass in the valve used in this refrigerator as a circular gap with its diameter of 3mm, width of 0.1mm, and length of 1mm, this set of parameters is numerically tested to have best performance for the refrigerator. The reservoir is assumed to be thermal insulated from its surroundings. The acoustic impedance of the Helmholtz resonator is determined by acoustic impedance equations in general acoustics.

The acoustic factors appeared in the thermoacoustic equations for all above components is presented in reference 11,12.

SYSTEM APPROACH PROCEDURES

We compiled a computer program for the system performance analysis of the orifice pulse tube refrigerator. The main procedures for numerical approach are as follows:

- 1 forming the system network model of the refrigerator (acoustic circuit of the refrigerator), including the system configuration, construction and connection relation of various components. At any connection position, the dynamic pressure remains the same, the algebraic sum of volume velocity is zero, and the mean temperature remains the same, the algebraic sum of total energy flux is zero. The

system network model of the orifice pulse tube is shown in Fig. 2.

- 2 given the operation conditions, including the operation frequency, the mass of filling gas, the effective heat exchange coefficient of each component to its environment, the volume velocity of the piston of wave generator, *etc.*.
- 3 dividing the refrigerator into a series of segments along the longitudinal direction with finite length small enough for each segment to be considered to have constant properties.
- 4 setting a initial mean temperature distribution, then find out the mean working pressure of operation according conservation of total mass, and calculate the physical properties of each segment.
- 5 dynamic pressure and velocity distribution calculation using the wave equations.
- 6 mean temperature and total energy flux distribution calculation using the energy-temperature equations.
- 7 taking the calculated mean temperature distribution to be the newly setting initial mean temperature, then repeating procedures (4) to (7) till the calculation achieves the goal of accuracy.
- 8 computation of the work flux, heat flux and system performance, and other parameters of interest for the refrigerator.

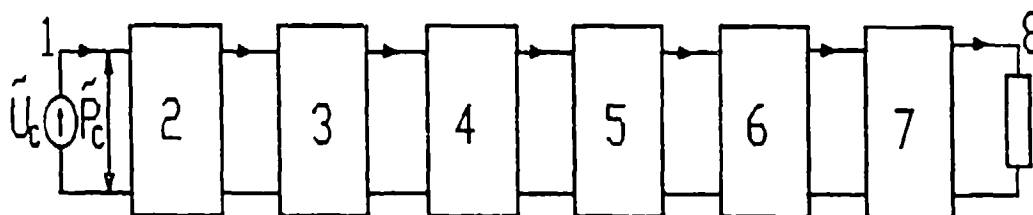


Figure 2 System network model of the orifice pulse tube refrigerator

1, wave generator; 2, connecting pipe; 3, hot-end heat exchanger; 4, regenerator; 5, cold-end heat exchanger; 6, pulse tube; 7, pulse tube hot-end heat exchanger; 8, Helmholtz resonator

SYSTEM MODEL RESULTS

The present thermoacoustic approach was used to analyze the performance of the orifice pulse tube refrigerator used by Liang *et al.* in their experiment. The design details, operation conditions and the measured system performance have reported in reference 13,14. The calculation results, together with Liang's experimental results, are given below. Computation was carried out on a PC-AT.

Figure 3 shows the refrigeration power, Q_c , versus the cold-end temperature, T_c , with the experimental results presented. The predicted cooling powers agrees with experimental results very well: the predicted lowest temperature is 56.2K, measured is 49K, the predicted cooling powers are 5.54W at 65K and 13.68W at 77K, while the measured are 6.6W at 65K and 12W at 77K.

Figure 4 shows the relative coefficient of performance of the refrigerator, COP/COP_c , versus the cold-end temperature, T_c , with the experimental results presented. The predicted work input from the wave generator agrees with experimental results well too. At 77K, the predicted work required is 487.4W, while the measured are 478W.

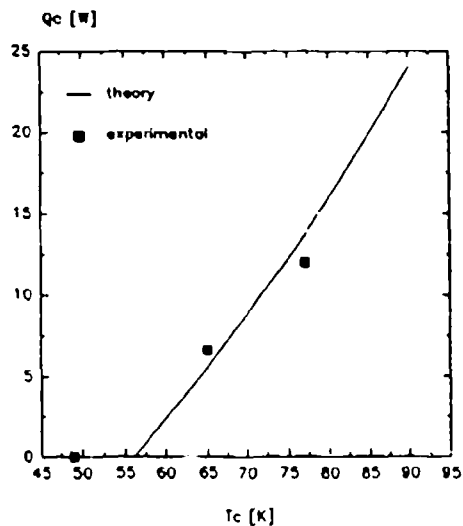


Figure 3 Refrigeration power

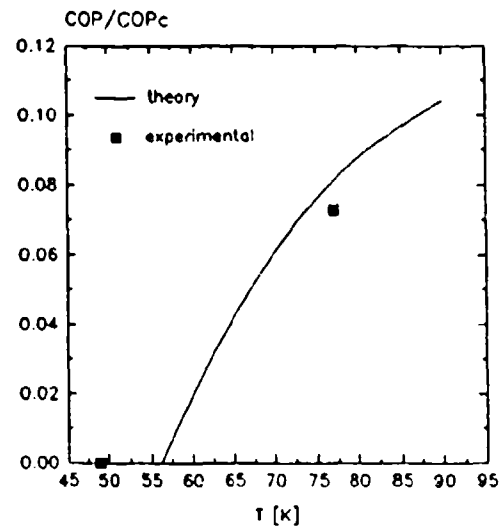


Figure 4 Relative effectiveness

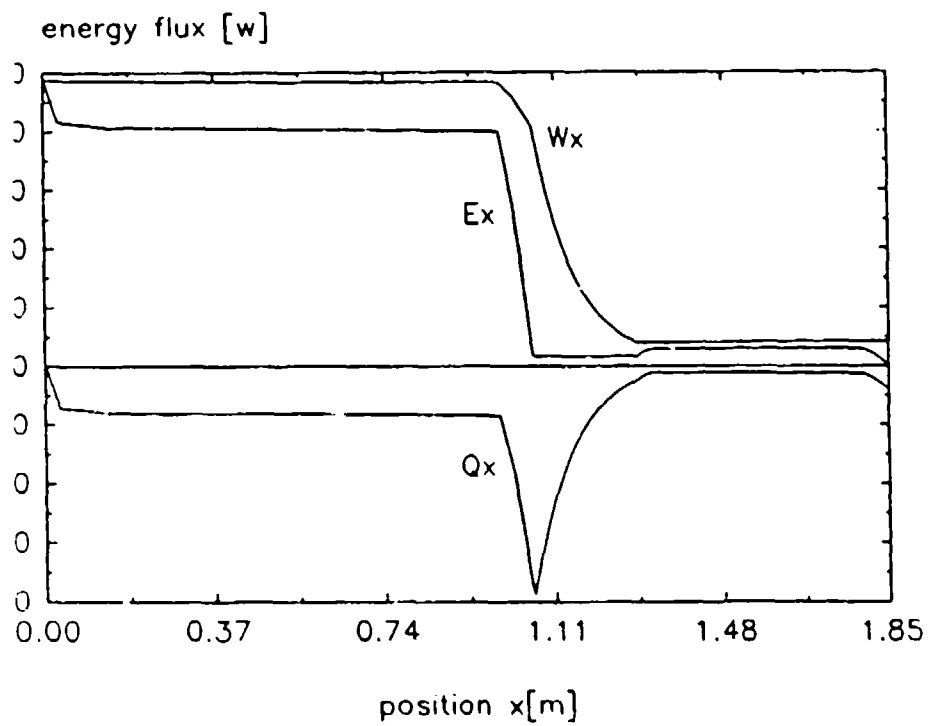


Figure 5 Energy flux of the orifice pulse tube refrigerator

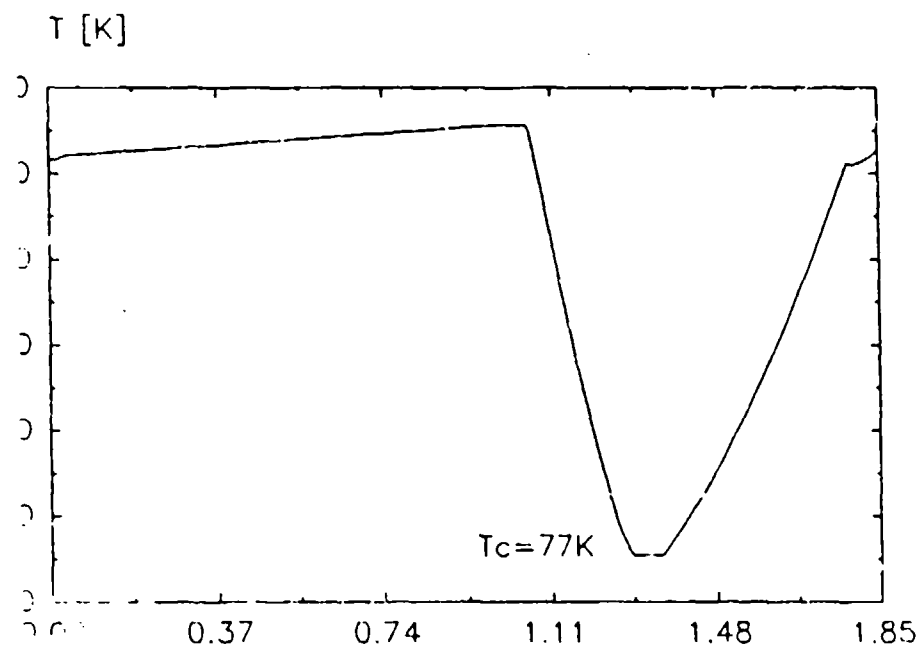


Figure 5 shows the energy flux (acoustic work flux, heat flux and total energy flux), w_x , Q_x , E_x , versus the position, x , with the cold-end temperature $T_c=77K$. This results shows that, from the wave generator through the cold end, the orifice pulse tube refrigerator works similar to a Stirling refrigerator. From the pulse tube through the reservoir, these part of components works similar to a expansion piston, it absorbs acoustic work from the regenerator. However, this second gaseous piston is not a perfect one, there exists a heat flow (approximately 11W) from the hot-end of the pulse tube to the cold-end, and this part of absorbed work is not recoverable, which is dissipated into heat in the orifice.

Figure 6 shows the mean temperature, T_o , versus the position, x , with the cold-end temperature $T_c=77K$. The temperature field becomes more strongly curved as the temperature decreases.

Figure 7 shows the pressure and volume velocity fluctuation, p , \dot{v} , versus the position, x , with the cold-end temperature $T_c=77K$. The results indicate that there

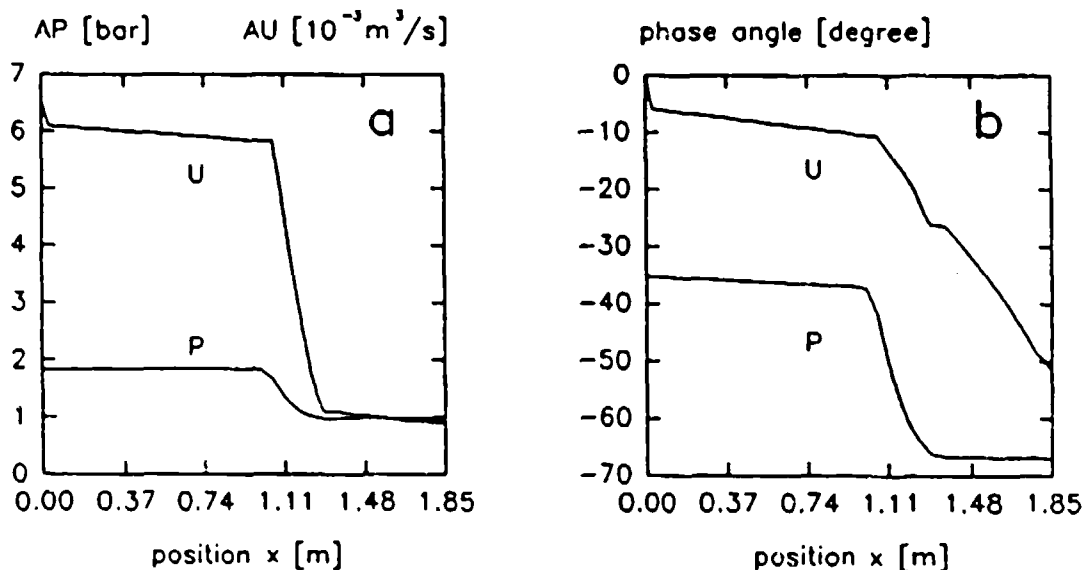


Figure 7 Pressure and volume velocity distribution in the orifice pulse tube refrigerator a. amplitude b. phase angle

is a significant difference in the amplitudes and phase angle of the pressure fluctuation and volume velocity fluctuation across the regenerator and pulse tube. It also shows that the traveling wave have a substantial fraction in the pulse tube.

CONCLUSIONS

The linear thermoacoustic approach developed for regenerative cryocoolers analysis reveals that the working mechanism of regenerative cryocoolers is rely on thermoacoustic effects, i.e., time averaged energy effects caused by the thermal interaction of the oscillatory gaseous fluid medium and the solid medium in Eulerian point of view.

The wave motion, temperature distribution and time averaged energy fluxes in regenerative cryocoolers is governed by the wave equations and energy-temperature equations respectively. They are influenced by the geometric arrangement, thermodynamic irreversibility, and operating conditions of the regenerative cryocoolers.

The thermoacoustic approach for regenerative cryocoolers analysis can be used to predict the flow dynamics and the thermal performance of the cryocoolers. The analysis is simple, more accurate than thermodynamics cycle analysis, and can be carried out on personal computer.

The case study for a orifice pulse tube refrigerator shows that the regenerator is responsible for the heat pumping effect in the pulse tube refrigerator, which consumes acoustic energy and transform it into heat energy to pump heat from its cold end to hot end, it works similar to the regenerator used in Stirling cryocooler. The pulse tube, the orifice and the reservoir act as a gaseous expansion piston similar to the solid expansion piston used in Stirling cryocooler, which absorbs the acoustic work flux coming from the regenerator. However, this second piston is not a perfect one, it brings a heat flow from the hot end to the cold end of the

pulse tube, this reduced the refrigeration power, and the absorbed acoustic work is dissipated into heat irrecoverably in the orifice, this reduces the effectiveness of the refrigerator.

Acknowledgements

This paper rely heavily on the author's Ph.D. dissertation" under supervision of Prof. C.S.Hong and Prof. F.Z. Guo. The author also likes to thank J.T. Liang for his supplying of the details and test results of the orifice pulse tube refrigerator studied in this paper.

References

- 1 Walker,G. *Cryocoolers* Plenum Press, New York, USA (1983)
- 2 Urieli,I and Berchowitz,D.M. *Stirling cycle engine analysis* Adam Hilger Ltd, Bristol, UK(1984)
- 3 Rott,N. Damped and thermally driven acoustic oscillations in wide and narrow tubes *ZAMP*(1969) 20 230
- 4 Rott,N. Thermally driven acoustic oscillations, Part III: Second order heat flux *ZAMP*(1975) 26 43
- 5 Muller,U.A. and Rott,N. Thermally driven acoustic oscillations, Part VI: Excitation and power *ZAMP*(1983) 34 609
- 6 Merkli,P. and Thomann,H. Thermoacoustic effects in a resonance tube *J fluid Mech* (1975) 70 part 1 101
- 7 Merkli,P. and Thomann,H. Transition to turbulence in oscillating pipe flow *J fluid Mech* (1975) 68 part 3 567
- 8 Wheatley,J.C. *et.al.* An intrinsically irreversible thermoacoustic heat engine

- J Acoust Soc Am* (1983) 74(1) 153
- 9 **Hofler, T.J.** Thermoacoustic refrigerator design and performance *PhD. dissertation* Department of Physics, University of California at San Diego, USA(1986)
 - 10 **Swift, G.W.** Thermoacoustic engines *J Acoust Soc Am* (1988) 84(4) 153
 - 11 **Xiao, J.H.** Thermoacoustic effects and thermoacoustic theory for regenerative cryocoolers (heat engines) *PhD. dissertation* Institute of Physics, Academia Sinica, China(1990) (in Chinese)
 - 12 **Xiao, J.H.** Thermoacoustic theory for cyclic flow regenerators. Part I: fundamentals *Cryogenics* (1992) 32 895
 - 13 **Liang, J.T. Zhou, Y and Zhu, W.X.** Development of a single-stage pulse tube refrigerator capable of reaching 49 K *Cryogenics* (1990) 30 49
 - 14 **Liang, J.T.** Experimental investigation of a orifice pulse tube refrigerator *MSc Thesis* Cryogenic Laboratory, Academia Sinica, China(1990) (in Chinese)

SOME PRELIMINARY EXPERIMENTAL RESULTS ON OSCILLATORY HEAT TRANSFER IN A PERIODICALLY REVERSING PIPE FLOW

Xiaoguo Tang and P. Cheng
Department of Mechanical Engineering
University of Hawaii
Honolulu, Hawaii 96822

ABSTRACT

Some preliminary experimental results have been obtained on oscillatory heat transfer induced by a sinusoidally reversing flow of air in a heated pipe with constant heat flux. The central heated tube (the test section) is connected at both ends to two coolers, and the heated fluid in the test section is displaced periodically and cooled by the coolers. Experiments were carried out for the Reynolds number (Re) ranging from 15 to 7,000, the dynamic Reynolds number (Re_ω) ranging from 8 to 181, and the dimensionless stroke (A_ω) ranging from 0.06 to 2.21. Because of the thermal history effect, the temperature of the displaced hot fluid returning from either one of the coolers during each half cycle is not constant but changes periodically with time. A correlation equation for the cycle-averaged Nusselt number is obtained in terms of the three similarity parameters: Re , Re_ω , and A_ω .

1. Introduction

During the past two decades, a considerable amount of work has been given to the experimental study of a periodically reversing flow in a pipe [1-3]. For example, Akhavan et al.[1] measured the velocity distribution in an oscillating flow with a laser Doppler anemometer. Their measured velocity profiles are found in agreement with their theoretical predictions. In another paper, Hino et al.[2] used a hot wire anemometer to investigate the

transition from laminar to turbulent flow in an oscillating pipe flow. They found that transition is characterized by both the Reynolds number and the dynamic Reynolds number. Similar conclusions have been observed by Seume and Simon [3].

Recently, the related problem of oscillatory heat transfer in a periodically reversing pipe flow with application to heat exchangers of a Stirling engine or cryocooler has received a great deal of attention. For example, Kornhauser and Smith [4] reported studies on oscillating heat transfer in a cylinder confined by a movable piston and restrained by a gas spring. Since the heat flux is out of phase with the temperature difference between the wall and the bulk mean temperature of the fluid, they define a complex temperature and derived a complex instantaneous Nusselt number. Hwang and Dybbs [5] performed an experiment for oscillating flow in an open-ended cooled tube, and presented their data graphically for the cycle-averaged Nusselt number as a function of the Reynolds number and the dynamic Reynolds number. Iwabuchi and Kanzaka [6] performed another experiment on oscillating flow and heat transfer, and correlated their data similar to those of a steady turbulent flow. Roach and Bell [7] performed experiments on heat transfer and pressure drop in a packed tube under the condition of rapidly reversing flow. They reported higher friction factors in both heater and cooler but could not find frequency dependence in either pressure drop or heat transfer data. Wu [8] obtained some data for friction factor as well as instantaneous and cycle-averaged Nusselt numbers for an oscillatory flow in a gap heat exchanger, and presented the data graphically as a function of the Reynolds number at given values of the oscillation frequency. In a recent paper, Seume and Simon [3] found that the Reynolds number Re , the dynamic Reynolds number Re_ω , and the dimensionless stroke A_ω are the three similarity variables for oscillatory heat transfer in a periodically reversing pipe flow.

In this paper, some preliminary heat transfer data have been obtained

on oscillatory heat transfer induced by a sinusoidally reversing flow of air in a heated pipe with constant heat flux. A multivariate statistical analysis [9] was employed to obtain a correlation equation for the cycle-averaged Nusselt number in terms of the three similarity variables: Re , Re_ω , and A_ω .

2. Description of Experimental Apparatus

A closed-loop test rig (see Fig.1), consisting of a pump, a sinusoidal motion generator, an angular velocity signal encoder, a test section, two mixing chambers, two heat exchangers (coolers), and a data acquisition system, was constructed for this experiment. The test section was a long copper tube (73 cm in length and 1.35 cm in diameter with $D/L = 0.0135$) which was heated under constant heat flux. Each end of the test section was connected to a water cooler (40 cm in length) having the same inside diameter as the test section. The working fluid (air) in the tube was driven by a double acting cylinder. The piston in the cylinder was driven by a crank shaft and yoke sinusoidal mechanism. The stroke of the piston can be adjusted from 0 to 70 mm with a speed from 7 to 570 rpm (i.e., 0.12 - 95 Hz). Two mixing chambers composed of plastic screens were inserted between the heating section and the cooling sections in order to provide a mixing cup temperature for the inlet and outlet of the heated tube. Fine type E thermocouples were attached on the screens to measure the mixing cup temperature. An IBM PS/2 computer, together with a plug-in analog-digital (AD) board and two analog input multiplexers, was used as a data-acquisition system.

3. Data Collection

The physical variables measured in the present study were the mean fluid velocity, the frequency and amplitude of oscillation, the wall

temperature of the heater, and the instantaneous bulk temperatures of the fluid entering to and exiting from the heated tube. A photoelectric pickup, a chopping wheel, and an angular signal encoder were employed to measure the angular position of the sinusoidal motion. The wall temperature was measured by three fast response film thermocouples located at both ends and at the middle of the test section. Five type E thermocouples were used to measure the bulk temperature of air at the inlet and outlet of the heated tube.

4. Results and Discussion

Forty experimental runs were performed for air ($Pr = 0.7$) in a heated tube with $D/L = 0.0185$ for the following range of the similarity parameters:

$$15 < Re < 7,000$$

$$7 < Re_\omega < 180$$

$$0.06 < A_\omega < 2.21$$

where $Re = \rho UD/\mu$, $Re_\omega = \rho \omega D^2/\mu$, $A_\omega = \pi U/\omega L$ with U being the cycle-averaged velocity of the fluid, ω the frequency of oscillation, μ and ρ being the viscosity and density of the fluid.

4.1 Bulk Temperatures at the Inlet and Exit of the Heating Tube

Fig. 2 shows the periodic bulk temperature variations of the fluid at one end of the heated tube during a complete cycle for four different experimental runs with $A_\omega > 1$. Since the fluid is reversing periodically, the bulk temperature shown in this figure represents the temperature of the entering fluid during the first half cycle (crank angle from 0° to 180°), and those of the exiting fluid during the second half cycle (crank angle from 180°

to 360°). Each of these curves can be idealized into four different phases as shown in Fig. 3. Point A is the temperature of the displaced hot fluid when it reverses its direction and re-enters the heated tube. Thus, the fluid temperature T_A is at a temperature close to the wall temperature of the heated tube. As time progresses, this temperature continues to drop because of the cooling effect on the displaced hot fluid. The duration of Phase I, which can be considered as the thermal history effect of the cooler, depends on the ratio of the fluid displacement to the length of the cooler and the effectiveness of the cooler. Thus, owing to the thermal history effect, the temperature of the entering fluid drops continuously toward the cooler temperature during the half cycle. Consequently, the heat transfer rate from the heated tube to the entering fluid decreases because of this effect. Phase II begins at point B when most of the displaced hot fluid has returned to the heated tube. As a result, the temperature of the fluid (T_B) entering the heated tube is now closest to that of the wall temperature of the coolers. Phase III begins at point C where the fluid begins to reverse its direction, and the entrance of the heated tube now becomes the exit. As time progresses, the temperature of the fluid exiting from the heated tube is getting higher because the fluid is being heated at constant heat flux. It can be shown that the duration of Phase III, which can be considered as the thermal history effect of the heater, depends only on the ratio of the fluid displacement relative to the length of the heater. The peak temperature T_D is closest to the wall temperature of the heated tube since this part of the fluid traveled twice along the heating section and was heated for the longest duration during the cycle. The drop in the exit fluid temperature during Phase IV is owing to the cooling effect of the cooler and heat conduction from the hot displaced fluid to the adjacent cooler fluid. At point E the displaced hot fluid has been completely blown out from the heated tube during the second half cycle. Exit fluid temperature is relatively constant during phase V.

Since the reversing flow changes its direction every half cycle, the thermal condition at the end of the half cycle becomes the initial condition of the next half cycle while at the same time the exit condition suddenly becomes the entrance condition. This results in a situation where the temperature of fluid entering the test section may be higher than that of the fluid exiting from the test section. This situation is represented by the shaded areas in Fig. 4 where the solid lines indicates the entering fluid temperature while the dashed lines indicate the exiting fluid temperature. Note that this situation occurs during the early part of both forwarding and returning strokes.

4.2 The Nusselt Numbers

Other quantities of interest are the instantaneous and cycle-average Nusselt numbers. The instantaneous Nusselt number is defined as

$$Nu = qD/k(T_w - T_b) \quad (2)$$

where q is the instantaneous heat flux between the wall and the fluid and T_w is the wall temperature; T_b is the instantaneous bulk temperature of the oscillating fluid in the heated tube which can be calculated as

$$T_b = (T_i + T_o + T_c)/3 \quad (3)$$

where T_i and T_o are the instantaneous bulk temperatures of the fluid at the inlet and outlet of the heated tube while T_c is the instantaneous bulk mean temperature of the fluid residing in the heated tube. The instantaneous Nusselt number is a function of the following parameters:

$$Nu = f(Re, Re_\omega, Pr, A_\omega, R, \tau) \quad (4)$$

where Re , Re_ω , A_ω are the Reynolds number, the dynamic Reynolds number, and the dimensionless fluid displacement mentioned earlier; Pr , R , and τ are the Prandtl number, the length ratio of the cooler to that of the heater, and the dimensionless time which are defined as

$$Pr = \alpha/\nu, \quad R = L_c / L, \quad \text{and } \tau = \omega t \quad (5)$$

where α and ν are the thermal diffusivity and the kinematic viscosity of the fluid, t is the dimensional time, and L_c is the length of the cooler.

Integrating the instantaneous Nusselt number over a complete cycle gives the cycle-averaged Nusselt number

$$Nu_{av} = \frac{1}{P} \int Nu \, d\tau \quad (6)$$

where P is the period of oscillation. For the present experiment with $R = 0.533$ and only air ($Pr = 0.7$) was used as the working fluid, the functional dependence of the cycle-averaged Nusselt number is reduced to

$$Nu_{av} = f(Re, Re_\omega, A_\omega) \quad (7)$$

which is a four dimensional space. A multivariate method [9] was used to obtain a correlation equation for the cyclic average Nusselt number based on forty data points. The result of this analysis gives

$$Nu_{av} = -0.494 + 0.0777 \left(\frac{A_\omega}{1 + A_\omega} \right)^2 Re^{0.7} - 0.00162 Re^{2.4} Re_\omega^{0.8} \quad (8)$$

which is valid for $15 < Re < 7,000$, $7 < Re_\omega < 180$, and $0.06 < A_\omega < 2.21$ for air

($Pr = 0.7$) with $R = 0.533$. To assess the accuracy of the correlation equation, the forty data points of the Nusselt number (Nu_{ex}) are plotted in the horizontal coordinate in Fig. 5, and the corresponding Nusselt numbers given by the correlation equation (Nu_{av}) are plotted in the vertical coordinate. An inclined straight line for $Nu_{ex} = Nu_{av}$ is also plotted in Fig. 5 for comparison purposes. Since most of the data points deviate only slightly from the straight line, it can be concluded that Eq.(8) correlates the experimental data quite well.

5. Concluding Remarks

Because of the thermal history effect and the ineffectiveness of the cooler, the temperature of the hot displaced fluid re-entering the heater decreases continuously during the first part of the half cycle. This effect decreases the heat transfer rate from the heater to the fluid. A method has been proposed for the definition of the instantaneous and the cyclic average Nusselt number in an oscillating and reversing flow. Based on preliminary experimental data, a multivariate statistical method was applied to obtain a correlation equation for the cycle-averaged Nusselt number in terms of the Reynolds number, the dynamic Reynolds number and the dimensionless Stroke.

REFERENCES

1. Akhavan, R. D., Kamm, R. D., and Shapiro, A. H., J. Fluid Mech., v.225, pp.423-444 (1991).
2. Hino, M., Sawamoto, M., and Takasu, S., " J. Fluid Mech., v.75, Part 2, pp.193-207 (1976).
3. Seume, J. R. and Simon, T. W., 21st IECEC Proceedings, pp.533-538 (1986).

4. Kornhauser, K. and Smith, J. L., Jr., On Flow in International Combustion Engines, v.1, edited by T. Uzman (1989).
5. Hwang, M. F. and Dybbs, A., ASME Paper #83-WA/HT-90.
6. Iwabuchi, M. and Kanzaka, M., " I. Mech. Engineers, C24/82, 135 (1982).
7. Roach, P. D. and Bell, K. J., Rept. # ANL/MCT-88-2, Argonne National Laboratory, Argonne, Illinois (1988).
8. Wu, P., 13th IECEC, 1 (1990).
9. Tabachnick, B. G. and Fidell, L. S., Using Multivariate Statistics, Harper and Row (1989).

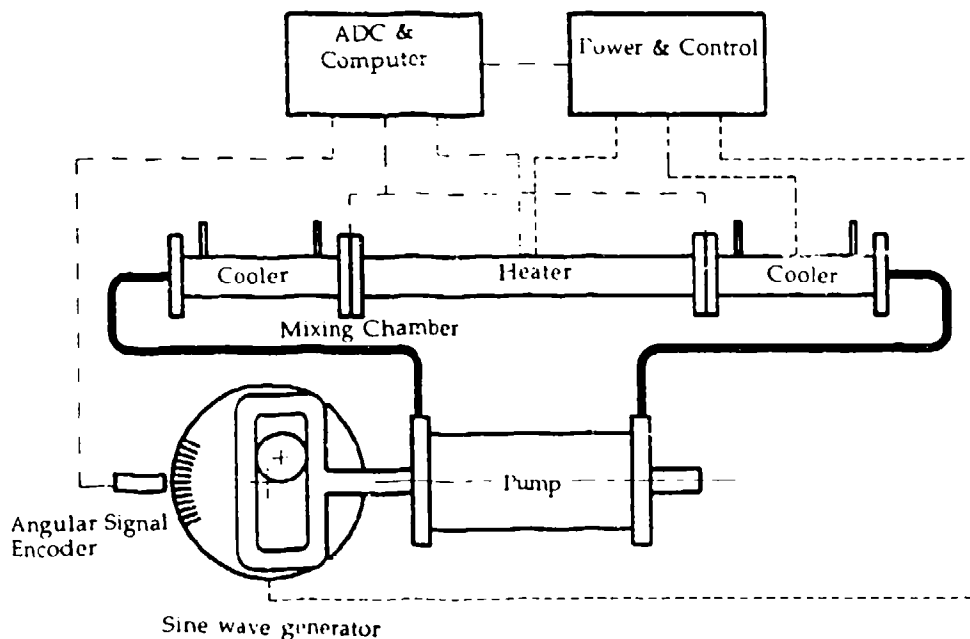


Fig. 1 Schematic diagram of the test rig

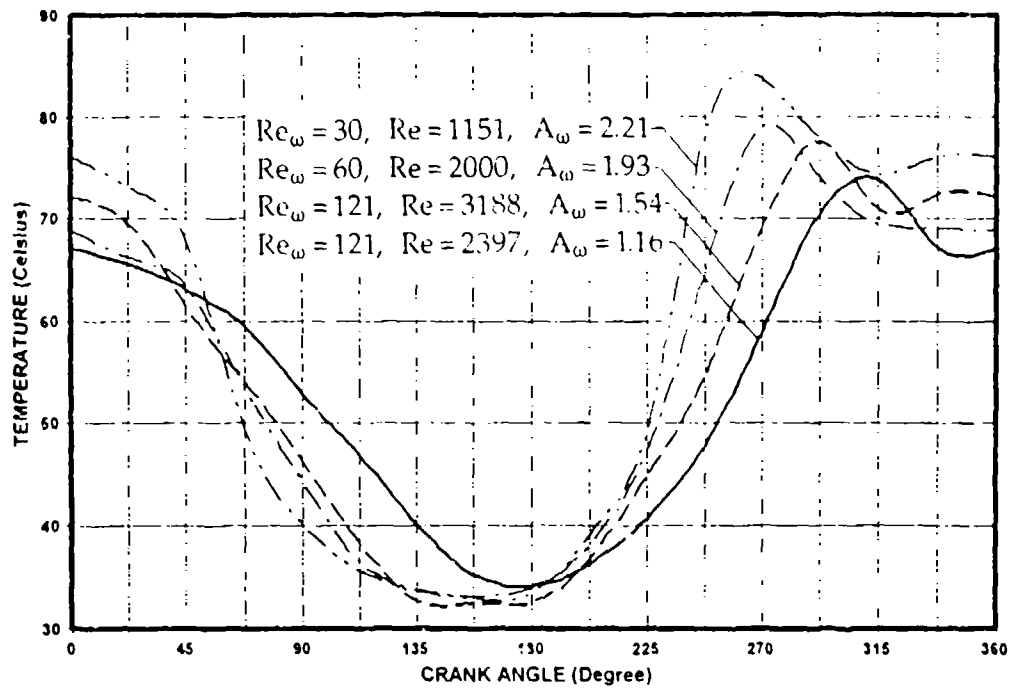


Fig. 2 Bulk fluid temperature variations at one end of the heater

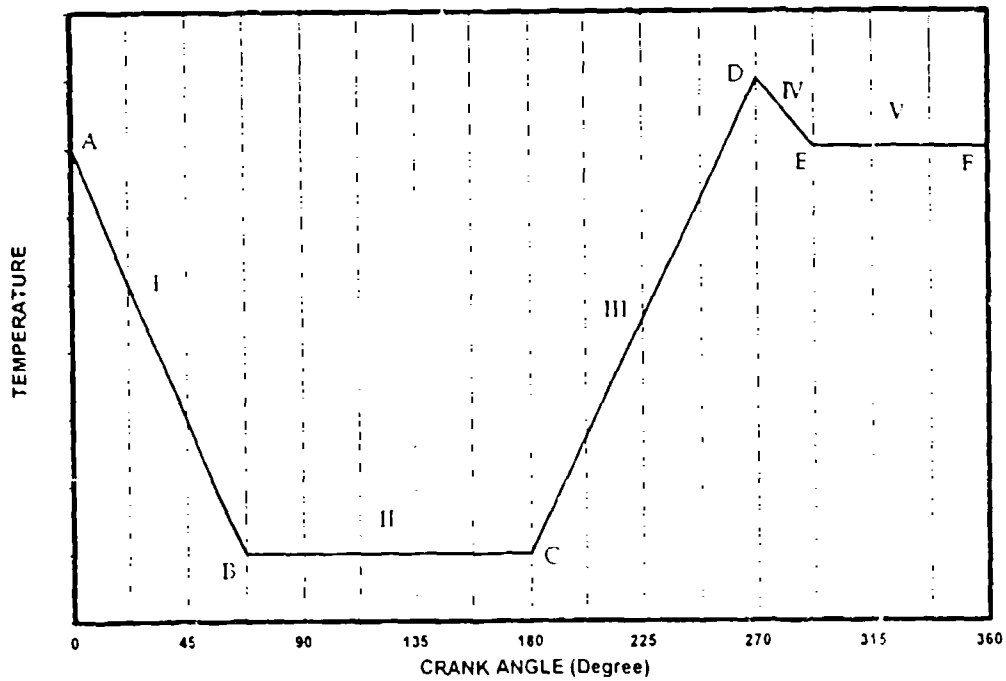


Fig.3 Idealization of bulk temperature variations

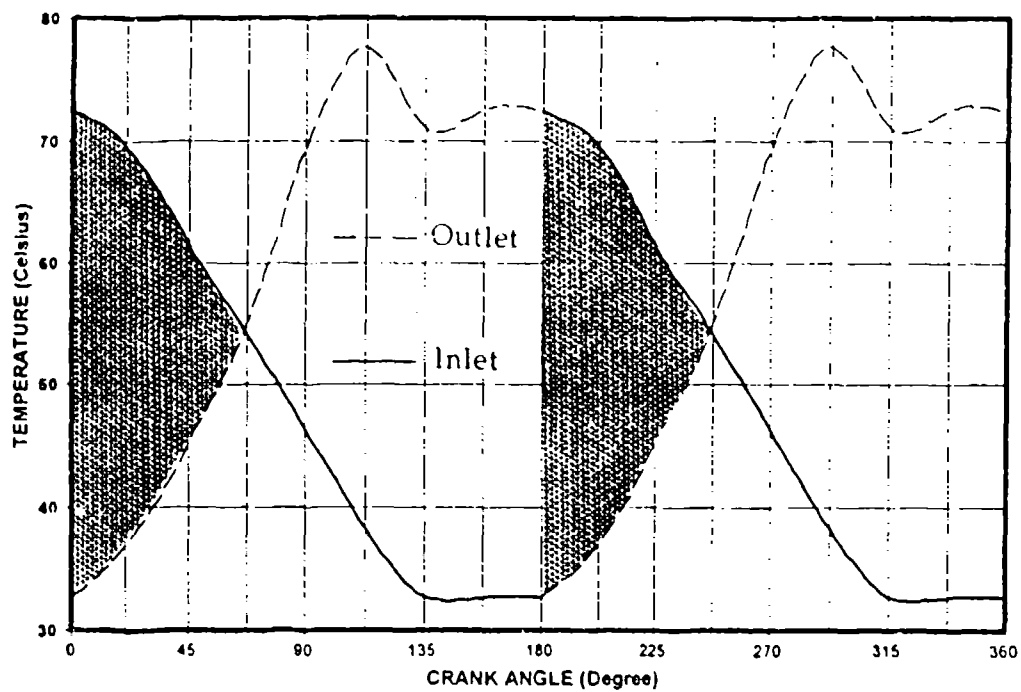


Fig.4 Inlet and outlet bulk temperature variations

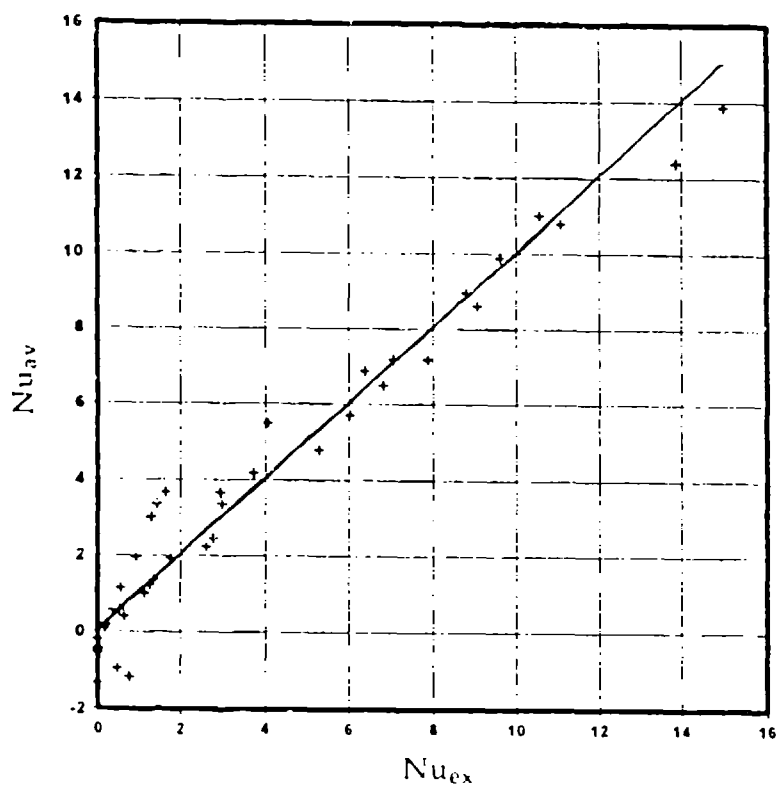


Fig. 5 Accuracy of the correlation equation

**THERMOELECTRIC COOLERS FOR THE
TWS, SFW, WAM AND SADARM PROGRAMS
AND ASSOCIATED MANTECH PROGRAM OBJECTIVES**

BY

**WILLIAM L. KOLANDER, BARRY MORRISON,
JIM BIERSCHEK OF MARLOW INDUSTRIES,
DALLAS, TEXAS**

**JIM FUHRER OF ARMY NIGHT VISION AND ELECTRO-OPTICS DIRECTORATE,
FORT BELVOIR, VIRGINIA
CAPTAIN TIM KOTTAK OF THE AIR FORCE MANUFACTURING DIRECTORATE
WRIGHT PATTERSON AFB, OHIO**

**PREPARED FOR THE
7th INTERNATIONAL CRYOCOOLER CONFERENCE**

**PRESENTED AT
SANTA FE, NEW MEXICO**

**ON
17 NOVEMBER 1992**

**THIS DOCUMENT IS UNCLASSIFIED
AND UN-RESTRICTED**

ABSTRACT
THERMOELECTRIC COOLERS FOR THE
TWS, SEW, WAM AND SADARM PROGRAMS
AND ASSOCIATED MANTECH PROGRAM OBJECTIVES

Authors: William L. Kolander, Barry Morrison, Jim Bierschenk of Marlow Industries, Inc. and Jim Fuhrer of Army Night Vision and Electro-Optics Directorate and Captain Tim Kottak of the Air Force Manufacturing Directorate.

The Mantech Program is comprised of a two year effort at Marlow Industries directed toward establishment of production rate capability for four DOD critical thermoelectric cooler devices. Contract DAAB07-91-C-K258 originated out of CECOM with technical and financial cognizance from the US Army Night Vision and Electro-Optics Directorate, Ft. Belvoir, VA., and the US Air Force Manufacturing Directorate at WPAFB, Ohio.

Performance parameters ranging from single stage, fast transient, low power consumption units through two stage ruggedized and six stage, low power consumption, large delta temperature units have been optimized and measured. Constraints such as high "G" set-back during launch have been evaluated, analyzed and resolved. Line drawings and graphs present the configurations of the coolers allowing systems designers to implement this technology.

Improved production rate capability via automated assembly, cleaning, inspection and testing work stations have been designed, procured and are being implemented allowing projected cost savings of \$80M.

The THERMOGENIC™ Division of Marlow Industries has initiated work on the next generation of thermoelectric materials to manage the technology required to extend performance to 120K and below.

1.0 INTRODUCTION AND BACKGROUND

Thermoelectric coolers (solid state semiconductor Peltier devices) have been designed, manufactured, qualified and delivered for numerous weapon systems, thermal viewers and missile guidance systems as well as space applications in accordance with explicit needs of the Department of Defense.. This paper discusses an on going

MANTECH program initiated to reduce cost and increase the production rate capability for four particular units which were designed specifically for the Sensor Fuzed Weapon (SFW), Seek and Destroy Armor (SADARM), Thermal Weapon Sight (TWS) and Wide Area Mine (WAM) programs. Many other applications will also benefit from the cost reductions in coolers provided by the automated production facility developed at Marlow Industries on the MANTECH program.

Having been involved in the early stages of the four program definition stages of the TWS, SFW, WAM AND SADARM programs, Marlow recognized early in 1988 that when all of the programs reach their maturity phases and large scale production rates are required, there will be a dramatic short-fall in industry capacity to manufacture the required coolers. This dilemma was presented to the program offices of each of the four systems and an effort was initiated to address these issues. It was also observed that the production prices and life cycle costs for the required TEC units would impact the affordability of the weapons and viewer systems. Figure 1-1 is a current estimate of the volume projections for the four programs through CY2005.

Mantech Thermoelectric Cooler Production Requirements (SFW, WAM, SADARM, TWS)

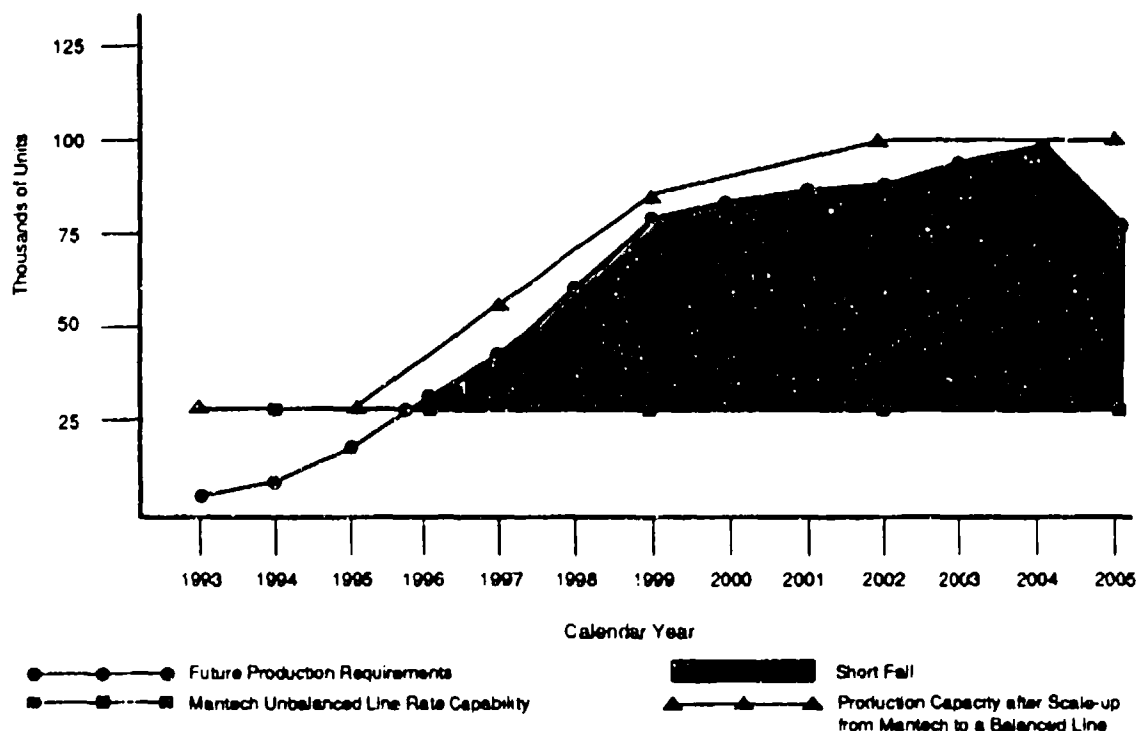


Figure 1-1

Because the production capacity shortfall has a multi-service impact, the US ARMY and USAF were challenged to initiate a co-operative effort which would provide the necessary thermoelectric cooler manufacturing capacity with acceptable unit cost and pricing budgets.

MANTECH effort is in month twenty of a twenty-four month contract. One of two Demonstrations To Industry which will be accomplished under this contract will be conducted at Marlow Industries, Inc.'s Dallas, Texas facility on 18 November 1992.

2.0 TE COOLER RELATED THEORY, TECHNICAL REQUIREMENTS/PERFORMANCE

Thermoelectric coolers (TECs) are small, light weight, solid state, low power consumption, vibrationless heat pumps that have no moving bearings, pistons or parts and use no CFC or other gases.

They obey the laws of thermodynamics as do conventional mechanical absorption pump refrigerators, Stirling cycle coolers and other devices involving the transfer of heat energy.

2.1 SINGLE AND MULTI-STAGE THERMOELECTRIC COOLERS

A single stage TEC is comprised of a matrix of thermoelectric couples, connected electrically in series and thermally in parallel. The thermoelectric couple consists of p- and n- type semiconductors rather than dissimilar metals as used by Peltier resulting in modules with superior performance. A TEC can be fabricated with as few as one couple or as many as several hundred couples contained between two or more ceramic plates. These plates form the top and base of the cooler and provide structural integrity as well as electrical insulation from, and thermal conduction to, the heat sink and the device being cooled. Regulating the direction and amount of current - with the use of a feedback loop and temperature controller - allows TECs to cool, heat or stabilize temperature (eg. temperature stabilization of "uncooled" FLIR detectors).

When a positive DC voltage is applied to the n-type thermo-element, electrons pass from the p- to the n- type thermoelement and the cold side temperature (T_c) will decrease as heat is absorbed. The heat absorption (cooling) is proportional to the current and the number of thermoelectric couples, and occurs when electrons pass from a low energy level in the p-type element, to a higher energy level in the n-type thermoelement. The heat is then conducted (transported) via this electron current through the "leg" or thermoelement to the hot side (T_h) and

liberated as the electrons return to a lower energy level in the p-type element.

Although the Peltier cooling is proportional to the current applied to the TEC, the power dissipated by Joule heating in the TEC is proportional to the square of the current, and it can be shown that half of this Joule heat must be pumped from the cold junction. For this and other reasons, an increase in current above a certain value will result in less net cooling because Joule Heating and other parasitic losses increase at a faster rate than the Peltier cooling. The value of current which yields the greatest cooling is termed "I_{max}".

Adequate heat sinking and close attention to configuration form factors are among the primary drivers that enable or impede TEC devices to perform the intended cooling function adequately. Figure 2-1 shows a simplistic single and multi-stage cooler to provide visualization of the cooling devices when relating to the fabrication cycle.

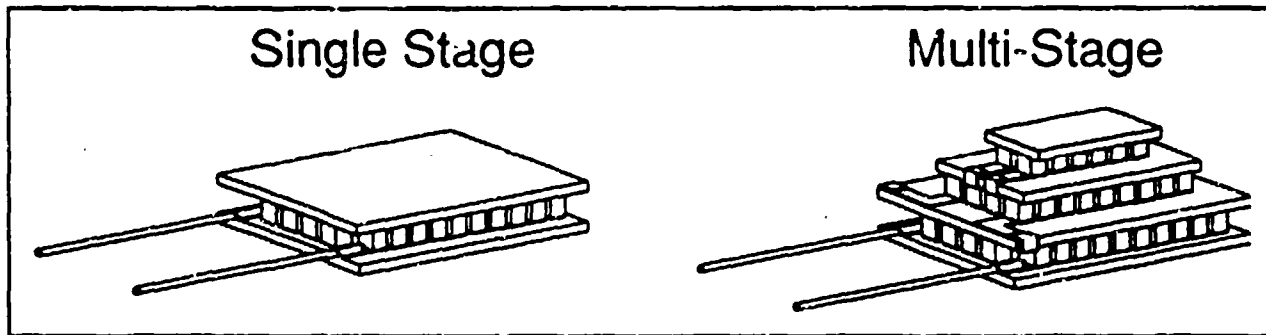


Figure 2-1

A multi-stage TEC is essentially two or more single-stage TECs, stacked vertically with fewer thermocouples in each ascending stage. They are therefore typically pyramid-shaped, because the lower stage requires more thermoelectric couples to pump the heat dissipated by the upper stages, in addition to the heat pumped from the cold side or device to be cooled.

2.2 SPECIFIC COOLER PERFORMANCE OF THE FOUR MANTECH COOLERS

2.2.1 SFW AND WAM THERMOELECTRIC COOLER MODULES

Performance curves for the SFW and WAM coolers are shown in Figure 2-2 and 2-3. This method of presentation for performance data is utilitarian since a potential user of the device can determine what the unit will do under

various trade-off operational conditions. Maximum heat pumping capability with no temperature differential and maximum temperature differential with no heat pumped are shown with the family of curves for all conditions between these two points.

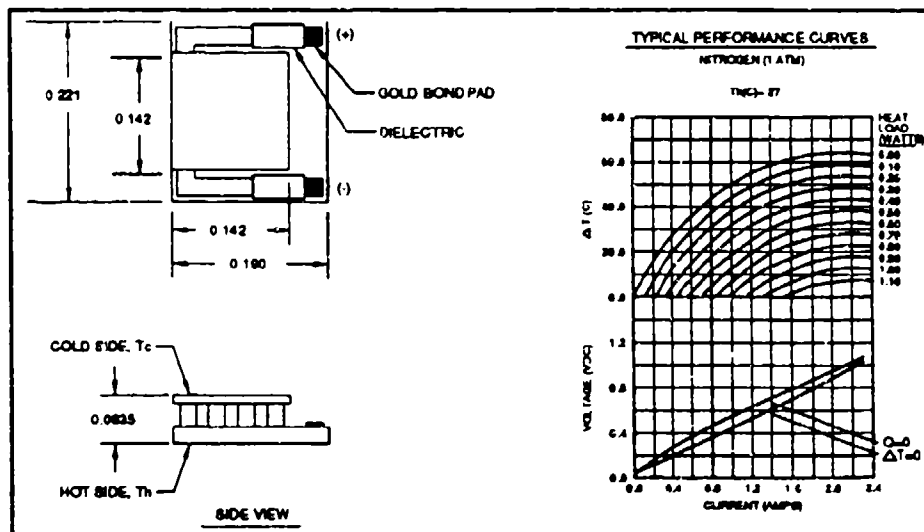


Figure 2-2, SFW Performance Characteristics

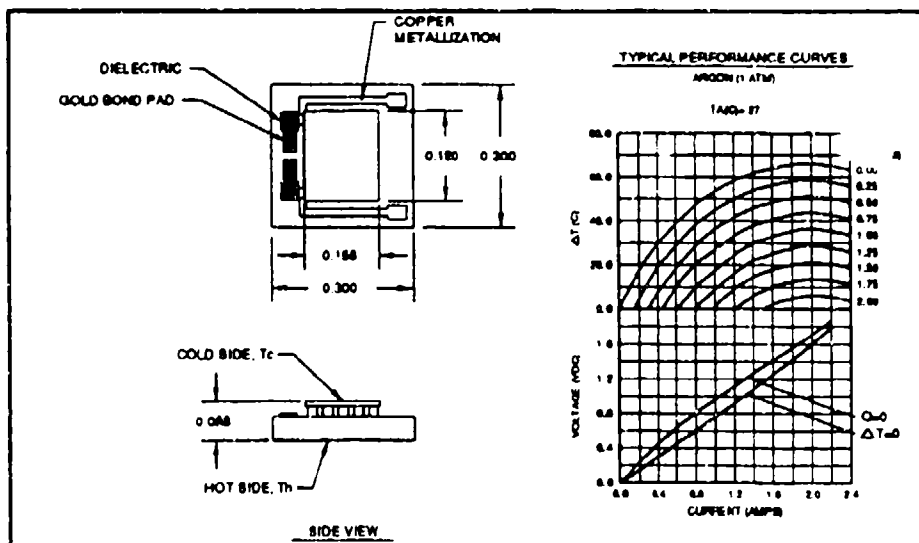


Figure 2-3, WAM Performance Characteristics

The SFW and WAM thermoelectric coolers are both single stage coolers that cool relatively simple infrared detector arrays or elements that are used in air-dropped or ground emplacement launching platforms. Both detector devices have few wires that come off of the cooled focal plane and the active Joule heating imposed by their biasing circuits are minimal. The units are both operating in a dry back-filled Argon atmosphere, so there are some conductive and convective loads which must be accommodated. Since the mission time is short and the hermetically sealed package containing the cooler/detector has no moisture in it, there is no concern for frosting or moisture condensation during the flight-search time.

Both devices require rapid cool down to accomplish their respective missions. Careful consideration of thermal masses, specific heat of constituent parts, size and thickness of parts as well as structural integrity of materials must be taken into account to optimize the total assembly operational performance characteristics. Fast Transient thermal modelling programs and algorithms had to be generated to analyze the designs to allow trade studies to converge on the optimized designs for the particular mission requirements.

Both WAM and SFW coolers are required to contain gold bond pads capable of accepting thermo-sonic ball and stitch bonds; this will allow automatic wire bonding and assembly during subsequent manufacture of the sensor products. Preliminary processes for this bonding pad accommodation have been developed and are presently being revised to increase throughput and provide better adherence of the ball or stitch bonds. Details of these bond pads can be seen on the line drawings in Figures 2-2 and 2-3.

2.2.2 THERMAL WEAPON SIGHT (TWS) COOLER

The TWS cooler is a six stage cooler which must reach temperatures well below 180K (-93 degrees Centigrade) and pump the required heat load with 3.5 watts of input power provided by batteries in the man-portable thermal viewer. While the response time is not deemed to be "Fast Transient", as are the requirements for the SADARM, SFW, and WAM, the cooler is capable of reaching the operating temperature much faster than a Stirling cycle or Brayton cycle cooler. Figure 2-4 contains a picture of this six stage cooler as contained within the Hughes Aircraft TWS unit. Other performance parameters are also contained within this figure that provide FPA operational temperature performance as a function of varying ambient temperatures.

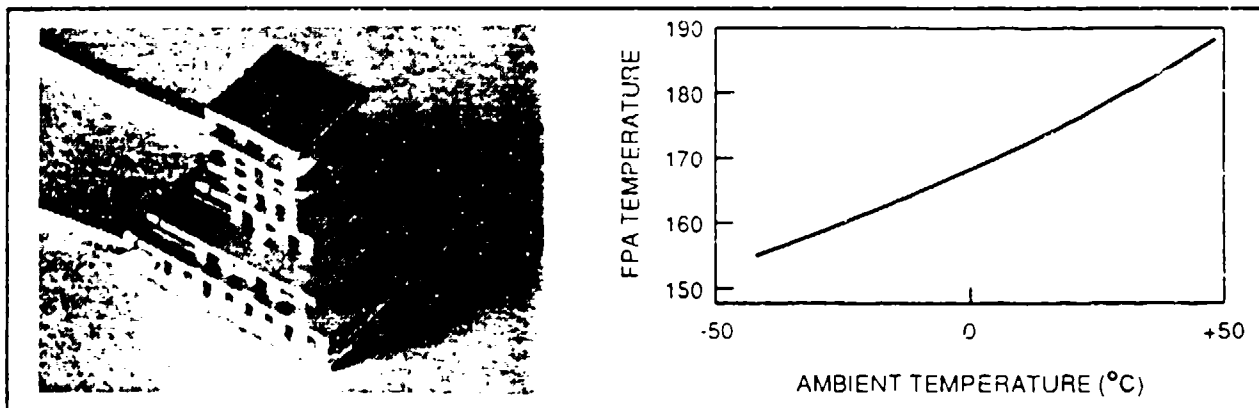


Figure 2-4

2.2.3 SEEK AND DESTROY ARMOR (SADARM)

The SADARM cooler contains two stages and pumps over 70 milliwatts from 235K (-38 degrees Centigrade) to a heat sink at +50 degrees Centigrade. This unit is again considered to be a "Fast Transient" unit since it must rapidly reach it's operating temperature.

Due to the fact that it is fired out of a 155mm Howitzer or the MLRS system and encounters severe high "G" setback and shock as well as centrifugal acceleration, the two stage TEC had to be potted with a closed cell potting compound to enable it to withstand this harsh environment. Potting the cooler derates its Delta Temperature by 8.5%.

Multiple trade off analyses had to be performed and multiple prototype units were fired during rail and gun fire tests to arrive at the current optimized design. Figure 2-5 contains a drawing which shows the dimensional characteristics of the cooler.

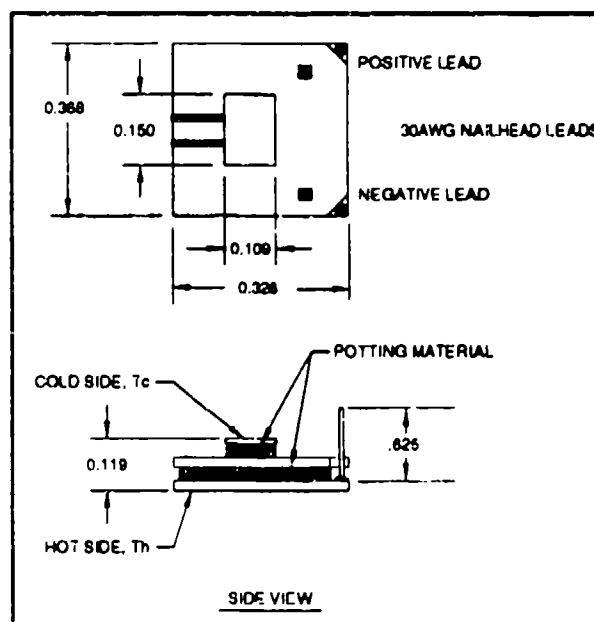


Figure 2-5

3.0 MANTECH CONTRACT SCOPE, STATUS AND ACCOMPLISHMENTS

3.1 CONTRACT SCOPE

This MANTECH program (Contract No. DAABO7-91-C-K258) is a joint US ARMY and US Air Force program initiated to significantly reduce the cost of thermoelectric cooling devices for the SFW, WAM, SADARM AND TWS programs and provide a manufacturing rate capability to accommodate planned and "surge" production rate requirements.

The specific technical requirements provide for a two-phase program. Phase 1 addresses single stage coolers for the SFW AND WAM programs and generic assembly processes and procedures capable of accommodating multi-stage TEC fabrication. Phase 1 requires the demonstration of a manufacturing capability which will support a 1000 unit/day production rate for the single stage coolers. Phase 2 similarly will demonstrate a combined 1000 unit/month production rate for the SADARM AND TWS program coolers. These two planned "Demonstrations to Industry" are contractual line items which are a part of the benefit transfer objectives set forth in the MANTECH contract statement of work.

Deliverable items under the contract include thermoelectric cooler units of each of the four device types manufactured using recently developed manufacturing technologies, technology transfer data items such as process specifications, tooling drawings, comprehensive reports and industry demonstrations.

3.2 CONTRACT STATUS AND ACCOMPLISHMENTS

Marlow Industries has investigated numerous options and alternate methods for the manufacture and test of thermoelectric cooler modules to contrast and expand from our previously existing "base-line" process. It was from this baseline process that we drew the comparisons of production rate capability, yields and cost. The new MANTECH optimized processes to be described here-after were chosen based upon the following criteria:

- | | |
|--------------|---|
| *Capacity | *Tooling requirements |
| *Throughput | *Yield rates |
| *Labor costs | *Other critical issues that accrued with time |
| *Risks | |

The specific elements of the fabrication process that are being addressed to effect the desired production rate capabilities and costs are shown below.

- *Thermoelement inspection and sorting
- *Thermoelement loading into a cooler module solder fixture
- *Solder reflow to solidify the cooler assembly
- *Provision of Wire bondable pads or provision for wire attach
- *TE cooler cleaning and drying
- *Application of low emissivity coatings to multi-stage coolers
- *Potting of coolers for High "G" environments
- *Automated screening, environmental and performance testing
- *Precision mounting of cooler modules in dewars and headers

The equipment layout for the improved MANTECH process for assembly, clean and test is shown in Figure 3-1. The unique attachments, jigs and fixtures to accomplish the various operations of the MANTECH program were funded by the government while Marlow Industries provided funds for the capital equipment to which they were attached. Marlow also has ongoing programs to develop and increase their thermoelectric cooler material performance and production capability.

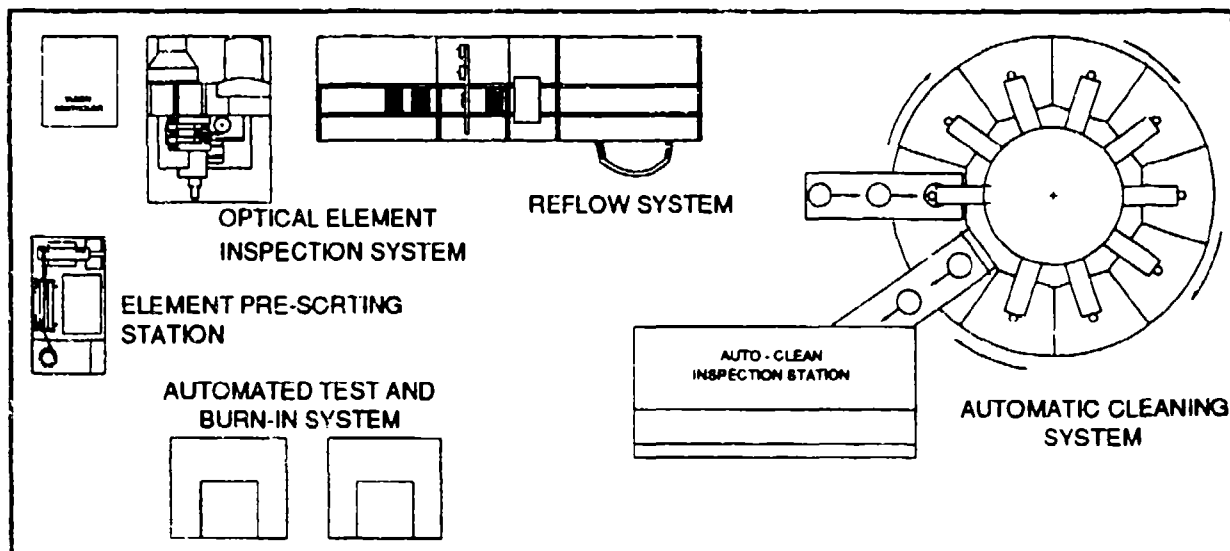


Figure 3-1, MANTECH Equipment Layout

Expanded explanation of the major stations and their functions will follow.

3.2.1 ELEMENT PRE-SORTING STATION

The baseline process used prior to MANTECH was accomplished by an operator sitting at a microscope to hand pick the good elements from among the pile of good elements, slivers, chips and shards. This was extremely time consuming and was subject to operator skill and state of alertness. Yields were poor and rate was a pacing item.

The new element pre-sorting station accepts the thermoelements from the front end where they have been grown, plated and cut into the required form factors for each cooler. The vibratory bowl orients the approximately cubic elements and presents them in the proper orientation to the roller bars which are precisely aligned to separate and remove chips and splinters of the semiconductor elements. Semi-screened "good" elements then progress into another vibratory station which separates bad elements by a screen mesh system. This station is shown in Figure 3-2.

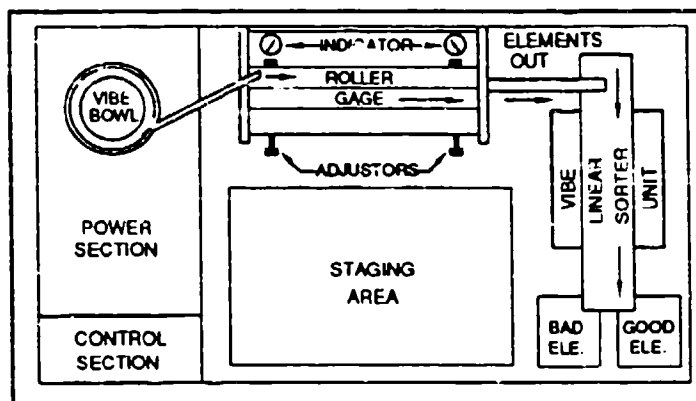


Figure 3-2

3.2.2 MANTECH VISUAL ELEMENT INSPECTION SYSTEM AND PICK AND PLACE SYSTEM

Baseline process consisted of three distinct processes which were inspection, orientation and insertion into the matrix. When performed manually the operator picked up the element with micro-manipulation tweezers, visually inspected it under a microscope, rotated it to the proper orientation and inserted it into a rubber matrix in the proper half-fill pattern.

Since it is so critical that no faulty elements get loaded into a thermoelectric cooler matrix, an additional element inspection station was required. Should one bad element get into a cooler it will be a reject since all elements are electrically in series. A three camera visual inspection station looks at three sides of each element and feeds the digitized video image to a computer that contains pattern recognition algorithms that make go/no-go decisions on

each element inspected. Elements with any of a large number of reject criteria are expunged from the assembly line. This assures that all elements that are incorporated into TEC units are of the highest quality available.

Figure 3-3 provides detail of this station.

Also included at this station is the automatic element pick and place system which incorporates vacuum chucks that pick the elements up, properly orient them, positions them in the matrix and rotates the partially filled matrix to a location where it is then fed to the other type semiconductor element station, which is an identical system, for the completion of the matrix fill operation.

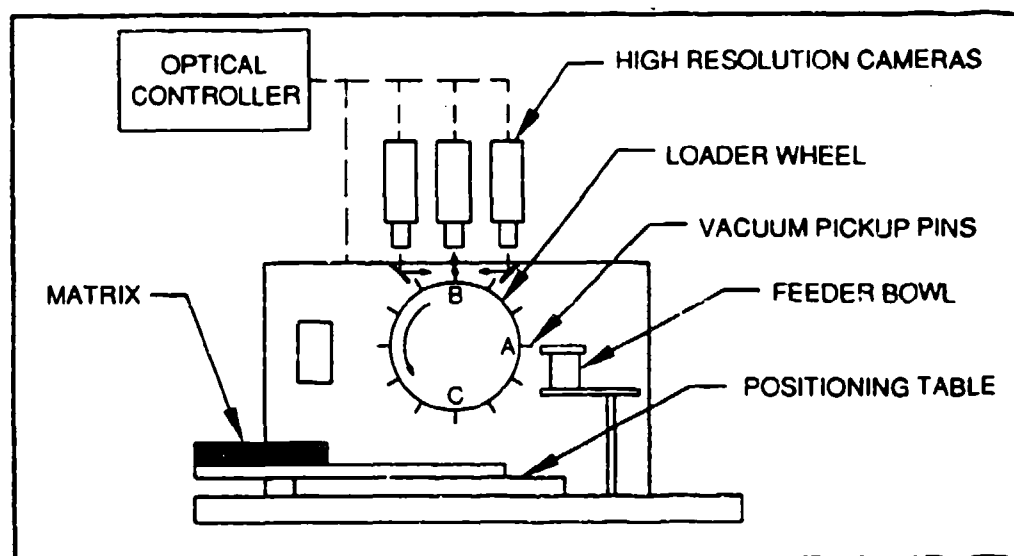


Figure 3-3

3.3.3 MANTECH REFLOW SYSTEM

Previously, the reflow operation consisted of taking a properly filled bottom ceramic-rubber matrix and placing a non-metallized ceramic on the top of the matrix and applying heat with a soldering iron until the bottom stage solder reflowed securing the thermoelectric elements to the base. The matrix was then removed and the top ceramic with pre-tinned metal pads on it that corresponded to the element pattern was placed on top of the elements. Again heat was applied until the solders reflowed and the total unit was then securely soldered together. A non-contact heating method was required for the MANTECH process to reflow the solders which were contained within the TEC structure while it was still an assemblage of un-attached piece parts. Since high tempera-

ture solders (183 Degrees Centigrade) or higher may be implemented, it was necessary to incorporate a heater mechanism capable of routinely accommodating these temperatures. After having evaluated condensation (vapor phase), radiant heating and hot nitrogen; infrared heating methods were investigated and chosen. This method provides the desired through-put rate and temperature range capability. An enlarged view of this station is presented in Figure 3-4.

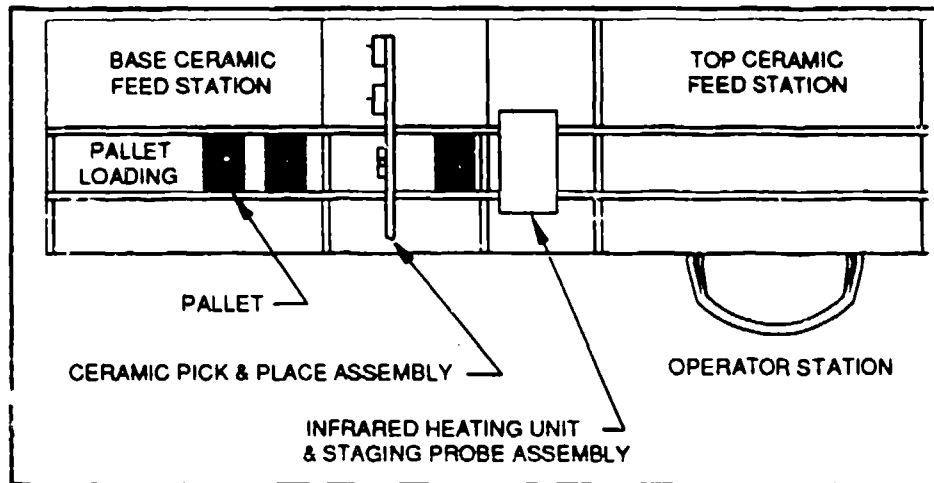


Figure 3-4

3.3.4 AUTOMATIC CLEANING SYSTEM

Prior cleaning techniques were quite laborious and frequently did not do an adequate job of cleaning off the flux residues and other chemical deposits that precipitate during the soldering operations. Many different techniques have been tried some of which were boiling in de-ionized water while agitating the water with ultrasonic devices and another was manual scrubbing with very small bristle brushes.

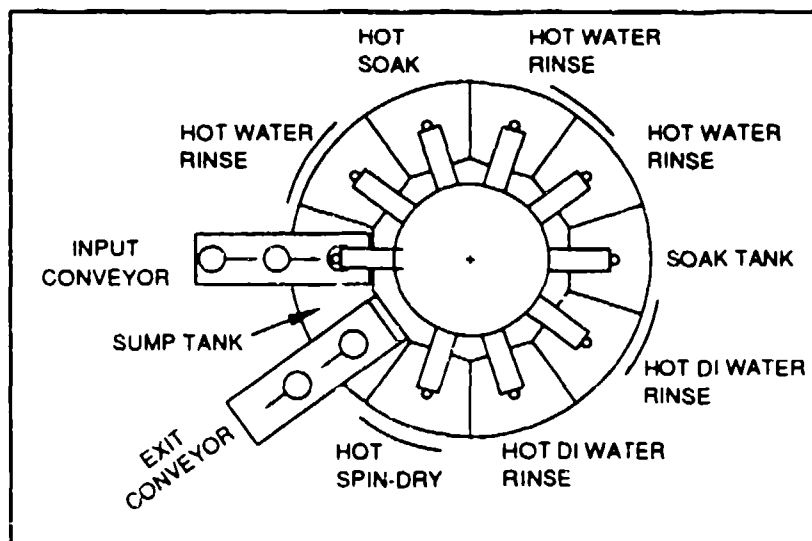


Figure 3-5

An automated cleaning system capable of accepting TEC modules from an input conveyor and rotating them around the various baths, chemical soaks, hot air dry stations and unload stations that comprise the system is shown in Figure 3-5.

3.3.5 AUTOMATED TEST AND BURN-IN SYSTEM

Manual test stations were previously used where the test operator had to attach the leads via alligator clips, bayonet connectors or solder attach posts. The power supply knobs then were adjusted to seek optimum performance characteristics for the particular module under test. Data was recorded by hand onto data sheets. Computations for adequacy of performance were then accomplished. Coolers were then disconnected and placed in a container.

Due to the large number of TEC units that must be processed and have their lot data correlated, analyzed, retained for trace-ability and stored, it was imperative that an automated system that could be computer controlled be developed. Figure 3-6 shows the resulting system that evolved and is being procured and installed at this time. Computer driven stimulus has been incorporated so that TEC units are subjected to burn-in and 100% parametric testing. The computer software also provides trend, yield and SPC data for facilitating in-process control and correction. Cooler connections are accomplished automatically with the use of Pogo pins and connection pads.

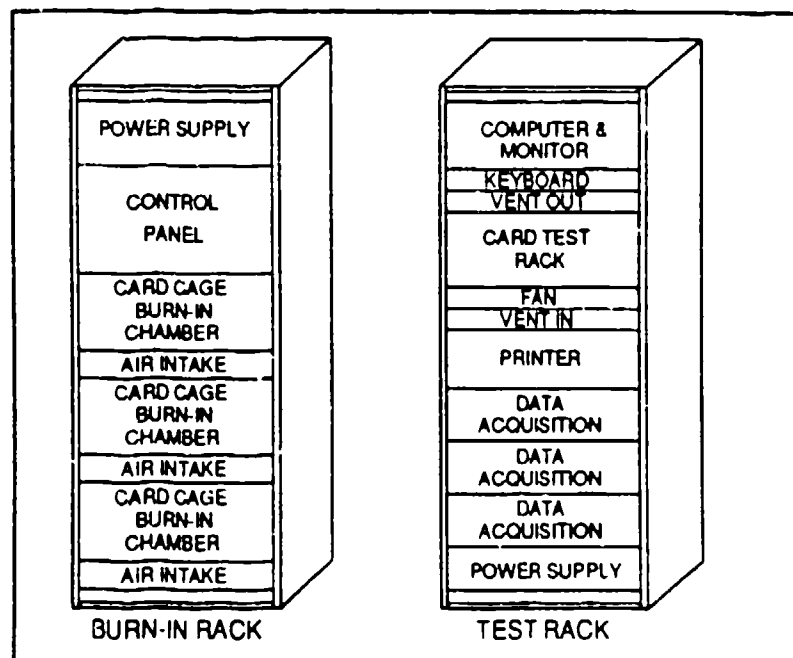


Figure 3-6
345

3.4 MANTECH BENEFITS FOR GOVERNMENT AND INDUSTRY

Some of the Contract objectives established in the statement of work are shown below. Data accrued to date shows that the goals and objectives set forth in the contract are being met or exceeded.

These goals are shown below.

- *Reduce TEC unit cost by Approximately 50%

- *Increase production rate capability to those set forth in the contract

Figure 3-7 presents the most recent estimate of combined WAM, SFW, SADARM and TWS cumulative savings through CY2005 in constant 1991 dollars. These savings are attributed to this MANTECH program.

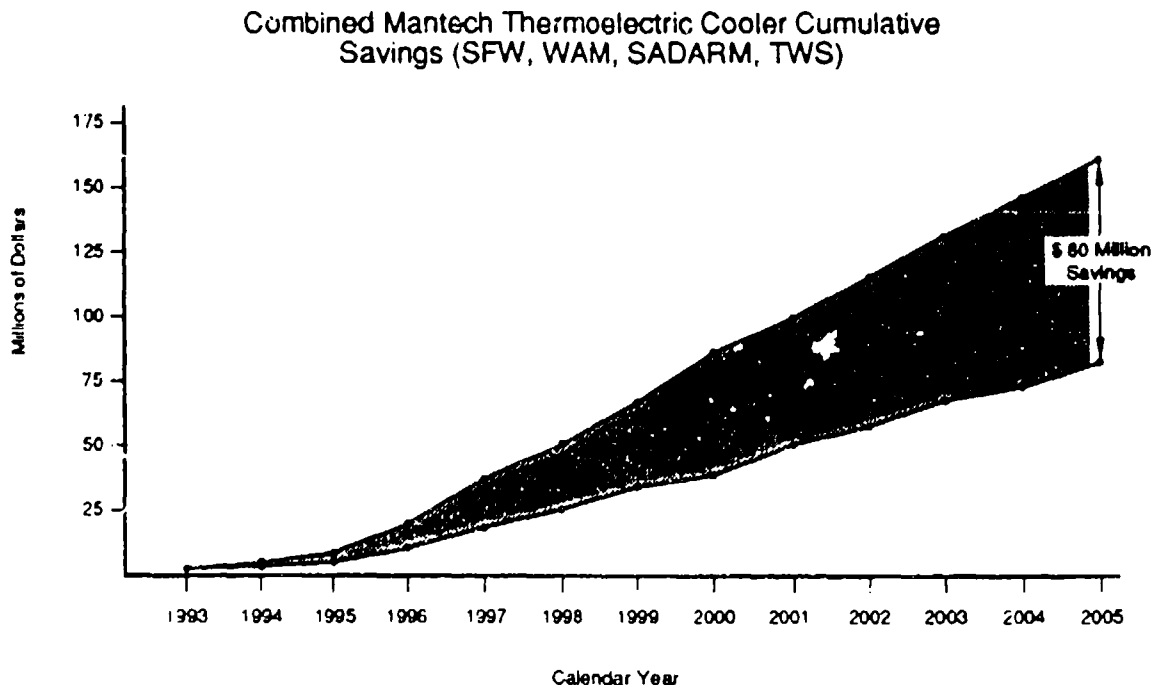


Figure 3-7

4.0 NEXT GENERATION COOLERS, BUILDING ON MANTECH SUCCESSES

4.1 THERMOGENIC™ PROGRAM

Current multi-stage thermoelectric cooler performance is shown in Figure 4-1 which shows the current state-of-

the-art cooling capability. It shows the cooling capability of custom built multi-stage coolers operating in most of the scenarios currently encountered. An example would be: At $T_{\text{hot}} = 300\text{K}$, it takes 17.5 watts to pump 100 milliwatts from T_{cold} of 175K with a six stage TEC for an Infrared Focal Plane Array (IRFPA) and it's attendant on FPA multiplexor.

A national THERMOGENIC™ program has been initiated that will be managed by Marlow Industries, Inc. of Dallas, Texas which is striving to define, characterize and synthesize a family of NEW AND INNOVATIVE thermoelectric materials capable of reaching 120K within four years and 77K within five years. Capabilities of national governmental laboratories, Academia, and industry are being pulled into this program at this time to accomplish these ambitious goals. Material modeling and preparation has already been initiated at some of the major U.S. National Laboratories and Universities with various measures of success reported.

**WATTS/WATTS ESTIMATES FOR OPTIMIZED TECs
AS A FUNCTION OF T_c AND T_h**

T_c / T_h	260	265	270	275	280	285	290	295	300	305	310	
160	230	265	300	426	490	560						
165	135	165	196	230	282	320	361					
170	85	103	126	154	175	197	221	246				
175	58	68	80	102	115	129	143	159	175	190		TWS Performance
180	36	43	50	70	79	88	97	107	118	129		6 Stage TEC
185	27	32	38	47	56	62	69	75	82	90	97	
190	19	22	26	32	37	45	50	54	59	64	70	5 - 6 Stage TEC
195			18	22	25	29	34	40	44	47	51	
200					18	22	25	29	33	36	39	5 Stage TEC
205							19	22	25	28	30	
210									20	22	23	4 - 5 Stage TEC
												4 Stage TEC

Assumptions/Notes:

- Intended for Preliminary estimates of TEC Power consumption
- Watts of TE Input power per watt of total heat pumped
- Assumes Optimized TEC design for each T_c/T_h combination
- Assumes "State of the Art" Tec Design and Materials
- Accurate to within Approximately +/- 20%
- Based on Total heat load between 125 and 300 watts

- Total heat load: all radiation, conductive, and active loads
- Operation in hard vacuum (better than 10^{-6} Torr)
- Design may or may not be practical to build
- Contact Marlow Industries if more accuracy is required
- Typical power limit of a practical TEC is 100 watts

Figure 4-1

The next generation of Thermoelectric/THERMOGENIC™ coolers will of necessity need to grow and proliferate from the work accomplished on the current MANTECH program. New processes and materials will have to be identified, developed and accommodated to be compatible with the extreme temperature differentials to be encountered in the TEC modules of the future. The new family of THERMOGENIC™ materials promise to provide a small, light weight cooler with no moving parts or focal plane vibration, no gases to destroy the environment/ozone layer and a rugged all solid state construction. Figure 4-2 provides a graphic view of the current state-of-the-art cooling capability and the projected benefit area which will be addressed by the innovative THERMOGENIC™ cooler.

The Problem / Opportunity

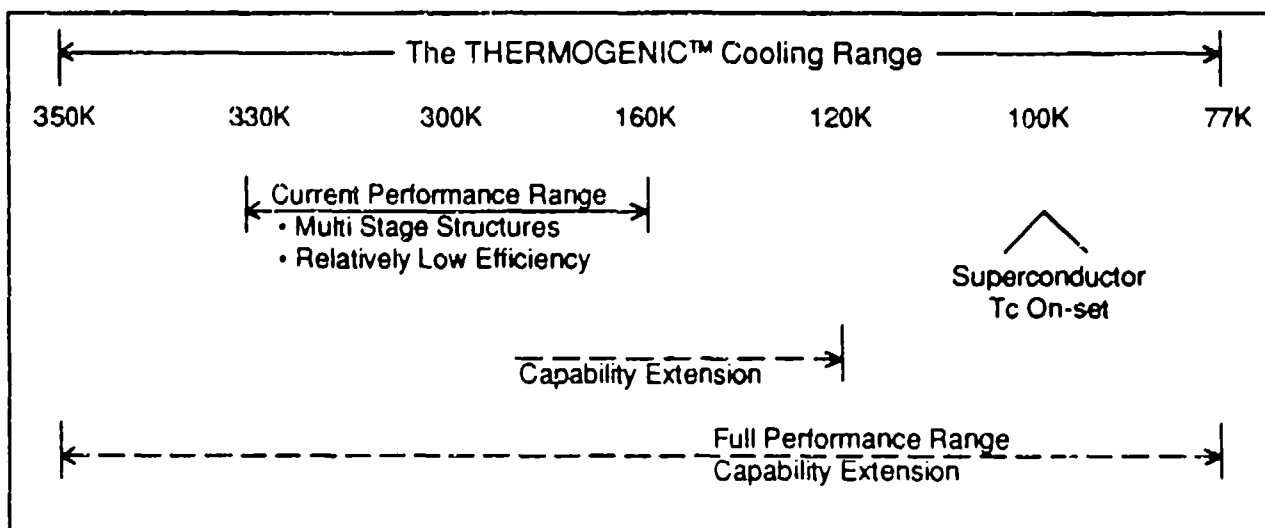


Figure 4-2

CRYOGENIC ATTACHMENT FIXTURE WITH HIGH STRENGTH AND LOW THERMAL CONDUCTION

Pat R. Roach
Space Projects Division
NASA Ames Research Center
Moffett Field, CA 94035

ABSTRACT

In the development of cryogenic systems for space application it is frequently necessary to securely anchor low-temperature components to high-temperature surroundings. This inevitably requires some trade-off between the conflicting requirements of high strength and of low thermal conduction through the anchor.

An attachment fixture using strands of Kevlar has been developed that is extremely strong and stiff while at the same time it allows only a tiny amount of heat to flow to the low-temperature component. The fixture consists of two metal beams at different temperatures that are connected by eight strands of pretensioned Kevlar in such a way that neither beam can move with respect to the other in any direction. The method by which the Kevlar is anchored allows the full strength and stiffness of the Kevlar to be achieved. The only thermal-conduction path from the high-temperature beam to the low-temperature beam is along the length of the thin Kevlar strands.

INTRODUCTION

A fixture that attaches a cryogenic component to its surrounding must meet much more difficult conditions when the system is part of a package that must be launched into space. The support fixture must be unusually strong and stiff to survive the high forces and severe vibrations of the launch without breaking or losing alignment between components. It is difficult to achieve the strength required without rather massive structures that conduct a large amount of heat.

At the same time, satellite systems designed for a long stay in space generally require an extremely low heat load into the lowest-temperature components to minimize the expenditure of non-renewable cryogen or else to minimize the heat that must be carried away by a cryocooler. This means that thermal conduction through the attachment fixture must be very low.

The main reason that bulky supports are chosen for high-strength applications is that the long, slender rods that would be desirable from a thermal conduction standpoint are unstable against buckling if very much compressive load is applied to them. It would be much better if such rods could be arranged so that they were always under tension. It is very difficult to achieve an arrangement of tension members that are all under a uniform, high tension, however.

DESIGN OF FIXTURE

A cryogenic attachment fixture has been developed that uses thin strands of high-strength Kevlar¹ fiber to achieve a high level of strength and stiffness while maintaining a very low level of thermal conduction through the fixture. This is accomplished through a method of winding Kevlar under high tension and anchoring it in a way that does not reduce its inherent strength and stiffness.

Figure 1 shows the design that accomplishes this; it is a modification of a previous development². The figure shows a cryogenic chamber attached to one of a pair of flat beams. The other beam is attached to a high-temperature base plate by a simple angle bracket. The two beams are coupled to each other by eight strands of Kevlar. The strands are under high tension and are anchored by epoxy³ to attachment plates on the ends of the beams. The geometry of the strands restrains relative motion of the two beams in any direction. Because the strands are pretensioned, there is no slack in the coupling between the two beams. This and the inherent stiffness of the Kevlar results in very little movement of one beam with respect to the other when a force is applied between them.

The flat beams of the fixture are of low-expansion Invar alloy. This is because the Kevlar has very little contraction when it cools to low temperature and the use of a material such as aluminum, which contracts much more than the Kevlar, would result in a loss of the pretension on the Kevlar at low temperatures.

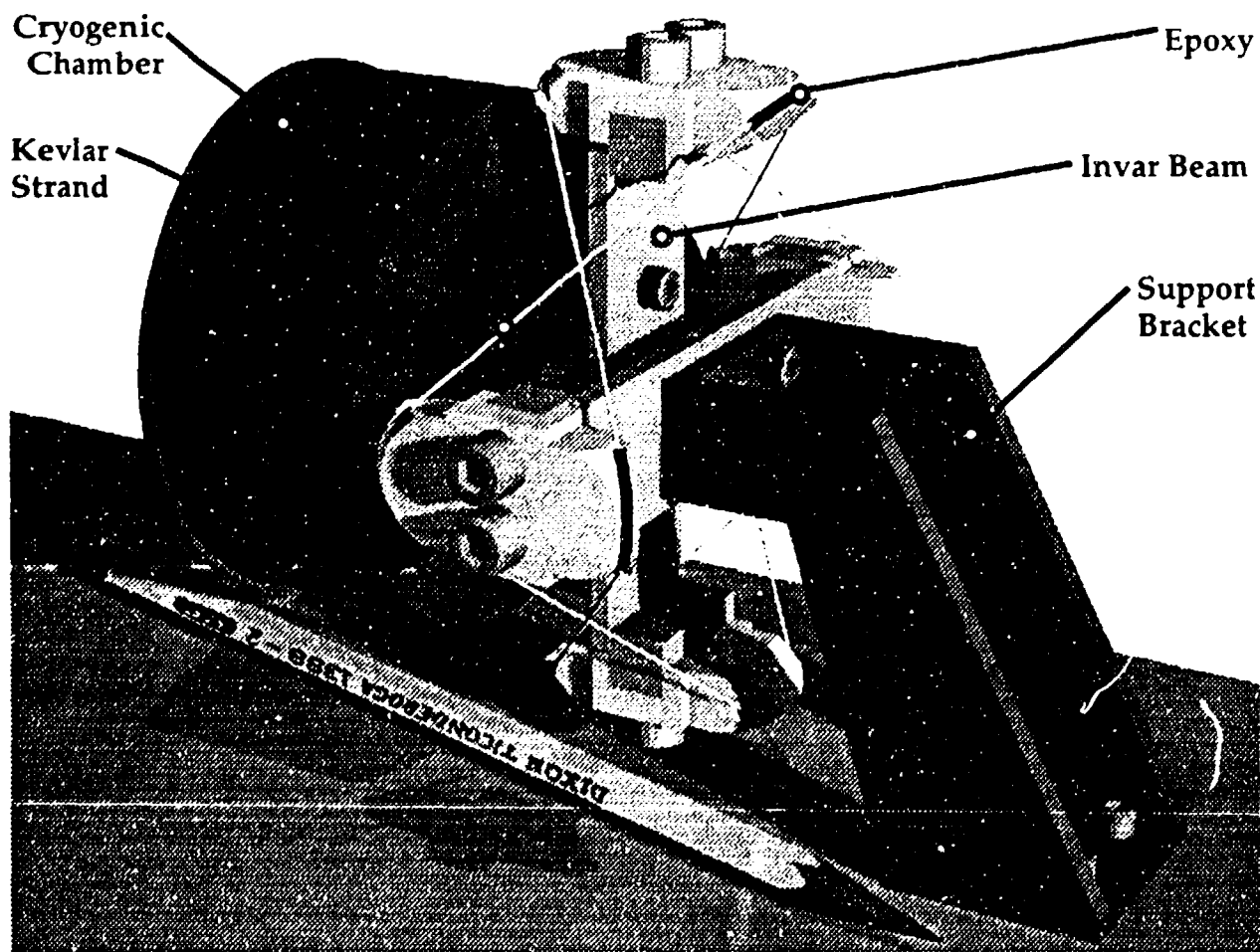


Fig. 1. Attachment fixture using Kevlar strands. A cryogenic chamber is shown mounted on one side of the fixture and the other side of the fixture is attached by a support bracket to a higher-temperature base plate.

To fully realize the strength and stiffness of the Kevlar, it is necessary to be very careful in the way the strands are anchored. The use of knots is undesirable because they seriously weaken the Kevlar. Wrapping several turns of Kevlar around a post to provide a buffer between the high-tension strand and the point where it is actually terminated is also undesirable because this compromises the high stiffness of the Kevlar. These extra turns can tighten up under high load, adding length to the strand that causes a loss of pretension when the load is removed. By anchoring the strands in grooves filled with epoxy, the design of Fig. 1 avoids both these drawbacks.

A particular advantage of this design is its modularity. The Kevlar strands are wound on the fixture ahead of time, producing a fixture of known spacing. Since the whole

unit can be bolted in place when needed, there is no need to go through the difficult process of tightening and equalizing the tension of strands that are applied in place.

When a load is applied to a fixture of this geometry, some strands increase their tension by a certain amount and other strands decrease their tension by the same amount. As long as all strands have a tension between zero and the breaking strength of the strands, the fixture behaves linearly and predictably. Therefore, to maximize the range of forces that the fixture will withstand and to achieve an equal range of positive and negative forces, all the strands should be pretensioned to approximately one-half the breaking force of the strands.

CONSTRUCTION

The fixture is assembled by attaching the two beams to a temporary spacer, mounting the fixture in a lathe and winding the Kevlar under the appropriate tension. The tension is determined by a special coupling⁴ that slips at a predetermined torque. Before going to the fixture, the Kevlar is wrapped several times around a brass shaft connected to the coupling; the coupling slips and feeds the Kevlar when the correct tension is reached. To prevent the strands from advancing along the shaft as it turns the shaft has a 15° taper that opposes this tendency. Note that there are two independent strands of Kevlar coupling the two beams; if one strand is followed from attachment to attachment the path returns to the starting point without overlapping the other strand. Both strands of the fixture are wound at the same time; a slip coupling for each strand is mounted on a pivot to allow the strands to be properly positioned as the fixture is slowly rotated in the lathe. The fixture is wound in multiple rotations so that each Kevlar link is actually built up of more than one strand. The multi-strand approach greatly improves the anchoring of the strands by the epoxy that is applied during winding; for the same total breaking strength, four strands have twice the surface area of a single heavy strand. The tension is maintained on the strands until the epoxy hardens; then the fixture is removed from the lathe and the temporary spacer is removed.

TESTING

The length of the Invar beams of the fixture is 7.4 cm, their width is 1.9 cm and their thickness is 0.25 cm. The attachment plates on the ends of the beams spread the Kevlar strands 3.0 cm apart at their tips. Braided Kevlar 29 of 223 N (50 lb) tensile strength and

0.13 mm² cross sectional area was used; the slip couplings tensioned the strands to 89 N (20 lb) during winding and four turns of Kevlar were applied for each link. This yielded an initial tension in each link of 356 N (80 lb) and a breaking force of 890 N (200 lb). Each link is 4.8 cm long and the four strands combine to make up a cross sectional area of 0.52 mm².

The fixture was tested in axial compression at 77 K. Simultaneous measurements of force and deflection were obtained and are shown in Fig. 2. The fixture failed at a load of 1962 N (441 lb) by breakage of the Kevlar, not by failure of the epoxy joints. Calculation of the tension in the links at the maximum load showed that the Kevlar closely approached its nominal breaking strength before failure. The deflection per unit force of the fixture is 0.000165 cm/N (0.00029 in/lb); this is about twice that of the previous configuration², which had additional aluminum U-beams attached to the Invar beams. These U-beams greatly reduced the bending of the Invar beams and, therefore, made the fixture stiffer but at the cost of greater weight.

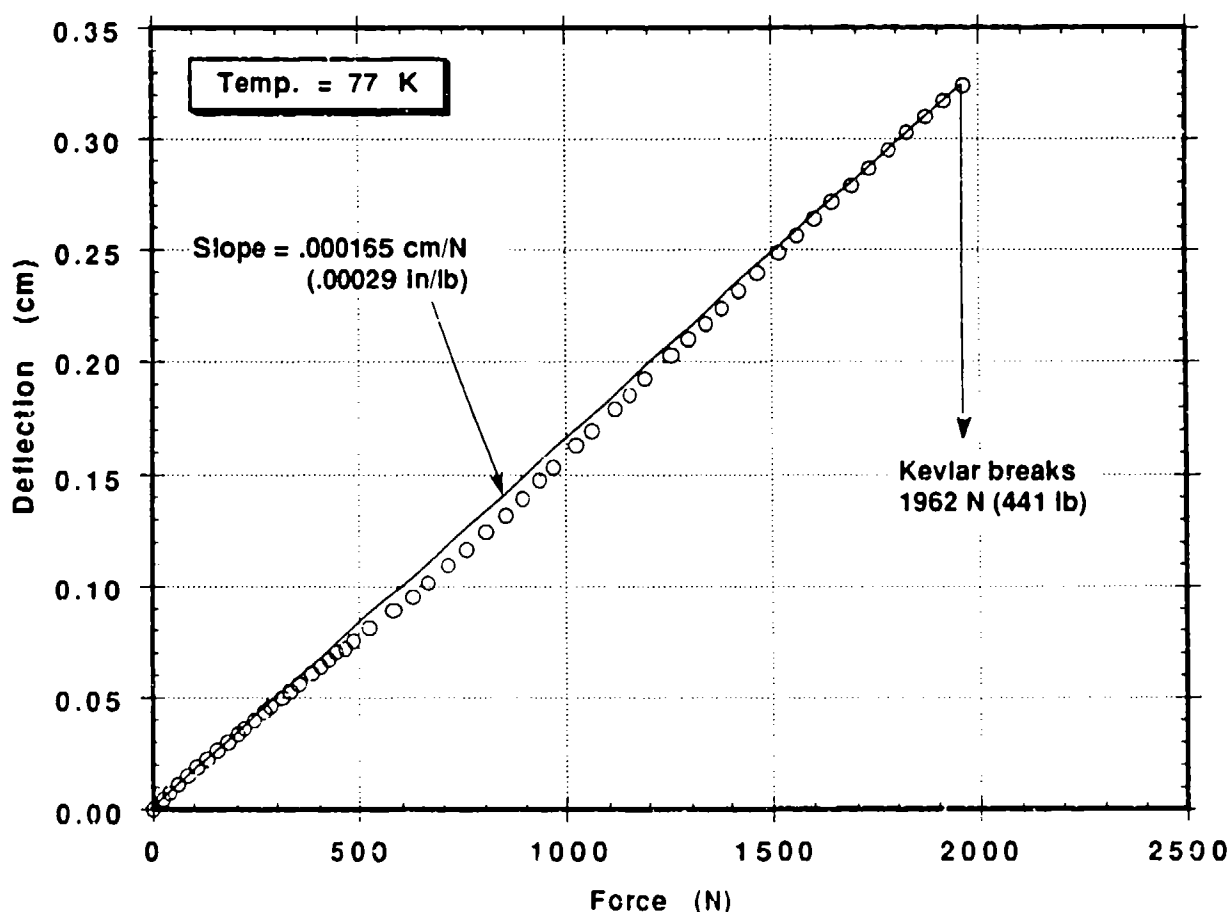


Fig. 2. Axial compression test of attachment fixture at 77 K.

CONCLUSIONS

An attachment fixture has been developed that combines the features of very high strength and very low thermal conductivity. It achieves these conflicting goals by a unique geometry and by taking maximum advantage of the properties of Kevlar. The low thermal conduction arises from the use of relatively thin strands of Kevlar that are highly stressed and from the fact that Kevlar has the typical low conductivity of other plastics⁵. A particularly useful aspect of the design is that the deflections and stresses in the beams and the strands can easily be calculated under typical load conditions; this allows the fixture to be used at stresses close to the breaking strength of the strands with considerable confidence.

Although the fixture is intended primarily for cryogenic applications, the concept is readily applicable to other temperature regions. The use of metallic strands and, perhaps, a brazing method of anchoring them could extend the usefulness of the concept to quite high temperatures. In addition, the small version described above can easily be scaled up to meet the requirements of larger tasks. It should also be pointed out that greater thermal isolation can be achieved by using smaller strands if less strength is acceptable, and conversely.

REFERENCES

1. Trademark of DuPont Co.
2. Pat R. Roach, Rev. Sci. Instrum. **63**, 3216 (1992).
3. Stycast 2850 FT with catalyst 24LV. Emerson and Cuming, Inc., Woburn, Massachusetts.
4. PIC Design Corp., Middlebury, CT; slip coupling T18-12.
5. B. Poulaert, J.-C. Chielens, C. Vandenhende, and R. Legras, Polymer Commun. **26**, 132 (1985).

HELIUM LIQUID- AND GAS-GAP HEAT SWITCHES

Ali Kashani
Atlas Scientific
Sunnyvale, CA 94086

Ben P.M. Helvensteijn
Sterling Federal Systems
Palo Alto, CA 94303

Frank J. McCormack and Alan L. Spivak
Trans-Bay Electronics
Richmond, CA 94804

ABSTRACT

Helium liquid-gap and gas-gap heat switches are operated at 2 K and 10 K, respectively. They are tested for their on- and off-conductance and turn-on and turn-off times. The measured on- and off-conductance of the heat switches are close to the theoretical values. The on- to off-conductance ratios of the heat switches are from 400 to 8000. The turn-on and turn-off times of the 10 K heat switches are less than one minute. The 2 K heat switches can be turned on in about one minute. However, the turn-off times are several minutes due to the adsorbed helium on the interior surfaces of the 2 K heat switches.

INTRODUCTION

Several future astrophysics missions planned by NASA, such as the Large Deployable Reflector (LDR), require a 2 K cryocooler. NASA - Ames Research Center is developing an adiabatic demagnetization refrigerator (ADR) which would operate between 2 K and 10 K and would provide 0.05 W of cooling at 2 K. The ADR would be the last stage of a multistage cryocooler to achieve 2 K cooling. The magnetic material selected for operating in the 2 - 10 K temperature range is Gadolinium Gallium Garnet (GGG). During the ADR cycle, thermal contact has to be made between the GGG and the 2 K heat source or

between the GGG and a 10 K heat sink. Liquid- and gas-gap heat switches are employed to eliminate the need for moving parts, thus increasing reliability.

All heat switches are configured as two matching surfaces which are separated by a narrow gap. A switch is on when its gap is filled with helium and is off when the gap is emptied. This is accomplished by an activated carbon pump (ACP). The carbon adsorbs helium when cooled and desorbs it when heated. The 2 K heat switches are liquid-gap heat switches to reduce the required heat transfer surface area, taking advantage of the high thermal conductivity of superfluid helium. The 10 K heat switches are gas-gap heat switches since the thermal conductivity of gaseous helium is considerably higher at 10 K.

In the ADR design two different approaches have been considered. In the first approach, both the 10 K and the 2 K heat switches are an integral part of the paramagnetic material. In this design one surface of either heat switch is formed by the GGG.¹ These heat switches are referred to as the internal heat switches. In the second approach the heat switches are linked to the GGG via thermal buses and are referred to as the external heat switches.

The evaluation of the heat switches for the ADR is based on their on- and off- thermal conductance and their turn-on and -off times. These parameters are greatly dependent on the performance of the ACP used for each heat switch. Adsorption of helium by various activated carbon samples have been measured.² The results are used in a numerical model that optimizes the ACP parameters for a given heat switch-ACP system. The activated carbon used in these tests is Barnabey-Cheney type PE.

The performance of each heat switch is determined by building and testing a prototype. Description of the prototype heat switches and the results of the tests conducted are presented here.

INTERNAL 10 K HEAT SWITCH

The internal 10 K heat switch, shown schematically in Fig. 1, consists of two concentric cylindrical copper tubes. The outside diameter of the inner cylinder is 3.81 cm and the inside diameter of the outer cylinder is 3.86 cm. The gap between the two tubes is 0.025 cm wide. The length of the inner cylinder is 12 cm, providing an effective heat transfer area

of 144 cm². The tubes are held together by two SS support tubes. The SS tubes are 0.012 cm in wall-thickness and 1.9 cm in length. The inner copper tube is capped at both ends and contains helium gas. A heater is placed in the internal gas volume of the heat switch to raise its temperature. A heater is placed on the outer copper tube to simulate the heat load on the heat switch.

An ACP is connected to the gap volume of the heat switch by a 0.16 cm-OD SS tube. It contains 60 mg of activated carbon and is pressurized to 10.9 kPa with helium gas at room temperature. A thermal link between the ACP and the helium bath removes the heat of adsorption of the activated carbon.

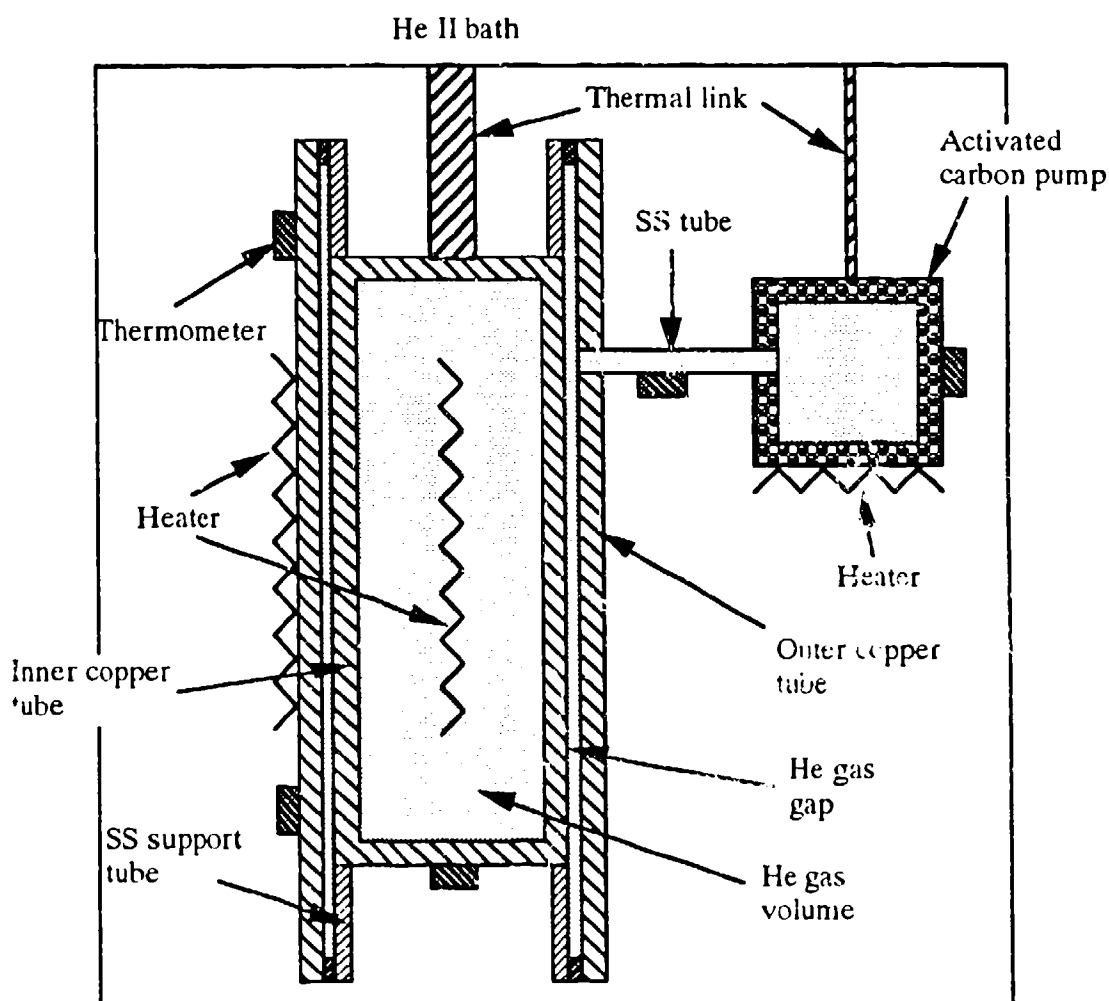


Fig. 1 Schematic of the internal 10 K heat switch.

The heat switch assembly is mounted in the vacuum can of a test cryostat with its internal gas volume thermally anchored to the helium bath. The off-conductance of the heat switch is tested by applying power to the outer tube. With 0.018 W applied, the temperature difference across the gap increases to 8.29 K. The experimental off-conductance, defined as the ratio of the heat flow rate to the temperature gradient, is $2.17 \cdot 10^{-3}$ W/K. The theoretical off-conductance is calculated to be $2.0 \cdot 10^{-3}$ W/K due to the heat transfer through the SS support tubes.

To measure the on-conductance the heater inside the inner tube is turned on, raising the temperature of the heat switch to approximately 10 K. Then, 0.223 W is applied to the outer tube as a heat load. The heat switch is turned on by heating up the ACP releasing helium into the gap. In the on-mode the temperature difference across the gap is 0.25 K. The experimental on-conductance of the heat switch is 0.89 W/K. The theoretical on-conductance is $K_{on} = k_g A/d$; where, k_g is the thermal conductivity of the gas, A is the heat transfer area and d is the gap width. This yields an on-conductance of 0.91 W/K. The on-to off-conductance ratio for the heat switch is greater than 400.

To measure the turn-on and turn-off times of the heat switch, a heat load is applied to the outer tube. The ACP heater is cycled on and off while monitoring the temperatures of the inner tube, the outer tube and the ACP. In Fig. 2, 0.005 W is applied to the outer tube heater. When the outer tube temperature is 11 K the ACP heater is turned on. A sharp decrease in the outer tube temperature occurs when the ACP temperature rises to 14 K indicating the on-mode of the heat switch. The turn-on time is on the order of 40 s. The ACP heater is turned off removing the gas from the heat switch. The time it takes for the temperature of the outer tube to rise to 11 K is measured again. This yields a turn-off time of less than one minute.

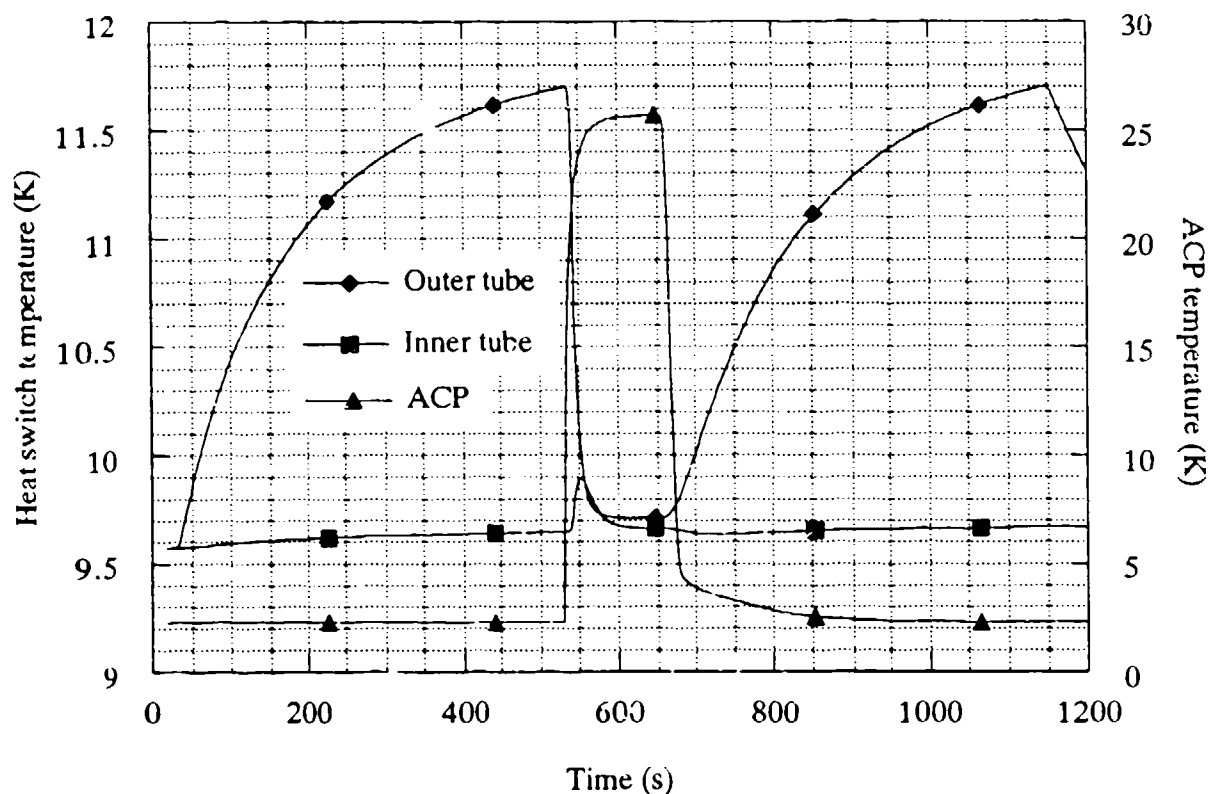


Fig. 2 Temperature profiles for the internal 10 K heat switch.

The previous case is repeated (Fig. 3) with the heat switch at 2 K. After the ACP heater is turned off the temperature of the outer tube begins to rise very slowly as compared to the 10 K test. This problem is attributed to the adsorption of helium on the 2 K surfaces of the heat switch. The adsorbed helium is pumped out at a slow rate, resulting in a long turn-off time. To confirm this a heat pulse is applied to the inner tube causing the heat switch temperature to rise. After the pulse the outer tube temperature is at its off-mode value while the inner tube temperature drops to 2 K indicating the switch is turned off. The adsorption of helium on cold surfaces has also been observed when the switch is operated at 4 K but does not appear to be significant at 10 K.

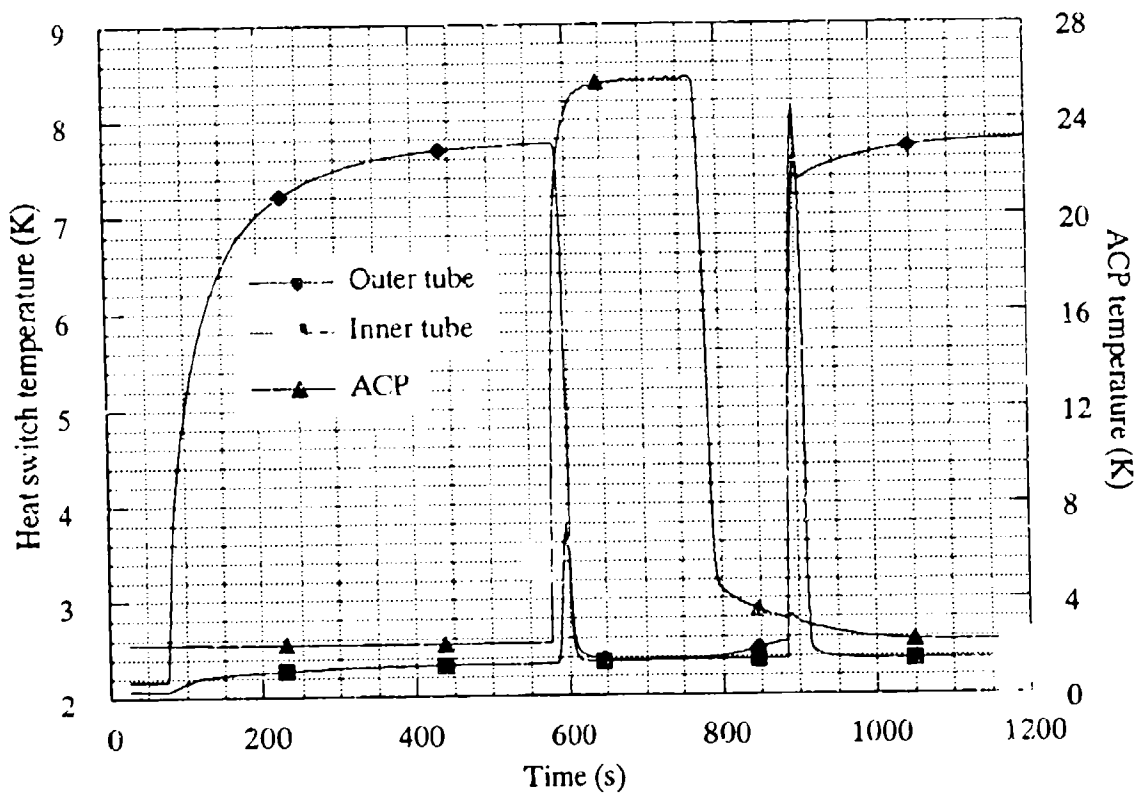


Fig. 3 Effect of adsorbed helium on the turn-off time.

EXTERNAL 10 K HEAT SWITCH

The external 10 K heat switch is based on the design delineated in Ref. 3. It consists of two finned copper cylinders, shown schematically in Fig. 4. The fin patterns on the two cylinders are a mirror image of one another. When put together the fins are separated by a gap of width 0.010 cm. A 0.012 cm-thick SS support tube holds the two pieces together and seals the gap volume. The fins are 2.54 cm long and 0.142 cm thick. The diameter of the heat switch is 2.45 cm. The effective heat transfer area of the heat switch is approximately 82 cm². To keep the copper fins from making contact in the assembled heat switch small glass beads are epoxied on the tips of the fins.

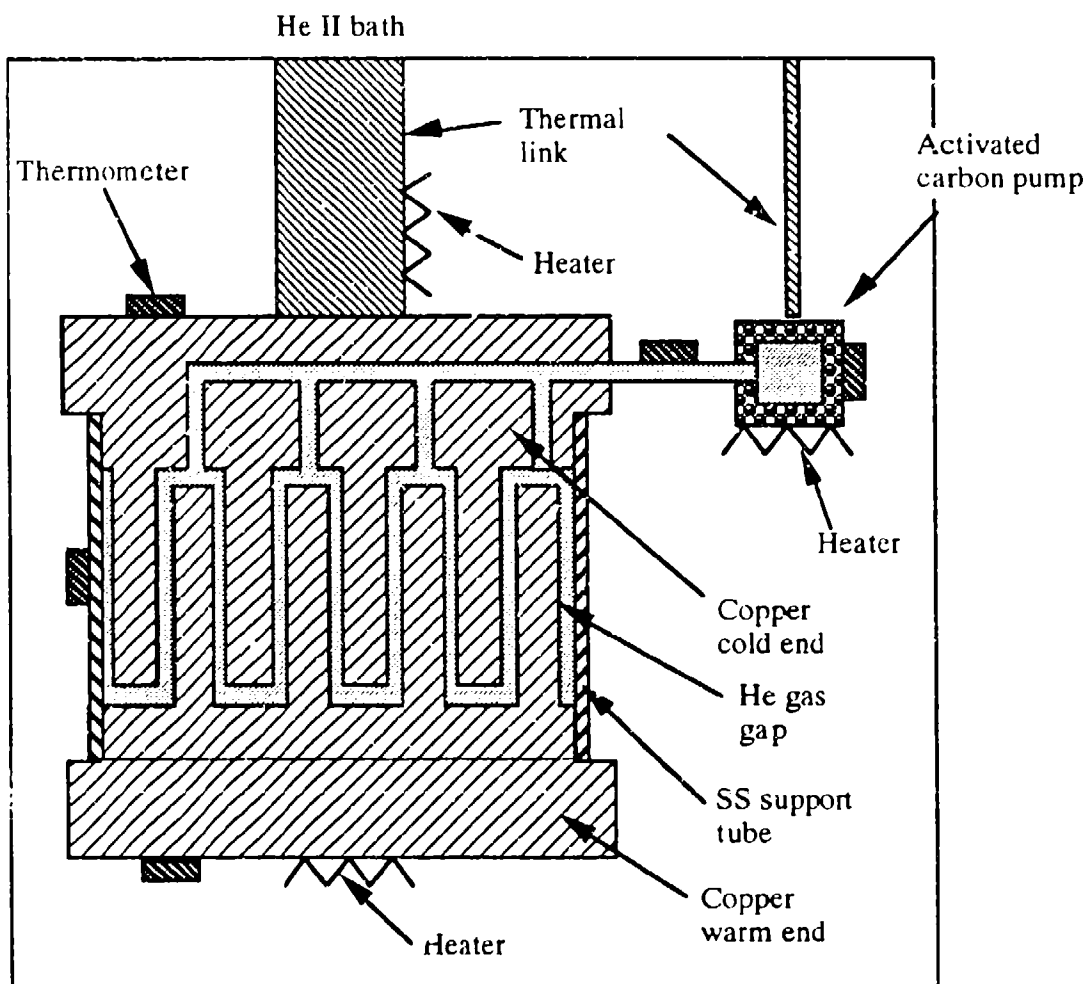


Fig. 4. Schematic of the external 10 K heat switch.

The ACP for this heat switch has an internal volume of 4.5 cm^3 and contains 20 mg of activated carbon. It is charged to 5.3 kPa at room temperature with helium gas. A copper wire is the thermal link between the ACP and the helium bath.

The heat switch assembly is placed in the vacuum space of the test cryostat with one end thermally anchored to the helium bath. The tests performed to find the on- and off-conductance are similar to those described for the internal 10 K heat switch.

The temperature gradient across the heat switch as a function of applied power is shown in Fig. 5 for both the on- and the off-mode. In the off-mode, when 0.007 W is applied to the

heat switch, the temperature difference between the warm end and the cold end is 7.77K. The measured off-conductance of the heat switch is $9 \cdot 10^{-4}$ W/K, while the theoretical off-conductance is $4.3 \cdot 10^{-4}$ W/K. The difference in these two results is partially due to the conduction through the glass beads.

In the on-mode, when 0.245 W is applied to the warm end of the heat switch a temperature difference of 0.18 K develops across the switch. The experimental on-conductance is 1.36 W/K. The theoretical on-conductance for this case is calculated to be 1.43 W/K using the equations developed in Ref. 3. The on- to off-conductance ratio of the heat switch at an input power of 0.007 W is nearly 8000.

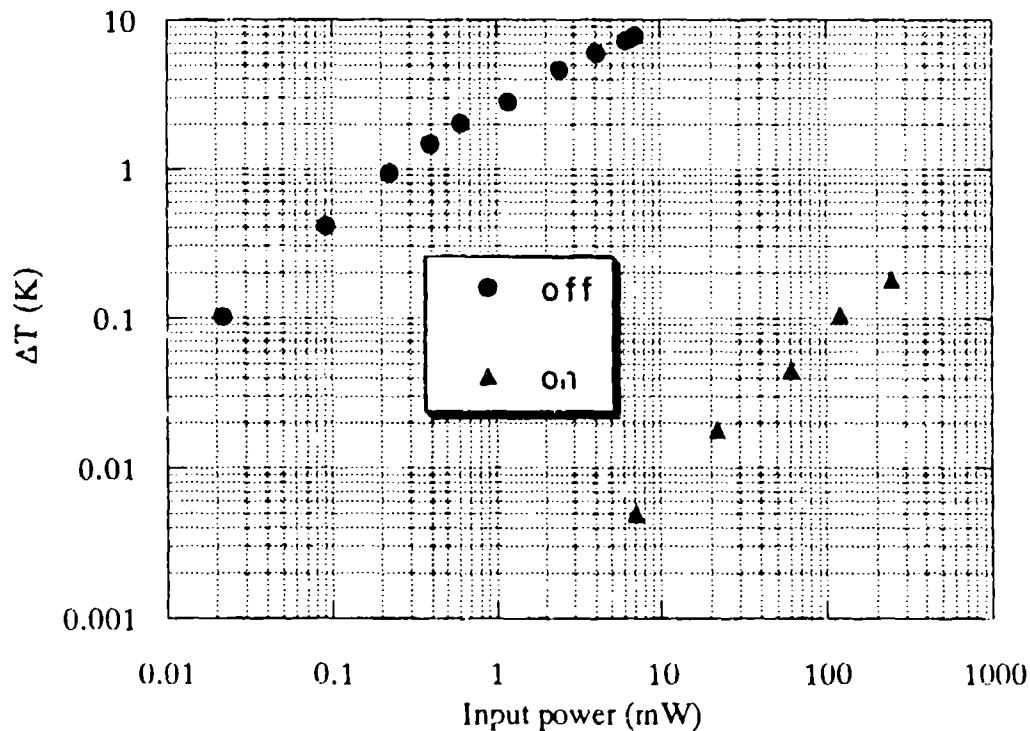


Fig. 5 Temperature difference across the heat switch vs. input power.

The procedure used to determine the turn-on and -off times of the heat switch is similar to the one used for the internal 10 K switch. In Fig. 6, a load of 0.007 W is applied to the heat switch. The turn-on time is on the order of 30 s; whereas, the turn-off time is less than one minute.

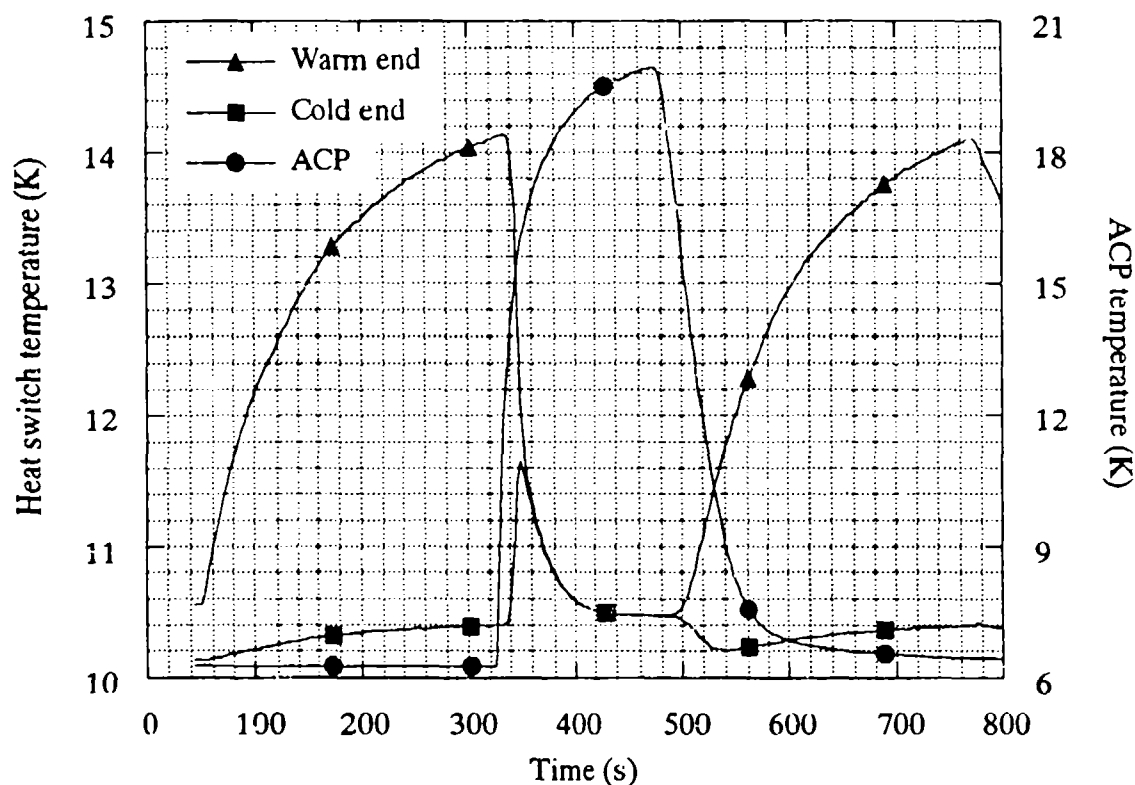


Fig. 6 Temperature profiles for the external 10 K heat switch.

To observe the transients of the heat switch during the on-mode the ACP temperature is varied incrementally as shown in Fig. 7, again applying 0.007 mW to the heat switch. The heat switch begins to conduct when the ACP temperature rises to 13 K and its conductance continues to increase until the ACP temperature reaches 20 K. The increase in conductance occurs in the transition between the free-molecular regime and the continuum regime of the gas. The transition is well predicted by the numerical model that is developed to characterize the performance of the heat switch-ACP system.

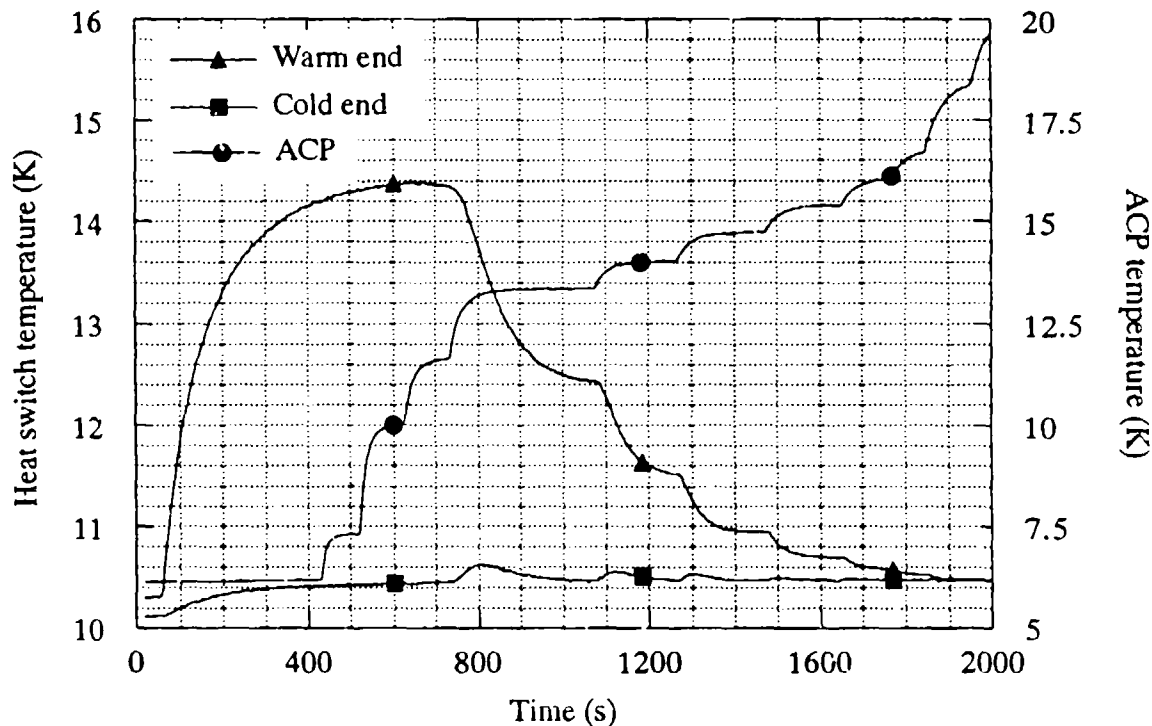


Fig. 7 The effect of gas pressure on the conductance.

INTERNAL 2 K HEAT SWITCH

The internal 2 K heat switch has been described in an earlier report.⁴ The switch consists of a brass cylinder with a blind-hole drilled at its centerline. A stainless steel He II tube, plugged at one end, is inserted into the hole. A gap width of 0.018 cm is maintained between the He II tube and the brass cylinder by a stainless steel support tube as shown in Fig. 8. The hole in the cylinder is 4.13 cm long and 0.251 cm wide. The SS extension tube is 2.0 cm long and has a wall-thickness of 0.025 cm. The ACP has 2 g of carbon and is charged with 5 atm of helium gas at room temperature.

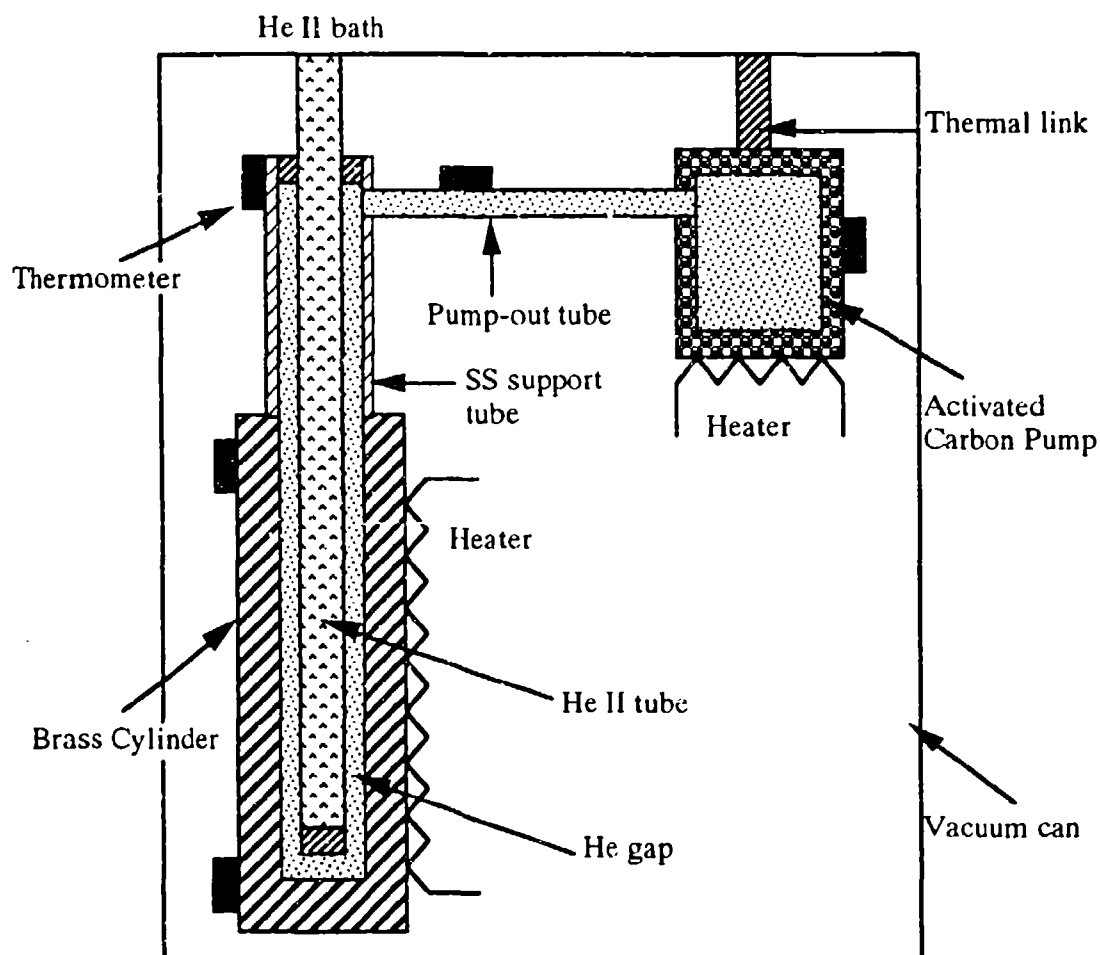


Fig. 8 Schematic of the internal 2 K heat switch.

The temperature difference across the switch as a function of applied power is shown in Fig. 9, for both the on- and the off-mode. The on- to off-conductance ratio is 3000 at 0.07 mW and goes down to 1000 at 0.6 mW. The on-conductance of the heat switch when filled with He II is about ten times higher than its on-conductance when it is filled with helium gas.

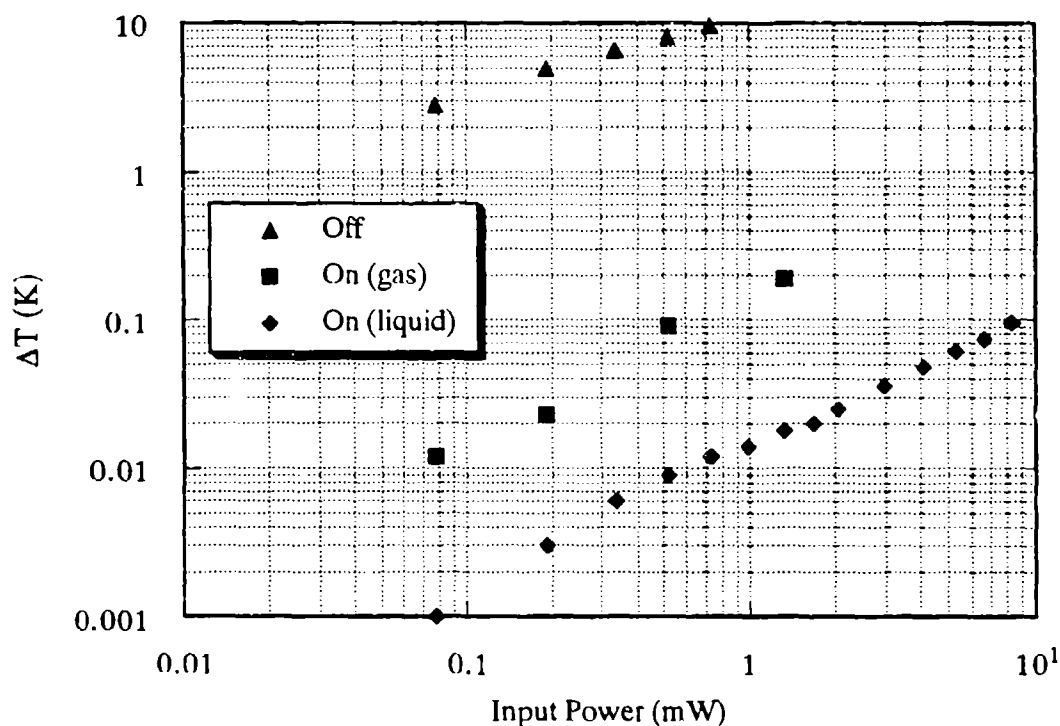


Fig. 9 Temperature difference across the heat switch vs. power input.

The turn-on time of the heat switch is on the order of three minutes. The turn-off time is on the order of six minutes. The long turn-off time is attributed to the adsorption of helium on the 2 K surfaces of the switch as noted in the 10 K heat switch tests.

EXTERNAL 2 K HEAT SWITCH

The external 2 K heat switch consists of two copper cylinders that are positioned end to end separated by a 0.018 cm-wide gap. The two cylinders are held together by a SS support tube which has a wall-thickness of 0.010 cm and is 1.0 cm long. A gap is also maintained between the SS tube and the longer cylinder as shown in Fig. 10. The diameter of the gap is 0.57 cm and the heat transfer surface area of the heat switch is 0.26 cm².

The ACP for this heat switch has a volume of 17.6 cm^3 and contains 1.7 g of activated carbon. It is charged to 2 atm with helium gas at room temperature. The ACP is connected to the He II bath by a brass thermal link.

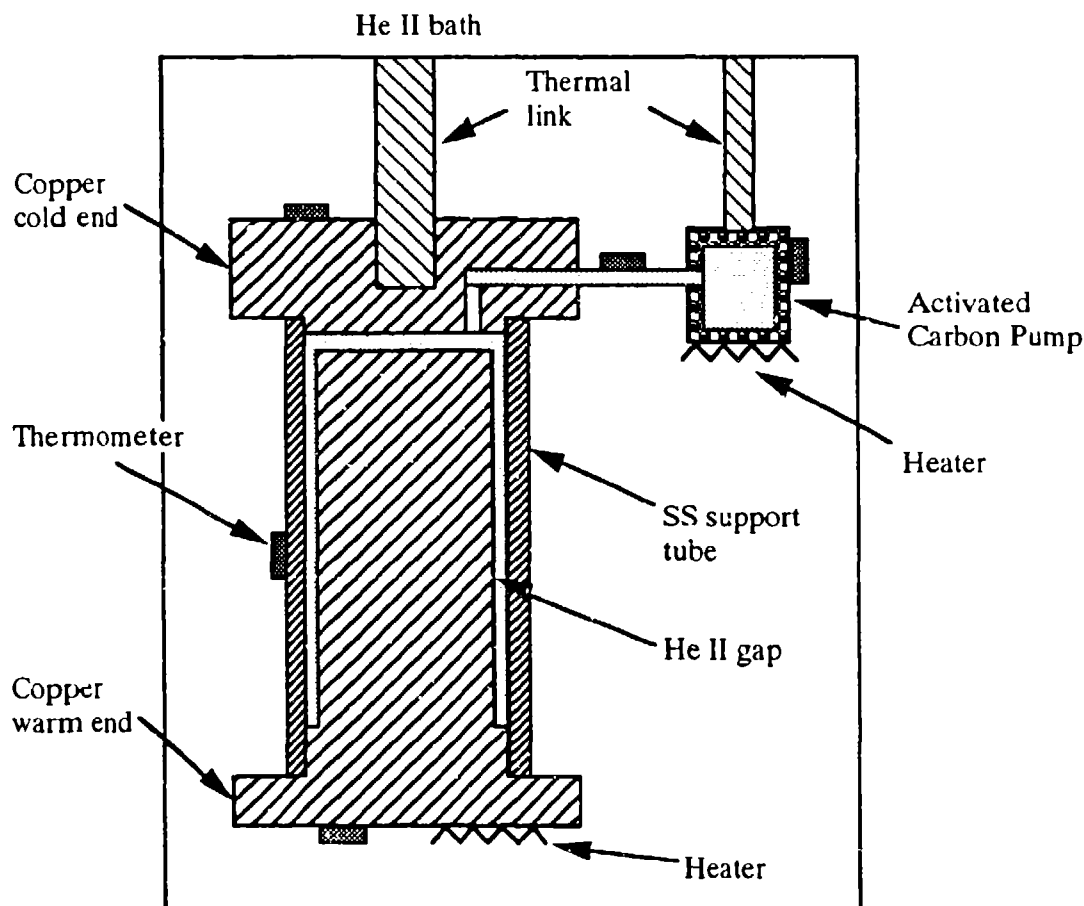


Fig. 10 Schematic of the external 2 K heat switch.

In Fig. 11, the temperature difference across the heat switch is plotted as a function of the input power for both the on- and the off-mode of the heat switch. The experimental off-conductance with 2 mW applied to the heat switch is $1.9 \times 10^{-4} \text{ W/K}$, while the theoretical value is calculated to be $1.8 \times 10^{-4} \text{ W/K}$. For the same input power the on-conductance is 0.29 W/K. The on-conductance decreases to 0.12 W/K as the applied power is increased to 5.3 mW. The theoretical on-conductance ranges between 0.08 W/K and 0.51 W/K. The

lower value is limited by the Kapitza boundary resistance between the He II and the copper. The on- to off-conductance ratio for an applied power of 2 mW is 1500.

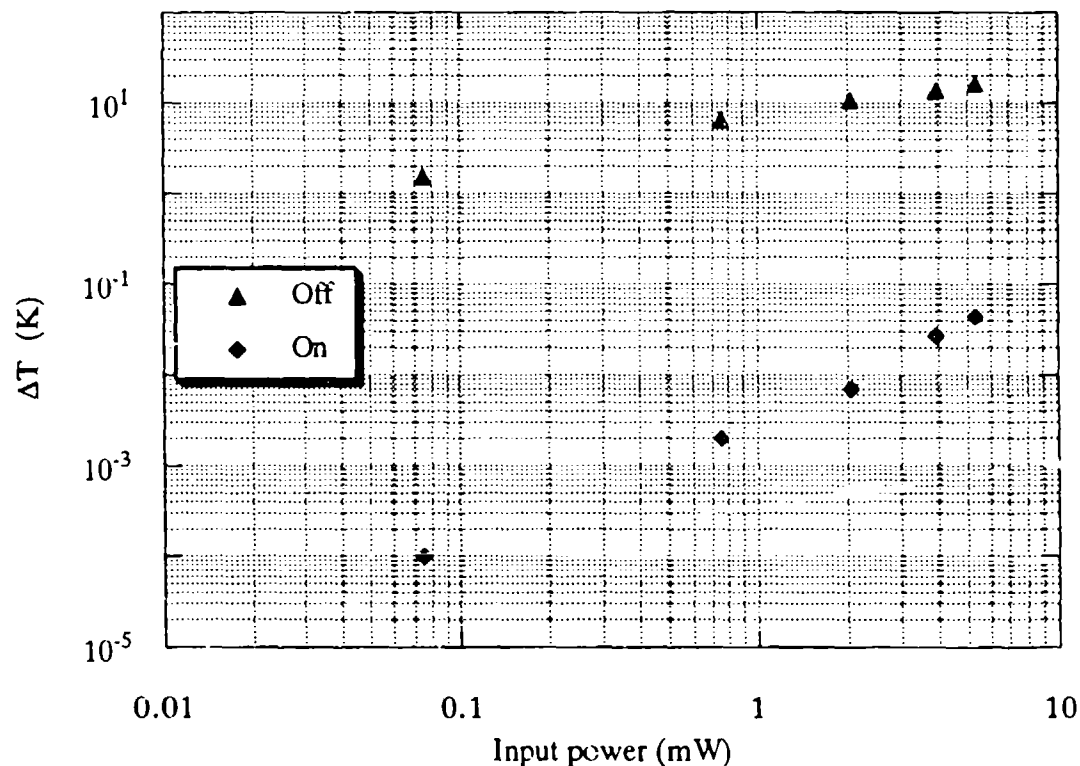


Fig. 11 Temperature drop across the heat switch vs. power input.

To test the turn-on and -off times of the heat switch transient tests are conducted. Figure 12 shows the temperature profiles of the warm end and the cold end of the heat switch along with that of the ACP for an input power of 2 mW. The temperature of the warm end decreases sharply once the ACP temperature rises to 13 K. Above this temperature the gas in the gap is in the continuum regime. This takes approximately 30 s to occur. As the temperature of the ACP reaches 29 K the helium condenses in the gap and the temperature difference across the heat switch drops to 7 mK. The time to reach this state is nearly three minutes; however, it can be shortened by increasing the rate at which the ACP is heated.

When the ACP is turned off the liquid is evaporated. This is denoted by a slight decrease in the heat switch temperature due to the evaporative cooling. After this point the switch conducts in the gas continuum regime which lasts for more than one minute. This time can be shortened by increasing the thermal conductance of the ACP thermal link. When the ACP temperature is sufficiently low transition to the gas free-molecular regime occurs. It takes an additional one minute for the switch to fully turn off. This is primarily determined by the amount of helium adsorbed on the surfaces of the heat switch. In comparing the turn-off times of both 2 K heat switches, it is evident that the external heat switch turns off more quickly. This is because the external heat switch has less surface area compared to the internal heat switch.

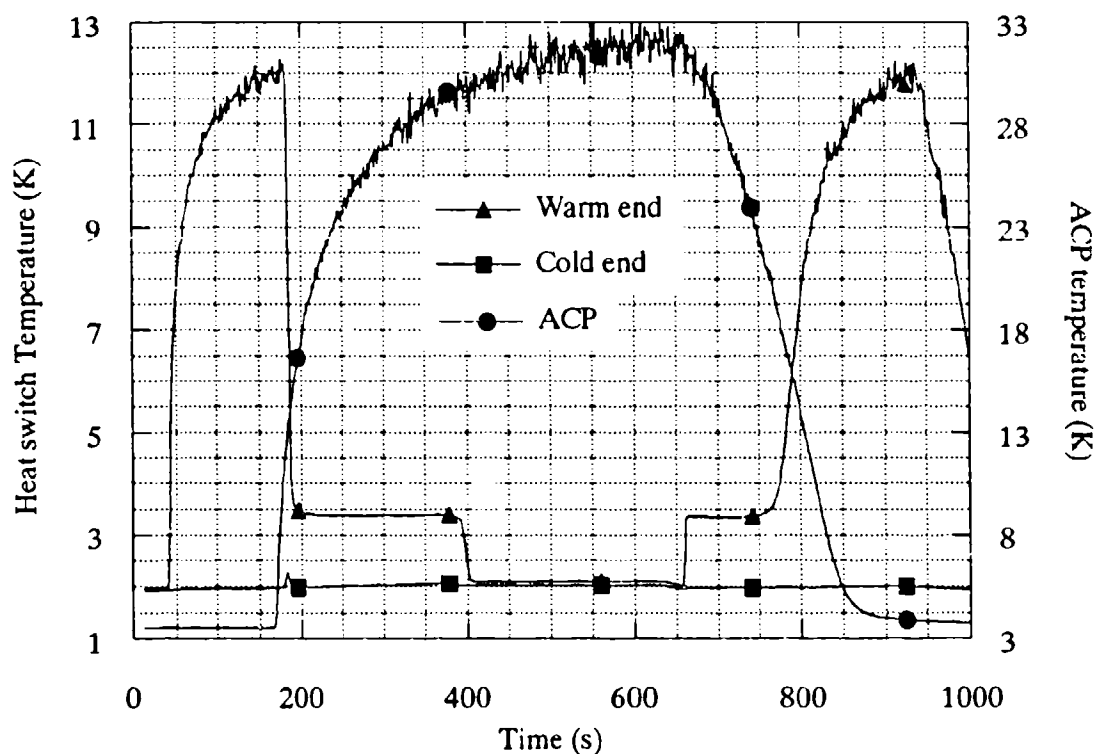


Fig. 12 Temperature profiles for the external 2 K heat switch.

CONCLUSIONS

All four heat switch designs tested in this study have on- and off-conductance close to their theoretical values. The on- to off-conductance ratios of the heat switches are between 400 and 8000. For the 10 K heat switches the turn-on and -off times are less than one minute. For the 2 K heat switches the turn-on time is on the order of three minutes. This time can be reduced by increasing the ACP temperature at a faster rate. The turn-off times of the 2 K switches are on the order of several minutes. This time is longer for the internal heat switch than for the external heat switch, because the external heat switch has less surface area as compared to the internal heat switch.

The model developed to determine the ACP parameters based on a given heat switch design has been successful in predicting the performance of the heat switch-ACP systems.

REFERENCES

1. B. P. M. Helvensteijn and A. Kashani, Conceptual Design of a 0.1 W Magnetic Refrigerator for Operation Between 10 K and 2 K, in: "Advances in Cryogenic Engineering," Vol. 35B Plenum Press, New York (1989), p. 1115.
2. B. P. M. Helvensteijn, A. Kashani and R. A. Wilcox, Activated Carbon Test Assembly, in: "Proc. Sixth Intl. Cryocooler Conf.," (1990) p. 103.
3. C. K. Chan, Gas Adsorption/Absorption Heat Switch, in: "JPL Publication 87-7" (1987).
4. A. Kashani, B. P. M. Helvensteijn and R. A. Wilcox, Development of a 2 K He II Gap Heat Switch, in: "Proc. Sixth Intl. Cryocooler Conf.," (1990) p. 355.

**A RADIATIVE COOLING SYSTEM FOR THE
EOS STRATOSPHERIC WIND INFRARED LIMB SOUNDER**

Donald J. Kuyper
AEC-Able Engineering Co., Inc.
Goleta, CA 93117

ABSTRACT

Advanced remote sensing instruments of the 1990's employ detector/sensor arrays with increased cooling power requirements over those of the past. Lower operating temperatures and increased bias power dissipation of on-focal-plane detectors and electronics have combined to require substantial increases in cooling power capability. The state-of-the-art of radiative cooler design has also progressed rapidly and compact radiative coolers with substantially increased cooling power are now a reality.

A radiative cooler must sometimes be located some distance from the instrument's cooled focal plane, to obtain an unrestricted view to cold space. Heat must then be transported from focal plane to cooler at cryogenic temperature. Heat can be efficiently transported by means of a metal rod conductor surrounded by a cooled thermal shield. AEC-Able recently completed a radiative cooling feasibility study for the Stratospheric Wind Infrared Limb Sounder (SWIRLS) instrument for the Earth Observing System (EOS). Analyses indicate that by using an advanced radiative cooler with an unrestricted view to cold space, 80 Kelvin refrigeration can be provided to the SWIRLS twin focal planes. The current presentation reports on the SWIRLS radiative cooling study including the design of the rod conductor and the cooling system thermal performance analyses.

1.0 INTRODUCTION

1.1 Instrument Mission

The SWIRLS investigation focuses on stratospheric structure, dynamics and transport, and the influence of natural and anthropogenic forcing on stratospheric change, including changes in

ozone. The primary data products of the investigation will be daily, monthly, seasonal, and annual global maps of wind, temperature, abundances of ozone and nitrous oxide, as well as fluxes of heat, momentum, ozone, nitrous oxide, and dynamical quantities such as potential vorticity.¹

1.2 Instrument Description

SWIRLS will provide the required direct measurements of wind by observing wind-induced Doppler shifts in the atmospheric thermal emission spectrum of nitrous oxide using a new gas correlation technique that employs electro-optic phase modulation (EOPM). EOPM gas correlation radiometry provides the high spectral selectivity needed to measure winds. The instrument is a six-channel limb-viewing radiometer with 3-km vertical resolution in the 20 to 60 km altitude range (Figure 1). The mass is estimated to be 150 kg. Thermal control of the optics and electronics is by radiator, central thermal bus, and heaters. Twin cold focal planes are cooled by a cryocooler to 80 Kelvin.

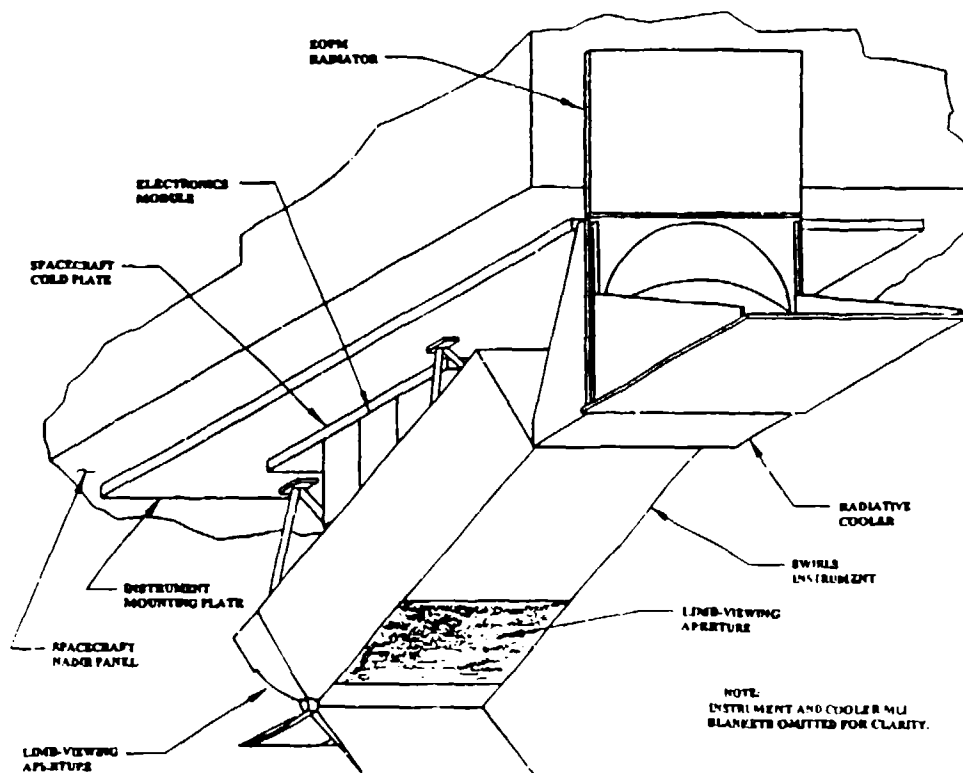


Figure 1 -- SWIRLS Instrument and Cooler on Spacecraft

A block diagram for the instrument is shown in Figure 2. The telescope and relay optics are mounted on an optical bench cooled to 200 K by radiation through the fore and aft limb-viewing apertures. The two EOPM's dissipate about 29 W of thermal power and are cooled by heat pipes and a remote radiator to 220 K. Figure 3 shows a schematic of the instrument thermal design.

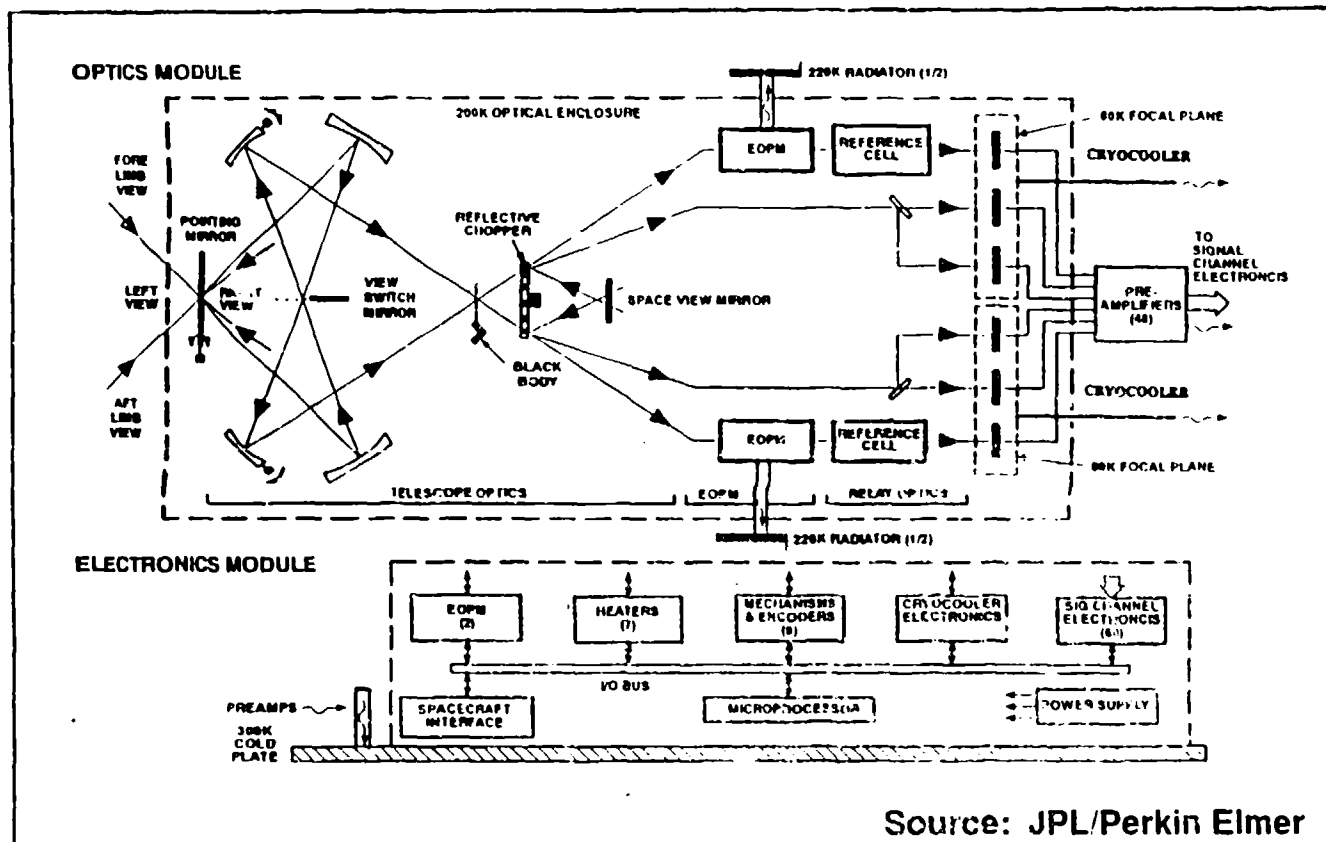


Figure 2 -- Instrument Block Diagram

1.3 Cryocooler Description

The cryocooler was originally baselined to be a matched pair of split-Stirling cycle cryoengines producing about 1 W of refrigeration power at 80 Kelvin. This presentation reports on the feasibility of employing a high-performance radiative cooler instead. No change in the instrument's electro-optical design was permitted to accommodate the radiative cooler.

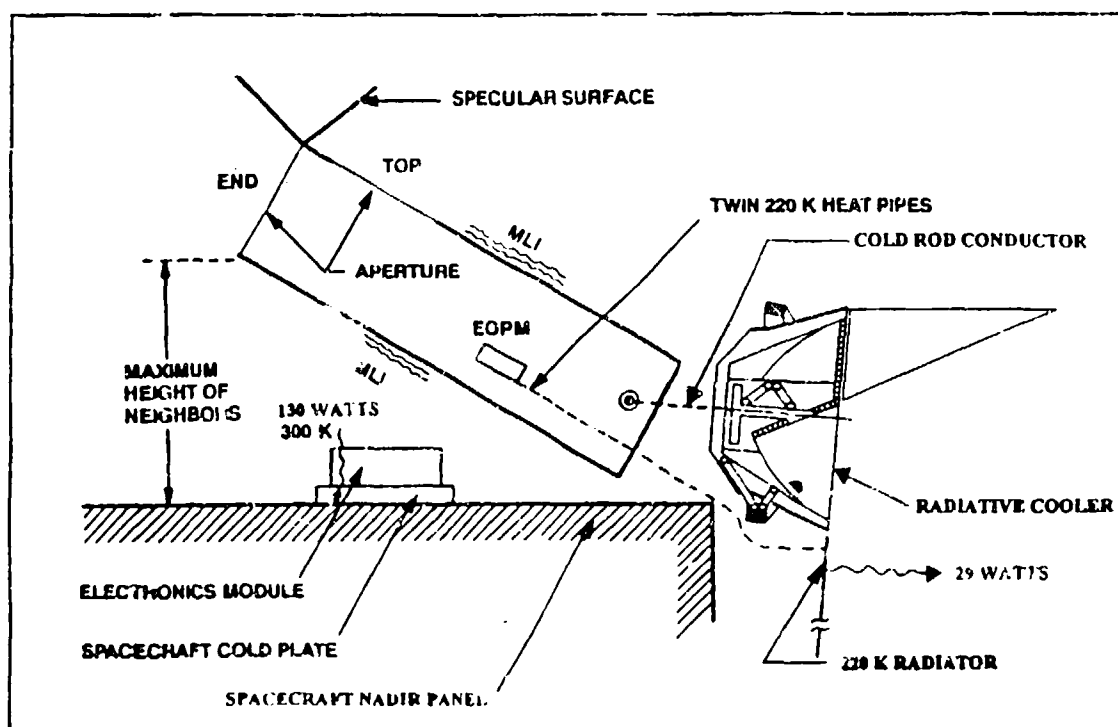


Figure 3 --Instrument Thermal Design Schematic

Compact radiative coolers with substantially increased cooling power are now a reality. As an example, a high-performance radiative cooler was developed for use on the Pressure Modulator Infrared Radiometer (PMIRR), an instrument aboard the JPL Mars Observer launched in late 1992. This cooler will operate in earth polar, sun-synchronous orbit without change.

To obtain an unrestricted view to cold space, a radiative cooler must sometimes be located some distance from the instrument's cooled focal plane detectors, and the cooling power must then be transported from focal plane to cooler at cryogenic temperature. For transport distances greater than a few centimeters, system designers often assume a cryogenic heat pipe is needed. However, focal plane cooling power can be efficiently transported by means of a metal rod conductor surrounded by a cooled shield, for distances as great as one meter.

The SWIRLS instrument employs two cooled focal planes separated from each other by about 30 cm (12 inches). Both of these focal planes are located about 38 cm (15 inches) away from the radiative cooler itself. The focal plane cooling loads are transported to the radiative cooler using conductive metal rods which are surrounded by cooled thermal shields. Analytical methods for optimizing the heat transport efficiency of metal rod conductors have been applied

SWIRLS. By using an efficiently-designed rod conductor, the cooled focal plane can be located some distance away from the radiative cooler. The application of the rod conductor involves only existing technology; no engineering development is required.

The PMIRR cooler is an upgraded version of the Landsat Thematic Mapper cooler, with increased thermal performance and vibration endurance, and reduced mass. It represents three generations of NASA/JPL-sponsored cooler engineering development. Each generation improves on the former's performance in spaceflight. The Thematic Mapper coolers have been operating successfully in space since 1982. Radiative cooling is a proven technology with a long, successful history; however there are practical limitations to the size and mass of a radiative cooler and to its threat survivability. For some remote sensing instruments, these practical limitations have been exceeded and only cryoengine detector cooling is feasible. This paper provides an analyses of the feasibility of employing radiatively-cooled detectors on the SWIRLS instrument for the EOS mission, using a modified PMIRR-type cooler (Figure 4) in combination with a rod conductor.

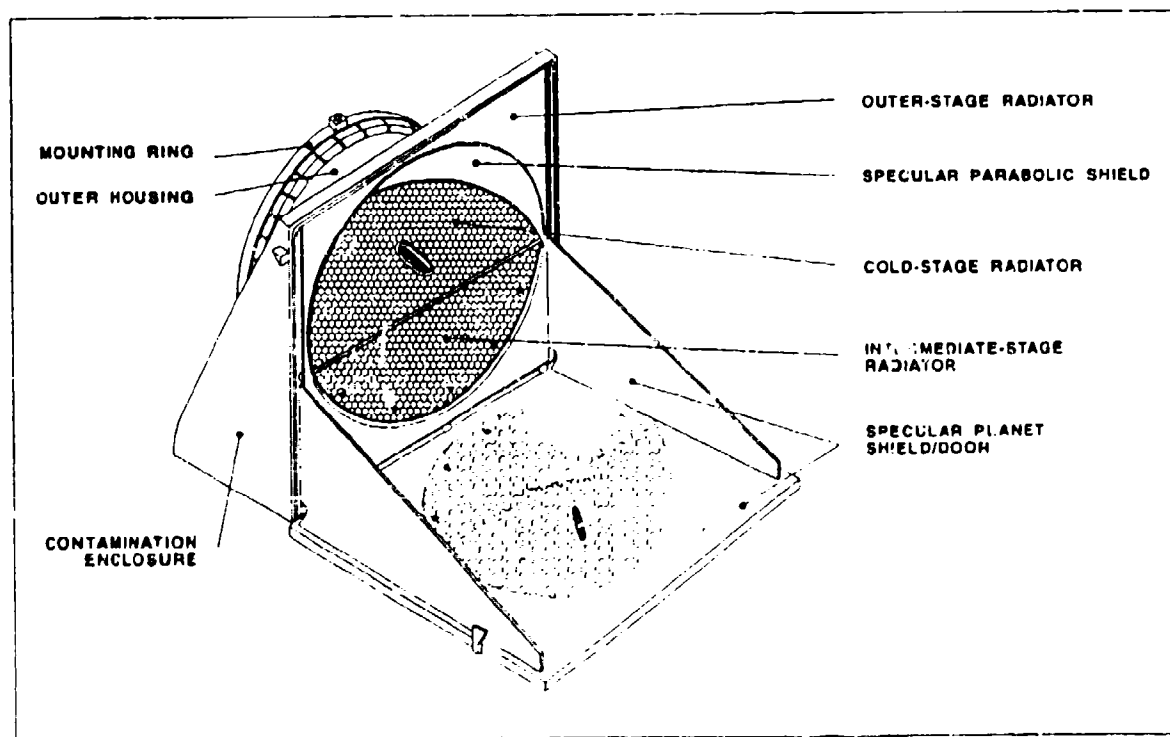


Figure 4 -- SWIRLS Radiative Cooler

2.0 RADIATIVE COOLING SYSTEM

2.1 System Design Requirements

The SWIRLS radiative cooling system consists of a radiative cooler component and a rod conductor component. The rod conductor transports heat from the cooled focal planes to the radiative cooler at cryogenic temperature.

The thermal performance requirement of the radiative cooling system was to provide a 80 K focal plane detector operating environment with an adequate cooling margin of safety over the life of the 5-year mission. Temperature control heaters were to be employed to maintain both of the twin cooled focal planes at the 80 K operating temperature.

Structural design requirements were also considered to the extent that they drove the thermal design. The launch/boost vibration environment at the cooler attach points was assumed to be severe - on the order of 15 g rms random overall level in all axes. After exposure to vibration, the cooled detector arrays mounted on each of the twin focal planes must remain within 0.013 mm (0.0005 inch) of their initial positions, in all axes. This means that focal plane fundamental frequencies of vibration must be kept high, to avoid any resonance conditions that could overstress the critical thermal isolation support members.

Following space operational cooldown both detector arrays must retain position within 0.013 mm in all axes when cold, as compared to the ambient position. The same requirement was in effect for instrument testing using a bench cooler in ambient air.

The radiative cooling system mass must be competitive with that of an alternate cryoengine cooling system, so that the overall mass of the SWIRLS instrument was not increased. The cryoengine compressors, displacers, and power supply/conditioning electronics, mounted on the instrument, had a mass of 10-12 kg; thus the mass of the radiative cooling system could not exceed this value.

2.2 Design Configuration

2.2.1 Radiative Cooler

The SWIRLS cooler is similar in design to a PMIRR cooler but with increased radiator area. The thermal design employs three thermally-isolated cooling stages. Without increasing the cooler outside envelope, the cold stage radiator area was increased 83%, and the intermediate stage 16%. This was accomplished by allowing the radiators an unrestricted hemispherical view of cold space, either by direct view or by reflected view off the specular thermal shields (Figure 5).

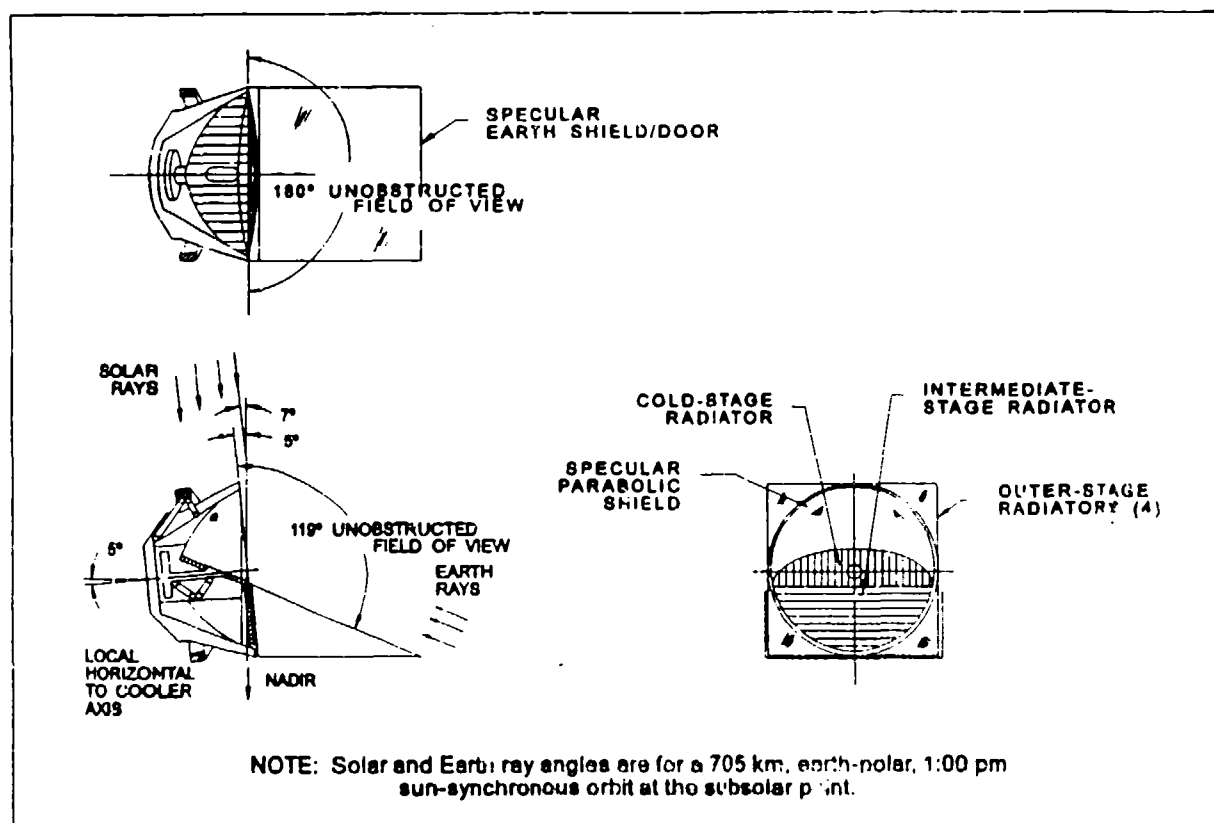


Figure 5 -- Cooler Environmental Radiation Schematic

The thermal design is arranged to reduce environmental loads and IR emissions falling on the cold radiator to a minimum. The design techniques employed to accomplish this are similar to those used on the TM and PMIRR coolers^{2,3}. The enlarged radiator areas, in combination with minimum tare heat loads from the environment and the cooler itself, results in high thermal performance. In earth polar orbit, the lowest temperature achievable is about 60 K.

At 80 K, 130 mW of focal plane cooling power are available; at 90 K, 240 mW; and at 116 K, 800 mW (Figure 6).

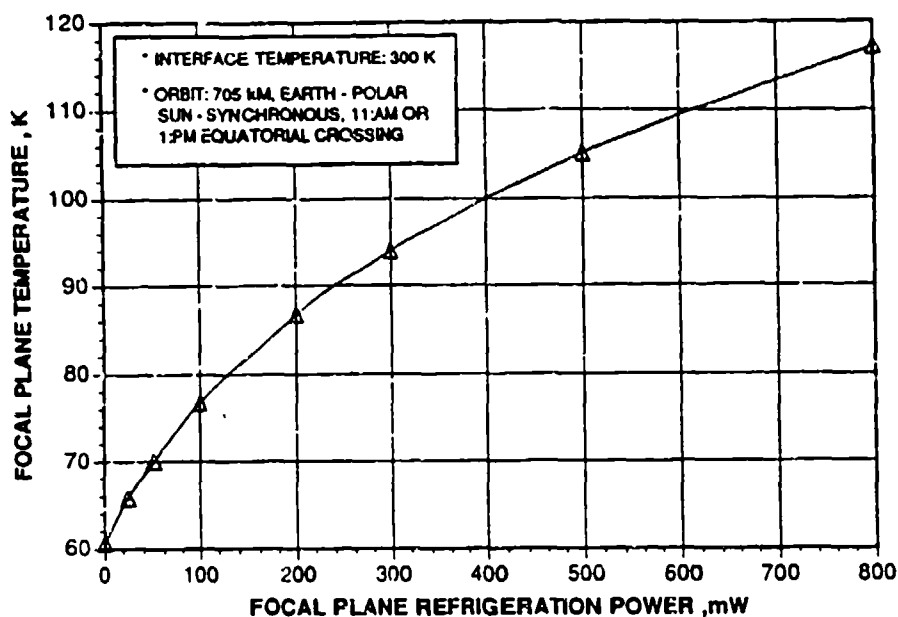


Figure 6 -- Radiative Cooler Refrigeration Power

2.2.2 Rod Conductor

Figure 7 is a cooling system sectional cutaway showing the radiative cooler, rod conductor, and twin cooled focal plane detector substrates. The rod conductor is of "T" configuration, with its long leg thermally grounded to the cooler cold stage. The two short legs of the "T" are each thermally grounded to a detector substrate using thermal straps. Figure 8 is an exploded view showing the above features. Each detector substrate is mechanically supported on eight fiberglass pretensioned bands. The bands are symmetrically arranged so that elastic symmetry will maintain the original position of the detectors during cooldown. The stiffness of the bands is such that the suspended substrate has a rigid-body response up to 500 Hz, in all axes.

The rod conductor is fabricated in one piece, from commercially-pure aluminum. It is supported at the intersection of the "T" by three fiberglass pretensioned bands and has a rigid-body response up to 200 Hz. Thermal shields surround the rod conductor and focal planes and are thermally grounded to the intermediate stage of the radiative cooler. The entire rod conductor/detector substrate/thermal shield assembly is enclosed in a vacuum manifold

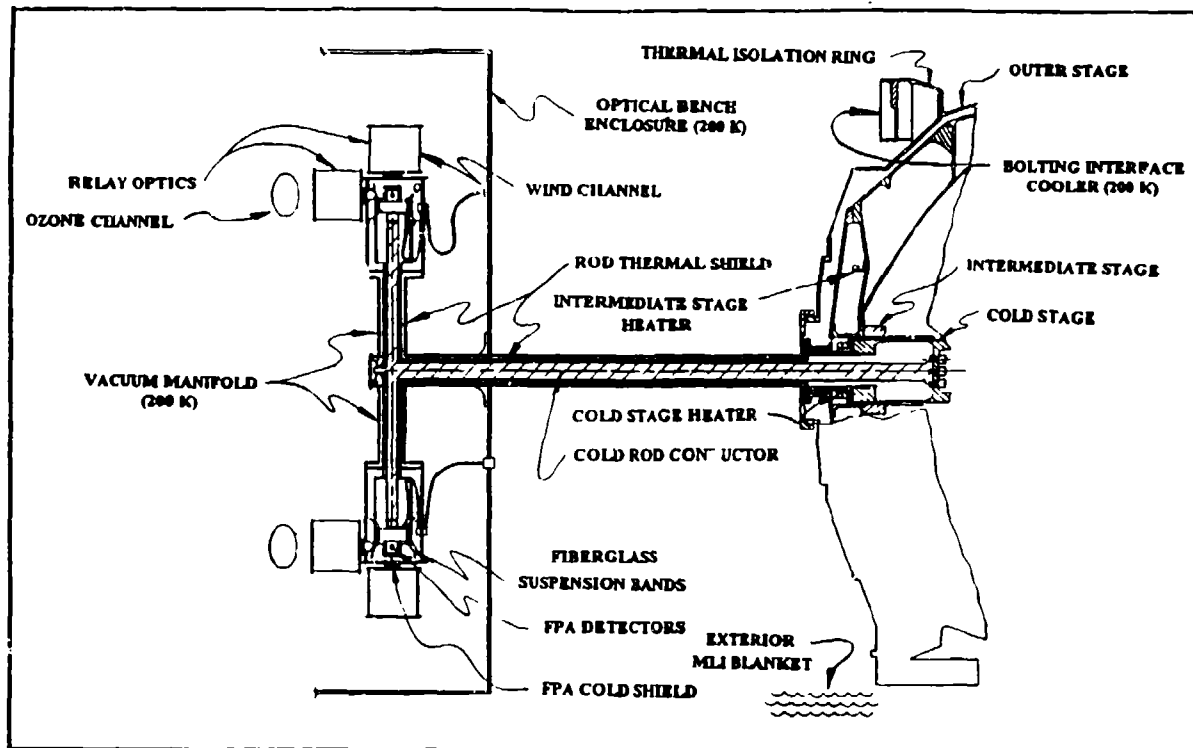


Figure 7 -- Cooling System Cutaway

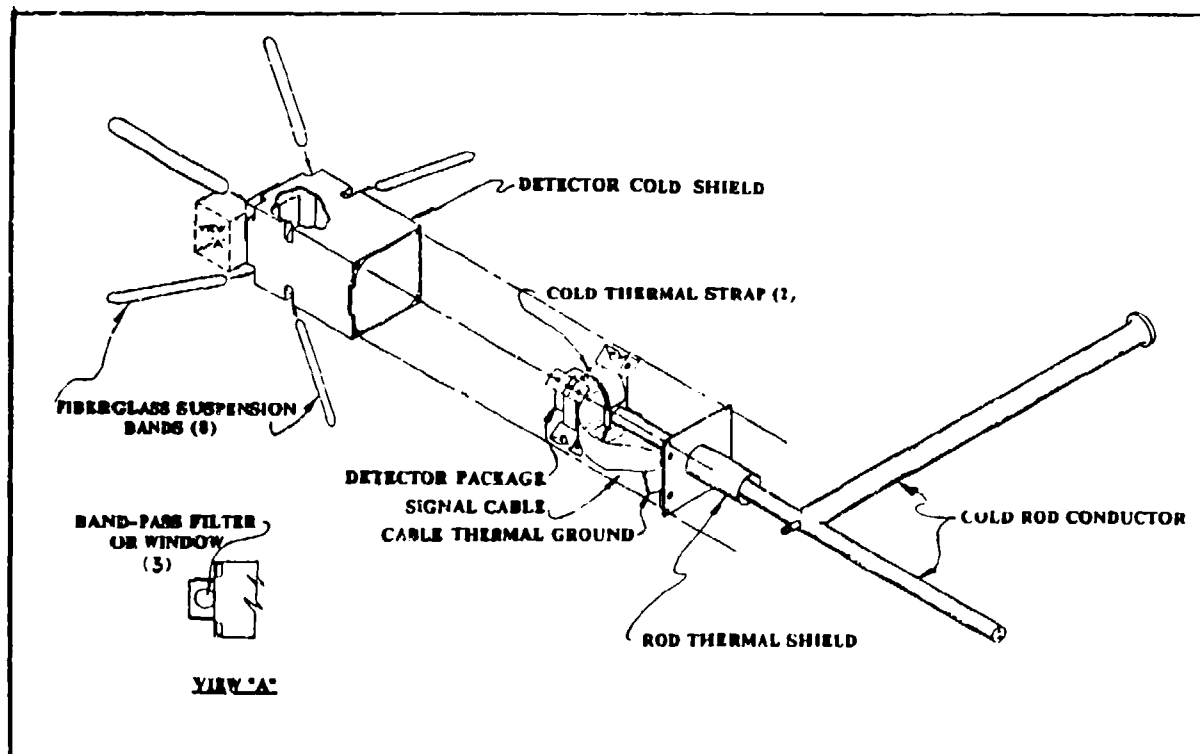


Figure 8 -- CFPA/Rod Conductor Exploded View

attached to the instrument optical bench. Each focal plane thermal shield or "detector cold shield" carries three windows (or band-pass filters). This maintains separation of the cold and intermediate stage cavities to prevent ice contamination when cold. To expose the cold detectors directly to a warm enclosure would invite icing. Even with these anti-contamination features, electric heaters are provided on the cold and intermediate stages for decontamination in space if needed.

To cool the instrument's detectors in ambient air for bench testing, the radiative cooler is first removed from the instrument. The rod conductor and thermal shield are attached to a test cold plate and the vacuum manifold evacuated. The test cold plate can then be cooled by inexpensive laboratory equipment, such as a dewar filled with liquid nitrogen. The detectors will be cooled to the desired temperature for bench testing by conduction through the rod.

3.0 THERMAL PERFORMANCE ANALYSIS

3.1 Environmental Loads and Radiation Interchange

Briefly, the SWIRLS radiative cooler thermal design employs three cooling stages with open faced honeycomb for the cold and intermediate stage radiator emitting surfaces (Figure 4). These stage radiators are shielded from direct view of the sun, planet, or spacecraft appendages. Planet energy is shaded from these radiators by a deployable shield which also serves as a door.

The radiative cooler is enclosed in a thermal blanket except for the planet shield, which utilizes thermal control paint on its outside surfaces. All inside surfaces of the planet shield are highly specular, so that solar energy impinging on it is reflected back to space except for a small diffuse component. Diffusely reflected solar energy and IR emissions from the planet shield can only fall directly on the intermediate stage radiator. The cold stage radiator "sees" cold space and IR emissions from a cooled, specular radiation shield mounted on the intermediate stage. Only diffusely reflected IR emissions and double-diffusely reflected solar energy from the planet shield can fall on the cold stage radiator.

The cooler outer stage, consisting of its outer housings mounted on a thermal isolator, employs four flat-plate fin radiators. These radiators are also shielded from direct view of the sun and spacecraft. The two lower fin radiators are shielded from direct view of the planet while the

two upper ones "see" only a portion of it. The SWIRLS instrument thermal design also requires a separate single-stage radiator to cool the two EOPM's to 220 K.

3.2 Thermal Analytical Model

A SWIRLS cooler thermal-analytical SINDA model was developed in a manner similar to an existing test-proven PMIRR cooler model except the radiator sizes were enlarged and new thermal nodes added to represent the rod conductor, twin focal planes, and thermal shields. Environmental loads for an Earth 705 km, polar, sun-synchronous, 1:00 pm equatorial crossing orbit were applied.

Both typical-case and worst-case design conditions were analyzed. These cases do not represent environmental load extremes, but represent instead choices to be made by the instrument's designer. Both cases assumed "hot" environmental conditions in terms of solar intensity, earth IR, and earth albedo loadings.

3.3 Predicted Thermal Performance

The results of the SINDA heat balance analyses are shown in Table 1. For typical-case design conditions the detector steady-state equilibrium operating temperature is 74.8 K, assuming a detector bias dissipation of 32 mW, or 1 mW per detector. The cooler is assumed to be structurally-attached and thermally-grounded to the 200 K optical bench.

For the worst-case design conditions the detector operating temperature is 80.4 K, assuming a detector bias dissipation of 64 mW, or 2 mW per detector. For this case, the cooler is assumed to be structurally-attached and thermally-grounded to the 300 K instrument mounting plate instead of the 200 K optical bench.

The above analyses indicate that the SWIRLS twin detector focal planes can be cooled to 80 K with an adequate cooling margin of safety, if the instrument designer adopts the typical case design conditions of Table 1. Focal plane temperature control heater power must be applied to raise the operating temperature from 74.8 K to 80 K.

Table 1 -- Predicted Thermal Performance

	Typical Case Design Conditions	Worst-Case Design Conditions
FPA bias power dissipation	32 mW (1 mW/PC detector)	64 mW (2 mW/PC detector)
Cooler bolting interface temperature	200 K	300 K
Cooler exterior blanket temperature	200 K	250 K
SWIRLS optical bench temperature	200 K	200 K
Vacuum manifold temperature	200 K	200 K
Predicted Steady-State Temperatures		
FPA detectors	74.8 K	80.4 K
FPA cold shield	126.7 K	134.9 K
Cold stage radiator	74.1 K	79.3 K
Intermediate stage radiator	125.7 K	133.9 K
Outer stage radiator	166.8 K	198.4 K
Specified FPA operating temperature: 80 K		

4.0 RADIATIVE/CRYOENGINE COOLING COMPARISONS

4.1 Cooling Load Comparison

How can a radiative cooler producing 130 mW of focal plane cooling power at 80 K compete successfully with a cryoengine with a cooling capability of 1 W at 80 K? The answer lies in examining the source of the cooling loads characteristic of each design application. The on-focal-plane power dissipation is no greater than 64 mW in both applications. The total heat load applied to the cryoengine cold head has been calculated at 836 mW, while the total heat load applied to the radiative cooler cold stage (i.e., the power radiated to space by the cold radiator) is 170 mW, as determined by a SINDA heat balance. Why is there such a difference in these heat loads?

For the radiative cooler application, there is an intermediate thermal shield interposed between the 80 K cold stage and the 200 K vacuum manifold not present in the cryoengine application. This intermediate stage is in thermal balance at 134 K, and is radiating 1.3 W to cold space.

Thus, much of the heat leaking in from the 200 K ambient optical bench is intercepted by the intermediate stage and diverted to space. Also, for the radiative cooler application, a more advanced low-heat-leak design for the focal plane structural supports was employed. Fiberglass bands suspend the focal planes from the 200 K vacuum manifold, instead of a titanium truss structure employed with the cryoengine design.

4.2 Cooling System Mass Comparison

A preliminary mass property analysis of a SWIRLS three-stage radiative cooler with a rod conductor and its associated thermal shield indicates that the required mass limit of 12 kg was not exceeded. The mass of the SWIRLS instrument with a radiative cooling system is no greater than that with the baselined cryoengine cooling system.

A radiative cooling system requires no input power or waste heat rejection. The additional cost and mass of providing means to accommodate these requirements at the spacecraft level are then eliminated. Preliminary estimates indicate substantial cost savings are available. A study to determine the focal plane operating temperature below which cryoengine cooling becomes more attractive from a total mass and projected area point of view has been carried out by Haskin and Dexter ⁴. This study showed a crossover temperature of 67-74 K for moderate cooling loads (0.1-1.0 W) and a higher crossover temperature of about 94 K for larger cooling loads (10 W). However, the empirical cooling system data collected for the study showed significant scatter, and thus these crossover temperatures should be considered only as indicative of general trends. The above comparison takes no account of threat survivability, and so may not be relevant to military applications.

5.0 CONCLUSIONS

Many advanced remote sensing instruments of the 1990's can successfully employ radiatively-cooled focal planes. Recent advances in radiative cooler design have made possible substantial increases in cooling power. A SINDA heat balance indicates that the SWIRLS instrument twin focal planes can be cooled to 80 K using a modified PMIRR-type, three stage radiative cooler with an unrestricted view to cold space.

If required, the cooled focal plane can be physically located outside of the radiative cooler. Heat can then be efficiently transported by means of a thermally-shielded rod conductor from

the focal plane to the cooler. A high-performance radiative cooler with a thermally-shielded rod conductor is a reliable, versatile and self-contained cooling system with no electrical power drain, no waste heat, and no induced vibration. Substantial cost savings are available which arise from spacecraft accommodation simplification and extended cooler service life.

The multi-stage design employed by an advanced radiative cooler provides a thermally-efficient method of dealing with the heat leak problem. Heat leaking in from the ambient environment is diverted to space by the intervening stages of the cooler, thus greatly reducing the heat load applied to the cold stage.

6.0 ACKNOWLEDGMENTS

The author wishes to acknowledge valuable contributions to the project reported herein made by T.J. Harvey and S.F. White of the AEC-Able Engineering Co.

7.0 SOURCE OF INFORMATION

Thermal design characteristics discussed in this paper were obtained from the Jet Propulsion Laboratory.

8.0 REFERENCES

1. D.J. McCleese and J.S. Margolis, "Remote sensing of stratospheric and mesospheric winds by gas correlation electro-optic phase modulation spectroscopy", Applied Optics **22**, 2528-2534, 1984.
2. D.J. Kuyper "Radiative cryogenic cooler for the Pressure Modulator IR Radiometer" Cryogenic Optical Systems and Instruments V SPIE, Vol. 1765 No. 23, July 1992.
3. T.T. Cafferty and D.J. Kuyper "Radiative cryogenic cooler for Thematic Mapper" Technologies of Cryogenically Cooled Sensors and Fourier Transform Spectrometers SPIE, Vol. 364 No. 10, August 1982.
4. W.L. Haskin and P. F. Dexter "Ranges of application for cryogenic radiators and refrigerators on space satellites" 17th Aerospace Sciences Meeting, AIAA 79-0179, January 1979.

NEW MAGNETIC REFRIGERANTS FOR THE
LOW TEMPERATURES REGION

Mihail D. Kuz'min
Theoretical Department, General Physics
Institute, Academy of Sciences of the
USSR, Vavilov Street 38, Moscow 117492
USSR

Alexander M. Tishin,
Sergey Y. Dan'kov
Physics Department, Moscow State
University, Moscow 119899, USSR

ABSTRACT

The thermodynamic and magnetic characteristics of rare earth orthoaluminates (ReOA) ReAlO_3 , the compounds with perovskite structure have been investigated theoretically. The opportunities of their using as working materials for 4.2-77 K magnetic refrigerators are considered. It is shown that magnetic properties of ReOA can be described well by means of mean field approximation (MFA). The magnetic entropy change, absorbed heat per unit volume and magnetocaloric effect under applied external magnetic field up to 30 T have been calculated within the limits of MFA. It appears that orthoaluminates are more advantageous than $\text{Gd}_3\text{Ga}_5\text{O}_{12}$, $\text{Dy}_3\text{Ga}_5\text{O}_{12}$ and $\text{Dy}_3\text{Al}_5\text{O}_{12}$, the garnets which so far have been considered the most promising refrigerants. The comparison of effectiveness of rare earth orthoaluminates shows that GdAlO_3 (GOA) and DyAlO_3 (DOA) are the most perspective among ReOA. DOA is more effective in weak and moderate magnetic fields, GOA is better within the strong field region. DOA appears to be an ideal material for the device using the rotation of a working body in a constant magnetic field.

WEDNESDAY SESSION

EXPERIMENTAL INVESTIGATION OF THE REGENERATIVE MAGNETIC REFRIGERATOR OPERATING BETWEEN 4.2 K AND 1.8 K

Sangkwon Jeong and Joseph L. Smith, Jr.
Cryogenic Engineering Laboratory
Massachusetts Institute of Technology, Cambridge, MA02139

Yukikazu Iwasa and Takenori Numazawa*
Francis Bitter National Magnet Laboratory, Cambridge, MA02139

ABSTRACT

This paper presents the construction and the experimental results from the successful operation of a prototype tandem regenerative magnetic refrigerator in the temperature range of 4.2 K to 1.8 K. The magnetic system of the tandem refrigerator has two virtually identical units, each consisting of a GGG (Gadolinium Gallium Garnet; $\text{Gd}_3\text{Ga}_5\text{O}_{12}$) magnetic core, a superconducting magnet, a warm end heat exchanger and a cold end heat exchanger. These components are united by a cryogenic displacer which shuttles 46 torr He^3 gas between the two units. Sub-atmospheric He^3 gas, rather than atmospheric He^4 , was chosen as the heat transport medium to avoid undesirable superfluidity in the regenerative magnetic core. The experimental net refrigeration rate was 19.2 mW at 1.8 K under the magnetic field swing of 0.4 T to 2.8 T. The refrigeration performance of the GGG magnetic core with irregularly shaped granules was 40 % less than the other magnetic core that contained about 70,000 GGG spheres, each 0.8 mm in diameter. The paper also describes design ideas for regenerative magnetic refrigerators that can reach warm end temperatures up to 15 K and cover a larger temperature span.

INTRODUCTION

There are a growing number of superconducting devices and detectors that require cooling below liquid helium temperature. Magnetic refrigeration has the potential to provide cooling for such devices, since it has been used as a cooling method to obtain temperatures below 1 K⁽¹⁾. While most magnetic refrigerators were one-shot process type for approaching zero Kelvin, a continuously operating magnetic refrigerator with reasonable

* a visiting scientist from the National Research Institute for Metals in Tsukuba, Japan

refrigeration capacity has also been in demand for engineering applications. The simplest magnetic refrigerator is a single Carnot type machine composed of four reversible processes: *adiabatic magnetization*, *isothermal magnetization*, *adiabatic demagnetization*, and *isothermal demagnetization*. The magneto-thermodynamic properties of most magnetic refrigerants, however, do not allow the single Carnot cycle to operate over a large temperature span with a reasonable magnetic field swing. This is why the regenerative concept was introduced for magnetic refrigerators⁽²⁾. The regenerative (or cascaded Carnot cycle type) magnetic refrigerator, having a porous magnetic core, is constituted with many independent single Carnot cycles along a temperature coordinate between warm and cold heat reservoirs. The first experimental apparatus attempted at MIT⁽²⁾ was for the temperature range of 4.2 K and 10 K using GGG wafers in the magnetic core. That device contained 3 atm. supercritical helium, the heat transport medium between the active magnetic core and the heat reservoirs. Even though the GGG core seemed to work well, the overall performance was not successful due to many extraneous factors such as axial conduction, large helium entrainment, and excessive dead volume.

This paper describes the second generation magnetic refrigerator developed in the Cryogenic Engineering Laboratory of MIT. Although the same magnetic material, GGG, was again used, the temperature range of the present device was shifted to 4.2 K~1.8 K from the range of 10 K~4.2 K. A magnetic refrigerator takes a more important role at temperatures below 4.2 K, which is the boiling temperature of liquid helium at 1 atm. An 1.8 K refrigerator is usually used for production of superfluid helium (He II), which is very useful for cooling sensors and other ultra-low temperature devices with its high heat transfer capability. The resolution of infrared sensors greatly improves as their operating temperatures are decreased due to less back-current noise. All key components have been redesigned based on our past experiences. The inherent sources of irreversibility in regenerative magnetic refrigerators are minimized by the design optimization of the system components, performed with a numerical analysis of the system.

SYSTEM DESCRIPTION

The experimental magnetic refrigerator is a tandem system as shown in Fig.1. The two magnetic systems, each consisting of a GGG magnetic core, a superconducting magnet, a warm end heat exchanger, and a cold end heat exchanger are connected by a cryogenic displacer. The displacer is a constant pressure actuator for moving the heat transport medium (46 torr sub-atmospheric He³ gas) through the two magnetic systems. The use of

low pressure He^3 gas as the heat transport medium avoids undesirable superfluidity and reduces the helium entrained in the porous magnetic core. The required He^3 mass flow can be achieved with a reasonable size displacer. The advantages of the tandem system are as follows:

- * Twice the refrigeration cycle frequency (2 refrigeration cycles / period),
- * Simplified displacer mechanism,
- * Potential simplification in magnet energization.

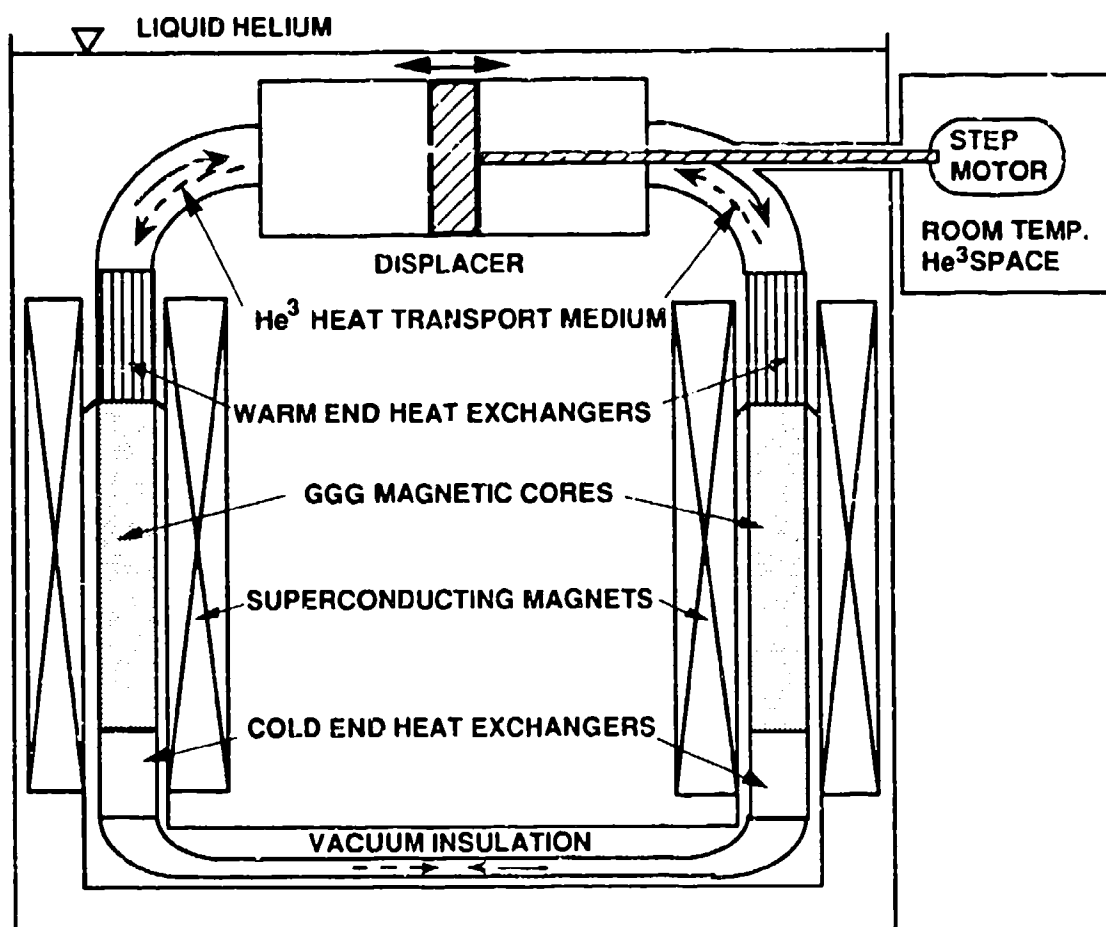


Fig.1. Schematic diagram of the tandem regenerative magnetic refrigerator.

The key components of the system (GGG packed bed magnetic core, warm end heat exchanger, cold end heat exchanger, superconducting magnet, and cryogenic displacer) are constructed with designs optimized with respect to given design constraints⁽³⁾. The assembled magnetic refrigerator is completely submerged in a liquid helium bath so that the

refrigeration is initiated from 4.2 K. The magnetic core and the cold end heat exchanger are thermally isolated from the 4.2 K bath by vacuum insulation. The temperature controlled heater in the cold end heat exchanger measures refrigeration capacity of the system by simulating a cooling load at 1.8 K.

A closed recycling He^3 system employing a charcoal adsorption pump is designed for the experimental apparatus because of the high cost of He^3 (\$89.70/STP liter). While the magnetic refrigerant (GGG) is stationary in the system, the heat transport medium (He^3 gas) is shuttled by the displacer which is driven by a step motor at room temperature. In order to keep the working space contamination free, because it is a 46 torr vacuum, the whole driving mechanism including the step motor is placed in the He^3 space. This configuration eliminates dynamic sealing.

The unique power charging method for the tandem superconducting magnets⁽⁴⁾ reduces the reactive power flow between the superconducting magnets and the power supply. Each magnet is divided into two parts and only one half is energized and de-energized. Actually each magnet consists of two identical separate coils; one for the persistent current mode and the other for the variational current mode. The persistent current coil and the variational current coil are physically wound together by juxtaposing them in a magnet winding machine. The measured mutual inductance between the persistent and variational coils is 1.0, which confirms that they are well coupled. The self inductance of each variational current mode coil is, therefore, only 25% of the total inductance of the magnet. Due to this reduced inductance, the reactive power requirement for charging the variational current mode coil is also reduced by a factor of 4.

In tandem mode, one magnetic unit is magnetized while the other one is demagnetized and vice versa. The magnetic field variations are 180° out of phase with respect to each other. For operation of the magnetic refrigerator, the persistent current mode coils which are connected in series, are first energized up to the maximum operating current level. They contribute half of the maximum field for both GGG magnetic cores. The variational current mode coils in the two units, connected in series, are then energized to the positive and negative maximum operating current level by a single bipolar power supply. As a result, at any given instant, the direction of the variational field in each coil adds to the persistent field in one core and subtracts from the persistent field in the other core. The combined field variation for each core, therefore, makes the tandem operation of the system possible.

EXPERIMENTAL RESULTS

The experiment of the tandem regenerative magnetic refrigerator was performed with a cycle time of 24 seconds. The persistent current was first charged up to 16 A, which provided 1.6 T for both magnetic cores. The current of the variational current mode coil, however, was varied only within ± 12 A due to the limitation of power supply. As a result, the system magnetic field swing was 0.4 T to 2.8 T. Fig.2 shows the temperature data of the magnetic refrigerator during its cool down transient operation.

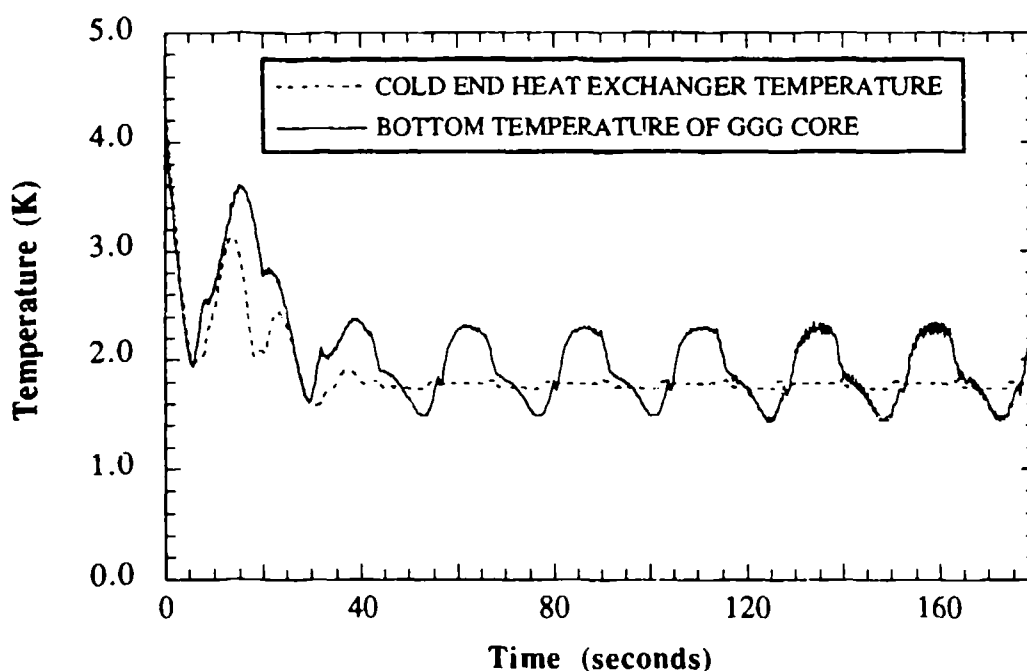


Fig. 2. Transient data of the regenerative magnetic refrigerator.

The cold helium flow from the bottom of GGG core is heated to 1.8 K during the demagnetization process in the cold end heat exchanger by the temperature controlled heater which gives us a direct measurement of refrigeration power. The initial temperature of the system was 4.2 K. After four to six cycles, the magnetic refrigerator easily reached its cyclic steady state.

For the successful tandem refrigerator operation, the synchronized control of the magnetic field variation and the heat transport medium flow is very important. Each process of the cycle of the regenerative magnetic refrigerator is described below and is shown in Fig.3.

- *Adiabatic magnetization* : The magnetic field steadily increases from 0.4 T to 0.8 T without shuttling helium gas (54 through 56 seconds). The GGG is adiabatically magnetized and increased in temperature.

- *Flow magnetization* : The magnetic field steadily increases to 2.8 T, while the helium gas is displaced from the cold end heat exchanger at 1.8 K to the warm end heat exchanger at 4.2 K (56 through 66 seconds). The helium flow is warmed by the magnetization of the GGG. The entropy pumping action is occurred at this time from the cold end heat exchanger to the warm end heat exchanger.

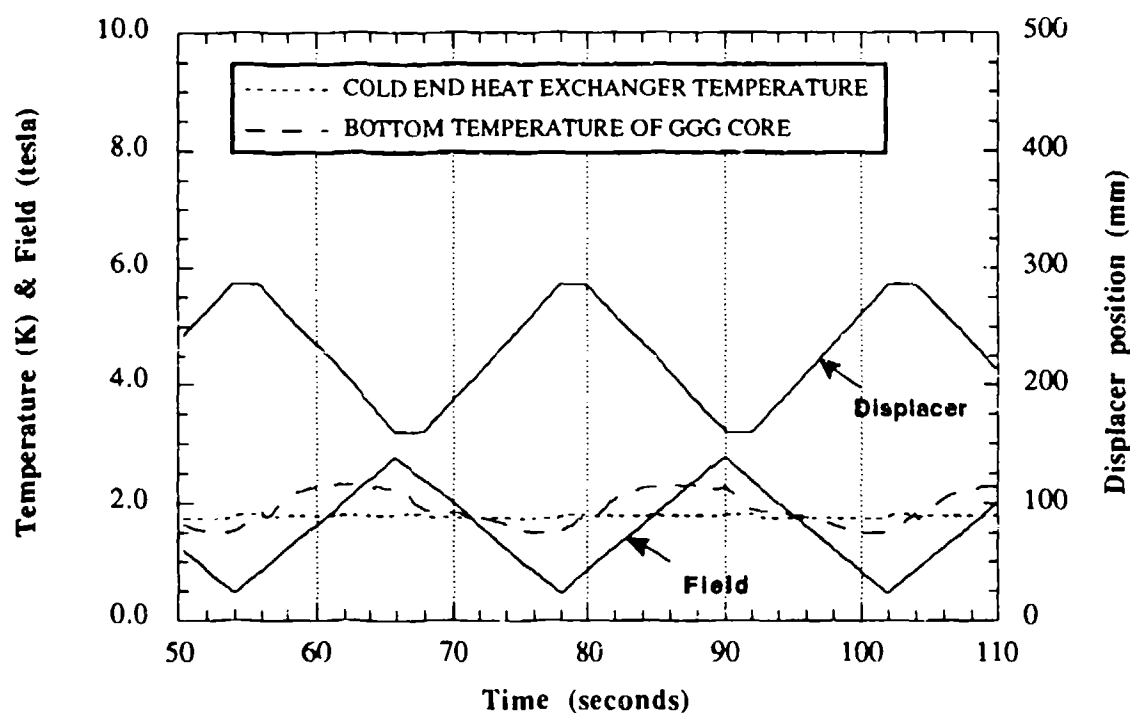


Fig. 3. Cyclic steady state data of the regenerative magnetic refrigerator.

- *Adiabatic demagnetization* : The magnetic field steadily decreases from 2.8 T to 2.4 T without moving the displacer (66 through 68 seconds). The GGG is adiabatically demagnetized and decreased in temperature.

- *Flow demagnetization* : As the field steadily decreases to 0.4 T, the helium flows from the warm end heat exchanger to the cold end heat exchanger. This down flow helium is cooled by the demagnetization of the GGG so that its temperature finally falls below 1.8 K at the bottom of the core (68 through 78 seconds). This is the active refrigeration process in the cycle.

The magnetic refrigerator operates successfully, producing net refrigeration power at 1.8 K. It is an interesting result to compare the performance of the two GGG cores in the tandem system, since one core is composed of uniform GGG spheres (0.8 mm diameter) and the other core is filled with crushed irregularly shaped GGG granules. The random packing porosity of the former core is 0.38 while that of the latter one is 0.40 due to its random shape and filling configuration. The granule packed GGG core produced just about 60 % of the net refrigeration power of the sphere filled GGG core. The high porosity filled by the entrained helium in the porous core generates irreversibility during adiabatic processes, which results in the loss of performance in the regenerative magnetic refrigerator. The whole net refrigeration power of the experimental tandem system, as a result, was 19.2 mW at 1.8 K. The refrigeration power can be increased by reducing the cycle time as long as the power supply can handle a high reactive power flow of the superconducting magnet. The other useful way to enhance the system performance of the regenerative magnetic refrigerator is to adjust the shuttle mass of helium flow so that the overall heat capacity balance between the magnetic refrigerant and the heat transport medium can be improved.

DESIGN IDEAS FOR NEXT GENERATION

The experiments described in this paper showed that the regenerative magnetic refrigerator operated successfully in the temperature range between 4.2 K and 1.8 K. Increasing the temperature span of continuous magnetic refrigerators, however, still remains a challenge. In this section, two design ideas of the magnetic refrigerator for the next generation are briefly discussed.

<Mixed magnetic refrigerant>

The goal of the mixed magnetic refrigerant is to achieve a relatively uniform magneto-caloric effect over a broader temperature range. Since the magnetic entropy change of the material is large near its transition temperature⁽⁵⁾, mixing two or more magnetic materials is a viable way to improve regenerative magnetic refrigerators. Even though GGG is the best magnetic refrigerant in the temperature range near 4.2 K, other magnetic materials may have larger magneto-caloric effects than GGG above 10 K, since the magneto-caloric effect of GGG decreases as the temperature increases. One of the promising substitutes for GGG is DAG⁽⁶⁾ ($\text{Dy}_3\text{Al}_5\text{O}_{12}$; Dysprosium Aluminum Garnet). Fig.4 compares the entropy-

temperature diagrams of both GGG and DAG. The broad entropy gap at constant temperature usually promises large magneto-caloric effect.

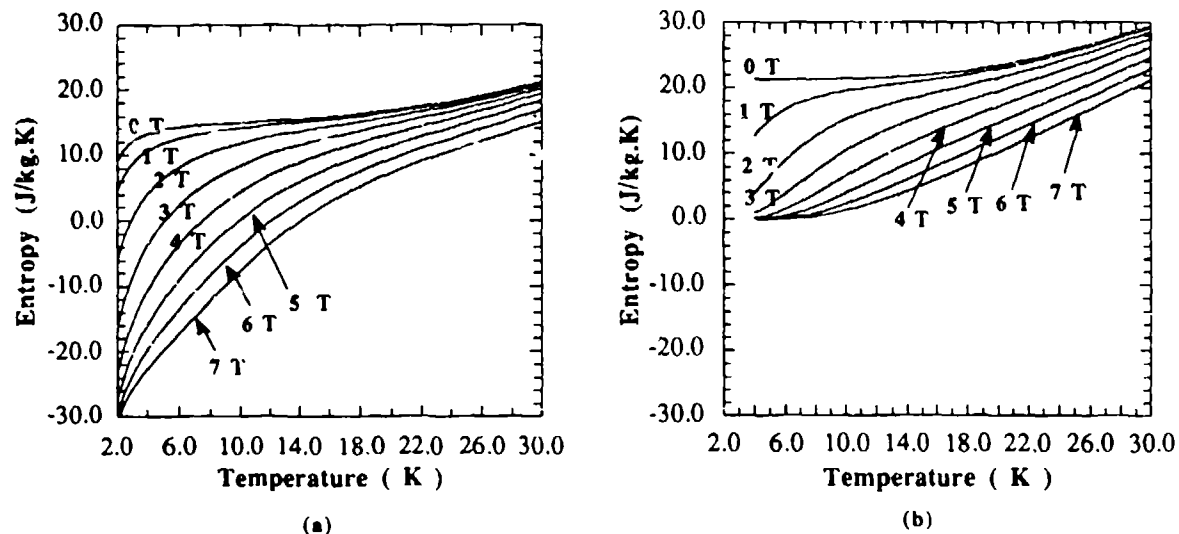


Fig.4. Entropy diagrams of GGG and DAG. (a) GGG (b) DAG.

If the warm end temperature of the regenerative magnetic refrigerator is 15 K, it may be desirable to use a mixed refrigerant of GGG and DAG. The packed bed magnetic core, which is the current GGG core of the tandem magnetic refrigerator, can easily utilize mixed magnetic refrigerants. Fig.5 shows a suggested material distribution for a regenerative magnetic refrigerator operating between 1.8 K and 15 K.

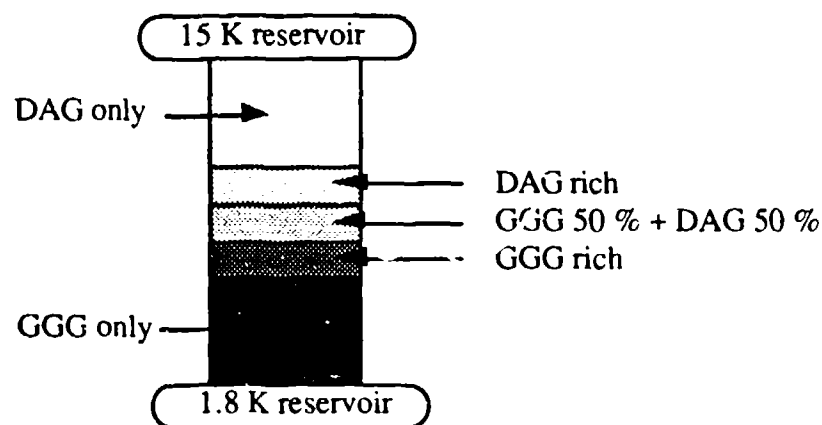


Fig.5. GGG to DAG transition in the regenerative magnetic core.

A gradual variation of composition in the packed bed core, from purely GGG to purely DAG along the temperature coordinate, avoids an abrupt magneto-caloric effect transition. The exact composition variation may need more analysis including the calculation of their magneto-thermodynamic properties. The heat capacity balance between the mixed magnetic refrigerant and heat transport medium is also an important factor to the successful operation of the system.

<Combination with G-M cryocooler>

The magnetic refrigerator which generally works well in low temperature ranges (< 4.2 K) with a small temperature span needs an additional cooling mechanism for its warm end reservoir. A reliable Gifford-McMahon cryocooler is one practical way. The combination between the magnetic refrigerator and the gas refrigerator can be done externally. On the other hand, it may be also possible to have an internal combination between them in a single coordinated configuration. Fig.6 is a conceptual design of such a device operating between 300 K and 1.8 K.

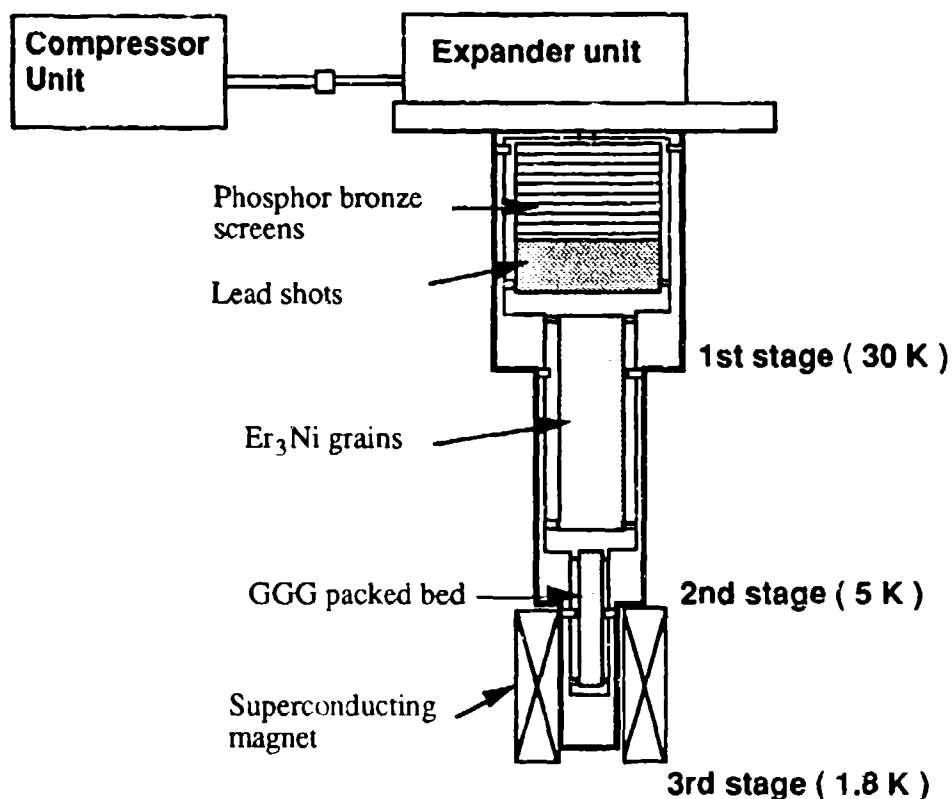


Fig.6. Schematic of magnetic G-M cryocooler.

The specific heat of a typical magnetic material shows a high peak near its transition temperature and can be varied by applied magnetic field, which makes it possible to use GGG as a low temperature magnetic regenerator material in the last stage of a G-M cryocooler. As shown in Fig.6, each stage has a different regenerator material. The magnetic field in the third stage enhances the regenerator characteristic of GGG. The cyclic operation of this magnetic G-M cryocooler is composed of the following four processes.

- *Process 1* : With the displacer at the bottom of the cylinder, the inlet valve is opened and the pressure within the upper expansion space and the regenerator is increased from a low pressure to a high pressure. GGG is demagnetized from a high field, H_{max} to a medium field, H_{med} while having just enough heat transfer with the gas to absorb the heat of compression of the gas.

- *Process 2* : With the inlet valve still open and the exhaust valve closed, the displacer is moved to the top of the cylinder. This action moves the gas which was originally in the upper expansion space down through the regenerator to the lower expansion space. During this process, GGG is continuously demagnetized to the minimum field, H_{min} . This magnetic process is equivalent to the flow demagnetization process of the previous magnetic refrigerator. Since the gas is cooled as it passes through the regenerator, the gas volume will decrease so that more gas will be drawn in through the inlet valve during this process to maintain a constant pressure within the system.

- *Process 3* : With the displacer at the top of the cylinder, the inlet valve is closed and the exhaust valve is opened, thus allowing the gas within the lower expansion space to expand to the initial pressure. This causes the gas in the lower expansion space to drop to a low temperature. GGG is magnetized up to a medium field, H_{med} . The exhaust gas takes thermal energy of magnetized GGG out of the system.

- *Process 4* : With the exhaust valve still open, the displacer is moved to the bottom of the cylinder. This action moves the gas up through the regenerator to the upper expansion space. GGG is continuously magnetized up to a high field, H_{max} . This is the flow magnetization process. During this process, the up flow gas is warmed by the magnetized GGG. This process completes the cycle and the low pressure gas is compressed again, returning to the process 1.

There are some practical problems, however, in this combined refrigerator.

- Gas (typically helium) entrainment effect in the third regenerator at high pressure.

- A.C. loss associated with the fast charging and discharging the magnet for the synchronization with the cycle frequency of G-M cycle, which is typically about 0.5 Hz.
- Phase transition in the bottom of the system, unless He^3 gas is used for the working medium.
- Large force to move GGG inside the strong magnetic field.

The ideas introduced in this section, even though not obviously practical, should be applicable for the next generation magnetic refrigerator experiments.

CONCLUSION

This paper presents the construction and the experimental results from the successful operation of a prototype tandem regenerative magnetic refrigerator in the temperature range of 4.2 K to 1.8 K. The inherent sources of irreversibility in regenerative magnetic refrigerators are minimized by the design optimization of the system components; GGG packed bed magnetic core, warm end heat exchanger, cold end heat exchanger, superconducting magnet, and cryogenic displacer. Under the magnetic field swing of 0.4 T to 2.8 T, the prototype machine produced 19.2 mW of net refrigeration power at 1.8 K. The experiment also revealed about 40 % loss of performance by the magnetic core that contained crushed irregularly shaped granules of GGG, compared to that achieved by the other magnetic core that had about 70,000 GGG spheres, each 0.8 mm in diameter. Finally the design ideas about a mixed magnetic refrigerant and a combined magnetic G-M cryocooler are described to extend warm heat reservoir temperatures up to 15 K and cover larger temperature spans.

ACKNOWLEDGMENTS

This work has been sponsored by Sumitomo Heavy Industries, Inc. with additional support from the National Research Institute for Metals in Japan.

REFERENCES

1. Giauque, W.F. & MacDougall, D.P., 1933, "Attainment of temperatures below 1° absolute by demagnetization of $\text{Gd}_2(\text{SO}_4)_3 \cdot \text{H}_2\text{O}$," *Phys. Rev.*, Vol.43, p.768.

2. Taussig, C.P., Gallagher, G.R., Smith, Jr., J.L., and Iwasa, Y., 1986, "Magnetic Refrigeration Based on magnetically Active Regeneration," *Proceedings of the Fourth International Cryocoolers Conference*, pp.79-88.
3. Jeong, S., Smith, Jr., J.L., Iwasa, Y., and Numazawa, T., 1990, "Design of the Regenerative Magnetic Refrigerator Operating between 4.2 K and 1.8 K," *Proceedings of the sixth International Cryocoolers Conference*, Vol.II, pp.189-198.
4. Jeong, S., 1992, "Development of the Regenerative Magnetic Refrigerator Operating between 4.2 K and 1.8 K," Ph.D.Thesis, Dept. of Mechanical Engineering, Massachusetts Institute of Technology, Cambridge, Massachusetts, pp.38-41.
5. Hashimoto, T., Kuzuhara, T., Sahashi, M., Inomata, K., Tomokiyo, A., and Yayama, H., 1987, "New application of complex magnetic materials to the magnetic refrigerant in an Ericsson magnetic refrigerator," *J. Appl. Phys.*, Vol.62, No. 9, pp.3873-3878.
6. Li, R., Numazawa, T., Hashimoto, T., Tomokiyo, A., Goto, T., and Todo, S., 1986, "Magnetic and thermal properties of $\text{Dy}_3\text{Al}_5\text{O}_{12}$ as a magnetic refrigerant," *Advances in Cryogenic Engineering*, Vol.32, pp.287-294.

A 4 K GIFFORD-McMAHON REFRIGERATOR FOR RADIO ASTRONOMY

Richard Plambeck, Niranjan Thatte, and Patrick Sykes
Radio Astronomy Lab, University of California
Berkeley, CA 94720

ABSTRACT

We have built a 3-stage Gifford-McMahon refrigerator which is designed to cool a superconducting junction to 4 K on a radio telescope. Using 50 grams of Er_3Ni spheres as the third stage regenerator, we measure no-load temperatures as low as 3.8 K at a cycle frequency of 72 rpm, and 2.2 K at 30 rpm. The third stage temperature can be maintained at 3.5 K with heat loads of 10 W on the first stage, 1 W on the second stage, and 50 mW on the third stage. At 72 rpm the refrigerator performance is impaired by the substantial pressure drop through the first and second stage regenerators; using a pressure transducer connected through a capillary tube to the third stage, we find that the helium pressure swing in the third stage expansion volume increases by 50 percent as the cycle frequency is decreased from 72 to 30 rpm.

Our prototype refrigerators exhibit occasional 0.5 to 1 K temperature excursions which occur over periods of a few minutes to a few hours. Tests suggest that this erratic behavior is primarily attributable to leakage of warm gas past the third stage seal.

INTRODUCTION

The most sensitive receivers available for millimeter-wavelength radio astronomy employ SIS (superconductor-insulator-superconductor) tunnel junction mixers which operate at temperatures of 4.5 K or lower. Such receivers are expected to operate continuously on radio telescopes for many months with minimal maintenance. Although SIS receivers commonly are cooled with hybrid Joule-Thomson/Gifford-McMahon refrigerators, JT circuits have a number of drawbacks: the heat exchangers are relatively bulky, the expansion valves tend to clog, and a separate helium compressor stage is required to handle the JT return gas. Typically the JT/GM coolers used in radio astronomy have refrigeration

capacities of 1 to 3 watts at 4.2 K. This is far greater than necessary: with careful design, the heat load on an SIS mixer can be kept to a few milliwatts.

In the past few years a number of groups^{1,2} have demonstrated that Gifford-McMahon cryocoolers utilizing Er_3Ni as a regenerator material can achieve refrigeration capacities of several hundred milliwatts at 4 K. Such refrigerators appear to be well-suited for use in cooling SIS receivers; they are considerably more compact than JT/GM systems, cool more quickly, and require only a single helium compressor.

We are constructing radio receivers for the Berkeley-Illinois-Maryland array (BIMA), an aperture synthesis instrument consisting of 9 millimeter-wave telescopes. Each telescope will be outfitted with a radio receiver covering 4 frequency bands, each requiring an SIS mixer. In this paper we describe the design and initial tests of 4 K GM refrigerators which will cool these receivers.

DESIGN

Two-stage GM cryocoolers described in the literature^{1,2}, with refrigeration capacities of up to 0.8 W at 4.2 K, typically use several hundred grams of Er_3Ni as the 2nd stage regenerator material. Because Er_3Ni spheres are expensive, and because our cooling requirements at 4 K are expected to be ≤ 25 mW, we chose to build a 3-stage refrigerator instead, using only about 50 g of Er_3Ni in the 3rd stage regenerator. We estimate that the heat loads on the refrigerator's 1st and 2nd stages will be 6 W and 0.5 W.

Thus far we have constructed 3 prototype refrigerators. We begin with a standard 2-stage GM cryocooler, machine off the plug at the end of the 2nd stage cylinder, and weld on a 3rd stage. Refrigerator #1 is a CTI model 350 cryocooler with an 8.9 cm long 3rd stage; refrigerators #2 and #3 are CTI model 1020CP cryocoolers with 15.2 cm and 11.4 cm 3rd stages, respectively. The inner diameter of the 3rd stage cylinder is 1.27 cm on all 3 prototypes. Several displacers of different designs were tested in each of the prototype refrigerators.

Figure 1 presents a cross sectional view of the 3rd stage cylinder and a typical displacer for refrigerator #3. Both the cylinder and the displacer are fabricated from 304 stainless steel. An 0.4 to 0.8 mm thick sheath of graphite-loaded polyimide (Envex 1315; Rogers Corp) epoxied to the outside of the displacer tube serves as a bearing surface. We attempt to maintain a radial clearance of 5 to 10 microns between the Envex bearing and the cylinder wall, to act as a clearance seal. A groove machined into the displacer also accommodates a split piston ring seal (CTI model 21 second stage seal).

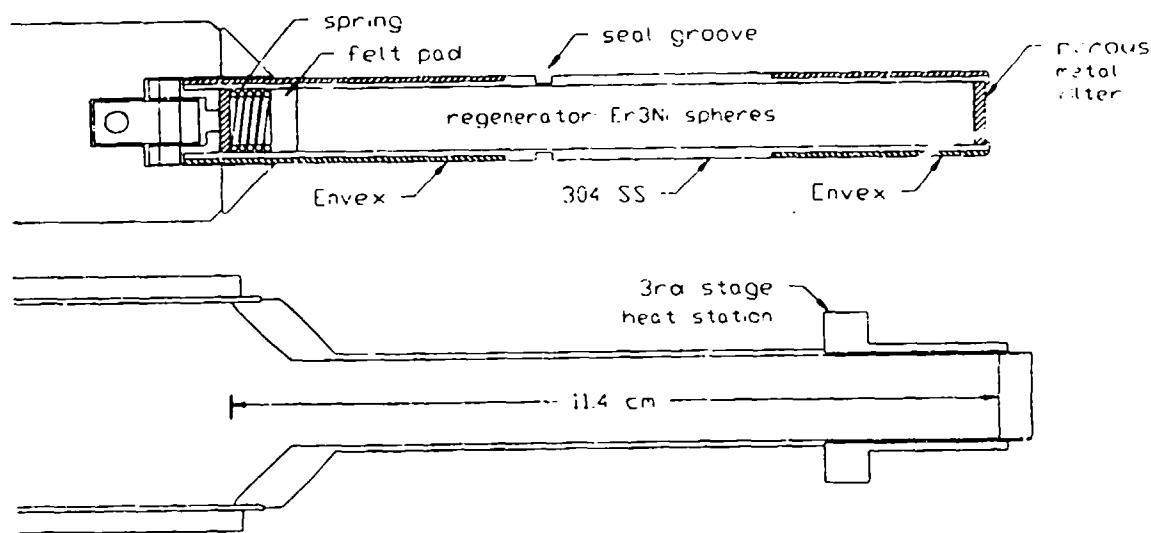


Fig 1. Cross sectional views of a 3rd stage cylinder and typical displacer.

The 3rd stage regenerator consists of Er₃Ni spheres, diameter range 180-450 microns, purchased from Toshiba America Electronics. We do not attempt to compress the spheres with a packing rod after pouring them into the displacer; instead, we install a spring-loaded felt pad at the warm end of the displacer to maintain pressure on the regenerator as settling occurs. Sintered stainless steel filters, with a pore size of 40 microns, are pressed into each end of the displacer to make certain that no Er₃Ni spheres escape.

The pin connections between the 1st, 2nd, and 3rd stage displacers are deliberately sloppy, to accomodate slight misalignments of the 3 cylinder sections. This makes it difficult to insert the displacer assembly into the cylinder, particularly if the refrigerator is mounted horizontally, as it will be on our radio telescopes. Accordingly, we machine a 45-degree chamfer into the warm end of the 3rd stage cylinder, and attach a mating cone to the end of the 2nd stage displacer. In this way the 2nd and 3rd stage displacers slip easily into their respective cylinder sections. We make no other modifications to the 1st or 2nd stage displacers.

On refrigerator #1 the 3rd stage displacer stroke is adjustable from 1.90 to 2.54 cm. On refrigerators #2 and #3, the displacer stroke for all 3 stages can be reduced from 3.18 to 2.54 cm, if desired, by substituting the crankshaft from a model 350 refrigerator. A 3-phase digital power inverter (Lenze Power Systems

model 8101) and Scott-T transformer allow us to operate the refrigerators at any cycle frequency from 4 to 100 rpm. All tests are done with a standard CTI model 1020 helium compressor.

TEST RESULTS

Refrigerators were installed in a test dewar with radiation shields attached to the 1st and 2nd stages. All 3 refrigerator stages were instrumented with silicon diode temperature sensors. The 3rd stage temperature was monitored independently with a germanium resistance thermometer and, at times, with a helium vapor gauge; temperatures measured with the silicon diode, GRT, and vapor gauge agreed within 0.1 K.

A computer connected to an a/d converter recorded the temperature of each stage at 15 second intervals. These measurements were done by sampling each sensor 100 times per second for 8 seconds; the temperature recorded was the mean of the highest and lowest values obtained during this interval. To monitor the temperature swings which are synchronized with each refrigerator cycle, we could also sample and record temperatures up to 200 times per second for short intervals. Pressure transducers in the helium supply and return lines near the expander also were monitored by the computer. Heaters were mounted on all 3 refrigerator stages to perform load tests.

A typical cooldown curve is shown in Figure 2. Operated at its normal cycle frequency of 72 rpm, the refrigerator cooled to 4.8 K in approximately 1.3 hours. Lower 3rd stage temperatures are reached by reducing the cycle frequency. In the example in Figure 2, the 3rd stage temperature drops rapidly to 3.7 K when the cycle frequency is reduced to 30 rpm. The 1st and 2nd stage cooling capacities decrease at 30 rpm, so these stages warm up slightly.

Measurements of the no-load 3rd stage temperature as a function of cycle frequency are shown in Figure 3 for five different displacers. Displacer parameters and regenerator masses are given in the figure caption. Note that lead spheres were used as the regenerator material for curve A, which reaches 4.75 K at 30 rpm. The heat leak onto the 3rd stage was measured to be approximately 10 mW during these tests.

Load tests showed that the 1st, 2nd, and 3rd stage temperatures were well isolated. An example is shown in Figure 4. Here, 50 mW applied to the 3rd stage raises its temperature from 4.25 to 4.7 K, but has no discernible effect on the 2nd stage; 2 W applied to the 2nd stage increases its temperature from 13.8 to 16.0 K, but increases the 3rd stage temperature by only 0.15 K.

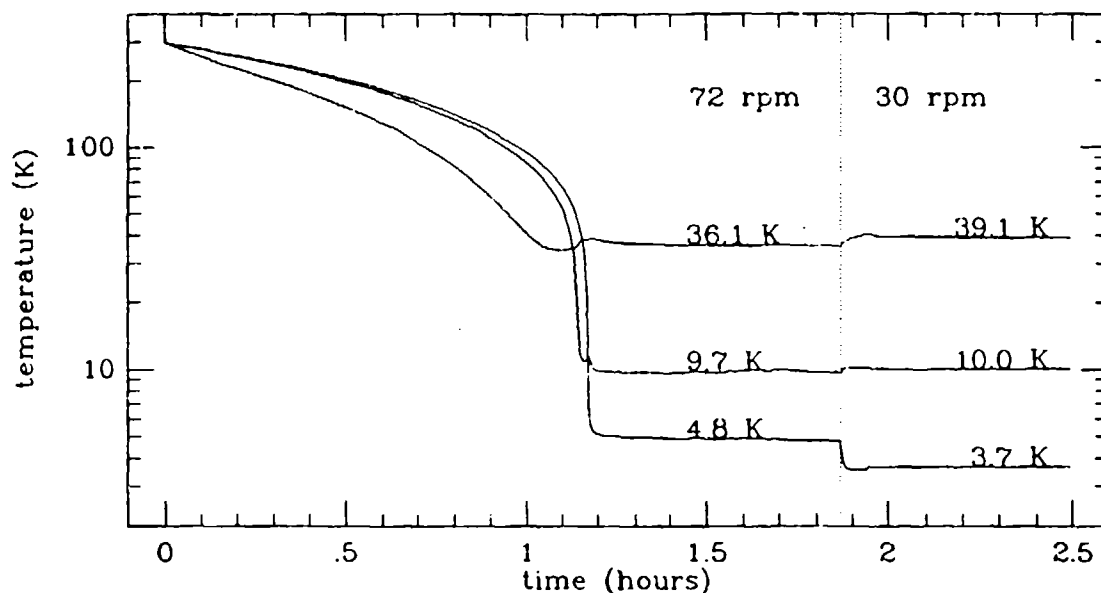


Fig 2. Typical cooldown curve. Temperatures of stages 1, 2, and 3 are plotted on a logarithmic scale. At 1.86 hours, the refrigerator was slowed from 72 to 30 rpm.

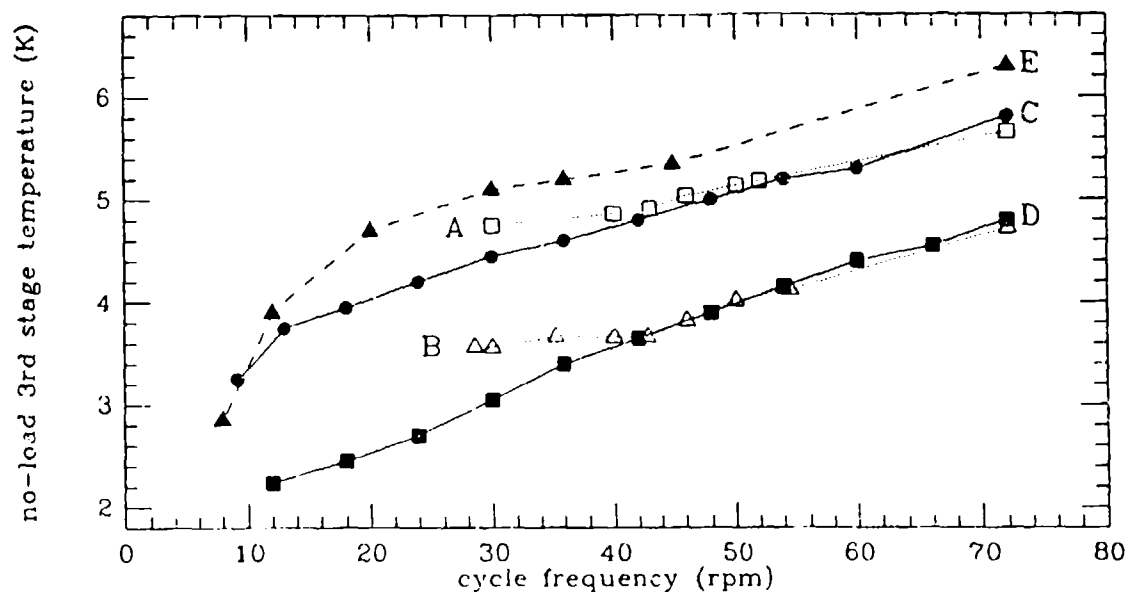


Fig. 3. No-load temperature vs. cycle frequency for 5 different displacers: A - refrigerator #1, 46 g of 350 micron diameter Pb spheres, 1.9 cm stroke, clearance seal; B - refrigerator #1, 30 g Er_3Ni , 1.90 cm stroke, clearance seal; C - refrigerator #2, 57 g Er_3Ni , 2.54 cm stroke, CTI seal; D - refrigerator #2, 53 g Er_3Ni , 3.18 cm stroke, CTI seal; E - refrigerator #3, 46 g Er_3Ni , 2.54 cm stroke, clearance seal.

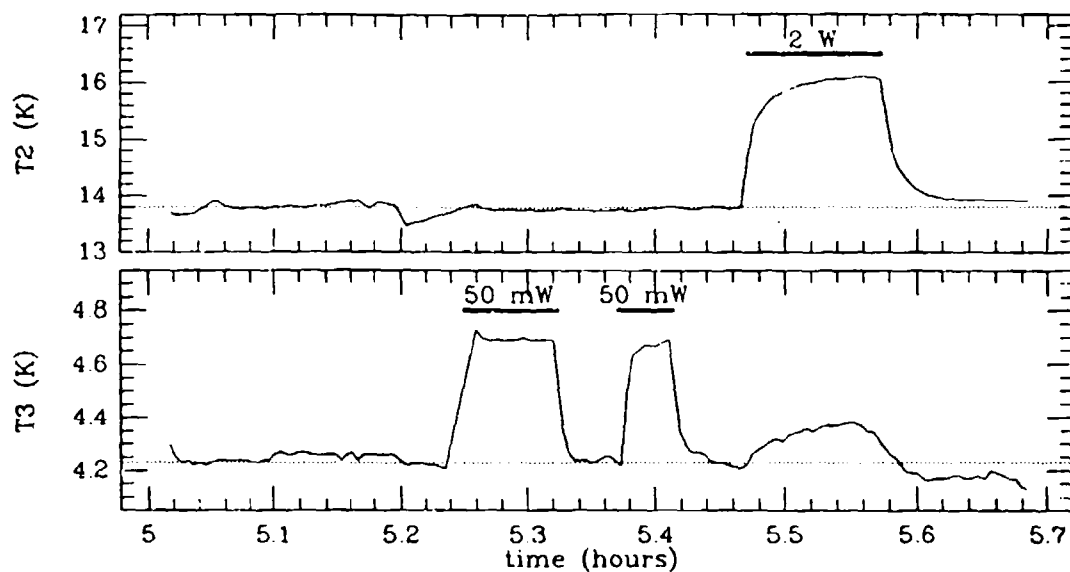


Fig. 4. Load test, demonstrating the excellent isolation between stages.
(Refrigerator #3, 2.54 cm stroke, 42 g Er_3Ni , 30 rpm, CTI seal.)

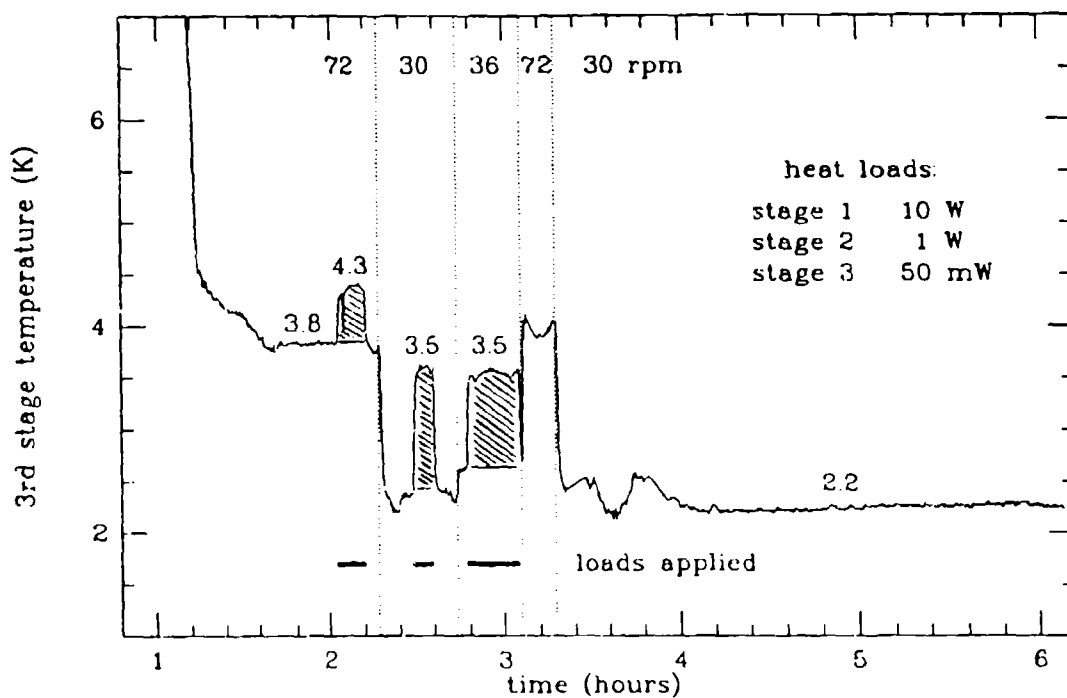


Fig. 5. Cooldown and load test of refrigerator #2, with 53 g. of Er_3Ni in the 3rd stage regenerator, a 2.54 cm stroke length, and a CTI seal.

Our best results to date, obtained with 53 g of Er_3Ni in refrigerator #2 (the long cylinder), are shown in Figure 5. With no loads applied, the 3rd stage cooled to 3.8 K at 72 rpm, 2.2 K at 30 rpm. With heat loads of 10 W on stage 1, 1 W on stage 2, and 50 mW on stage 3, the 3rd stage temperature was 4.3 K at 72 rpm and 3.5 K at 36 rpm. At 36 rpm the 1st and 2nd stage temperatures stabilize at 65 K and 13.6 K with the loads applied.

WHY IS IT NECESSARY TO REDUCE THE CYCLE FREQUENCY?

Our results, as well as those of other groups^{1,2}, indicate that it is essential to reduce the refrigerator cycle frequency in order to achieve the very lowest temperatures. Why is this so?

(1) limited thermal diffusivity of Er_3Ni ?

Ogawa et al.³ have measured the thermal conductivity of Er_3Ni at low temperatures (it is slightly lower than that of stainless steel), and have calculated the penetration depth for heat as a function of cycle frequency. Their calculations show that heat transfer in spheres of radius 0.1 to 0.2 mm, as used in our regenerator, is essentially perfect at a cycle frequency of 60 rpm. Indeed, our data (curve A in Figure 3) show that reducing the cycle frequency also lowers the 3rd stage temperature for a lead regenerator, even though lead has a thermal diffusivity more than 3 orders of magnitude greater than Er_3Ni .

(2) improved heat transfer?

Halving the mass flow rate through the regenerator reduces the heat transfer coefficient by about 40%, but doubles the time that gas spends inside the regenerator. Thus, reducing the cycle frequency might be expected to lower the 3rd stage temperature by improving heat transfer in the regenerator. To test this hypothesis experimentally, we tested lead spheres of 3 different diameters in one refrigerator. At 72 rpm the 3rd stage cooled to 6.4 K with 33 g of 350 micron diameter Pb spheres; to 6.5 K with 31 g of 200 micron spheres; and to 6.9 K with 34 g of 100 micron spheres. The corresponding temperatures at 30 rpm were 6.1 K, 6.1 K, and 6.3 K. Although the heat transfer coefficient increases by a factor of 5 as the sphere diameter decreases from 350 to 100 microns, the 3rd stage temperatures did not improve. Thus, heat transfer does not appear to limit the regenerator efficiency.

(3) flow channeling?

When spheres are packed into a tube, there is a disordered zone next to

the wall. If helium flows preferentially through this zone, heat transfer to the regenerator matrix will be reduced. Slowing the cycle frequency might allow thermal diffusion laterally within the regenerator, minimizing the effect. In an attempt to test the importance of flow channeling, we artificially increased the displacer wall area by inserting a V-shaped piece of brass shim stock down the length of the displacer before filling it with Er_3Ni spheres. This increased the effective regenerator perimeter by a factor of almost 2. Third stage temperatures measured with and without the shim stock in place were equal within 0.1 K; thus, there is no evidence that flow channeling limits the regenerator performance.

(4) pressure drops

Having ruled out the 3 possibilities listed above, we focussed on pressure drops within the regenerator as a possible factor limiting the refrigerator performance at higher cycle speeds. In order to monitor the helium pressure at the cold end of a refrigerator, we drilled a hole into the end of refrigerator #3 and connected a room temperature pressure transducer to the cold end via a capillary tube (length 50 cm, ID 0.8 mm). The additional void volume and heat leakage introduced by the capillary tube had little deleterious effect except at very low cycle frequencies: at 6 rpm the 3rd stage reached 2.4 K without the capillary, 3.2 K with it.

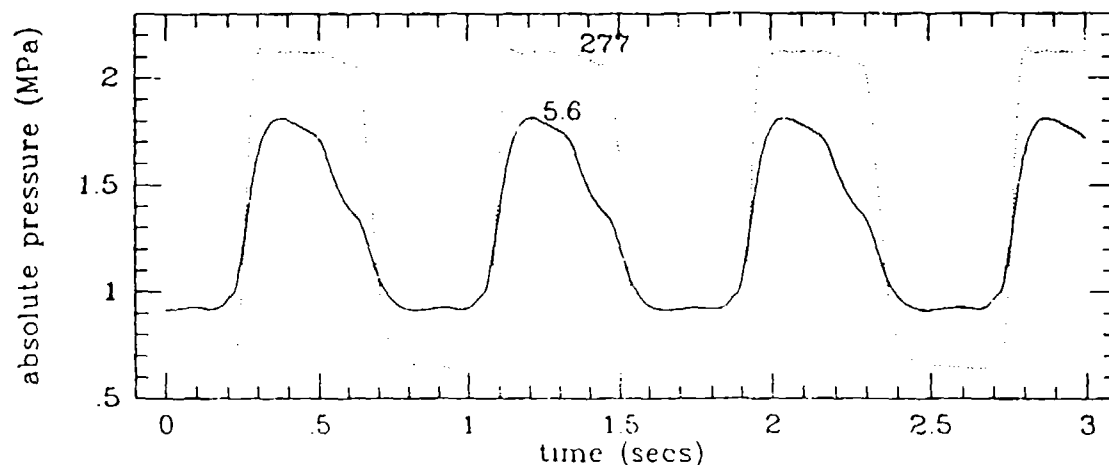


Fig. 6. Helium pressure swing in the 3rd stage expansion volume, monitored through a capillary tube with a room temperature transducer. The refrigerator cycle frequency is 72 rpm. The dotted curve was obtained when the 3rd stage was at 277 K, the solid curve when it had cooled to 5.6 K. (Refrigerator #3, 2.54 cm stroke, 45 g Er_3Ni , clearance seal.)

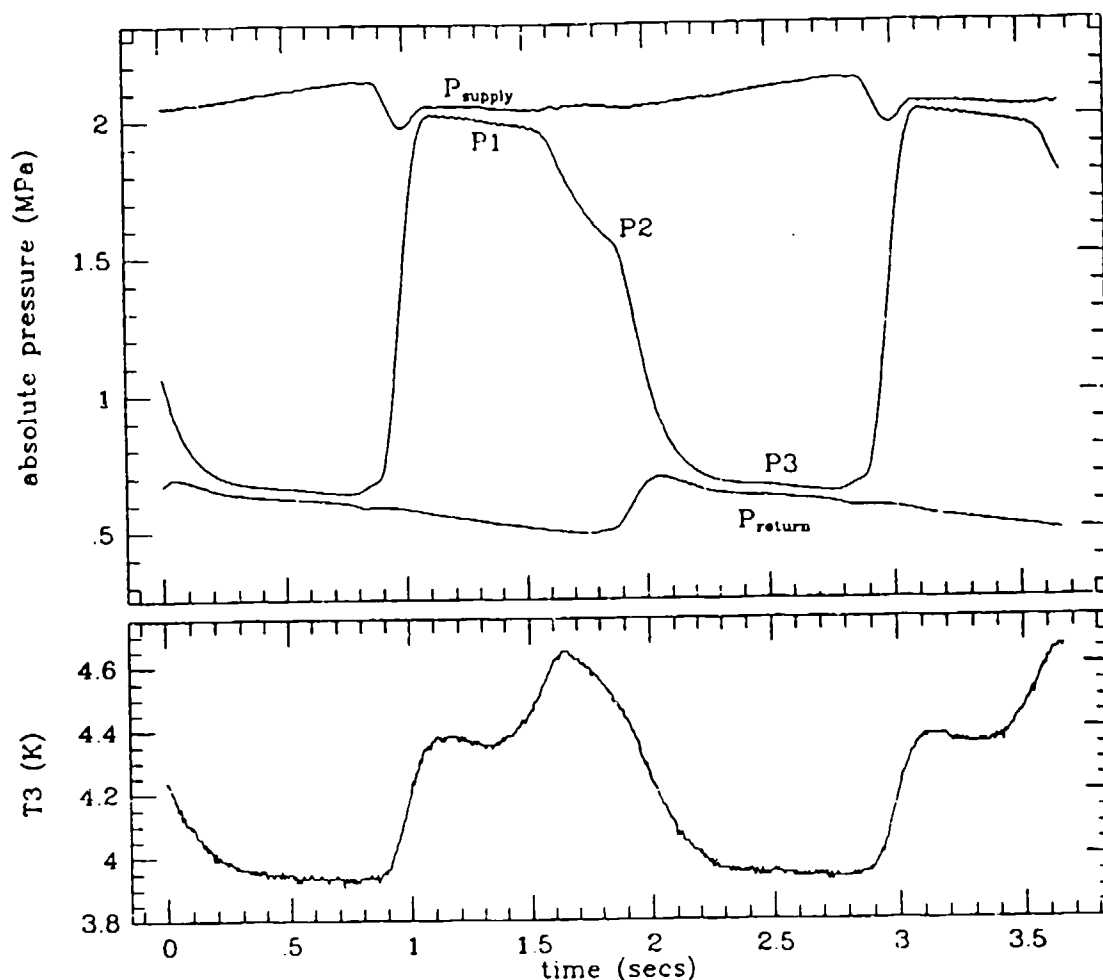


Fig. 7. (top panel) Helium pressures in the 3rd stage expansion volume, and in the supply and return lines just outside the expander, at 30 rpm cycle frequency. The inlet valve closes at about 1.6 seconds on this plot; the exhaust valve opens at about 1.9 seconds. (bottom panel) Corresponding 3rd stage temperature swing. (Refrigerator #3, 2.54 cm stroke, 45 g Er_3Ni , clearance seal.)

Figure 6 compares the 3rd stage pressure curves measured through the capillary shortly after the refrigerator was turned on (277 K) and after it was fully cold (5.6 K). At 72 rpm the cold end pressure swing decreases dramatically as the refrigerator cools and the helium mass flow increases. In part this is because the compressor capacity is marginal; in part it is due to pressure drops in the regenerators or valves. Most of the regenerator pressure drop should occur in 1st or 2nd stages; the pressure drop through the 3rd stage regenerator is expected

to be very low (probably less than 0.01 MPa) owing to the high density and low viscosity of helium below 10 K.

The pressure swing in the 3rd stage expansion volume increases considerably as the cycle frequency is reduced. Figure 7 shows the pressure and temperature curves measured at 30 rpm. At this speed the pressure drop through the regenerators and valves is small, about 0.05 MPa. The inlet valve closes well before the displacer reaches maximum cold volume; in the interval before the exhaust valve opens, helium continues to flow through the cold displacer, and the pressure decreases from $P_1 = 2.0$ MPa to $P_2 = 1.55$ MPa. Thus, the pressure drop P_2 - P_3 which occurs as the exhaust valve opens is only 0.9 MPa. The 3rd stage temperature follows the gas pressure swing, although the temperature increase near the end of the inlet stroke (at about 1.65 secs on the plot) suggests that warm gas leaks into the expansion volume along the outside of the regenerator.

We generated plots like the one in Figure 7 for seven different cycle speeds, from 72 rpm to 6 rpm. Figure 8 displays the pressures and temperatures measured from these data. As in Figure 7, P_{supply} and P_1 are measured about 1/3 of the way through the inlet stroke; P_3 , P_{return} , and T_{low} are measured midway through the exhaust stroke; and P_2 is the cold end pressure just before the exhaust valve opens. Helium in the 3rd stage working volume cools more as the pressure differential (P_2 - P_3) increases. Thus, even if the regenerator efficiency does not improve as the cycle frequency decreases, the 3rd stage reaches lower temperatures. Clearly, maximizing the pressure swing at the cold end of the regenerator is crucial to obtaining good performance.

(5) regeneration of leakage gas

At cycle frequencies below 30 rpm, the curves in Figure 8 show that the helium pressure swing in the 3rd stage working volume remains relatively constant, yet in some of our tests the 3rd stage cools dramatically as the cycle frequency is reduced to very low values. For example, curve E in Figure 3 drops from 5.1 K at 30 rpm to 2.85 K at 8 rpm. Evidently, some other factor can act to improve the regenerator performance at very slow speed. We speculate that in such cases warm gas leaking past the 3rd stage seal degrades the refrigerator performance at higher cycle frequencies, whereas at very low cycle frequencies heat transfer through the displacer wall is sufficient to bring the leakage gas into thermal equilibrium with the regenerator, leading to a dramatic improvement in performance.

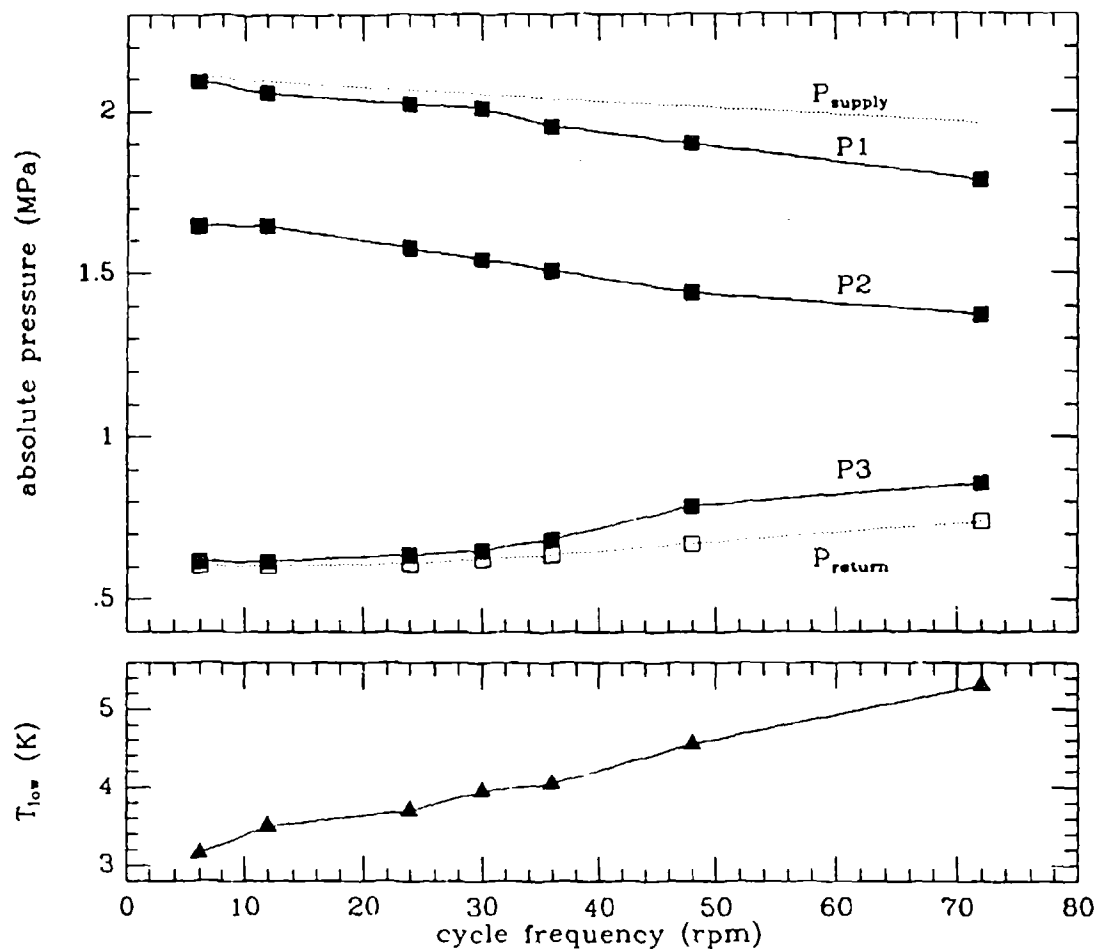


Fig. 8. (top panel) Helium pressures in the 3rd stage expansion volume, monitored at 7 different cycle frequencies; P_{supply} , P_1 , P_2 , P_3 , and P_{return} are measured as indicated in Figure 7. (bottom panel) Lowest 3rd stage temperature as a function of cycle frequency. (Refrigerator #3, 2.54 cm stroke, 45 g Er_3Ni , clearance seal.)

SHORT TERM TEMPERATURE STABILITY

An undesirable feature of the 4 K refrigerator, from our point of view, is the relatively large temperature swing (often about 0.5 K) which occurs with each cycle. We fear that such temperature variations will modulate the gain or noise properties of our SIS junctions. Because metals have very low specific heats at 4 K, the thermal mass associated with the SIS mixer block and mounting straps will do little to smooth out these temperature swings: at 4 K the 0.5 gram

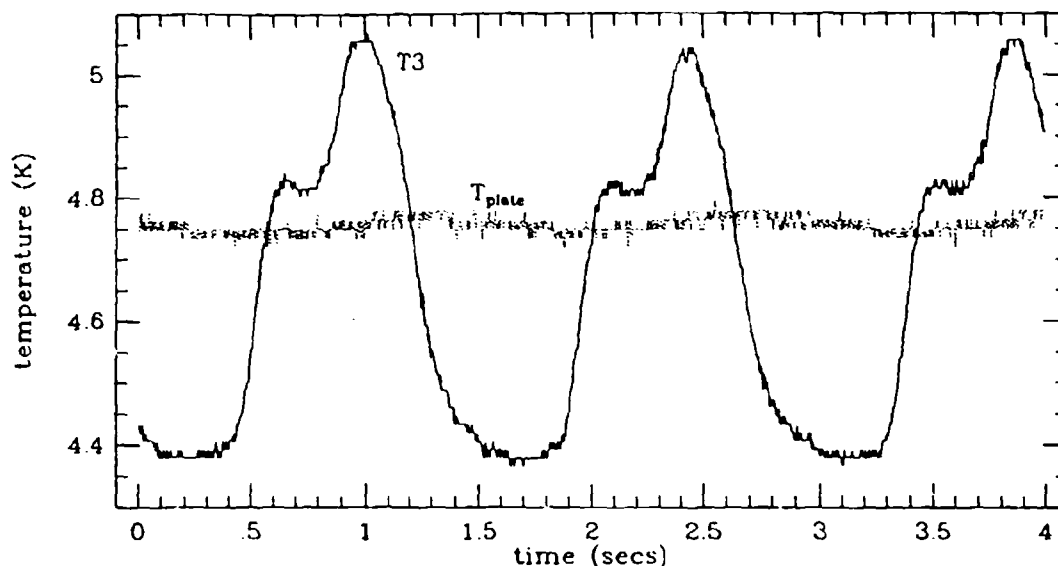


Fig 9. Temperature swing measured directly on the 3rd stage (T_3) and on a plate thermally loaded with 10 g of Er_3Ni powder (T_{plate}). The cycle frequency is 42 rpm.

of helium in the refrigerator's 3rd stage has a heat capacity equal to that of 17 kilograms of copper!

Fortunately, the heat load on the SIS mixer block is expected to be so low that we can tolerate considerable thermal resistance between the mixer block and the 3rd stage heat station. A thermal "capacitor" consisting of a modest quantity of Er_3Ni or other high heat capacity material mounted on the mixer block then can filter out the 3rd stage temperature variations quite effectively. An experimental test of such a filter is shown in Figure 9. In this experiment the thermal capacitor consisted of 10 g of Er_3Ni powder which was mixed with thermally conductive epoxy and spread onto a copper plate. The plate was attached to the 3rd stage heat station by brass washers, designed to produce a thermal resistance of approximately 25 mK/mW. The temperatures of the 3rd stage heat station and the copper plate were monitored simultaneously with two silicon diode sensors. With the refrigerator operating at 42 rpm, the temperature swing measured directly on the 3rd stage was 0.68 K; the swing measured on the test plate was less than 0.05 K.

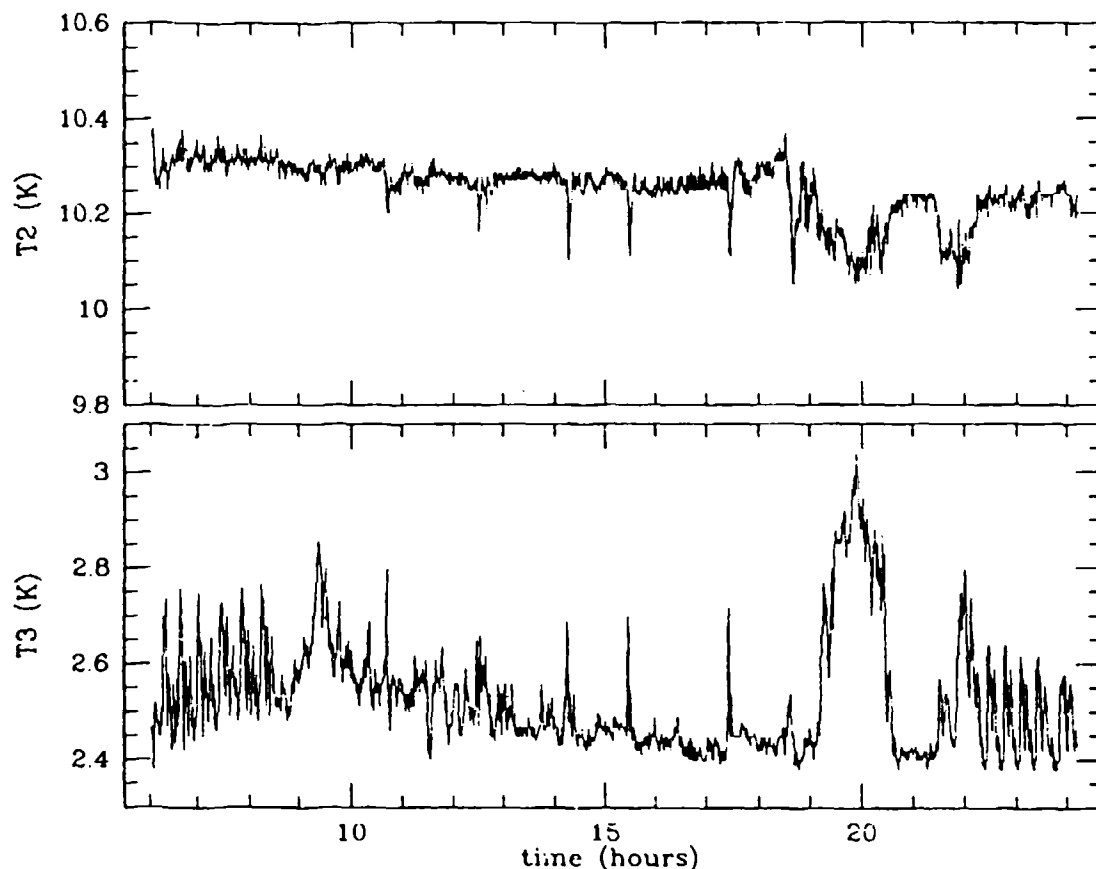


Fig. 10. Correlated 2nd and 3rd stage temperature fluctuations. Temperatures were measured every 15 seconds over an 18 hour interval. (Refrigerator #2, 3.18 cm stroke, 53 g Er_3Ni , CTI seal.)

LONG-TERM TEMPERATURE STABILITY

Our prototype refrigerators sometimes exhibit temperature excursions which occur over time scales of minutes to hours. An example of such behavior is shown in Figure 10, where we plot the 2nd and 3rd stage temperatures for a machine running at about 2.6 K. The temperatures were monitored every 15 seconds over a span of 18 hours. The 3rd stage temperature drops as low as 2.4 K, but spikes up to 2.7 K quasiperiodically. Many of the temperature spikes last only a minute or two, yet there is a period of 1.5 hours where the temperature hovers at about 2.8 K. Often the 2nd stage temperature decreases at the moment the 3rd stage temperature increases, suggesting that at these times cold gas bypasses the 3rd stage regenerator during the exhaust stroke.

Another example of temperature instability (one of the worst we have seen)

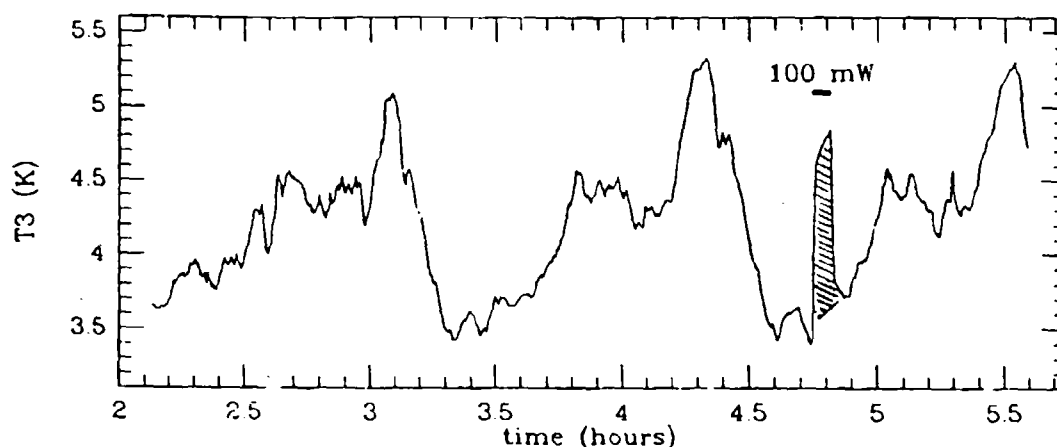


Fig. 11. "Worst case" temperature fluctuations on the 3rd stage. To calibrate the equivalent heat leak, a 100 mW load was applied partway through the run. (refrigerator #3, 2.54 cm stroke, 62 g Er_3Ni , CTI seal.)

is shown in Figure 11. In this case the temperature cycles between 3.5 K and 5 K with a period of about 1.2 hours. As shown in the figure, a 100 mW heat load raises the 3rd stage temperature by approximately 1 K. Therefore, we infer that an intermittent heat leak of about 150 mW is responsible for the temperature instability.

Significantly, the displacers used in both of these tests were outfitted with rubbing seals. Our tests show that displacers with clearance seals are less likely to show such extreme temperature swings. Thus, we suspect that most such temperature excursions are attributable to gas leaking intermittently past the third stage seal. Presumably, the quasiperiodic behavior arises because the seal rotates slowly in its groove.

CONCLUSIONS

A 3-stage Gifford-McMahon refrigerator utilizing 50 g of Er_3Ni spheres as the 3rd stage regenerator appears to be well suited for cooling SIS mixers in a radio astronomy receiver. A prototype refrigerator was able to maintain 1st, 2nd, and 3rd stage temperatures of 65 K, 13.6 K, and 3.5 K with heat loads of 10 W on the 1st stage, 1 W on the 2nd stage, and 50 mW on the 3rd stage. The 3rd stage temperature drops as low as 2.2 K with no load.

At a cycle frequency of 72 rpm the refrigerator performance is degraded by pressure drops within the displacers. As the cycle frequency is decreased, the helium pressure swing in the 3rd stage expansion volume increases markedly, allowing operation at lower temperatures. Intermittent gas leakage past the 3rd stage seal can cause erratic temperature excursions. Temperature cycling synchronous with the refrigerator cycle can easily be smoothed out by attaching a thermal mass - e.g., Er_3Ni powder embedded in epoxy - to the load.

ACKNOWLEDGEMENTS

This work was supported by National Science Foundation grant 9100307. We thank John Lugten and Bruce Andeen for helpful discussions.

REFERENCES

1. T. Kuriyama, M. Takahashi, H. Nakagome, H. Seshako, T. Eda, and T. Hashimoto, "Two-stage GM refrigerator with Er_3Ni regenerator for helium liquefaction," Proc. 6th International Cryocoolers Conf., vol II, p. 3 (1991).
2. T. Inaguchi, M. Nagao, and H. Yoshimura, "Two-stage Gifford-McMahon cycle cryocooler operating at about 2 K," Proc. 6th International Cryocoolers Conf., vol. II, p. 25 (1990).
3. M. Ogawa, R. Li, and T. Hashimoto, "Thermal conductivities of magnetic intermetallic compounds for cryogenic regenerator," Cryogenics, vol. 31, p. 405 (1991).

DYNAMIC CHARACTERISTICS OF REGENERATORS USED IN CRYOCOOLERS

B. J. Huang and C. W. Lu
Department of Mechanical Engineering
National Taiwan University, Taipei, TAIWAN

ABSTRACT

Dynamic characteristics of regenerator under cyclic isothermal flow is investigated. A basic transfer-function model of regenerator is first derived and used to study the dynamic response of a regenerator connecting a reciprocating piston and a reservoir. Darcy's law in dynamic form is derived. It is shown that quasi-steady assumption of Darcy's law holds in gain within the bandwidth f_{cut} . However, a phase lag exists and has to be corrected.

INTRODUCTION

Regenerators used in cryocoolers such as Stirling, Gifford-McMahon or pulse-tube refrigerators are operated under transient- or cyclic-flow conditions. The regenerator connects the compression and expansion spaces such that the working fluid is heated or cooled by the regenerator matrix in a thermodynamic cycle. The reciprocating motion of piston and displacer or the filling and exhausting processes of gas in cryocoolers will generate a cyclic pressure wave as well as a cyclic flow across the regenerator. The thermal performance analysis of a cryocooler thus becomes extremely complicated since the transient solution of unsteady-state model will be involved. Quasi-steady approximation was therefore frequently used in the regenerator modelling in order to simplify the analysis. No criterion, however, has ever been given to validate this approximation.

The phenomenon of a cyclic flowrate induced cyclic pressure wave across a regenerator is basically a system dynamics problem. Earlier researches on regenerator performance with cyclic flow are mainly focused on modeling and predictions of transient temperature profiles^{1,2}, the regenerator inefficiency³⁻⁶, and heat transfer measurements^{6,7}. Very little attention was paid to the dynamic behavior of regenerators. Guo⁸ has experimentally observed that there is a phase shift and amplitude attenuation for a cyclic pressure wave across a regenerator. Furthermore, they tried to qualitatively interpret the dynamic behavior of a regenerator by using a four-end linear network model.

The present study intends to derive a transfer-function model of regenerator by using small perturbation approximation and linear system theory. The regenerator model is further used to derive a dynamics model to study the dynamic responses of a regenerator connecting a reciprocating piston and a reservoir (Fig. 1). A criterion for the validation of quasi-steady approximation in regenerator modelling will then be derived.

TRANSFER-FUNCTION MODEL OF REGENERATOR

Regenerator is essentially a porous medium made from metallic wire screen meshes or powders filled in a cylindrical vessel. In the derivation of dynamics model of regenerators, the following assumptions are made: (1) the flow in the regenerator is one-dimensional; (2) the working gas is an ideal gas; (3) gas viscosity ν is constant; (4) the porous medium is homogeneous and isotropic; (5) there is no temperature difference across the regenerator.

Governing Equations

The continuity equation can be written in terms of mass flowrate relation $\dot{m} = \rho A_{f,r} w$:

$$\frac{\partial p}{\partial t} + \frac{RT_0}{A_{f,r}} \frac{\partial \dot{m}}{\partial x} = 0. \quad (1)$$

The momentum equation of a regenerator is basically the revised Darcy's law² which can be written in terms of mass flowrate \dot{m} :

$$\frac{1}{A_{f,r}} \frac{\partial \dot{m}}{\partial t} + \frac{1}{A_{f,r}^2} \frac{\partial (\dot{m}|\dot{m}|/\rho)}{\partial x} + \frac{\partial p}{\partial x} + \frac{\alpha \epsilon \nu}{A_{f,r}} \dot{m} + \beta \rho \left(\frac{\epsilon}{\rho A_{f,r}} \right)^2 \dot{m}|\dot{m}| = 0. \quad (2)$$

The inertia term (the second term) of Eq.(2) can be ignored since the gas flow inside the regenerator is not very high in practice, usually $Re < 500$. The last term of Eq.(2) can also be omitted and the associated effect can be included in a modified parameter α' . Therefore, Eq.(2) becomes

$$\frac{1}{A_{f,r}} \frac{\partial \dot{m}}{\partial t} + \frac{\partial p}{\partial x} + \frac{\alpha' \epsilon \nu}{A_{f,r}} \dot{m} = 0. \quad (3)$$

where α' is a modified parameter which will vary with a reference flowrate \dot{m}_r , i.e. $\alpha' = f(\dot{m}_r)$.

Small Perturbation and Linearization

Under cyclically steady conditions, the mass flowrate and pressure can be written as the sum of mean and periodic perturbation terms, that is, $\dot{m}(x,t) = \bar{\dot{m}}(x) + \tilde{\dot{m}}(x,t)$; $p(x,t) = \bar{p}(x) + \tilde{p}(x,t)$.

Hence, $\tilde{m}(x) = 0$, $\tilde{p}(x) = p_0 = \text{constant}$. Substituting these relations into the governing Eqs. (1) and (3), and assuming small perturbations, i.e. $\tilde{p}(x, t) \ll \bar{p}(x)$, we obtain the following equations which are similar to those of a RLC circuit,

$$\frac{\partial \tilde{p}}{\partial t} + \frac{1}{C_F} \frac{\partial \tilde{m}}{\partial x} = 0 \quad (4)$$

$$L_F \frac{\partial \tilde{m}}{\partial t} + \frac{\partial \tilde{p}}{\partial x} + R_F \tilde{m} = 0 \quad (5)$$

where R_F , C_F , L_F are respectively the flow resistance, capacitance and inductance per unit length of regenerator, which are defined as, according to the analogy to a RLC circuit,

$$R_F \equiv \frac{\bar{\alpha} \nu \epsilon}{A_{fr}}; \quad C_F \equiv \frac{A_{fr}}{RT_0}; \quad L_F \equiv \frac{1}{A_{fr}}. \quad (6)$$

Here, $\bar{\alpha}$ represents the parameter α' evaluated at the peak value of flow fluctuation \dot{m}_0 . Eqs.(4) and (5) are the linearized equations for regenerators.

Basic Transfer-function Model of Regenerator

Eqs.(4) and (5) can be solved by using Laplace transform, assuming zero initial conditions, to lead to

$$\tilde{m}(x, s) = \frac{\tilde{m}_2(s)}{\sinh(\lambda_b L)} \sinh(\lambda_b x) + \frac{\tilde{m}_1(s)}{\sinh(\lambda_b L)} \sinh[\lambda_b (L - x)] \quad (7)$$

$$\tilde{p}(x, s) = \frac{\tilde{p}_2(s)}{\sinh(\lambda_b L)} \sinh(\lambda_b x) + \frac{\tilde{p}_1(s)}{\sinh(\lambda_b L)} \sinh[\lambda_b (L - x)], \quad (8)$$

where $\tilde{m}(0, s) = \tilde{m}_1(s)$; $\tilde{m}(L, s) = \tilde{m}_2(s)$; $\tilde{p}(0, s) = \tilde{p}_1(s)$; $\tilde{p}(L, s) = \tilde{p}_2(s)$, and λ_b is the characteristic value defined as

$$\lambda_b^2 = s(R_F C_F + s L_F C_F). \quad (9)$$

Eqs(7) and (8) represents a distributed-parameter dynamics model accounting for the spatial variation of mass flow and pressure waves along the regenerator. It is preferable to write the dynamics model in terms of the boundaries or input/output of the regenerator. Substituting Eq.(7) into Laplace of Eq.(4) and Eq.(8) into Laplace of Eq.(5), we obtain

$$\tilde{m}_2(s) = [\cosh(\lambda_b L)] \tilde{m}_1(s) - \left[s C_F \frac{\sinh(\lambda_b L)}{\lambda_b} \right] \tilde{p}_1(s) \quad (10)$$

$$\tilde{p}_2(s) = - \left[(L_F s + R_F) \frac{\sinh(\lambda_b L)}{\lambda_b} \right] \tilde{m}_1(s) + [\cosh(\lambda_b L)] \tilde{p}_1(s). \quad (11)$$

Hence, Eqs.(10) and (11) can be written in a matrix form:

$$\begin{bmatrix} \tilde{m}_2(s) \\ \tilde{p}_2(s) \end{bmatrix} = \begin{bmatrix} \cosh(\lambda_b L) & -sC_F \frac{\sinh(\lambda_b L)}{\lambda_b} \\ -(L_F s + R_F) \frac{\sinh(\lambda_b L)}{\lambda_b} & \cosh(\lambda_b L) \end{bmatrix} \cdot \begin{bmatrix} \tilde{m}_1(s) \\ \tilde{p}_1(s) \end{bmatrix} \quad (12)$$

Eq.(12) is the basic transfer-function model of regenerator which accounts for the dynamic responses across a regenerator.

DYNAMIC RESPONSE OF REGENERATOR IN A CYCLIC FLOW SYSTEM

Dynamics Model of Regenerator in a Cyclic Flow System

Dynamic response of a regenerator in a cyclic flow system which consists of a reciprocating piston and a reservoir (Fig. 1) is studied here. For convenience, Eq.(10) is rearranged to yield

$$\tilde{m}_1(s) = \left[\frac{sC_F \sinh(\lambda_b L)}{\lambda_b \cosh(\lambda_b L)} \right] \tilde{p}_1(s) + \frac{\tilde{m}_2(s)}{\cosh(\lambda_b L)}. \quad (13)$$

Substituting Eq.(8) into Laplace form of Eq.(5) will yield

$$\tilde{p}_2(s) = \frac{\tilde{p}_1(s)}{\cosh(\lambda_b L)} - \left[\frac{L_F s + R_F}{\lambda_b A_{fr}} \frac{\sinh(\lambda_b L)}{\cosh(\lambda_b L)} \right] \tilde{m}_2(s). \quad (14)$$

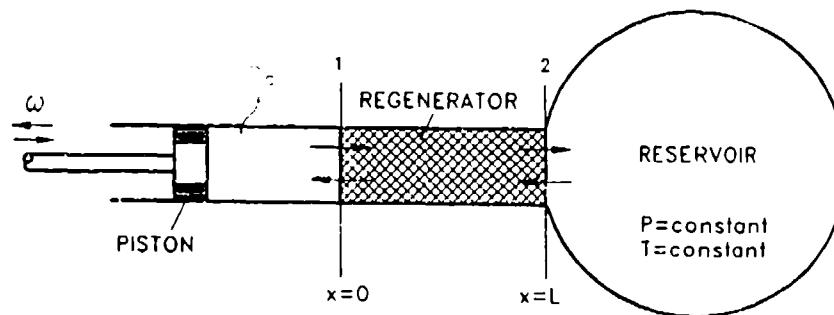


Fig.1 A cyclic flow system.

The dynamics of regenerator connected in the present cyclic flow system can be described by three transfer-function models: $G_{pp}(s)$, $G_{mp}(s)$, $G_{mm}(s)$, where $G_{pp}(s)$ represents the response of pressure wave at the reservoir side induced by the pressure wave at the piston side, and since $\tilde{p}_2(s) = 0$ for a reservoir,

$$G_{vp}(s) = \frac{\tilde{p}_2(s)}{\tilde{p}_1(s)} = 0. \quad (15)$$

On the other hand, from Eq.(14), for $\tilde{p}_2(s) = 0$,

$$\tilde{p}_1(s) = \left[\frac{L_F s + R_F}{\lambda_b} \sinh(\lambda_b L) \right] \tilde{m}_2(s). \quad (16)$$

Combining Eqs. (16) and (13), we also obtain

$$G_{mm}(s) \equiv \frac{\tilde{m}_2(s)}{\tilde{m}_1(s)} = \frac{1}{\cosh(\lambda_b L)} \quad (17)$$

where $G_{mm}(s)$ represents the response of mass flow at the reservoir side induced by the piston-side mass flow fluctuation.

The response of mass flowrate wave at the reservoir side induced by the pressure wave at the piston side is represented by the transfer function model $G_{mp}(s)$ which is derived from Eq.(16):

$$G_{mp}(s) = \frac{\tilde{m}_2(s)}{\tilde{p}_1(s)} = \frac{1}{L_F s + R_F} \frac{\lambda_b}{\sinh(\lambda_b L)}. \quad (18)$$

For convenience, Eq. (18) can be written as (since $\tilde{p}_2(s) = 0$),

$$G_{mp}(s) = \frac{\tilde{m}_2(s)}{\tilde{p}_1(s) - \tilde{p}_2(s)} = \frac{\tilde{m}_2(s)}{\Delta \tilde{p}(s)} = \frac{1}{L_F s + R_F} \frac{\lambda_b}{\sinh(\lambda_b L)}. \quad (19)$$

Eq.(19) can be considered as a dynamic form of Darcy's law which is used to describe the dynamic responses of a regenerator in the present cyclic flow system.

Specifications of a Cyclic-Flow System

The geometry of the regenerator used in the present analysis has a diameter $D = 40 \text{ mm}$ and a length $L = 30 \text{ mm}$, which is the same as that used by Tanaka *et al*⁷ in an oscillating flow test. Four kinds of screen mesh wire are adopted in the analysis: 150,200,250,400 mesh. The physical properties of regenerators are listed in Table 1 in which the porosities are calculated by the Chang's formula¹⁰ and the parameters α and β in the momentum Eq. (2) are converted from the oscillatory-flow friction correlation of Tanaka *et al*⁷: $f_h = A/Re_h + B$, where $A = 175$, $B = 1.60$; $Re_h (= u_{max} d_h / \nu)$ is the Reynolds number based on the hydraulic diameter of regenerator d_h and the peak velocity u_{max} ; $d_h = 4\epsilon d_m / \phi(1 - \epsilon)$; $\phi = 4$ for screen wire meshes; f_h is the friction factor defined as $f_h = \Delta p d_h / (\rho u_{max}^2 L/2)$, where $\Delta p (= p_1 - p_2)$.

Table 1. Regenerator properties.

	150 mesh	200 mesh	250 mesh	400 mesh
wire diameter d_m , mm	0.06604	0.05334	0.04064	0.02540
porosity ϵ	0.732	0.707	0.735	0.686
hydraulic diameter d_h , mm	0.1803	0.1287	0.1127	0.0554
α , mm^{-2}	2691.6	5281.8	6896.6	28417.0
β , mm^{-1}	4.4370	6.2155	7.0972	14.417

The relation between the parameters α and β and the modified parameter α' is derived as

$$\alpha' = \alpha + \frac{\beta}{\nu} u_{max} = \alpha + \frac{\beta}{d_h} Re_h, \quad (20)$$

where $\alpha = A/2d_h^2$; $\beta = B/2d_h$. The peak velocity u_{max} is related to the driving mechanism and reciprocating frequency of piston. For the crank case used by Tanaka *et al*⁷, u_{max} follows the relation $u_{max} = 1.042\pi V_p N/60A_r\epsilon = 1.042\pi V_p f/A_r\epsilon$, where V_p is the swept volume of piston. The parameter α' modified for a cyclic mass flowrate, denoted $\bar{\alpha}$, thus becomes

$$\bar{\alpha} = \alpha + \frac{\beta}{\nu} \cdot \frac{1.042\pi V_p f}{A_r\epsilon}. \quad (21)$$

Frequency Responses of Regenerator in a Cyclic Flow System

$\bar{\alpha}$ is seen from Eq.(21) to be function of $\alpha, \beta, \nu, f, \epsilon$ etc.; while α, β are function of d_h alone. $\bar{\alpha}$ can be seen to be function of standard screen wire mesh size, gas viscosity ν and cyclic flow frequency.

1. Flow-to-Flow Response $G_{mm}(s)$

The frequency response of flow fluctuation at the reservoir side \tilde{m}_2 can be seen from the Bode plots of flow- to-flow model $G_{mm}(j\omega)$ (Fig. 2). It is seen that both the gain and the phase tend to decrease more rapidly with increasing frequency for regenerator with dense wire screen mesh. This means that attenuation of flow fluctuation at the reservoir side will be stronger for regenerators with larger wire screen mesh (dense screen). The magnitude of unity (i.e. 0 db) represents no attenuation on flowrate at the reservoir side.

It is more convenient to define a bandwidth at the -3 db gain which specifies the cutoff frequency f_{cut} . f_{cut} is the frequency upper limit below which attenuation of the dynamic fluctuations is negligible.

It can be seen from Table 2 that f_{cut} decreases with increasing wire mesh number. However, it can be easily shown that the phase angle at f_{cut} remains constant at -57.66° . This indicates that only a phase lag on flowrate at the reservoir side (induced by the piston-side flowrate fluctuation) has to be considered for a cyclic frequency lower than f_{cut} . For instance, for the regenerator length and diameter used in the present study, f_{cut} for the 400-mesh screen regenerator is 90 Hz. Therefore, only a phase lag of $< 57.66^\circ$ needs to be considered for frequencies < 90 Hz.

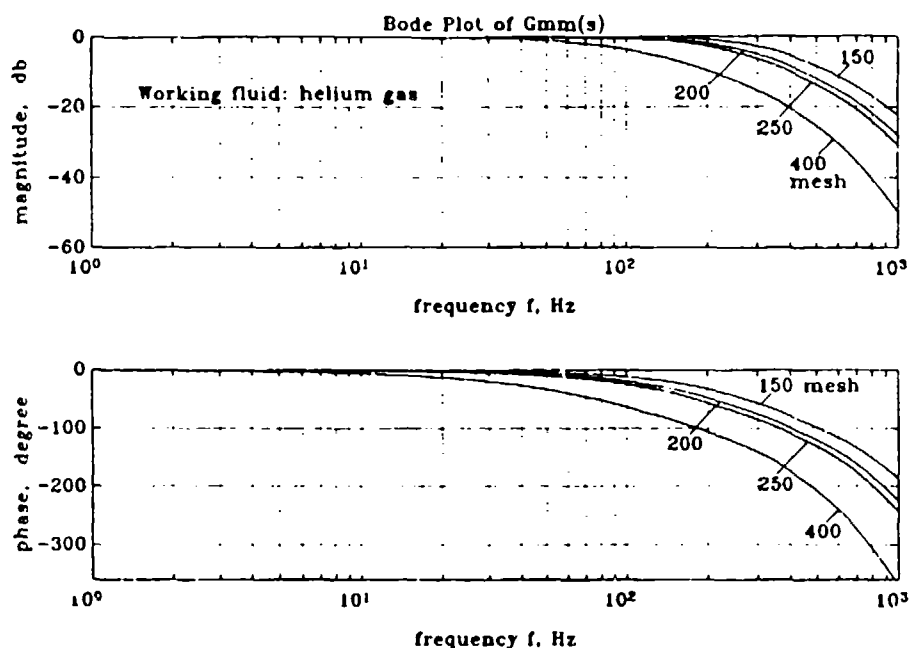


Fig. 2 Flow-to-flow frequency response of $G_{mm}(s)$.

Table 2. Cutoff frequency of $G_{mm}(j\omega)$ for helium gas.

Wire Screen Mesh No.	f_{cut} , Hz	phase angle at f_{cut}
150	304	-57.66°
200	234	-57.66°
250	205	-57.66°
400	90	-57.66°

The effect of working fluid on $G_{mm}(s)$ is seen from Fig. 3 to be quite strong. For air and nitrogen gases, the magnitude and phase of $G_{mm}(j\omega)$ drops more rapidly than helium gas. The cutoff frequency f_{cut} or bandwidth is reduced by two folds for air and nitrogen gas. However, the phase lag at f_{cut} still remains constant (-57.66°).

The attenuation and phase shift of flowrates across the regenerator can be clearly seen from Fig. 4 which is drawn for 400-mesh regenerator operating at 100 Hz with helium gas. \dot{m}_2 is seen to lag \dot{m}_1 by 57.66° .

Table 3 shows that the bandwidth of regenerator for air and N_2 in the 200-mesh regenerator is much narrower than helium gas. However, the corresponding phase shifts at f_{cut} are the same, -57.66° . This indicates that the use of helium gas as a working fluid is superior to air or nitrogen gas in the aspect of system dynamics.

Table 3. Cutoff frequency of $G_{mm}(j\omega)$ for 200-mesh regenerator.

Working fluid	f_{cut} , Hz	phase angle at f_{cut}
air	103	-57.66°
N_2	104	-57.66°
helium	234	-57.66°

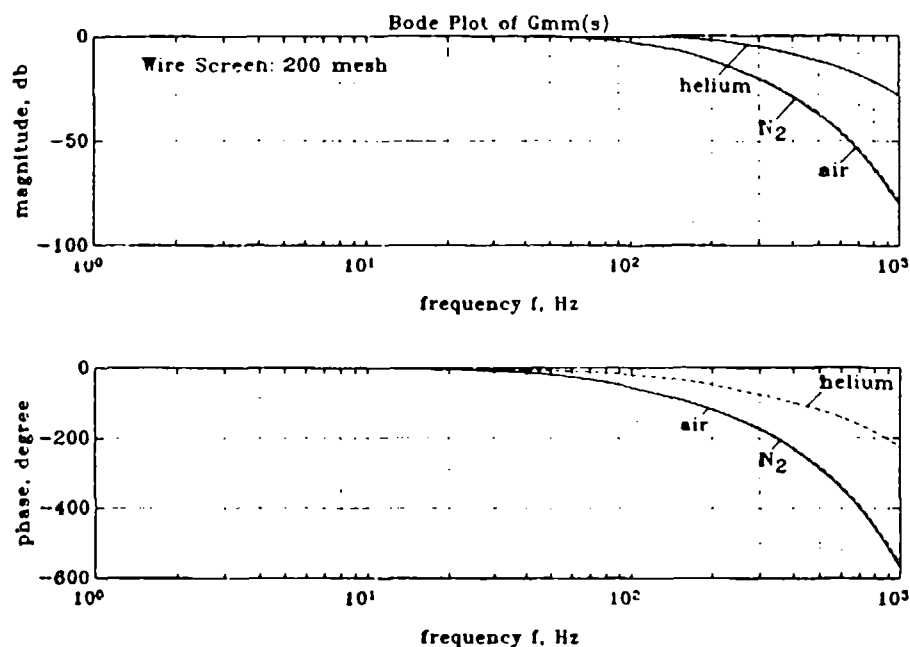


Fig. 3 Flow-to-flow frequency response of $G_{mm}(s)$ for various gases.

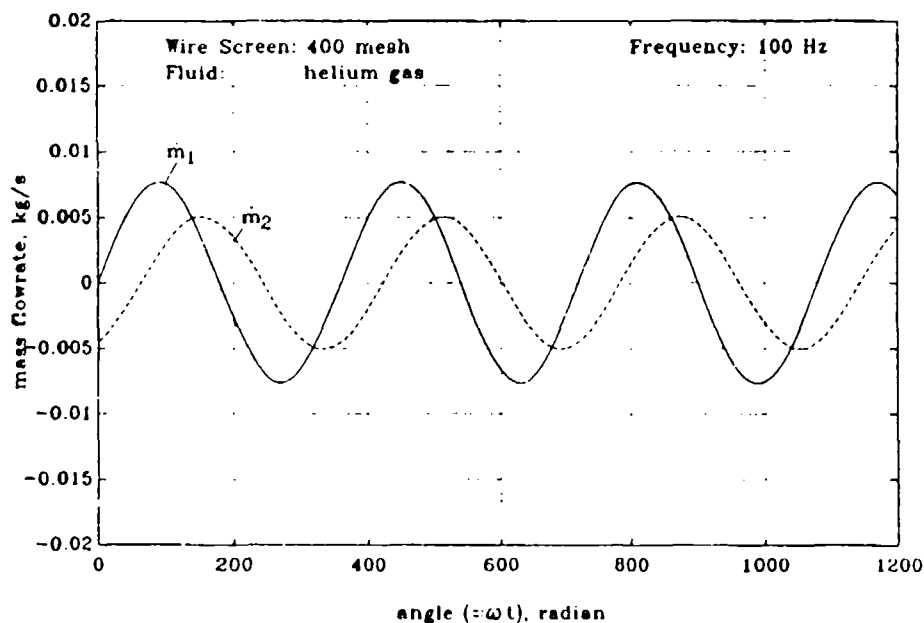


Fig. 4 Time responses of \dot{m}_2 induced by \dot{m}_1 for 400-mesh regenerator.

2. Pressure-to-Flow Response $G_{mp}(s)$

The frequency response of helium flow at the reservoir side \tilde{m}_2 which is induced by pressure wave across the regenerator $\Delta\tilde{p}$ can be seen from the Bode plots of pressure-to-flow model $G_{mp}(j\omega)$ (Fig. 5). The gain is seen to decrease more rapidly with

increasing frequency for loose wire screen (small mesh number). The bandwidth f_{cut} and the corresponding phase angle ϕ_{cut} are shown in Table 4. It is seen that the bandwidth increases with increasing mesh number. This is due to the fact that for a loose regenerator, the flow capacitance effect is stronger and causes stronger attenuation effect (with narrower bandwidth) on flow fluctuation.

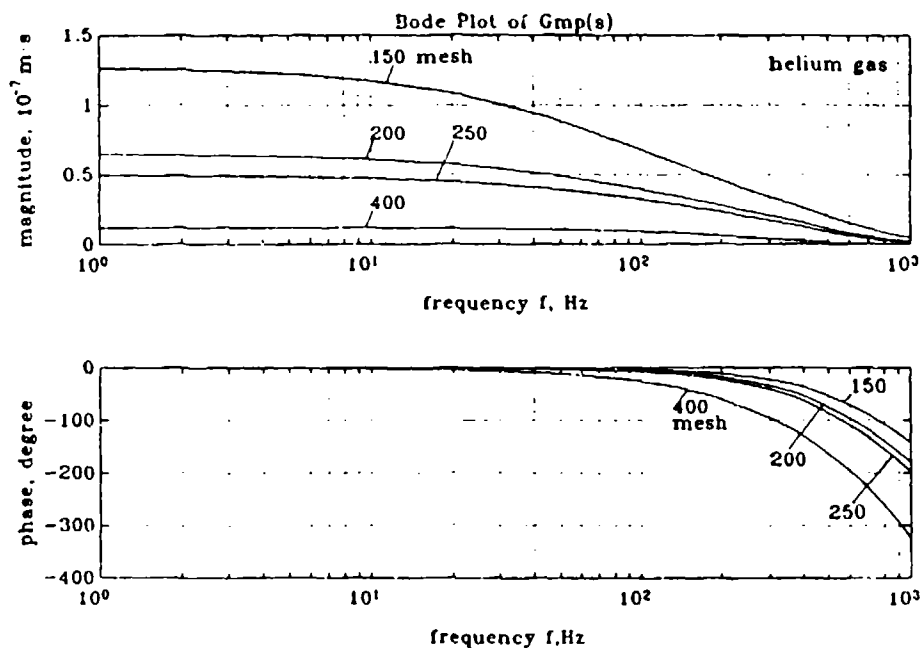


Fig. 5 Pressure-to-flow frequency response of $G_{mp}(s)$.

Table 4. Cutoff frequency of $G_{mp}(j\omega)$ for helium gas.

Wire Screen Mesh No.	f_{cut}, Hz	phase angle at f_{cut}
150	48	-1.47°
200	65	-3.70°
250	74	-5.60°
400	115	-30.0°

An example of time response of reservoir-side flowrate \dot{m}_2 induced by the pressure drop $\Delta p (= p_1 - p_2)$ for 400-mesh regenerator at 100 Hz is shown in Fig. 6.

It is quite interesting to see that Eq.(19) will be reduced to a constant gain of $A_{fr}/(\bar{\alpha}\nu\epsilon L)$ and zero phase shift at very low frequencies ($\omega \rightarrow 0$), that is,

$$\lim_{\omega \rightarrow 0} |G_{mp}(j\omega)| = \frac{1}{R_f}, \quad (22)$$

where R_f is the total flow resistance of regenerator defined as $R_f \equiv \bar{\alpha}\nu\epsilon L/A_{fr} = R_F L$. This indicates that the regenerator will obey steady-state form of Darcy's law at low

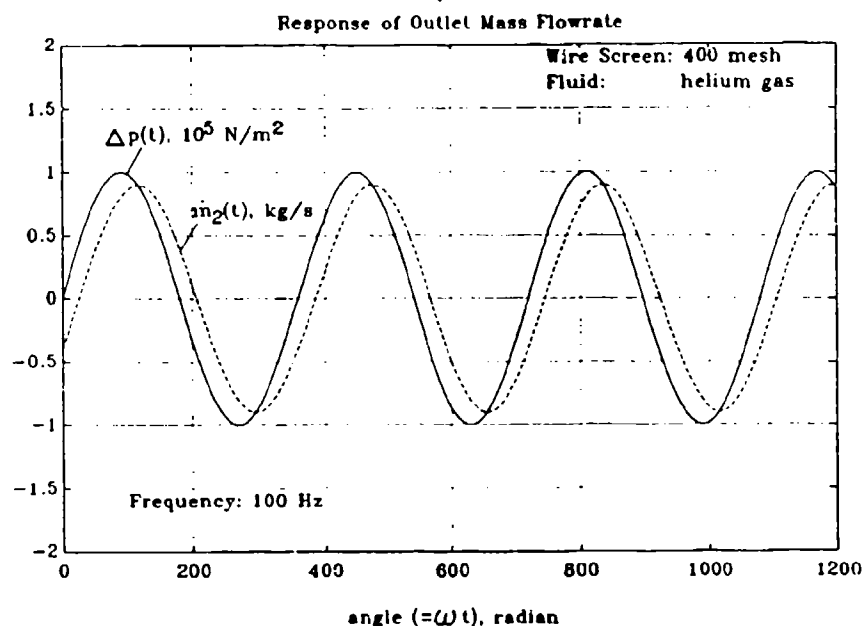


Fig. 6 Time response of \dot{m}_2 induced by Δp for 400-mesh regenerator.

operating frequencies. That is, quasi-steady approximation of Darcy's law holds within the bandwidth. However, a phase shift exists as shown in Table 4 and has to be corrected if quasi-steady approximation of Darcy's law was used.

It is interesting to note that the phase lag increases abruptly from 250 mesh to 400 mesh. The 400-mesh regenerator has a wider bandwidth but with larger phase lag. On the other hand, the 150-mesh regenerator has a narrower bandwidth but with very small phase lag so that quasi-steady approximation can hold for both gain and phase shift.

Table 5 and Fig. 7 shows that for the 200-mesh regenerator, the bandwidth of $G_{mp}(j\omega)$ for air or N_2 is much narrower than helium gas. However, the corresponding phase lag at f_{cut} is smaller for air or nitrogen. This verifies that the use of helium gas as a working fluid is superior to air or nitrogen gas since the bandwidth is much wider and the phase lag is smaller.

Table 5. Cutoff frequency of $G_{mp}(j\omega)$ for 200-mesh regenerator.

Working fluid	f_{cut}, Hz	phase angle at f_{cut}
air	9	-0.5°
N_2	10	-0.6°
helium	65	-3.7°

DISCUSSIONS AND CONCLUSIONS

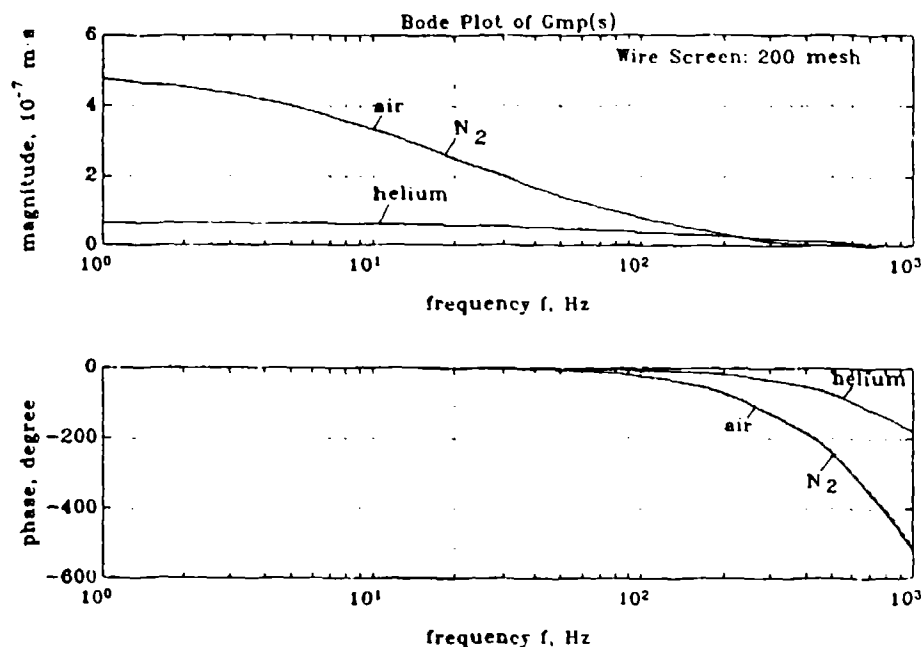


Fig. 7 Pressure-to-flow frequency response of $G_{mp}(s)$ for various working fluids.

A basic transfer-function model for an isothermal and cyclic flow in regenerator is derived and further used to study a system dynamics of a regenerator connecting a reciprocating piston and a reservoir.

The frequency response of mass flow at the reservoir side of regenerator induced by the pressure and flow waves at the piston side are shown to approach zero in gain at high frequencies (acoustic range), but approach a constant value at low frequencies. Quasi-steady approximation can thus hold within the bandwidth or cutoff frequency f_{cut} . f_{cut} is shown to be dependent on the regenerator design (wire mesh size, porosity, length, diameter, and material etc.) and working gas.

For flow-to-flow response $G_{mm}(j\omega)$, f_{cut} is seen to decrease with increasing wire screen mesh number of regenerator. Both the gain and the phase of flow-to-flow response $G_{mm}(j\omega)$ tend to decrease more rapidly with increasing frequency for regenerator with dense wire screen mesh. This indicates that the flow-to-flow attenuation is stronger for regenerators with larger wire screen mesh (dense screen). The use of air or nitrogen gas will introduce a stronger attenuation than helium. However, the phase angle at f_{cut} remains fixed irrespective of screen mesh numbers and working gases.

For pressure-to-flow response, $G_{mp}(j\omega)$, the cutoff frequency or bandwidth f_{cut} increases with increasing regenerator mesh number. This indicates that the attenuation of mass flowrate fluctuation is stronger for regenerators with larger void volume (i.e. loose screen). It is shown that quasi-steady approximation of Darcy's law holds within the bandwidth f_{cut} . However, a small phase shift exists and has to be corrected.

Regenerators used in Stirling machines or cryocoolers are usually operated under transient- or cyclic-flow conditions. The thermal performance analysis is thus quite complicated since the transient solutions of unsteady-state models are involved. The

present analysis can be used to simplify the modelling of regenerator by using quasi-steady approximation as long as the operating frequency of the machine is within the bandwidth of regenerator. The system dynamics model of regenerator similar to Eq. (21) can be easily derived according to the present analysis for Stirling cooler. However, the pressure fluctuation at the reservoir side will be nonzero (i.e. $\tilde{p}_2(s) \neq 0$) due to the introduction of another reciprocating displacer or cold head in a Stirling cooler.

The basic transfer-function model of regenerator, Equation (12), derived in the present study can also be used to develop a linear network model of Stirling¹¹ or pulse-tube cryocoolers by connecting the similar models one by one for each components of the machine. The thermal performance prediction of cryocoolers can then be simplified a great deal.

Acknowledgment — The present study was supported by the National Science Council, Taiwan, R.O.C., through Grant No. NSC81-0401-E002-587.

NOMENCLATURES

A_f	free-flow area of regenerator, m^2
C_p	heat capacity at constant pressure, J/kgK
D	regenerator diameter, m
d_h	hydraulic diameter of regenerator, m
d_m	screen wire diameter, m
f	cyclic frequency, Hz
f_h	friction factor of regenerator
L	regenerator length, m
\dot{m}	mass flowrate, kg/s
N	reciprocating speed of oscillating piston, rev/s
p	pressure, N/m^2
R	universal gas constant, m^2/Ks^2
Re_h	Reynolds number $(= d_h u_{max}/\nu)$.
s	Laplace transfer variable
T_o	system mean temperature, K
t	time, s
u_{max}	peak velocity of gas inside the regenerator, m/s
V_p	swept volume of piston, m^3
w	velocity inside regenerator, m/s
x	position in regenerator, m

Greek Letter

α	first coefficient in momentum Equation (2)
β	second coefficient in momentum Equation (2)

- ϵ porosity of regenerator
- ρ gas density, kg/m^3
- λ_b characteristic parameter, eqn(19), m^{-1}
- ν kinematic viscosity of gas, m^2/s
- ω angular frequency, rad/s

Subscripts

- 1 regenerator end at piston side
- 2 regenerator end at reservoir side

REFERENCES

1. Modest, M.F. and Tien, C.L.: "Analysis of Real-gas and Matrix-Conduction Effects in Cyclic Cryogenic Regenerators," *ASME J. Heat Transfer*, pp.199 - 205 (May, 1973).
2. Modest, M.F. and Tien, C.L. : "Thermal Analysis of Cyclic Cryogenic Regenerators." *Int. J. Heat Mass Transfer*, Vol.17, pp.37-49 (1974).
3. Rea, S.N. and Smith, J.L. Jr.: "The Influence of Pressure Cycling on Thermal Regenerators". *ASME J. Engng. Ind.*, pp.563-569 (August, 1967).
4. Qvale, E.B. and Smith, J.L., Jr.: "An Approximate Solution for the Thermal Performance of a Stirling-Engine Regenerator," *ASME, J. Eng. for Power*, Series A, No.2, April 1969, pp.109-112.
5. Köhler, J. W., Stevens, P.F., de Jonge, A.K., and Beuzekom, D.C.: "Computation of regenerators used in regenerative refrigerators," *Cryogenics*, pp.521-530 (Sep. 1975).
6. Walker, G. and Vasishta, V.: "Heat Transfer and Flow Friction Characteristic of Dense-Mesh Wire-Screen Stirling-Cycle Regenerator," *Advanced in Cryogenic Engineering*, Vol. 16, pp. 324-332 (1970).
7. Tanaka, Yamashita and Chisaka: "Flow and Heat Transfer Characteristics of Stirling Engine Regenerator in an Oscillating Flow," *JSME International Journal, Series II*, Vol.33, No.2, pp. 283-289 (1990).
8. Guo, F.Z., Chou, Y.M., Lee, S.Z., Wang, Z.S. and Mao, W.: "Flow Characteristics of a Cyclic Flow Regenerator," *Cryogenics*, Vol.27, pp.152-155 (1987).
9. Jacob, M.: "Heat Transfer, Chapter 35. Regenerator". Vol. 2, Wiley and Sons, New York, (1957).
10. Chang, W.S.: "Porosity and Effective Thermal Conductivity of Wire Screens," *ASME J. Heat Transfer*, Vol. 112, pp.5-9 (1990).
11. Guo, F.Z.: "Network Model of Cyclic Flow Regenerator for Stirling Cryocooler," *Cryogenics*, Vol.30, September Supplement, pp.199-205, (1990).

REGENERATOR PERFORMANCE AND REFRIGERATION MECHANISM FOR 4 K GM
REFRIGERATOR USING RARE EARTH COMPOUND REGENERATOR MATERIALS

Toru Kuriyama, Masahiko Takahashi, and Hideki Nakagome
Energy and Mechanical Research Laboratories
Toshiba Research and Development Center
Ukishima, Kawasaki, Kanagawa, Japan

Takasu Hashimoto, Tatsuji Eda, and Masanori Yabuki
Department of Applied Physics
Tokyo Institute of Technology
Oh-Okayama, Meguro, Tokyo, Japan

ABSTRACT

This paper describes the experimental results of a two-stage Gifford-McMahon (GM) refrigerator using rare earth compounds as a regenerator material. The purpose of this study was to improve the 4.2 K refrigeration performance and to reveal the refrigeration mechanism in the liquid helium temperature level, where helium gas is regarded as a non-ideal gas.

First, optimization for the intake and exhaust valve timing and the pressure-volume (PV) work at an expansion space were investigated to improve the 4.2 K refrigeration performance. A maximum refrigeration capacity of about 0.8 W at 4.2 K was obtained by a usual sized (32 mm in the second cylinder diameter and 32 mm in the displacer stroke) GM refrigerator.

Secondly, the helium gas temperature distribution in the second regenerator were measured to examine the refrigeration mechanism at the 4.2 K level, and the mass flow rate in the second regenerator was calculated from the temperature signal. The data clearly showed a difference in the refrigeration mechanism between the non-ideal gas region (about 5 K) and the ideal gas region (above 10 K).

INTRODUCTION

A two-stage GM refrigerator is commonly used in many cryogenic systems, such as a cryopump and a shield cooler for an MRI magnet. Usually lead (Pb) is preferred as the second regenerator material. The lowest temperature for a typical two-stage GM refrigerator, however, is limited to about 8 K level because of the low heat capacity of Pb below 10 K.

Recently, many efforts to lower the cooling temperature of the GM refrigerator have been growing by using rare earth compounds as the regenerator material^{(1),(2)}. The authors achieved the cooling temperature below 4.2 K by the two-stage GM refrigerator⁽³⁾ with an erbium 3 nickel (Er_3Ni)⁽⁴⁾ regenerator material and obtained a refrigeration capacity of about 0.3 W at 4.2 K.

The refrigeration mechanism, however, in the liquid helium temperature region (4.2 K) has not been clarified, because helium gas is regarded as a non-ideal gas in this temperature level. In this research, optimization of the refrigerator operating conditions, such as the valve timing and the PV work, to improve the refrigeration performance at the 4 K level have been achieved. The temperature distribution and the mass flow rate in the second regenerator were also investigated. The refrigeration mechanism difference between a non-ideal gas and an ideal gas are also discussed.

IMPROVEMENT OF 4.2 K REFRIGERATION PERFORMANCE

Test Apparatus

Optimization of the refrigerator operating condition, such as the valve timing and the PV work, to improve the 4.2 K refrigeration performance were investigated by the usual sized two-stage GM refrigerator. The first and second cylinder sizes were 70 mm and 32 mm in diameter and the expansion volumes were 97.4 cm³ and 25.7 cm³, respectively. The hybrid structure was adopted for the second regenerator material with

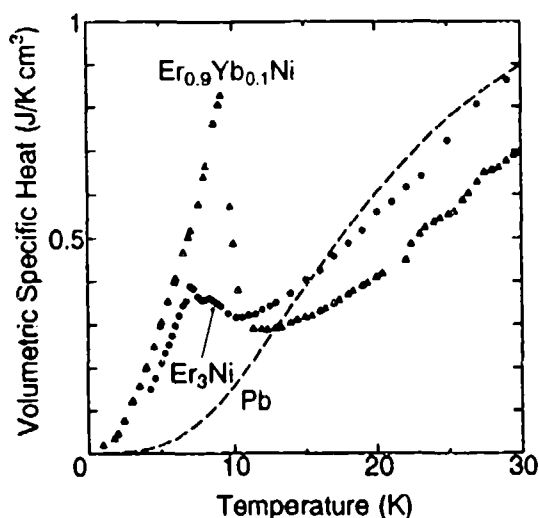


Fig. 1
Volumetric specific heat
for regenerator materials

Er_3Ni and erbium 0.9 ytterbium 0.1 nickel ($\text{Er}_{0.9}\text{Yb}_{0.1}\text{Ni}$)^(a). The authors have already improved the 4.2 K refrigeration performance by this structure compared with Er_3Ni only^(a). Figure 1 shows the volumetric specific heat for Er_3Ni , $\text{Er}_{0.9}\text{Yb}_{0.1}\text{Ni}$, and Pb. The volumetric specific heat for $\text{Er}_{0.9}\text{Yb}_{0.1}\text{Ni}$ has a sharp peak around 9 K and is much larger than that for Er_3Ni below about 11 K. In the hybrid regenerator, Er_3Ni spheres (216 g ; 0.18 to 0.42 mm in diameter) occupied one-half volume of the higher temperature part and $\text{Er}_{0.9}\text{Yb}_{0.1}\text{Ni}$ spheres (212 g ; 0.18 to 0.42 mm in diameter) occupied one-half volume of the lower temperature part. The total electric input power to the compressor unit was 6.6 kW.

The first and second displacers were driven by an AC induction motor. The reciprocating speed could be varied by changing the electric frequency. Carbon glass resistance (CGR) thermometers and electrical heaters were placed at both refrigeration stages. A displacement transducer and a pressure transducer were also mounted to obtain the PV diagram at the expansion space.

Optimization of Valve Timing

The gross refrigeration capacity (Q) at the expansion space is calculated from the following equations⁽⁷⁾

$$Q = (\int P dV + \int H dM) \times f \quad (1)$$

$$= W + H \quad (2)$$

where

- P : Pressure of expansion space
- V : Volume of expansion space
- h : Enthalpy of helium gas in an expansion space
- M : Mass of helium gas in an expansion space
- f : displacer reciprocating frequency
- W : PV work at an expansion space
- H : Enthalpy deficit at an expansion space

The term of W in Eq. (2) denotes the PV work and the term of H is the enthalpy deficit at the expansion space. For the ideal gas, the enthalpy deficit (H) is zero and the PV work (W) is equal to the gross refrigeration capacity (Q).

The value of H, however, is negative in the liquid helium temperature level, and the calculated gross refrigeration capacity for the constant temperature of 4.2 K ($Q_{4.2K}$) is less than 20 % of $W^{(1)}$.

Still more, in the real refrigerator which was used in this study, when the mean temperature is 4.2 K, the second stage temperature fluctuated from 3.85 K to 4.55 K synchronized with the displacer reciprocation. So, the gross refrigeration capacity, which considered the temperature fluctuation from 3.85 K to 4.55 K, ($Q_{3.85K-4.55K}$), was calculated and compared with that for the constant temperature of 4.2 K ($Q_{4.2K}$). The result showed that this temperature fluctuation also greatly reduced the gross refrigeration capacity. For example, the calculated value of $Q_{3.85K-4.55K}$ was about 35 % of $Q_{4.2K}$.

The gas intake and exhaust valve timing of the refrigerator was optimized to minimize the temperature fluctuation at the second expansion space to improve the 4.2 K refrigeration performance. For a usual GM refrigerator, the intake valve opens slightly before the displacer reaches the minimum expansion volume. When the intake valve opens, the high pressure helium gas is supplied to the expansion space and the temperature in the expansion space rises rapidly by an adiabatic compression. Therefore, the authors changed the intake valve opened at the moment when the expansion volume was minimum. This valve timing reduced the temperature rise by the adiabatic compression.

Figure 2 compares the PV diagrams of the second expansion space taken by the usual valve timing and the valve timing for this work at 30 rpm reciprocating speed. In spite of the different shape for the PV diagrams, the calculated PV works (W) for the usual timing and this work took almost the same at each reciprocating speed. The value of the PV work in Fig. 2 was 19 W.

Figure 3 shows the temperature fluctuation measured at the second stage for both valve timings. The temperature fluctuation for this work was reduced in the order of 20 % compared with that for the usual valve timing.

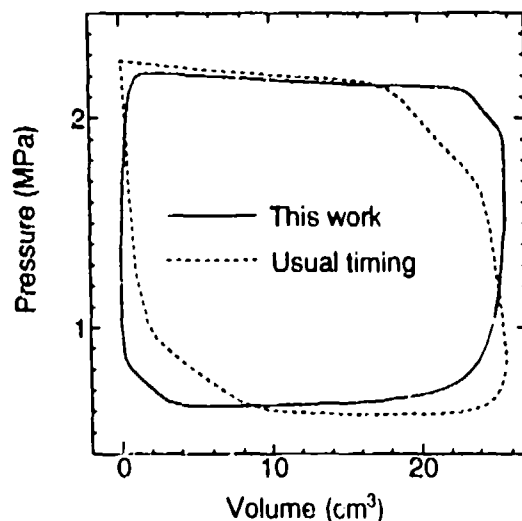


Fig.2
PV diagrams
for usual timing
and this work
at 4.2 K
(Reciprocating
speed : 30 rpm)

The relations between the reciprocating speed and the 4.2 K refrigeration capacity are shown in Fig. 4. In spite of the same PV work (W), the 4.2 K refrigeration capacity for this work was improved more than 20 % compared with the usual valve timing. A maximum refrigeration capacity of 0.79 W was obtained at a 30 rpm reciprocating speed. The effect of reducing the second stage temperature fluctuation by changing the valve timing is shown clearly to improve the 4.2 K refrigeration performance.

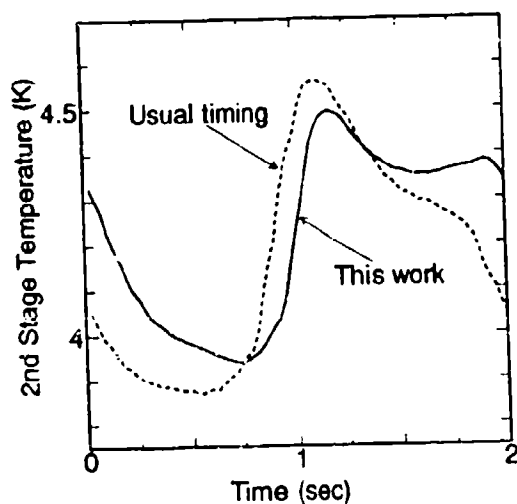


Fig. 3
Temperature fluctuation
for usual timing
and this work
(Reciprocating
speed : 30 rpm)

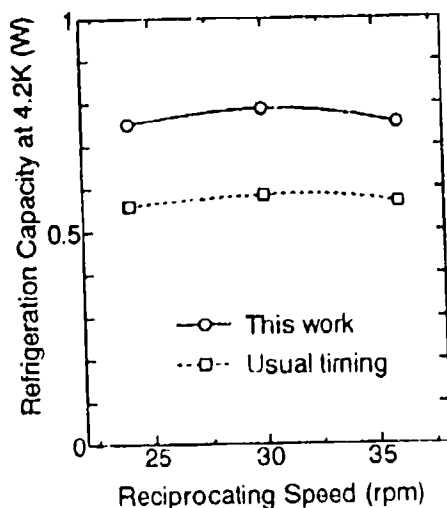


Fig. 4
4.2 K refrigeration
capacity for usual
timing and this work
(Reciprocating
speed : 30 rpm)

Optimization of PV Work

Effects of the pressure level and the mass flow rate to the refrigeration performance at 4.2 K was studied. The pressure range and the mass flow rate to the refrigerator were varied by regulating the compressor bypass valve. The intake and exhaust valve timing was set at the usual timing. Table 1 shows the condition of the pressure level and the mass flow rate to the GM refrigerator for this experiment. The PV diagrams at the second expansion space at 4.2 K were shown in Fig. 5, when the first stage temperature was 35 K and the reciprocating speed was 36 rpm. The PV works (W) for "a", "b", and "c" shown in Fig. 5 were 20.9 W, 16.9 W, and 14.2 W, respectively.

Figure 6 shows the mass change of helium gas in the second expansion space at 4.2 K calculated from the instantaneous pressure, expansion volume, and temperature for each condition. The mass in the second expansion space changed sinusoidally synchronized with the expansion volume and was independent of the pressure change. Moreover, in spite of the different PV works (W) shown in Fig. 5, the helium mass for the individual conditions at 4.2 K were almost the same. Consequently, the helium mass in the expansion space at 4.2 K level highly depended on the expansion volume and wasn't affected by the pressure level.

Table 1 Pressure level and mass flow rate

Conduction	Supply pressure (MPa)	Return pressure (MPa)	Mass flow rate (g/sec)
a	2.3	0.7	3.10
b	2.1	0.8	2.56
c	2.0	0.9	2.26

This feature can be explained by the helium gas non-ideality. Figure 7 shows the temperature dependency of the helium gas density for 2.0 MPa and 0.8 MPa. Figure 8 shows the relation between the temperature and the density ratio of 2.0 MPa helium gas to that of 0.8 MPa. For the ideal gas, the density ratio shows the same value as the pressure ratio of 2.5, which is shown in Fig. 8 by a dotted line. Helium gas can be regarded as the ideal gas above about 15 K. The density ratio, however, rapidly decreases with decreasing temperature and the density ratio is only about 1.1 at 4.2 K. This is the reason why the mass flow rate at the expansion space were almost the same for different pressure levels and depended only on the expansion volume.

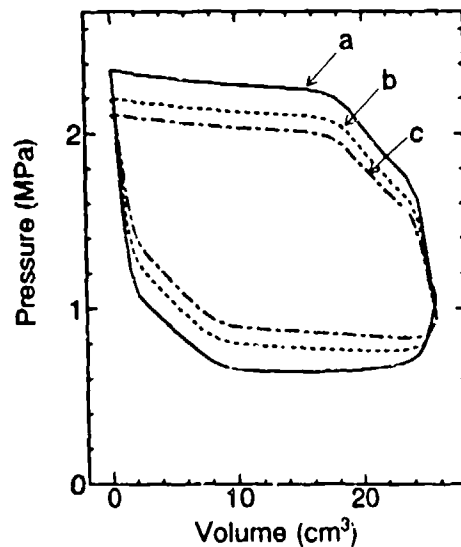


Fig. 5
PV diagrams at second
expansion space
first stage : 35 K
second stage : 4.2 K
(a,b,c are indicated
in Table 1)

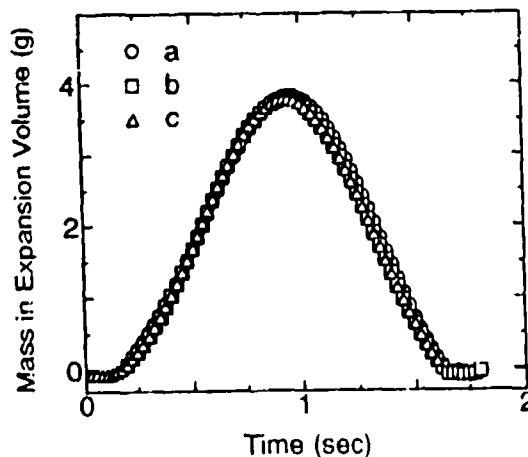


Fig. 6
Mass change of helium in
second expansion space
first stage : 35 K
second stage : 4.2 K
(a,b,c are indicated
in Table 1)

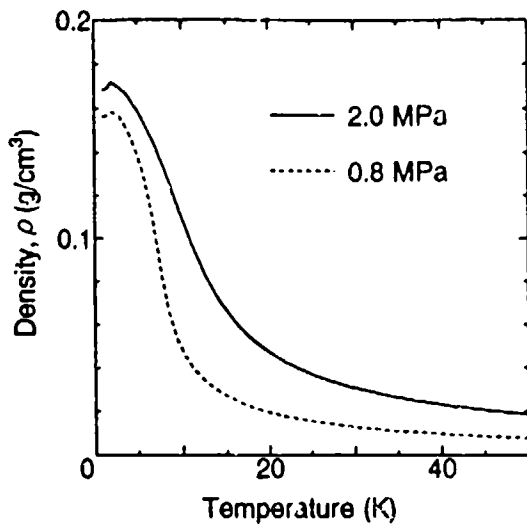


Fig. 7 Helium gas density

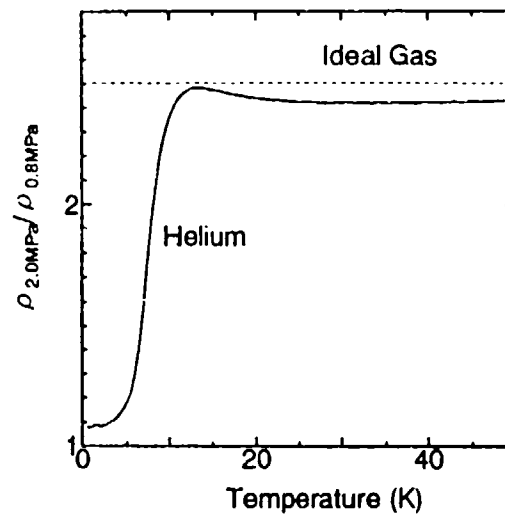


Fig. 8 Density ratio for 2.0 MPa and 0.8 MPa helium

Figure 9 shows the relation between the 4.2 K refrigeration capacities and the first stage temperature. In the case of the lower first stage temperature (below about 45 K), a larger PV work results in a larger 4.2 K refrigeration capacity. But the refrigeration capacity for condition "a", which had the largest PV work, decreased rapidly with increasing the first stage temperature. The refrigeration capacity for condition "c", which had the smallest PV work, exceeded that for condition "a" at the first stage temperature of about 52 K and maintained the 4.2 K refrigeration capacity as high as 75 K of the first stage temperature.

The reason why a large PV work couldn't maintain the 4.2 K refrigeration capacity for larger temperature span in the regenerator could be explained by the regenerator inefficiency. The mass flow rate at the cold end of the second regenerator for each condition was almost the same, which is shown in Fig. 6. At the higher temperature part in the regenerator, however, a larger PV work resulted in a larger mass flow rate, since helium gas is regarded as the ideal gas. So, regenerator inefficiency was considered to be the largest for condition "a", and the 4.2 K refrigeration capacity decreased rapidly with increasing temperature span in the second regenerator.

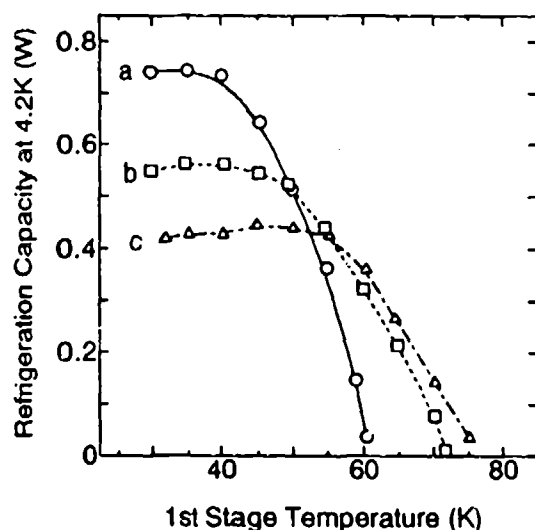


Fig. 9
Relation between
4.2 K refrigeration
capacity and first
stage temperature
(a,b,c are indicated
in Table 1)

REGENERATOR MECHANISM FOR 4 K GM REFRIGERATOR

Optimization of the refrigerator operating condition for the 4.2 K refrigeration performance was investigated in the previous section. In this section, the temperature distribution and the mass flow rate in the regenerator is investigated and the influence of the non-ideal gas on the regenerator mechanism is discussed.

Experimental Apparatus

Figure 10 shows a schematic diagram of the experimental apparatus. In this apparatus, the second regenerator and the second displacer were separated. Five CGR thermometers were put into the second regenerator to measure the helium gas temperatures. The symbols "A" to "E" indicate the positions where the CGR thermometers were placed. The first and second cylinder sizes were 70 mm and 32 mm in diameter and the maximum expansion volumes were 123.2 cm³ and 25.7 cm³, respectively. Germanium thermometers were attached to the first and second refrigeration stages. In this apparatus, Er_{0.9}Yb_{0.1}Ni spheres (440 g; 0.18 to 0.42 mm in diameter) were filled in the second regenerator. The pressure and the displacement were also measured to obtain the PV diagram.

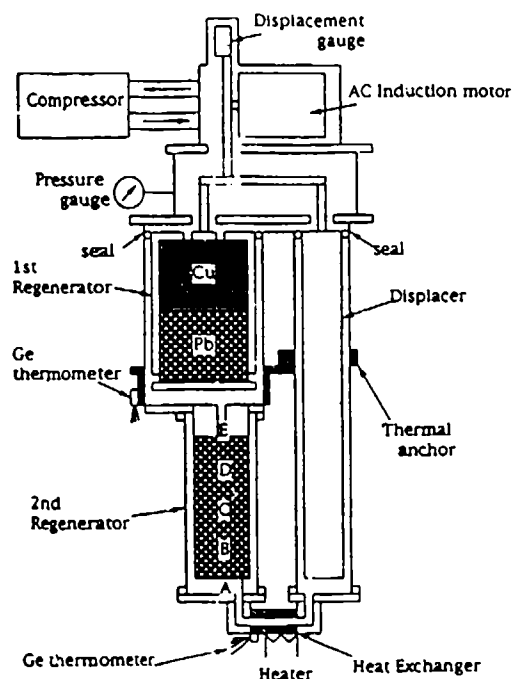


Fig. 10
Schematic diagram
for experimental
apparatus
(A,B,C,D,E indicate
CGR positions)

Temperature Distribution in Second Regenerator

Figure 11 shows the experimental result obtained at 24 rpm reciprocating speed. Mean temperatures of position "A" (T_A) and "E" (T_E) were 5.1 K and 20.5 K, respectively. Figure 11-(1) shows the pressure and the expansion volume change in a cycle, and Fig. 11-(2) shows the temperature fluctuation at each position in the second regenerator. The intake valve opened from 1 to 2, and a high pressure helium gas was supplied to the expansion volume. Then, the exhaust valve opened from 3 to 4, and helium gas was exhausted to the compressor.

Figure 12 shows the maximum and minimum temperature distributions in the second regenerator. The solid line indicates the result where T_A was 5.1 K and T_E was 20.5 K, which represents a non-ideal gas condition. The dotted line indicates the result where T_A was 13.0 K and T_E was 24.9 K, which represents an ideal gas condition. For the ideal gas condition, the temperature profile was smooth and the amplitude of the temperature fluctuation at each position (A-E) was almost equal. For the non-ideal gas condition, however, a steep temperature gradient from

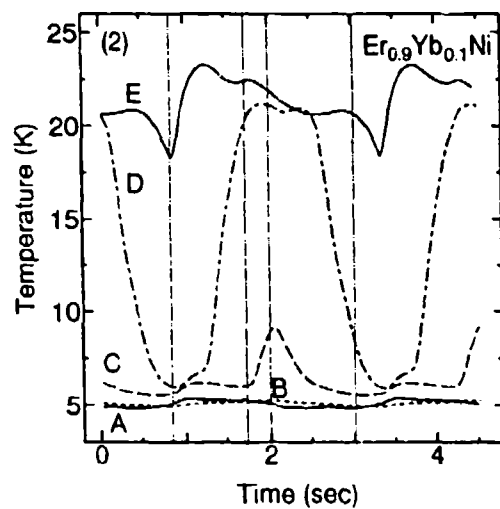
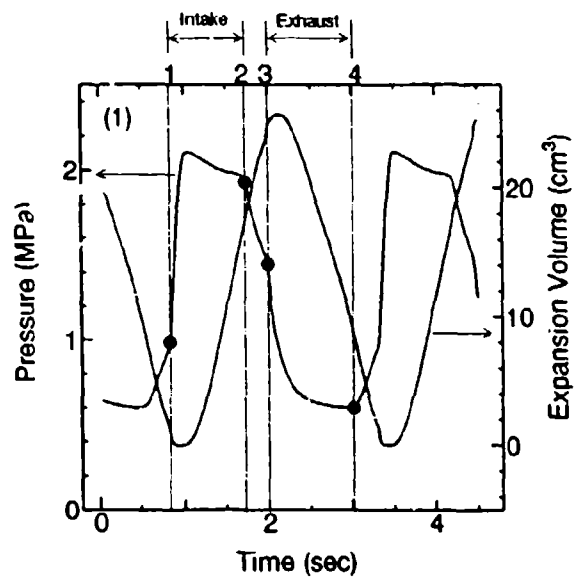


Fig. 11 Experimental results

(1) Pressure and expansion volume change

(2) Temperature fluctuation in second regenerator

(A,B,C,D,E are indicated in Fig. 10)

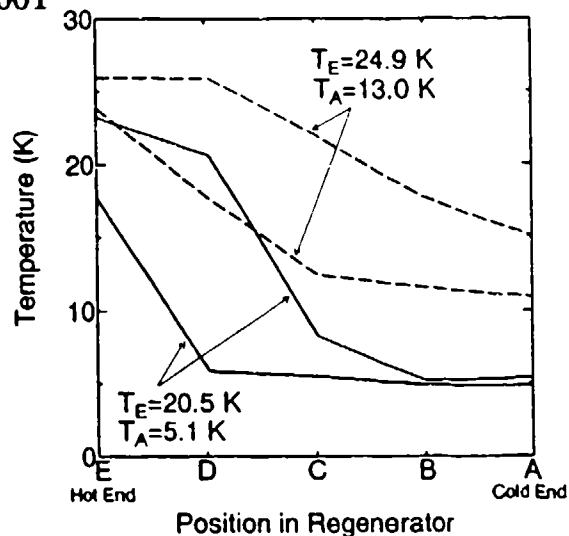


Fig. 12
Temperature distributions
in second regenerator at
(A,B,C,D,E are indicated
in Fig. 10)

the 20 K level to the 7 K level was observed in the range from the hot end, "E", to the middle point, "C", in the regenerator. The amplitude of temperature fluctuation in this part ("E" to "C") was very large. Especially, the temperature at "D" fluctuated from 5.8 K to 20.4 K in a cycle. On the other hand, from the middle point, "C", to the cold end, "A", the temperature gradient was very small, and the temperature fluctuation was greatly reduced to less than 0.5 K. Thus, the temperature distribution in the second regenerator for the ideal gas condition and the non-ideal gas condition were greatly different.

Mass Flow Rate Distribution in Second Regenerator

The mass flow rate at each section in the second regenerator was also calculated from the instantaneous temperature, pressure and expansion volume in a cycle. Figure 13 shows the average mass flow rate distributions in the second regenerator for the ideal gas condition and the non-ideal gas condition. Generally, the mass flow rate for the non-ideal gas condition is larger than that for the ideal gas region. This is because the helium gas density is larger in the lower temperature level. Another distinctive feature for the non-ideal gas condition is that the mass flow rate increases from the hot end, "E", to the cold end, "A". On the contrary for the ideal gas condition, the mass flow rate decreases from the hot end to the cold end.

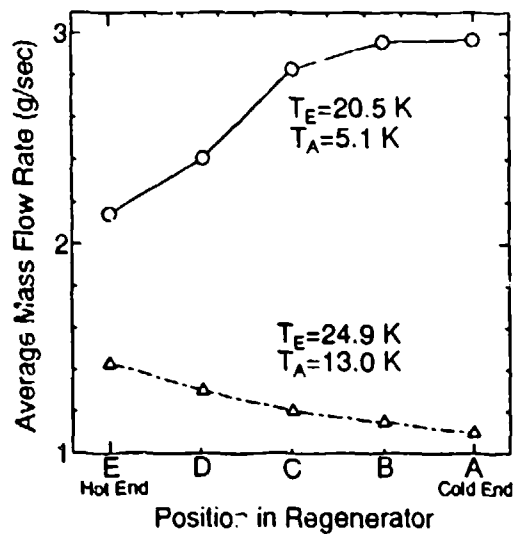


Fig. 13
Average mass flow
rate in second
regenerator at
reciprocating speed
(A,B,C,D,F are indicated
in Fig. 10)

CONCLUSIONS

A two-stage GM refrigerator which used rare earth compounds as the second regenerator material was investigated. The following conclusions have been drawn from the experimental results.

- (1) Optimizations for the intake and exhaust valve timing to the 4.2 K refrigeration performance was investigated. A maximum refrigeration capacity of 0.79 W was obtained by the valve timing which reduced the temperature fluctuation at the expansion space.
- (2) The effect of the PV diagram to the 4.2 K refrigeration performance was investigated. The result showed that the 4.2 K refrigeration capacity highly depended on both the PV work and the second regenerator temperature span.
- (3) The temperature distribution in the second regenerator was measured, and the mass flow rate at each section were calculated.

REFERENCES

- (1) T. Kuriyama, R. Hakamada, H. Nakagome, Y. Tokai, M. Sahashi, R. Li, O. Yoshida, K. Matsumoto and T. Hashimoto, "High Efficient Two-Stage GM Refrigerator with Magnetic Material in the Liquid Helium Temperature Region", Advances in Cryogenic Engineering, Vol.35B (1990) pp. 1261-1269.
- (2) M. Nagao, T. Inaguchi, and H. Yoshimura, "Helium Liquefaction by a Gifford-McMahon Cycle Cryocooler", Advances in Cryogenic Engineering, Vol.35B (1990) pp. 1251-1260.
- (3) T. Kuriyama, M. Takahashi, H. Nakagome, H. Seshake, T. Eda, and T. Hashimoto, "Two-Stage GM Refrigerator with Er₃Ni Regenerator for Helium Liquefaction", Proceedings of the 6th International Cryocooler Conference Vol.II, (1990) pp. 3-14.
- (4) M. Sahashi, Y. Tokai, T. Kuriyama, H. Nakagome, R. Li, M. Ogawa and T. Hashimoto, "New Magnetic Material R_sT System with Extremely Large Heat Capacities used as Heat Regenerators", Advances in Cryogenic Engineering, Vol.35B (1990) pp. 1175-1182.
- (5) T. Hashimoto, M. Ogawa, A. Hayashi, M. Makino, R. Li, and K. Aoki, "Recent progress on rare earth magnetic regenerator materials", Advances in Cryogenic Engineering, Vol.37B (1992) pp.859-865.
- (6) T. Hashimoto, T. Eda, M. Yabuki, T. Kuriyama and H. Nakagome, "Recent Progress on Application of High Entropy Magnetic Materials to the Regenerator in Helium Temperature Range", to be Presented at 7th International Cryocooler Conference.
- (7) G. Chen, G. Sun, and J. Liang, "The Influence of Non-Ideal Effects of Actuating Medium on the Performance of a Plastic Cryocooler", Proceedings of the 12th International Cryogenic Engineering Conference, (1988) pp. 571-575.

A STIRLING CYCLE CRYOCOOLER FOR 4 K APPLICATIONS

D. STACY, J. McCORMICK, P. WALLIS
CREARE INC.
HANOVER, NH 03755

INTRODUCTION

The 4 K cooler operates approximately on the Stirling thermodynamic cycle and embodies an innovation first described by Daney [1] and Roubeau [2]. This innovation embodies two identical Stirling cycle coolers operating 180° out-of-phase and sharing a counterflow heat exchanger in lieu of individual regenerators, as illustrated in Figure 1. This scheme allows heat released by the downward flowing stream to be absorbed by the upward flowing stream, effectively substituting direct gas-to-gas recuperation for the more conventional gas-to-solid matrix regeneration.

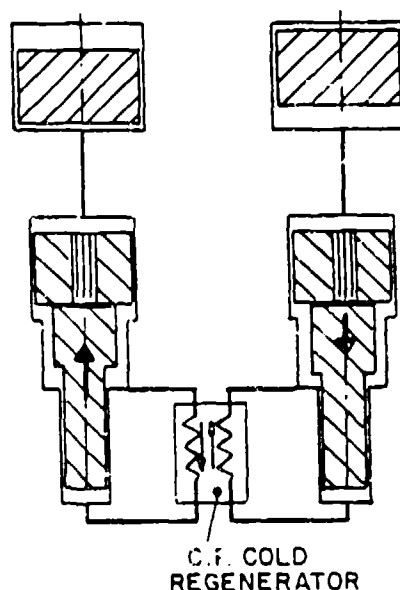


Figure 1. 180° DUAL STIRLING COOLER WITH RECUPERATIVE REGENERATION

The 4 K cooler concept embodies a further innovation which perfects the realization of recuperative regeneration. The expander volume is cycled on a non-sinusoidal schedule in order to produce a symmetric waveform of recuperator thermal loading.

THERMODYNAMIC CYCLE DESIGN

Regenerative cooling cycles, such as the Stirling, which operate below the critical temperature of the working fluid (helium) benefit strongly from low operating pressures. For example, the expander provides more gross cooling power at subcritical pressures than at supercritical pressures for the same temperature, swept volume, and cycle pressure fluctuation. Heat absorbed by the working fluid in an expansion process is represented as:

$$dQ = dH - V_E dp \quad (1)$$

Substituting from Maxwell's relations, Eqn. 1 can be manipulated into the form:

$$dQ = \beta T_E V_E dP \quad (2)$$

where β is the isobaric expansivity, a thermodynamic property. In the ideal gas regime, $\beta T = 1$, and Eqn. 2 reduces to the familiar form for computing expansion work in an ideal gas. At temperatures below 10 - 20 K, however, helium is not an ideal gas at supercritical pressures, as illustrated in Figure 2. βT for supercritical pressures rapidly approaches zero as temperature drops below 4 K, driving the gross cooling output of a given expander toward zero. Suitably low pressures enable the expander to retain cooling performance consistent with (or slightly better than) the ideal gas case.

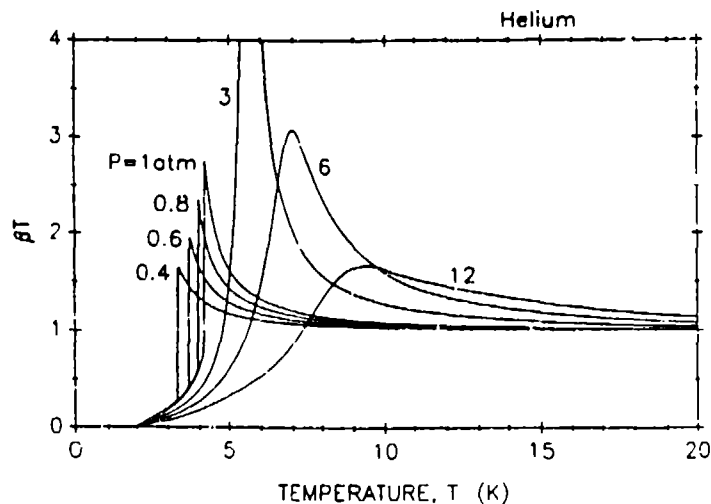
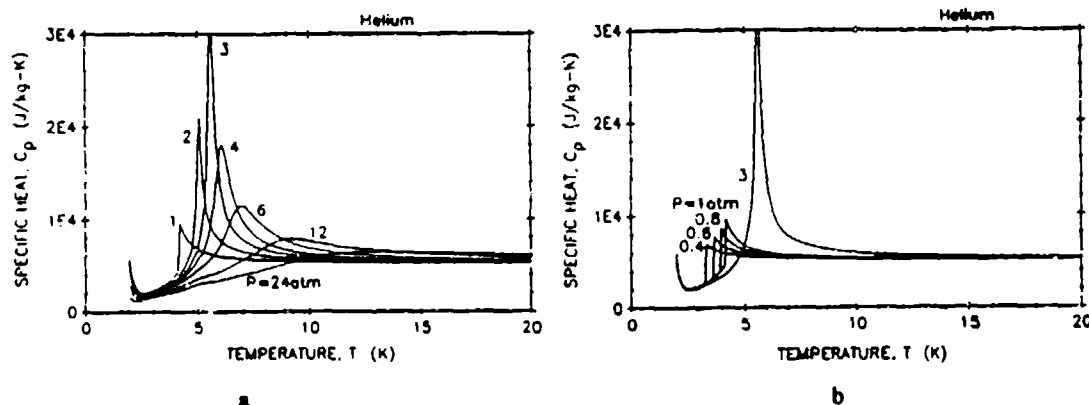


Figure 2. HELIUM PROPERTIES

Low pressure operation also eliminates peaks in important thermodynamic properties such as specific heat capacity, as illustrated in Figure 3a. A heat capacity peak tends to flatten the

temperature gradient in that section of the regenerator, making prediction of the temperature profile difficult and its stability questionable. Correct design of the regenerator requires an accurate knowledge of the temperature distribution. As can be seen in Figure 3b, low pressure operation avoids the problems of non-ideal variation in the helium gas properties.



Figures 3 a & b . HELIUM PROPERTIES

Very low cycle pressures are beneficial, and perhaps necessary, for Stirling cycles lifting from 4 K. A low pressure multi-stage cycle lifting from 4 K all the way to 300 K, however, would be unacceptably large and heavy at the warm end. Cycle optimization studies demonstrated clear advantages in size and weight with a hybrid cycle approach, cascading a multi-stage high pressure Stirling (or other) cycle cryocooler above a low pressure Stirling cycle operating between 4 K and approximately 20 K. The thermodynamic design pursued in this program was therefore for a single-stage low pressure Stirling cycle lifting to 20 K.

CYCLE DESIGN CODE

The thermodynamic cycle was designed with the assistance of a proprietary computer code, FORTIT B, developed under previous SBIR projects. FORTIT is a simple numerical code which starts in the isothermal expander with a prescribed pressure and volume waveform and marches up through the regenerator to the compressor, computing heat transfer and pressure drop parameters from laminar, quasi-steady relationships. Outputs include the compressor swept volume and volume waveform necessary to have provided the originally assumed pressure waveform. Gas in the regenerator is initially assumed to be in local thermal

equilibrium with the regenerator walls, and the temperature and pressure are used to compute the thermodynamic state in each regenerator node. Change in state from node to node is then used to compute instantaneous heat flux, from which the local film ΔT is computed by means of a quasi-steady laminar Nusselt number. The actual gas temperature in each node thus computed is then used to call up the gas enthalpy from the Oxford University helium properties code HEPROP. The product of enthalpy and mass flow rate provides the instantaneous enthalpy flux up or down the regenerator in each node. Cyclic integration of the enthalpy flux provides the net enthalpy flux down the regenerator in each node; the loss associated with heat transfer irreversibility.

FORTIT also calculates the conduction of heat down the metal of the regenerator, using the appropriate temperature dependent metal conductivity from a database. Both conduction and enthalpy flux depend upon the local temperature gradient in the regenerator. For steady-state conditions, the First Law requires that the sum of conduction and enthalpy flux is constant for all regenerator nodes. Starting from a pure conduction temperature profile, the code iterates on temperature profile until the First Law criterion is satisfied within prescribed convergence limits. The code acronym derives from FORtran Temperature ITeration.

TAILORED WAVESHAPES

Recuperation overcomes the low temperature performance deterioration of conventional regenerator matrix materials due to declining heat capacity. Effective implementation of the recuperative Stirling concept at low temperatures, however, depends for its success on further thermodynamic innovations. First, the instantaneous rate of heat transfer out of one gas stream must match with high precision the instantaneous rate of heat transfer into the other gas stream throughout the thermodynamic cycle, requiring temporal symmetry in the recuperator thermal load waveform. Mechanical implementation of the Stirling cycle typically invokes sinusoidal waveforms of compressor and expander volume in time for reasons of kinematic simplicity and/or resonant operation. Such machines however produce a decidedly asymmetric cycle of mass flow (and thermal loading) on the regenerator, as illustrated in Figure 4. This thermal loading asymmetry results in imperfect recuperative cancellation in the 180° dual Stirling cycle implemented with sinusoidal volume waveforms, as shown in Figure 5. The uncanceled residual thermal load in Figure 5 represents a net regenerative demand on the heat capacity of

the metal in the heat exchanger. The present 4 K cooler concept perfects the implementation of the recuperative Stirling invention by distorting or "tailoring" the expander volume waveform so as to provide symmetric thermal loading waveforms and perfect recuperation. This result can be achieved for waveform tailoring of the expander, the compressor, or both, and an infinite number of symmetric thermal load combinations are possible. The volume waves which produce symmetric thermal load waves, however, also influence the expander PV diagram (gross cooling) and the heat exchanger effectiveness loss. Optimum volume cycles will provide recuperative symmetry while also maximizing net expander cooling output. The design reported herein used a sinusoidal compressor volume and skewed sinusoid expander volume cycles to provide recuperative symmetry, maximized net cooling, and relatively simple drive and control requirements. Figure 6 illustrates the selected expander volume waveform and the resulting waveforms for system pressure and regenerator mass flow rate (which corresponds relatively well to thermal load). Figure 7 compares the expander PV for the Figure 6 cycle with a sinusoidal cycle with similar net cooling output.

The final key thermodynamic innovation in the 4 K cooler concept is the use of elastic metal diaphragms to form the positive displacement compressor and expander volumes. The diaphragms define, seal, and displace the working volumes. This geometry is chosen primarily because it provides expansion and compression processes very close to the ideal isothermal processes which grace the Stirling cycle with Carnot efficiency in the limit. Practically speaking, diaphragms also serve the function of reciprocating bearings and seals, providing a non-wearing mechanism with high reliability and long life potential.

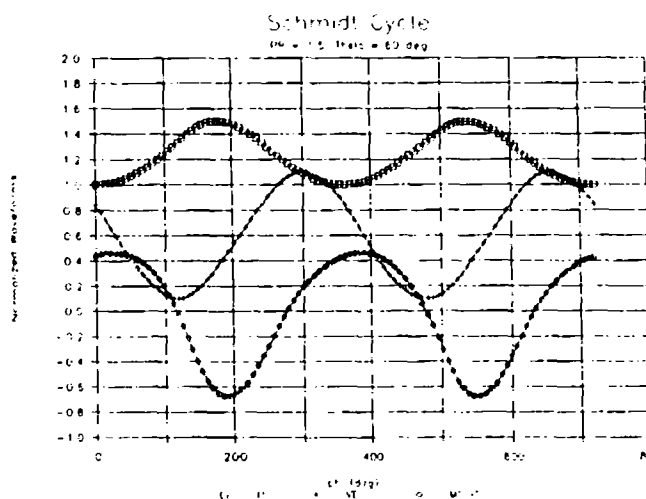


Figure 4. STIRLING REGENERATOR
THERMAL LOADING WITH
SINUSOIDAL VOLUME CYCLES

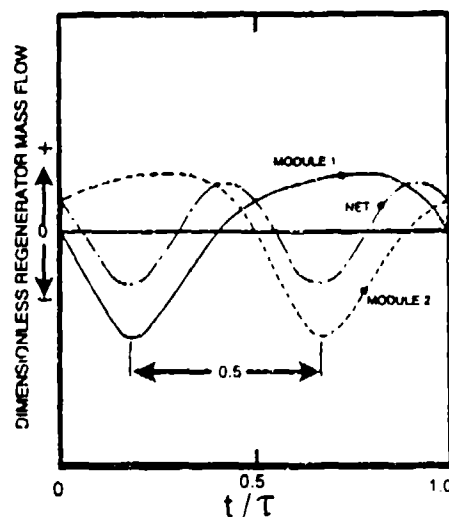


Figure 5. 180° STIRLING REGENERATOR
THERMAL LOADING WITH
SINUSOIDAL VOLUME CYCLES

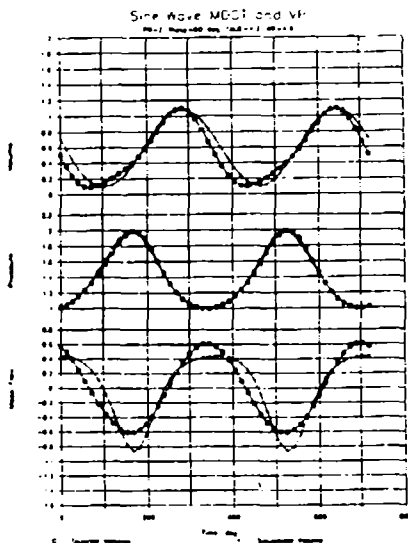


Figure 6. TAILORED EXPANDER/SINUSOIDAL COMPRESSOR PRESSURE AND REGENERATOR MASS FLOW WAVES

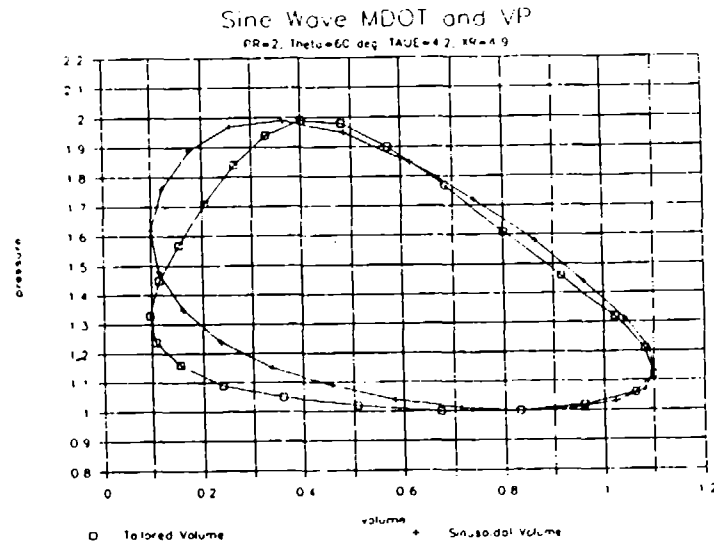


Figure 7. EXPANDER PV DIAGRAMS

REGENERATOR DESIGN AND FABRICATION

The commercial CFD code, FLUENT, was employed to compute the lateral distribution of flow across the regenerator channels as a function of the number and geometry of inlet and discharge ports. The simplest geometry, with a single inlet and discharge port at diagonally opposite corners of the regenerator, produced the computed flow field illustrated in Figure 8. Significant distortions of the flow field were predicted over 25% of the regenerator length at each end with this geometry. While it is obvious that a very fine mesh of small ports is desirable from a flow distribution sense, the separation between ports includes an irreducible minimum gasket width for reliable sealing. Increases in the number of ports therefore reduce the fractional plate width available for flow porting in order to accommodate the increased number of gaskets.

A design was finally selected which effectively divides the channel into four symmetric parallel flow streams with one inlet and one discharge port each. Because the flow systems are symmetric about the port center lines, this translates into two full ports at one end and one full port flanked by two half ports at the other end. This design confines significant lateral

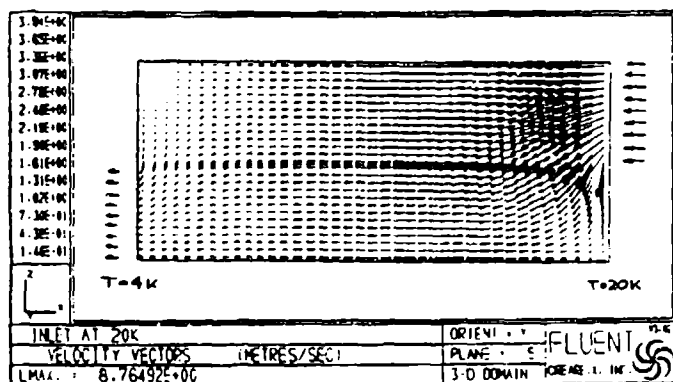


Figure 8. COMPUTED FLOW FIELD FOR SINGLE PORT CHANNEL DESIGN

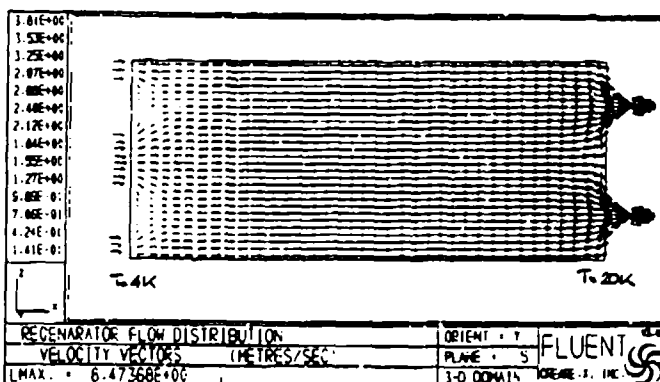


Figure 9. COMPUTED FLOW FIELD FOR "4 PORT" CHANNEL DESIGN

flow distortions to approximately 10% of the regenerator length at each end. The FLUENT output is shown in Figure 9, and the embedded distortion data are amplified in Figure 10. Calculations were performed at several planes across the hydraulic diameter, and Figure 10 displays the bulk integrated flow distortion results. Figure 11 displays the design implementation of the "4 port" scheme.

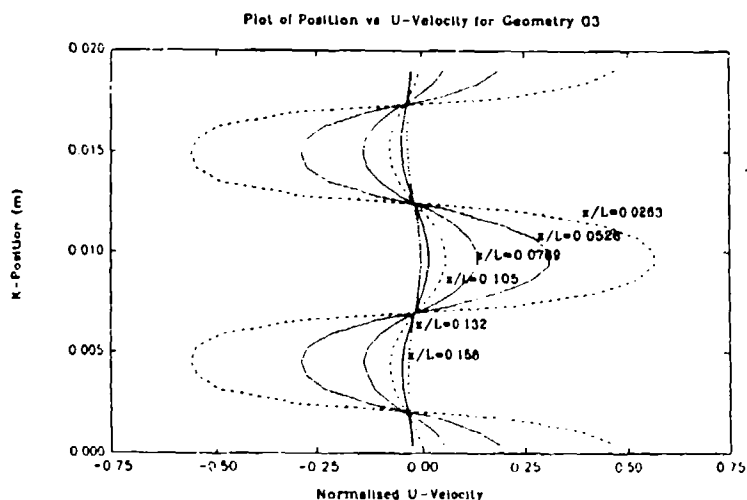


Figure 10. "4 PORT" CHANNEL NORMALIZED FLOW VS. LENGTH

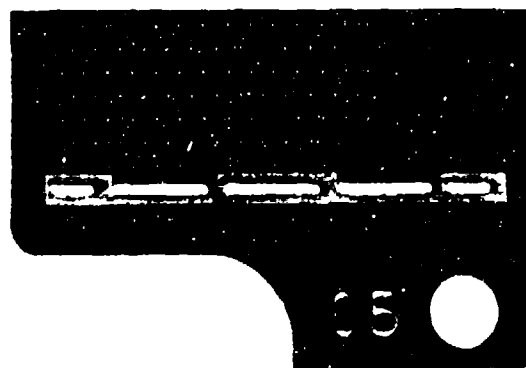


Figure 11. "4 PORT" CHANNEL DETAIL

The second concern in regenerator design is non-uniform flow distribution across the many parallel channels of the regenerator caused by the expected tolerance on plate-to-plate spacing. This tolerance would arise both from material thickness tolerance and from variations in material yield during the diffusion bond fabrication process. Although research indicated that plate-to-plate spacing precision of 1 micron could be held, the extreme sensitivity of maximum channel-to-channel flow imbalance to plate spacing suggested that channel flow variations of 10% could result. This degree of flow imbalance in turn would have a significant impact upon regenerator effectiveness, as illustrated in Figure 12. The parameter C_L/C_H corresponds to the mass flow ratio between adjacent channels, and the parameter F_L indicates the fraction of the heat exchanger channels afflicted by the mass flow imbalance.

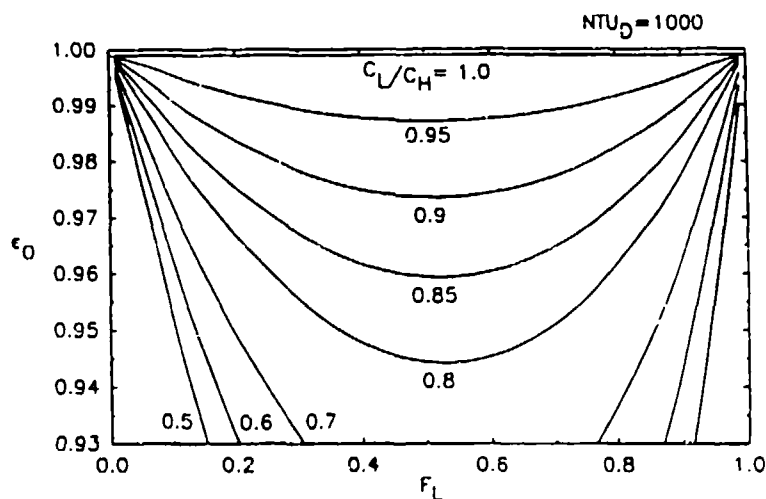


Figure 12. HEAT EXCHANGER EFFECTIVENESS VS. FLOW DISTRIBUTION UNIFORMITY

DESIGN

The regenerator is a parallel plate heat exchanger consisting of 40 "A" channels alternating with 40 "B" channels serving the "A" and "B" Stirling cycles. Porting into each channel consists of two full ports at one end and one full port plus two half ports at the other. Plate spacing is maintained by a matrix of spacer buttons which constitute about a 10% flow blockage (included in the thermodynamic design calculations). The pitch between spacers is based upon maintaining acceptably small deflections of the heat exchanger "plates" relative to normal plate spacing under the influence of cyclic channel-to-channel pressure fluctuations. Channel perimeters are sealed by a thin metal "gasket" of thickness similar to the plate spacing buttons. Typical regenerator components are shown in Figure 13.

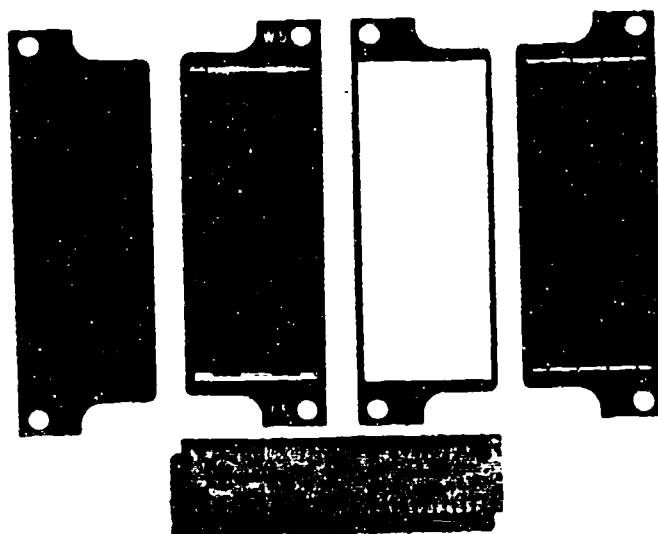


Figure 13. REGENERATOR COMPONENTS

To attenuate the impact of potential flow maldistribution, two design features are incorporated in the regenerator. The first provides multiple transverse headers between alternating flow channels down the length of the regenerator. Figure 14 from Fleming [3] shows the effectiveness of transverse headers in reducing the performance impact of maldistribution by promoting periodic flow redistribution. The second design feature is intended to promote transverse thermal mixing between maldistributed flow streams. This feature constitutes transverse copper "bars" which readily conduct heat perpendicular to the flow direction, effectively remixing the gas temperature in all channels at any elevation. In the simple parallel plate heat exchanger configuration, each flow stream exchanges heat only with the two adjacent channels, and performance is very dependent upon local flow matching in those channels. With transverse conductors, the gas in each channel is also able to exchange heat (via the conductors) with gas many flow channels distant on either side. This invention effectively increases the statistical probability of having a good C_l/C_h ratio by thermally connecting a large number of channels subject to a random value distribution of individual channel flow rate and heat load parameters. This feature might find good application in any miniature heat exchanger, where channel tolerance is a large fraction of the nominal channel dimension. Additionally, it could be useful for combating the thermal instability problems of cryogenic heat exchangers, where temperature dependent viscosity effects provide positive feedback to exacerbate flow maldistribution.

Implementation of this design concept is illustrated in Figure 15 which represents an edge view section of the concept. The clearance between the transverse conductor "wire" and the hole through the spacer "donut" provides a cross header through which alternating flow channels can redistribute their flow. This transverse header and conductor detail is terminated at the extreme ends of the plate stack with two blind side plates which capture the transverse conductor wires and complete the sealing of the gas boundary. Figure 16 shows one plate of the transverse mixed regenerator design.

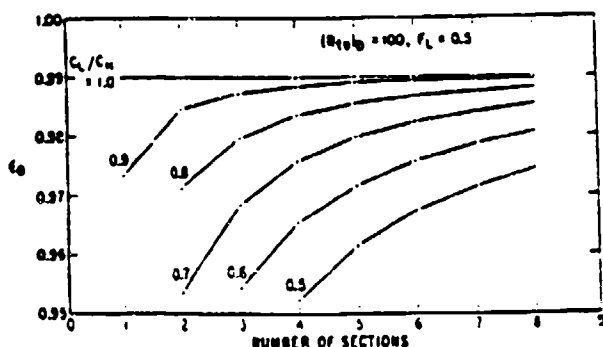


Figure 14. IMPACT ON MALDISTRIBUTED
HEAT EXCHANGER EFFECTIVENESS
OF INTERMEDIATE HEADER SECTIONS

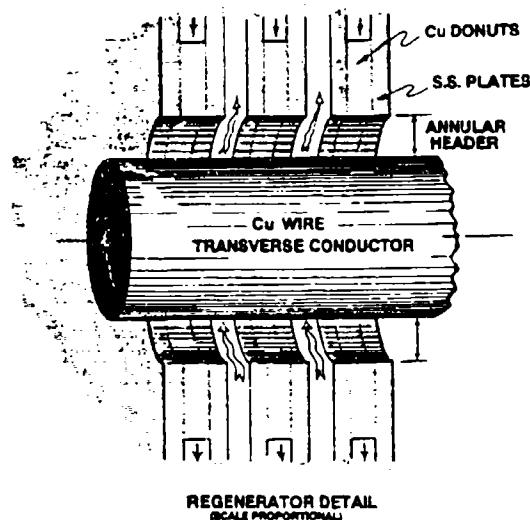


Figure 15. REGENERATOR DETAIL
(SCALE PROPORTIONAL)

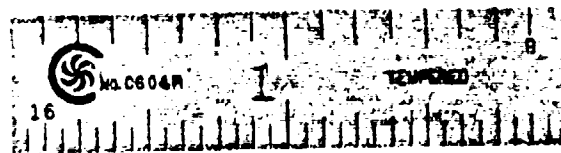


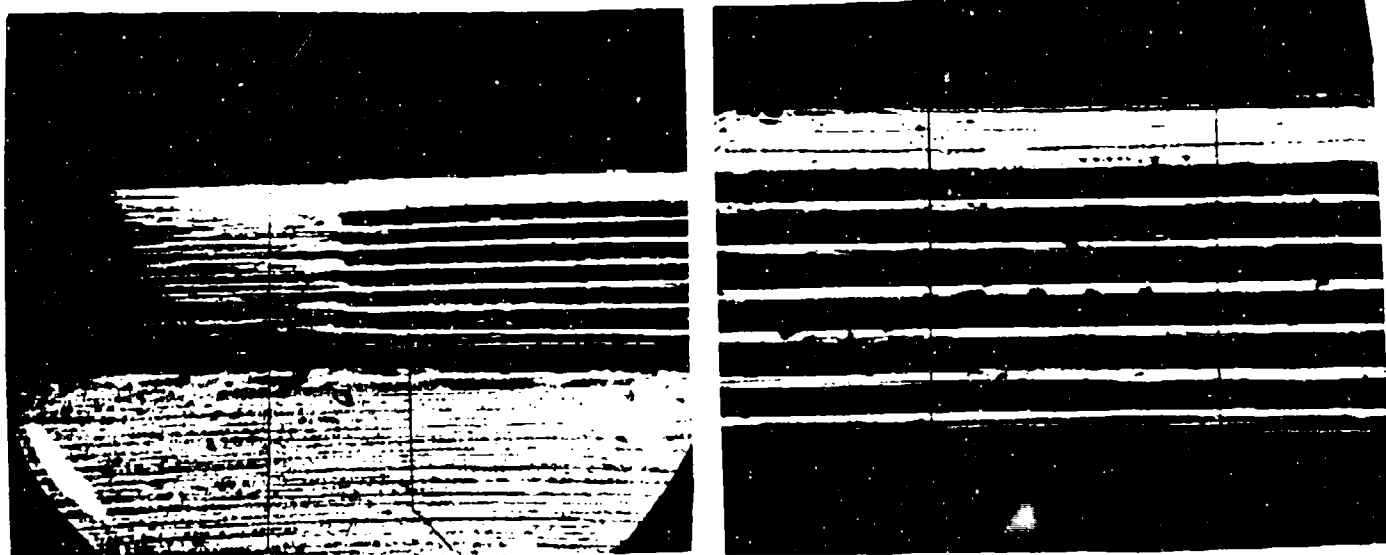
Figure 16. PHOTOGRAPH OF TRANSVERSE MIXED REGENERATOR PLATE

MATERIAL AND FABRICATION TECHNIQUES

The heat exchanger plates are fabricated of 38 micron (1.5 mil) Type 304 stainless steel. The plate perimeter gaskets are also of 38 micron Type 304 stainless. The pure copper spacer buttons are 42 microns (1.7 mils) thick. The regenerator plates and perimeter gaskets are assembled by diffusion bonding.

Chemical photo etching processes are used to form the regenerator plate details and the perimeter gasket pieces. The etching process includes locating features so that the individual components may be precisely aligned on fixturing pins for accurate registration prior to diffusion bonding.

Multi-plate sample stacks of diffusion bonded regenerator components were first leak checked to 10^{-9} std cc/sec, then potted and sectioned for destructive microscopic inspection of internal plate spacing precision. Internal plate-to-plate spacing uniformity, shown in Figs. 17 a and b, was found to be within $1 \mu\text{M}$.



Figures 17 a & b. REGENERATOR SECTIONS, PLATE SPACING

DIAPHRAGM DESIGN

Diaphragms in the 4 K cooler design are of Type 304 stainless steel shim stock. Deflections are on the order of 0.25 mm, and gas pressure differential is a maximum of 0.6 atm. Thickness of the diaphragms was based upon two criteria: keeping the combined stress from deflection and pressure loading beneath 100 MPa, and keeping the volumetric bulge due to pressure differential beneath 5% of the swept volume. Application of these criteria resulted in selection of 0.25 mm thickness for expander diaphragms and 0.50 mm thickness for compressor diaphragms.

The diaphragm design incorporates a thick rigid hub and a thin flexible annular web region with radius ratio of about 0.6. The annular geometry in these proportions provides the lowest peak elastic stress per unit of volume swept. The 100 MPa peak stress limit falls well below the 99.999% fatigue endurance probability at 10^{10} cycles of reversing stress, well beyond 10 years of operating life at the 10 Hz design frequency. Diaphragms therefore provide the basis for a highly reliable long life 4 K cooler with a simple, passive, and robust reciprocating bearing system. The machine design incorporates pairs of diaphragms on a common axis linked by a thin walled structural tube, constraining the system to a single degree of freedom along the axis of reciprocation.

Diaphragms inherently perform the function of sealing the positive displacement working volumes of the expander and compressor. This flexural sealing technique avoids rubbing wear and obsoletes high precision, close running "clearance seals", simplifying construction and promoting long life.

4 K COOLER LAYOUT

The 4 K cooler layout includes two diaphragm expanders and two diaphragm compressors interconnected by the recuperative regenerator. The expander heads share a common 4 K "deck", to which a load heater is attached for purposes of measuring cooling capacity. The compressor heads similarly share a common 20 K deck which is thermally connected to a 20 K heat sink provided by helium boil off. The compressor head deck and the expander head deck are suspended beneath a 300 K motor deck by thin-walled tubes which provide alignment while limiting structural heat leak. The compressor and expander diaphragm hubs are each

connected to mating diaphragm hubs on the motor deck by similar thin-walled tubes which serve to transmit diaphragm stroking forces from motors located on the motor deck. This overall arrangement is illustrated in Figures 18 and 19.

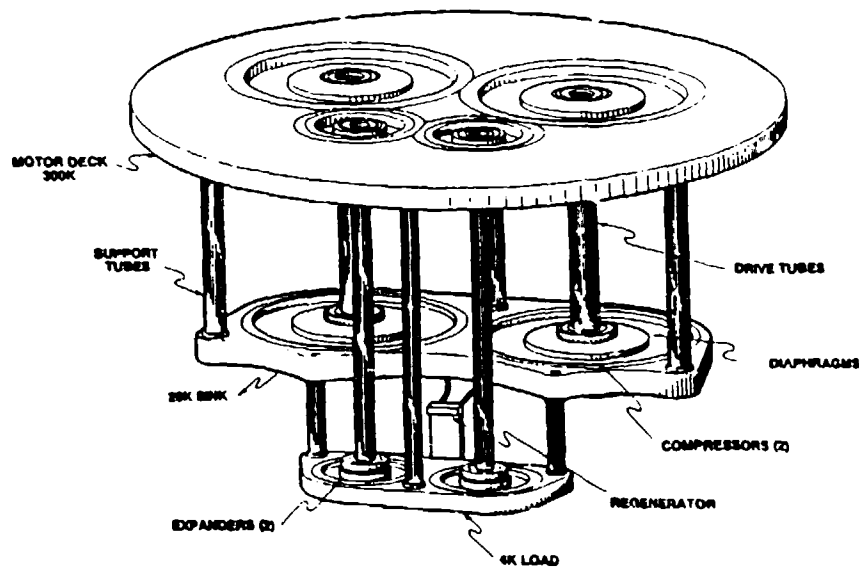


Figure 18. 200 mW 4-20 K COOLER ASSEMBLY

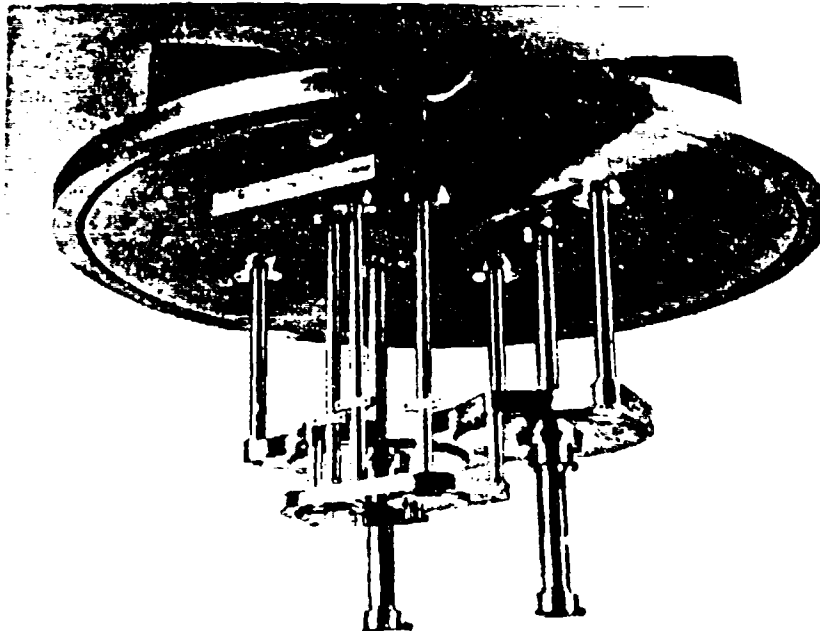


Figure 19. CRYOCOOLER COLD END ASSEMBLY

Rotary DC servo motors drive the reciprocating compressor and expander assemblies through conventional kinematic crank shaft and connecting rod mechanisms, with the four motor deck diaphragms serving as cross heads. A programmable control is employed to provide the tailored expander volume waveforms specified from the thermodynamic design.

The cooler is fabricated primarily of Type 304 stainless steel, chosen for its cryogenic properties and relatively low thermal conductivity. Copper inserts are used where high conductivity is desired, such as for distributing heat from the load heaters to the expander deck heads and from the compressor deck heads to the heat sink heat exchangers. The working gas boundary is hermetically sealed by furnace brazed joints. Construction of the 4 K cooler is currently 75% complete.

FACILITY INTEGRATION

The 4 K cryocooler was designed to integrate into a vertical bell jar vacuum system for testing. The 300 K motor deck sits atop a 24 inch diameter spool piece, which in turn rests upon the baseplate of the vacuum system. The spool contains numerous passthrough nozzles for instrumentation leads and plumbing connections to provide 20 K heat sinking. The zone defined by the motor deck, the spool, and the facility baseplate operates at vacuum levels between 10^{-6} and 10^{-5} torr, maintained by a diffusion pump backed by a rough pump. The zone above the motor deck is covered by a 24 inch diameter bell jar, and this region is evacuated by the rough pump. This scheme limits the potential for fouling the cold surfaces of the cryocooler by volatile contaminants from the motor and drive system bearing lubricants. At the same time, maintenance of nominal vacuum above and below the 24 inch diameter motor deck prevents structural deflections of the deck which would interfere with proper maintenance of diaphragm to head clearance. Spring loaded check valves installed in the motor deck and facing in both directions prevent any possibility of distorting the deck through improper sequencing of vacuum system controls during pump down.

Experimental heat sinking from the 4 K cooler is provided by expendable helium cryogen. Copper heat exchangers of brazed construction are attached to the underside of the compressor head deck. Cold helium gas is supplied to the heat exchangers at the bottom end and flows upward through the exchangers toward discharge nozzles located near the deck end. Waste

heat from the deck meanwhile conducts downward through the copper structure of the exchanger counter to the helium flow direction. In this fashion, the exchanger provides "counterflow" performance between a conductive heat stream and a convective coolant stream, utilizing the sensible cooling capacity of the helium gas between 4 K and 20 K while maintaining the compressor deck at 20 K. Helium flow control provides course temperature control of the compressor deck, and trim heaters on the deck provide fine control under experimental conditions. Heat exchanger construction is illustrated in Figure 20.

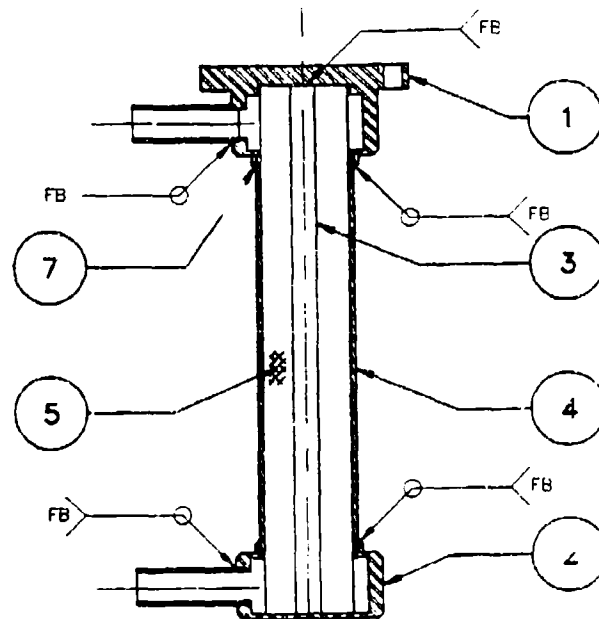


Figure 20. HEAT SINK HEAT EXCHANGER

CONCLUSIONS

Analytical results show that practical and efficient refrigeration between 4 K and approximately 20 K is feasible through the use of a low pressure recuperative dual Stirling cycle approach. The low pressures necessary to successfully implement this approach suggest cascading the 4 to 20 K cooler beneath a more conventional 20-300 K high pressure refrigeration cycle to minimize system mass and volume.

The feasibility of fabricating miniature parallel plate heat exchangers suited to the requirements for 4 K cooling and with 1 micron plate spacing precision and hermetic leak tight integrity has been demonstrated.

The performance and efficiency of Stirling cycle cryogenic refrigerators may be enhanced and extended by optimizing compressor and expander volume cycles on thermodynamic rather than kinematic criteria. Higher performance is possible as designs move beyond simple harmonic motion and into programmable linear drivers.

Finally, 4 K cryocoolers of very long operating life at high reliability and efficiency appear feasible by means of diaphragm design concepts. These results are particularly pertinent to the cooling of sensitive scientific instruments aboard orbiting satellites and installed in remote unattended locations.

ACKNOWLEDGEMENTS

We gratefully acknowledge the support of NASA/GSFC and of NASA/JPL and the SBIR program in funding this research.

BIBLIOGRAPHY

1. Daney, D.E., *Refrigeration for Cryogenic Sensors and Electronic Systems*, NBS SP 607, (1981) 48.
2. Roubeau, Pierre M., *Refrigeration for Cryogenic Sensors and Electronic Systems*, NBS SP 607, (1981) 3.
3. Fleming, R.B.; Advances in Cryogenic Engineering; V.12, K.D. Timmerhaus, ed., New York, NY: Academic Press, 1967, Paper E-4, pp. 352-362.

SUPERFLUID STIRLING REFRIGERATOR WITH A COUNTERFLOW REGENERATOR

J. G. Brisson and G.W. Swift
Condensed Matter and Thermal Physics Group,
Los Alamos National Laboratory, Los Alamos, New Mexico 87545

Abstract

A superfluid Stirling refrigerator has been built with a counterflow heat exchanger. Sensors have been developed to measure pressure, concentration, volume, and adiabatic temperature rise in the working fluid, ^3He - ^4He . The refrigerator is found to operate on both the ^3He , which behaves like an ideal gas, and the phonon/roton gas found in the ^4He component of the working fluid.

SUPERFLUID STIRLING REFRIGERATOR WITH A COUNTERFLOW REGENERATOR

J. G. Brisson and G.W. Swift
Condensed Matter and Thermal Physics Group,
Los Alamos National Laboratory, Los Alamos, New Mexico 87545

Introduction

The superfluid Stirling refrigerator (SSR) uses a ^3He - ^4He liquid mixture as a working fluid. It operates at temperatures below 2 K where the ^4He component of the working fluid is superfluid. The ^3He component of the working fluid, to first approximation, behaves thermodynamically like an ideal gas in the inert background of superfluid ^4He .¹ Using pistons equipped with a superleak bypass, it is possible to expand and compress the ^3He solute "gas". The SSR is a Stirling machine equipped with these "superleaked" pistons to take advantage of the properties of the ^3He solute to cool below 1 K. The proof of principle was shown by Kotsubo and Swift in 1990.^{2,3}

There are three other techniques for cooling below 1 K: 1) the ^3He - ^4He dilution refrigerator which utilizes the endothermic heat of mixing of ^3He into ^4He to reach temperatures below 0.010 K; 2) the evaporation of ^3He which can reach temperatures of 0.3 K; and, 3) adiabatic demagnetization of a paramagnetic salt. There are several advantages of the SSR over each of the other techniques. The power consumption of a dilution refrigerator is typically on the order of kilowatts; whereas, the SSR consumes tens to hundreds of watts. The SSR has the potential to cool below 0.3 K and out perform the evaporative ^3He refrigerator. Adiabatic demagnetization often requires magnetic shielding between the refrigerator and the object to be cooled; obviously, the SSR requires no such shielding. The dilution refrigerator and the evaporative ^3He refrigerator are not naturally suited to a zero gravity environment, whereas the SSR is unaffected by zero G.

Design and Construction

The refrigerator designed by Kotsubo and Swift^{2,3} (K&S) was intended as only a proof of principle. The workers themselves suggest several improvements on the design of their refrigerator. We have incorporated several of their suggestions and added some of our own.

A schematic diagram of our refrigerator is shown in fig. 1, and more details of the design are shown in fig. 2. This refrigerator is actually two SSR's operating 180 degrees out of phase with each other. This allows the use of a counterflow heat

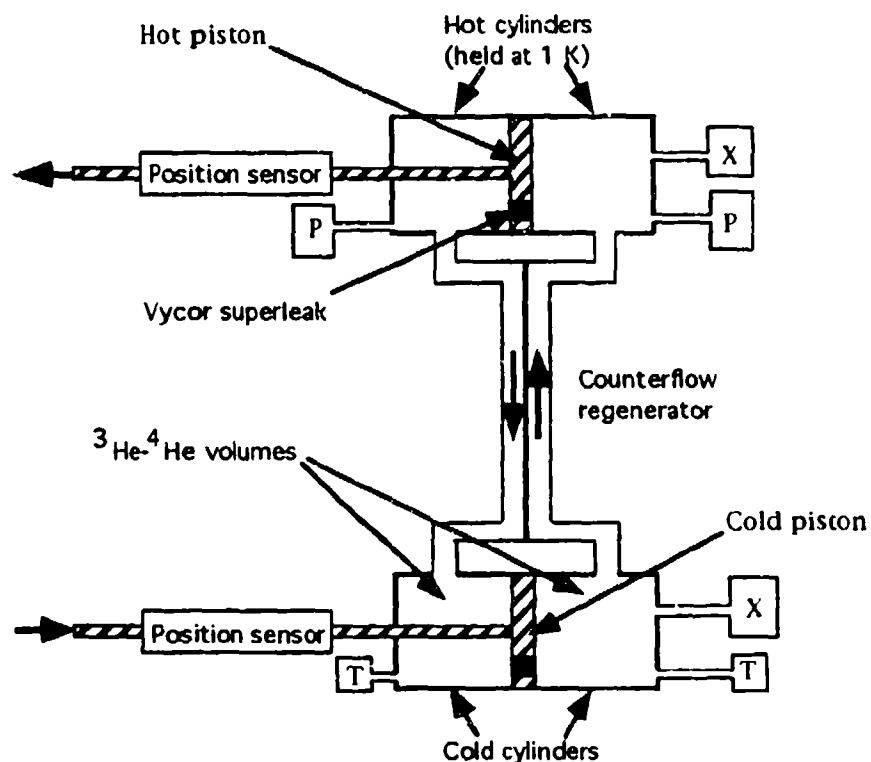


Figure 1. Schematic diagram of the present SSR. Concentration gauges are labeled with an "X", pressure gauges with a "P" and thermometers with a T. The heavy arrows show fluid flow direction in the regenerator corresponding to the piston motion direction shown at the position sensors. The moving parts are crosshatched.

exchanger to act as a regenerator for each of the SSR's which is simpler than the K&S ^3He jacketed regenerator.

The counterflow regenerator shown in fig. 2 consists of a total of 238 0.305 mm O.D. CuNi tubes with 0.038 mm walls. These tubes are silver soldered in a hexagonally close packed array with alternating rows corresponding to each "half" of the SSR. We use silver solder to insure that the solder does not become a superconductor at our operating temperatures and spoil the thermal conduction between the tubes. The length of the regenerator is approximately 20.3 cm.

The design of the regenerator was done with a program written following the criteria outlined by Swift, Migliori and Wheatley⁵. We were interested in designing a regenerator that would operate at higher frequencies than K&S's SSR. This regenerator allows operation of our SSR at periods of 20 seconds per cycle, as opposed to 2.2 to 14.3 minutes for the K&S refrigerator.

The parallel SSR design also takes advantage of both sides of the piston. The previous design required an inert volume on the back side of each piston to allow the collection of the ^4He that flowed through the superleak. In the present design both sides of the piston are involved in the compression and expansion of the refrigerant. This doubles the cooling power per stroke without increasing heating due to piston motion. It also eliminates slow (on the time scale of a week) changing of the cooling

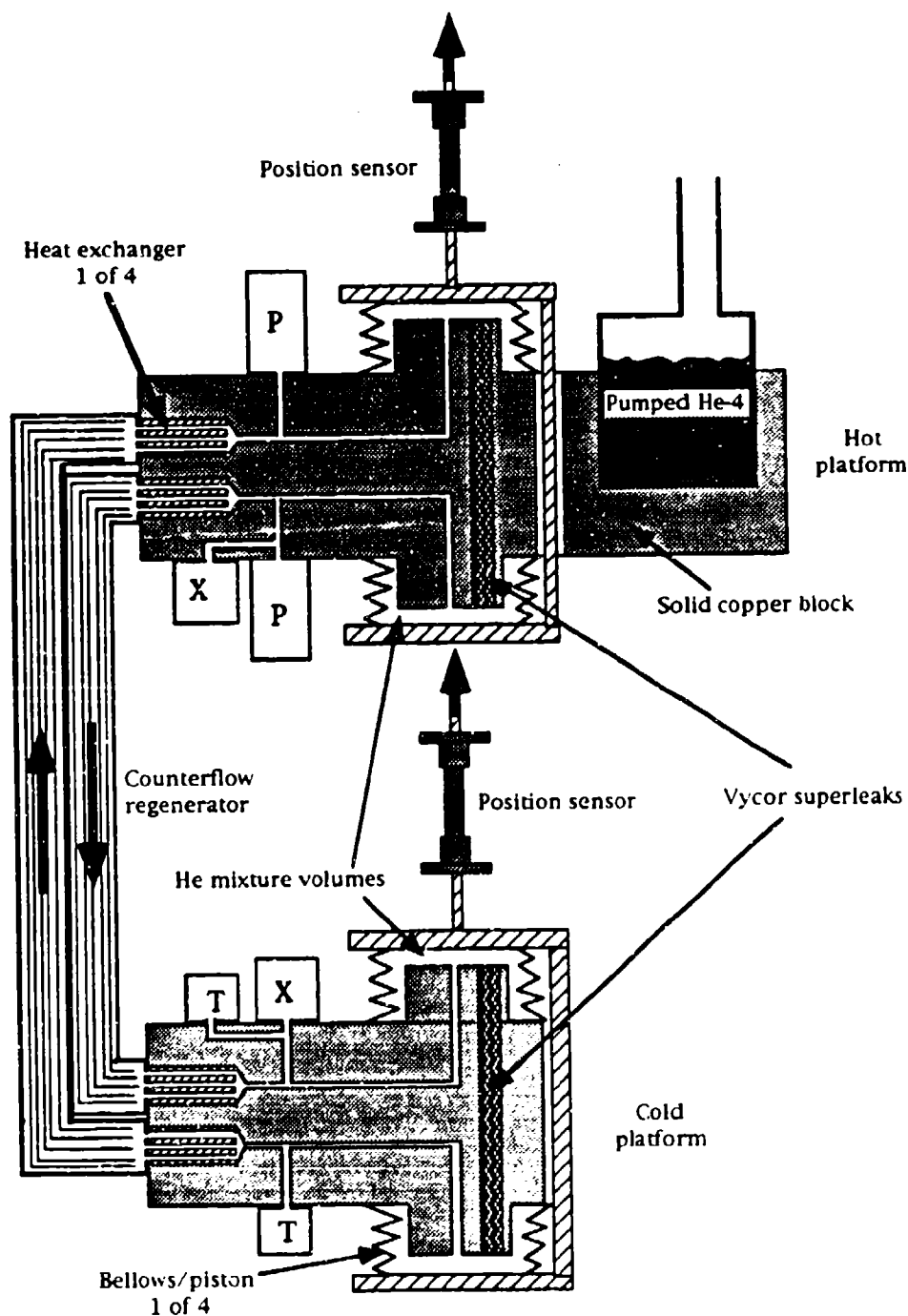


Figure 2. The SSR. Pressure gauges are delineated with a "P", concentration gauges with an "X" and thermometers with a "T". The heavy arrows show fluid flow direction in the regenerator corresponding to the piston motion direction shown at the position sensors. The moving parts are shown with widely-spaced crosshatching.

power, the osmotic pressure and other characteristics of the refrigerator due to diffusion of ^3He into the inert piston volume in the K&S design.

The pistons are made with welded bellows⁴ which have convolutions that nest into one another to minimize the dead volume. The hot platform pistons are rigidly connected together and driven by rigid push rods from room temperature. The cold platform pistons are similarly driven.

We have moved the pumped ^4He pot onto the same platform as the hot pistons to avoid possible thermal gradients and the complications of a heat pipe in the K&S design.

The K&S drive mechanism was highly non-sinusoidal. We have redesigned the drive mechanism so that this refrigerator operates with a sinusoidal drive.

The heat exchangers are copper cylinders press fit into the large copper blocks the pistons are mounted on. The hot platform heat exchangers are 1.14 cm long with four 0.8 mm diameter holes drilled longitudinally through the cylinder. The low temperature heat exchangers are 1.14 cm long with 12 0.51 mm diameter holes.

The pressure gauges of the flexible diaphragm type described by Straty and Adams.⁶ The concentration gauges are of coaxial capacitor type described by Kierstead;⁷ the ^3He concentration is obtained from the dielectric constant of the mixture. The thermometers shown in fig. 2 are intended to measure the heating/cooling due to the adiabatic compression/expansion of the ^3He . They are made by suspending a chip of carbon made from a 220 Ω Speer resistor on thin manganin wires inside a hollow Stycast 1266 envelope. The helium mixture is admitted into the Stycast chamber through a 0.8 mm diameter capillary.

The two fill lines into each of the SSR halves are sealed with low temperature pneumatic valves mounted on the pumped helium platform. These valves are actuated using pressurized ^4He . If we did not use these valves, operation of the SSR would cause the mixture to oscillate up and down the fill capillaries and put a significant heat load on the refrigerator.

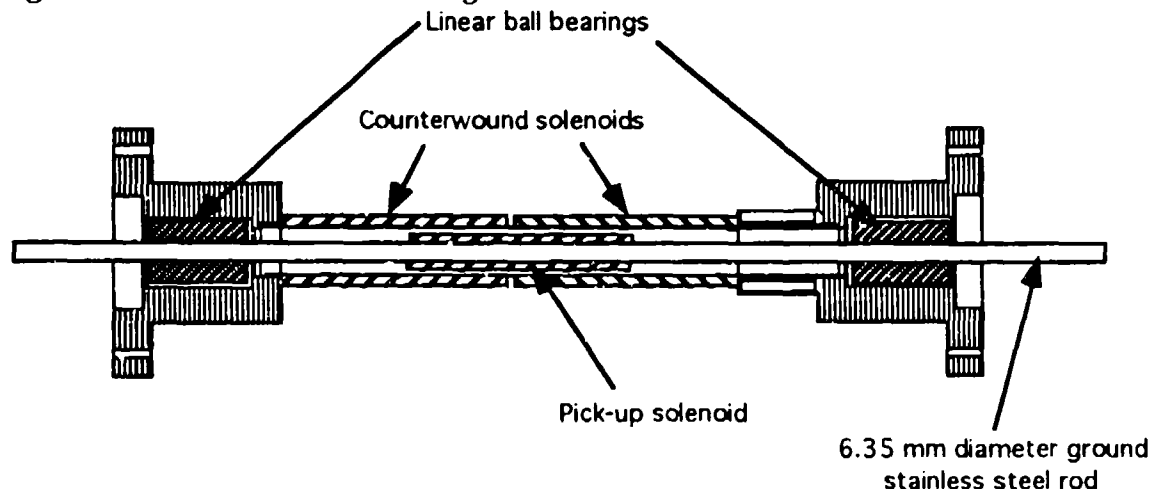


Figure 3. Anatomy of a position sensor. The pick-up solenoid is mounted on the moveable stainless steel rod. As the rod moves the pick-up coil samples the spatially varying field set up by the counterwound solenoids. Monitoring the output signal of the pick-up coil determines the position of the rod.

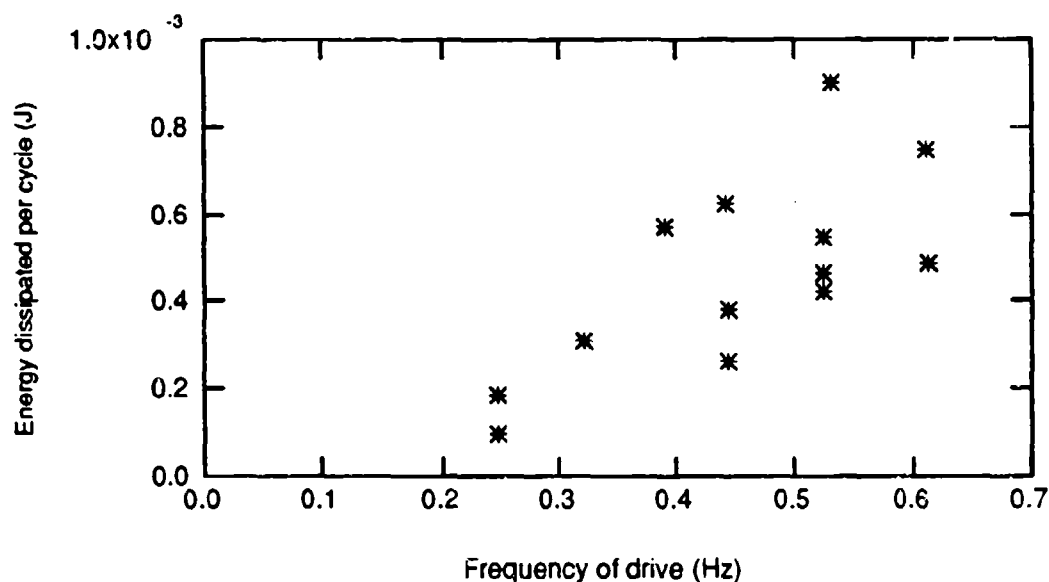


Figure 4. The energy dissipated per cycle by the bearings in a position sensor for a stroke of 1.47 mm.

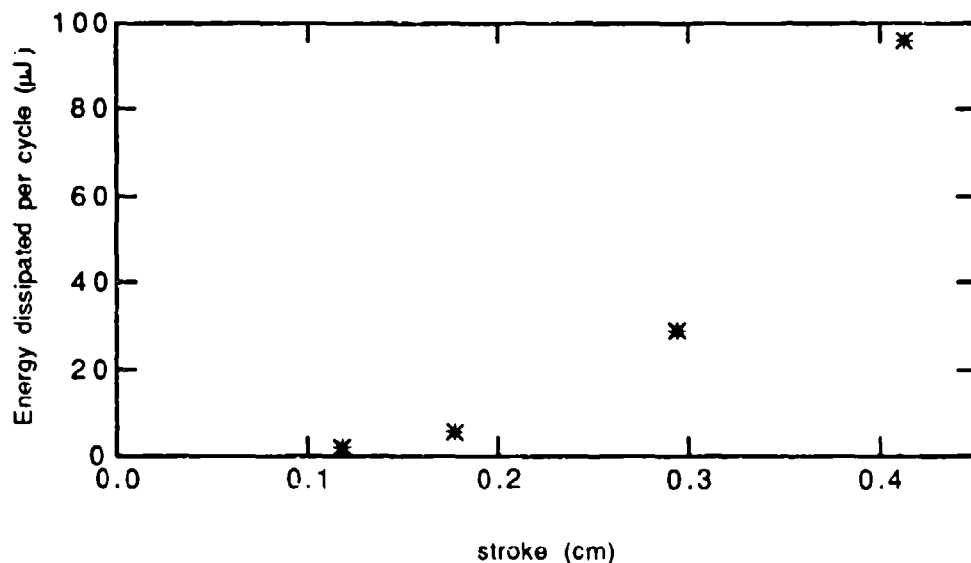


Figure 5. Energy dissipated per cycle versus stroke in the bellows used in the current SSR.

The linear position sensors, shown in fig. 3, are mounted at 1 K to monitor the positions of the pistons in situ. The position sensor consists of two counterwound copper coils on a thin walled stainless steel tube. A pick-up coil wound on a ground stainless steel rod rides inside the counterwound coils. We generally drive the outer coils with a 1 mA 1 kHz signal and monitor the output voltage of the pick-up coil as a measure of position. The resolution of this system is better than 0.025 mm.

The unusual aspect of the position sensor is that it uses linear ball bearings at low temperature (1 K). Figure 4 shows the results of measurements of the heating from the motion of the bearings. The stroke used in the data in fig. 4 is typical for the current SSR. The frequency of operation for our SSR is approximately 0.05 Hz, a period of 20 seconds. We anticipated the power dissipation of the position sensor to be less than 10 microwatts each during the operation of our refrigerator. We thermally linked both position sensors to 1 K since our 1 K pumped ^4He pot could handle up to 6 mW of power.

The energy dissipated per stroke in the bellows as a function of the stroke length is shown in fig. 5. The stroke lengths used to date are 1.52 mm resulting in an anticipated dissipation due to the bellows of 0.1 microwatts per bellows with a 20 second cycle time.

A calibrated germanium resistance thermometer⁸ was mounted on the outside of the cold platform. A 220 Ω Speer resistor was used to monitor the temperature of the hot platform.

Heat Flush and Deviation of ^3He concentration from Ideal Gas Behavior

One of the more interesting points in the initial work of K&S is the deviation of the ^3He concentration from the ideal gas behavior. We were interested in understanding this deviation.

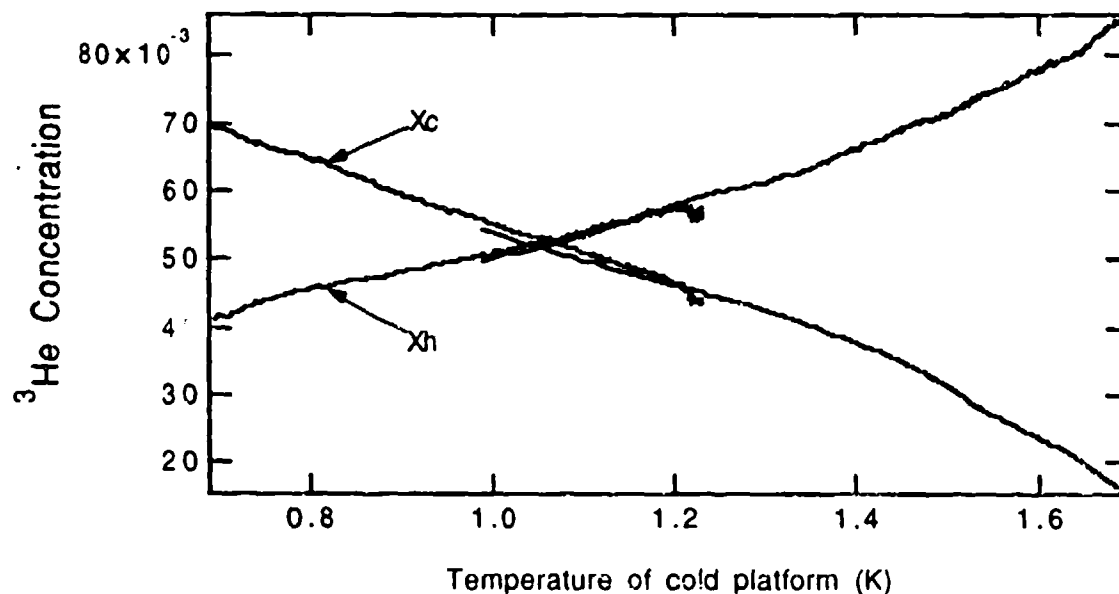


Figure 6. The concentration of ^3He in ^4He at the hot (X_h) and cold (X_c) platforms as a function of the cold platform temperature. The temperature of the hot platform was held at 1.05 K. This graph is the result of two data runs. The disparity in the overlap of the two data runs is due to slight variation in temperature of the warm platform and differing volumes in the pistons between runs.

The concentration gauges were calibrated at 1 Kelvin by measuring their capacitances when evacuated and full of ^4He , and using the known dielectric constant of ^4He . During calibration, we also compared the pressure and temperature dependences of the capacitance to the known temperature dependences of the dielectric constant. We found that the gauges had an inherent pressure dependence equivalent to 4.5% ^3He concentration per atmosphere of total pressure. This was not accounted for in the K&S work and could explain some of the deviations they saw from the ideal gas law.

With mixture in the SSR, we made measurements of the concentrations while holding the hot platform at a constant temperature and varying the temperature of the low temperature platform. The resulting data are shown in fig. 6. The two traces in fig. 6 would be straight lines if the ^3He solute behaved as an ideal gas.

Khalatnikov⁹ suggests that, for low concentrations of ^3He , the mixture should obey

$$(1) \quad \mu_0(p, T) - \frac{kTX}{m_4} = \text{constant}$$

where $\mu_0(p, T)$ is the chemical potential per unit mass for pure ^4He , k is Boltzman's constant, T is the temperature, X is the number concentration of ^3He in ^4He , and m_4 is the mass of the ^4He atom. This equation can be used to determine the concentration gradient between two fluid packets which are at different temperatures.

Since the pressure gradients within our SSR are small we can consider μ_0 to be a function of T only. Then the difference in the chemical potential between two fluid packets at T_1 and T_2 is

$$(2) \quad \Delta\mu_0 = - \int_{T_1}^{T_2} S_4 \, dT \approx -\frac{1}{\rho_4} \int_{T_1}^{T_2} \rho_4 S_4 \, dT$$

here ρ_4 is the mass density of pure ^4He , and S_4 the entropy per unit mass of pure ^4He .

The second integral in eq. 2 is the fountain pressure of ^4He .¹⁰ If we decide to reference our fountain pressure, P_f , to zero temperature then

$$(3) \quad P_f(T) = \int_0^T \rho_4 S_4 \, dT.$$

If we similarly reference the chemical potential to zero temperature, we find

$$(4) \quad \mu_0 = -\frac{1}{\rho_4} P_f.$$

Equation 4 can be substituted into eq. 1 and with some manipulation we find

$$(5) \quad P_f + n_3 kT = \text{constant}$$

where n_3 is the number density of the ^3He . The second term is the osmotic pressure of the ^3He , P_3 . We can rewrite eq. 5 as:

$$(6) \quad P_f + P_3 = \text{constant}$$

within the SSR. This important equation gives the deviations from the ideal gas behavior $P_3 = \text{constant}$. For the data shown in fig. 6, the sum of the fountain pressure

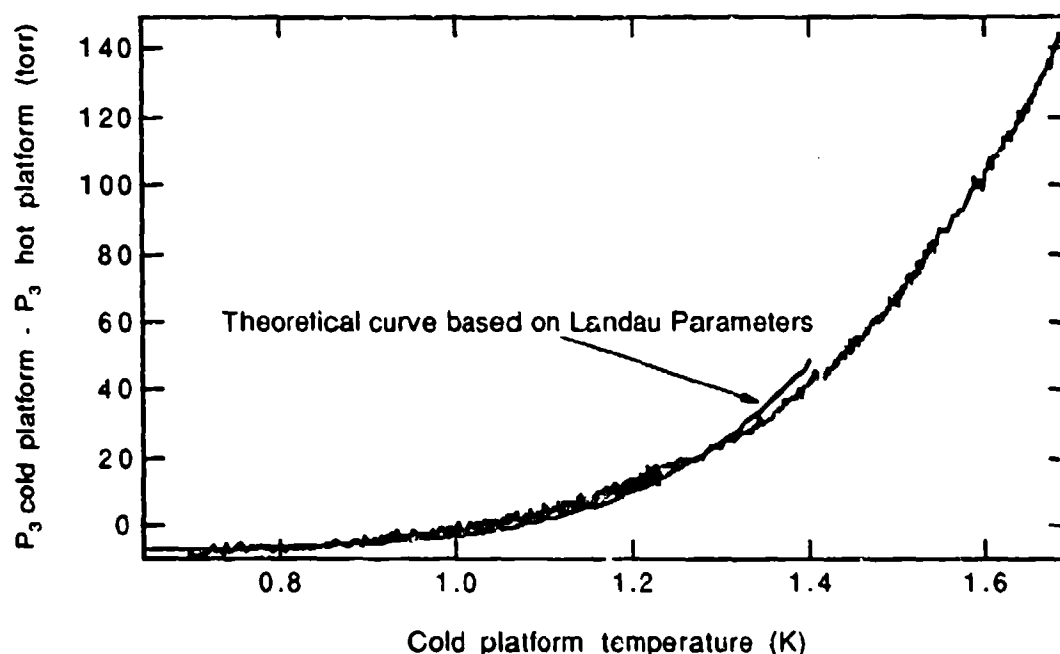


Figure 7. Plot of the difference in ^3He osmotic pressures between the cold platform and hot platform for the data shown in fig. 6. The theoretical curve is plotted for temperatures less than 1.4 K where the Landau model is appropriate. See text for discussion.

and the osmotic pressure of the hot platform should equal the same sum for the cold platform or

$$(7) \quad P_f(T_{\text{hot}}) - P_f(T_{\text{cold}}) = P_3(T_{\text{cold}}) - P_3(T_{\text{hot}}).$$

The difference in osmotic pressures of the data shown in fig. 6 is plotted against the temperature of the cold platform in fig. 7. According to equation 7, this should be the same as a plot of the difference in the fountain pressures of the pure ^4He at the same temperatures. This can be calculated from the Landau model of the phonon/roton gas in liquid ^4He . Using the Khalatnikov's expression for the free energy per unit volume of the phonon/roton gas,¹¹ the thermodynamic relation $P = -\left(\frac{dF}{dV}\right)_T$ (here F is the free energy of the system), and the dispersion parameters given by Wilkes,¹² we arrive at the pressure of the phonon roton gas, P_{pr} as:

$$(8) \quad P_{\text{pr}} \text{ (in torr)} = 1.88 T^4 + 13800 T^{3/2} \exp\left(-\frac{8.65}{T}\right)$$

where T is in Kelvins. Note that the Landau model is only appropriate at low temperatures and breaks down for temperatures above 1.4 K. $P_f = P_{\text{pr}}$ provided the dispersion parameters are not strong functions of volume. Equation 8 is used to calculate the difference in the fountain pressures in equation 7. A plot of the left hand side of eq. 7, using eq. 8, versus the cold platform temperature is shown in fig. 7. There is excellent agreement between the theoretical and experimental curves.

This treatment of the fountain and osmotic pressures suggest a reinterpretation of the working fluid in the SSR as a three fluid medium: an inert superfluid background, a phonon/roton gas, and an ideal gas of ^3He .

Equation 7 also suggests a limitation in the operation of an SSR. If the refrigerator is operated with the warm platform at a high temperature and with a low concentration of ^3He , there will be temperatures where eq. 7 cannot be satisfied. These temperatures correspond to the flushing of all ^3He from the hot platform piston by the phonon/roton gas. The flushing of the ^3He from the hot piston allows superfluid counterflow within the refrigerator and quenches any further cooling by the SSR.

Performance of the Refrigerator

This refrigerator has been operated to a temperature of 528 mK with an 8% mixture and a piston stroke of 1.52 mm. The peak to peak pressure amplitudes in the refrigerator are of the order of 30 torr. There has been no attempt to date to optimize performance. All these results are preliminary.

There have been indications that there are asymmetries in the refrigerator and we have found it necessary to install more gauges in order to sort out these effects so that we may work towards understanding and optimizing the performance of the refrigerator.

The installation of both pressure gauges and the position sensors allows us to make indicator diagrams of the SSR which will ultimately lead to determining the work and the thermodynamic efficiency of this refrigerator.

Present and Future Work

We are currently running the SSR to map out performance as a function of average concentration, speed and stroke. We will be investigating the effect of imbalances of average concentration and stroke in each half of the SSR since these will have a large impact on the counterflow regenerator's effectiveness. We also expect to investigate the behavior when the hot platform temperature is approximately 1.5 K to understand the operation of the SSR in the regime where the working fluid is comprised of both the ^3He and the phonon/roton gas. The operation of the SSR hot platform from a ^3He refrigerator will allow the study of the SSR in the Fermi fluid regime.

Future practical work will include a pulse-tube¹³ version as a first step in the elimination of moving parts from the SSR, and will include the addition of a vortex refrigerator¹⁴ to our cryostat to provide a lower starting temperature.

References

1. J. Wilks, The Properties of Liquid and Solid Helium, (Clarendon, Oxford, 1967) P.232.
2. V. Kotsubo & G.W. Swift in Proceedings of the Sixth International Cryocoolers Conference, edited by Geoffrey Green and Margaret Knox (David Taylor Research Center, Bethesda, Md 1991)
3. V. Kotsubo & G.W. Swift, J. Low Temp. Phys **83**, 217, (1991)
- 4 Type 60030-1 from Metal Bellows Corporation, Sharon, Mass.
5. G.W. Swift, A. Migliori, and J. Wheatley, J. Appl. Phys., **54**, 6834 (1983)
6. G.C. Straty and E.D. Adams, Rev. Sci. Instrum. , **40**, 11, 1393 (1969)
7. H. A. Kierstead, J. Low Temp. Phys **24**, 497, (1976)
8. Lakeshore Cryotronics, Inc. 64 E. Walnut St. Westerville. Ohio 43081
9. I. M. Khalatnikov, An Introduction to the Theory of Superfluidity, (W.A Benjamin, Inc. , New York, 1965)
10. J. Wilks, The Properties of Liquid and Solid Helium, (Clarendon, Oxford, 1967) pg 44
- 11 I. M. Khalatnikov, An Introduction to the Theory of Superfluidity, (W.A Benjamin, Inc. , New York, 1965)Pg 12,13
- 12 J. Wilks, The Properties of Liquid and Solid Helium, (Clarendon, Oxford, 1967) p.111 & 196
13. F.A. Stass & A.P. Severijns, "Vorticity in He II and its application in a cooling device", Cryogenics **9**, 422 (1969)
14. R. Radebaugh, "A review of pulse tube refrigeration", Adv. Cryogenic Eng. **35**, 1191 (Plenum, NY, 1990)

GRADED AND NONGRADED REGENERATOR PERFORMANCE*

W. Rawlins and K. D. Timmerhaus
University of Colorado
Department of Chemical Engineering
Boulder, Colorado

R. Radebaugh, J. Gary, and P. Bradley
National Institute of Standards and Technology
Boulder, Colorado

ABSTRACT

A method to measure regenerator performance, in situ, in an orifice pulse tube refrigerator has been successfully developed. This was accomplished by inserting two, 2 mm long, tungsten wires with diameters of 4 μ m perpendicular to the fluid flow at the cold end of the regenerator. One wire, used as a resistance thermometer, measured temperature fluctuations and the other, used as a constant temperature anemometer, measured mass flow rates. The dynamic measurement of temperature and mass flow rates at the cold end of the regenerator permitted calculation of the ineffectiveness of the regenerator. This paper compares the performance between two different regenerators constructed from stainless steel mesh: one with a graded mesh (where three different mesh sizes are used for the matrix material) and another with a single mesh size throughout. Both experimental and numerical model results are presented. The numerical model indicated that there was only a very slight advantage to using a graded mesh in a regenerator, whereas experiments showed the graded mesh regenerator to have a slightly higher ineffectiveness.

INTRODUCTION

The orifice pulse tube refrigerator (OPTR) uses a variation of the Stirling cycle. The OPTR, unlike the Stirling refrigerator, has no moving displacer and thus has promise of

*Research sponsored by NASA/Ames Research Center. Contribution of NIST not subject to copyright.

greater dependability. The main disadvantage of the OPTR is that, for the same refrigeration power of a Stirling refrigerator, higher mass flow rates are required. Since higher mass flow rates usually degrade regenerator performance, it is necessary to construct regenerators having a high effectiveness, defined as

$$\epsilon = \frac{\dot{Q}_{act}}{\dot{Q}_{max}} = \frac{\text{actual heat transfer rate}}{\text{maximum possible heat transfer rate}} \quad (1)$$

Since regenerators in cryocoolers generally have an effectiveness greater than 95%, it is convenient to define a term specifying the ineffectiveness as

$$\lambda = 1 - \epsilon = \frac{\dot{Q}_{max} - \dot{Q}_{act}}{\dot{Q}_{max}} = \frac{\dot{Q}_{reg}}{\dot{Q}_{max}}, \quad (2)$$

where \dot{Q}_{reg} represents the heat load on the cold end of the refrigerator. Rawlins et al.¹ showed that the ineffectiveness of a regenerator in oscillating systems such as the OPTR can be expressed as

$$\lambda = \frac{\oint \dot{m} T dt}{m \Delta T} = \frac{\dot{Q}_{reg}}{f C_p m \Delta T}, \quad (3)$$

where \dot{m} is the mass flow rate, T the temperature (both measured at the cold end of the regenerator), f the frequency of oscillation, C_p the heat capacity at constant pressure, and t the time. It is convenient to reference ineffectiveness measurements to the cold end of the refrigerator; therefore, m represents the total mass which flows through the cold end of the regenerator in one half cycle. The difference between the average temperatures at the hot and cold ends of the regenerator is defined as ΔT .

In the past it has not been possible to measure regenerator ineffectiveness using Eq. (3) since this requires nearly instantaneous measurement of both the gas mass flow rate and gas temperature. To evaluate regenerator losses, investigators in the past have devised other less direct methods to measure regenerator ineffectiveness.^{2,3} A method has now been developed to make these instantaneous measurements which introduces a relatively small void volume, pressure drop, or flow disturbance at the cold end of the regenerator.⁴ Measurements have also been made of the mass flow rates and temperatures at the warm

ends of both the pulse tube and the regenerator. A literature search reveals that this is the first time such measurements have been made, allowing the performance of a regenerator to be evaluated during OPTR operation. These experimental measurements were compared to a numerical model developed at NIST called REGEN 3.1.

Graded mesh regenerators are often used in cryocoolers (i.e., coarse or more open meshes at the warm end graduating to finer meshes at the cold end, see Fig. 1) rather than

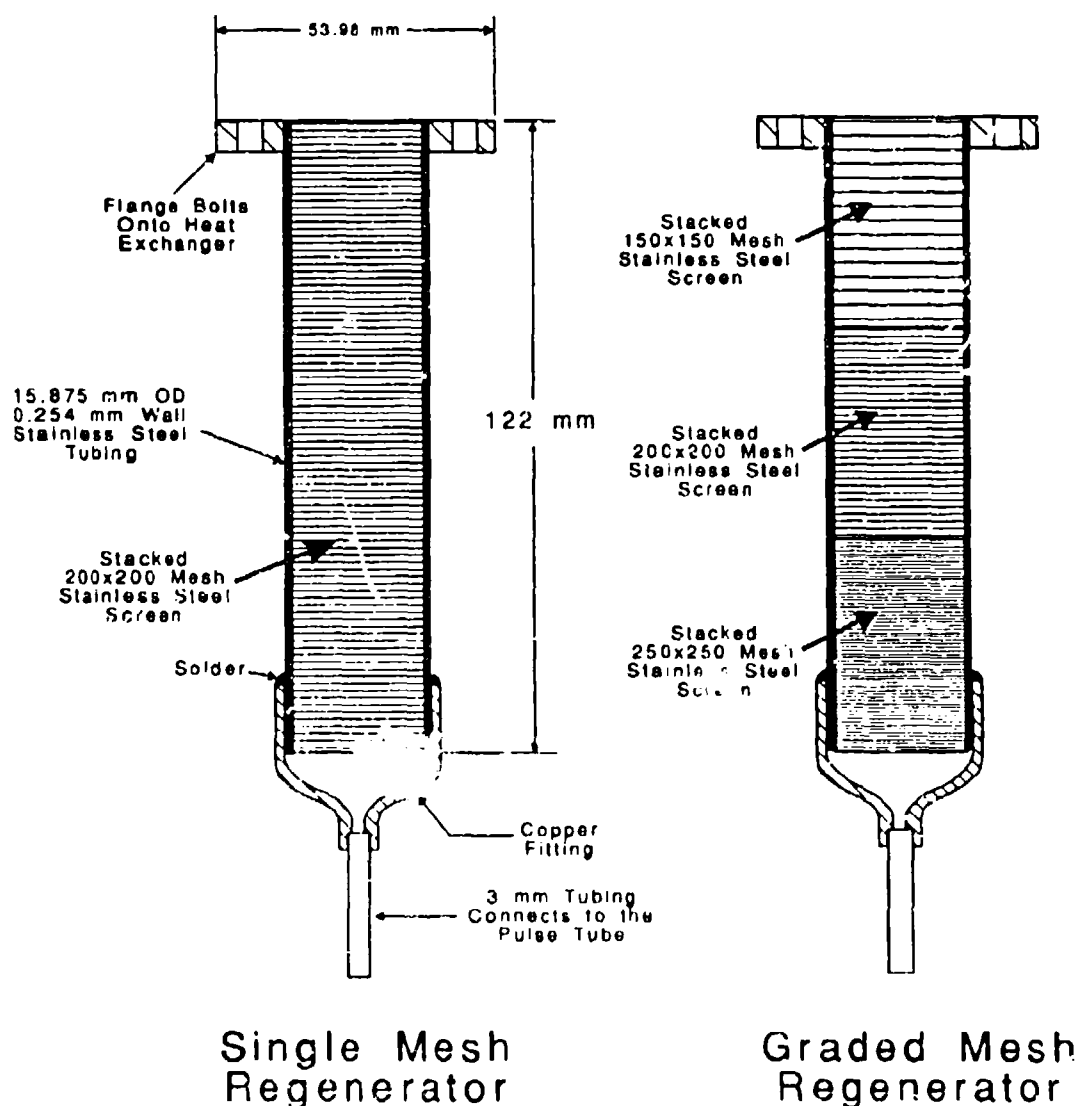


Fig. 1 Schematic of the graded and nongraded mesh regenerators.

a single mesh of intermediate size. The graded configuration should maintain the same overall available heat transfer area as in the single mesh regenerator but, due to the higher viscosity at the warm end and the lower viscosity at the cold end of the gas, the pressure drop in the regenerator should be reduced. A numerical model was first used to test this hypothesis and then two regenerators were constructed to experimentally test the two configurations. The comparison was made between two regenerators constructed from stainless steel tubing with an inner diameter of 15.4 mm, a length of 0.122 m, and a wall thickness of 0.25 mm, filled with the stacked stainless steel mesh. The first third of the graded mesh regenerator, starting at the cold end, was filled with 250x250 mesh screen. The middle third was filled with 200x200 mesh screen, and the last third or warm end, with 150x150 mesh screen. The mesh designation is not a S.I. unit but is a standard industry designation of the number of wire strands used per inch in the horizontal and vertical directions to fabricate the mesh screen. The wire diameters used to form the 250x250, 200x200, and 150x150 mesh screens were 40.64 μm , 53.34 μm , and 66.04 μm , respectively. The second regenerator was filled entirely with 200 mesh screen. The porosity of both regenerators was 0.65. The total surface area available for heat transfer in the graded and nongraded regenerators was approximately equivalent at 0.6193 and 0.5966 m^2 , respectively,

NUMERICAL MODEL

The numerical model used for the regenerator evaluation was developed at NIST by Gary and Radebaugh.⁵ This model assumes sinusoidal fluctuations in the mass flow rates at the warm and cold end regenerator boundaries. The results from this model for the two regenerators are compared in Figure 2. In this figure the ineffectiveness of the regenerator is plotted as a function of the average mass flow rate at the cold end of the regenerator. The model predicts a slightly lower ineffectiveness for the graded regenerator. The average value for the ineffectiveness computed by the model for the graded regenerator was 0.005 66 and for the single mesh regenerator 0.005 96, with standard deviations of 0.000 09 and 0.000 23, respectively, indicating little difference between the predicted performance of the two regenerators.

EXPERIMENTAL MEASUREMENTS

The mass flow rate was measured at the cold end of the regenerator using a technique called constant temperature anemometry (CTA)⁶ and the temperature was

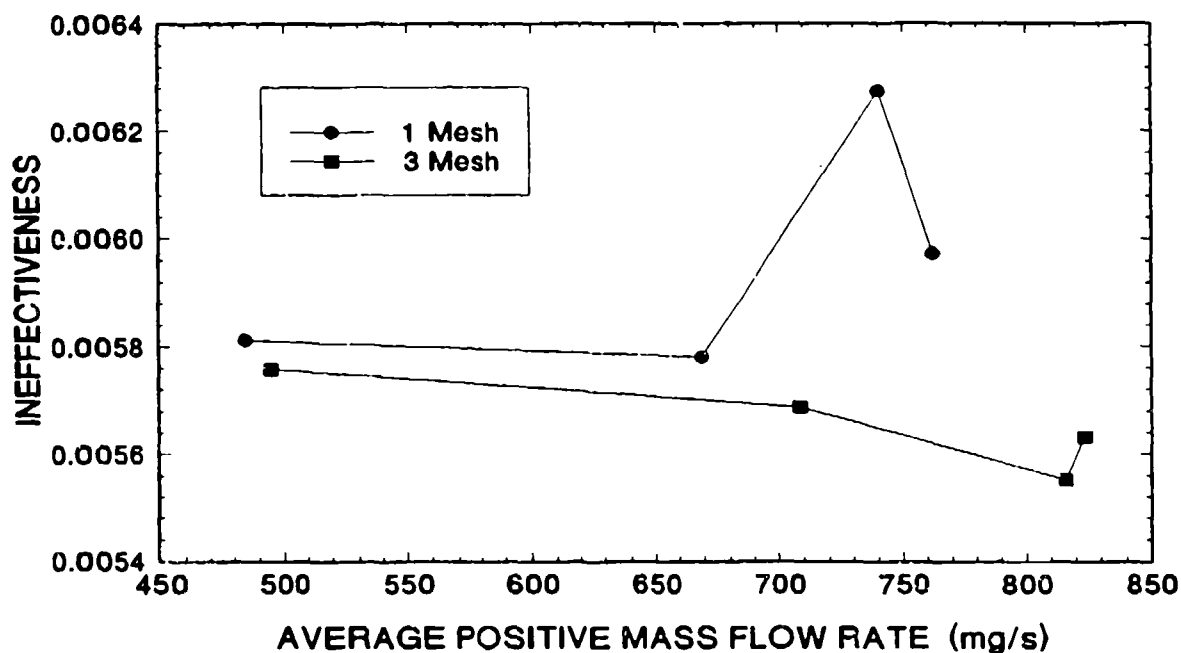


Figure 2 Comparison of the ineffectiveness of the graded and nongraded mesh regenerators from the numerical model as a function of the average mass flow rate at the cold end of the regenerator.

evaluated using a resistance temperature detector (RTD). Both sensors were constructed using a 2 mm length of tungsten wire with a diameter of 3.8 μm supported by two needles. These wires were inserted, with their lengths perpendicular to the fluid flow, inside the 3 mm tubing between the cold end of the regenerator and the pulse tube. The responses of the CTA and the RTD were approximately 20 μs and 260 μs , respectively; these were adequate to resolve the oscillating mass flow rates and temperatures at 30 Hz. Both regenerators were operated at similar frequencies, pressures, and orifice turns in the OPTR. Figure 3 shows an example of the mass flow rates calculated from the voltage outputs of the CTAs at the warm and cold ends of the regenerator and the warm end of the pulse tube. The temperature fluctuations calculated from measurements from the RTD at the cold end of the regenerator are shown in Fig. 4. The results displayed in Figs. 3 and 4 are from the same experimental run for the single mesh regenerator operated at 14.61 Hz and 3.5 orifice turns.

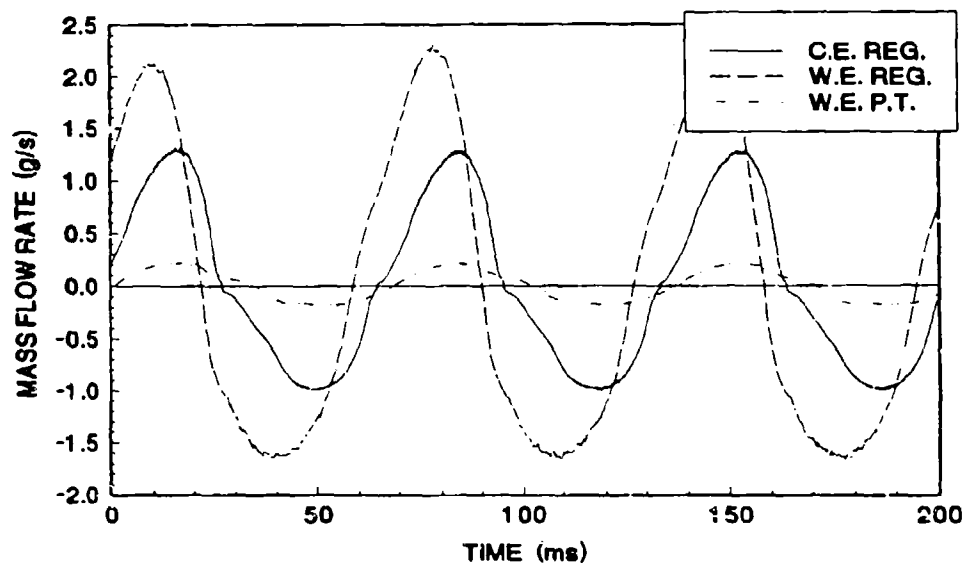


Figure 3 Experimentally determined mass flow rates in the OPTR at 14.61 Hz for the single mesh regenerator using the CTA voltage output.

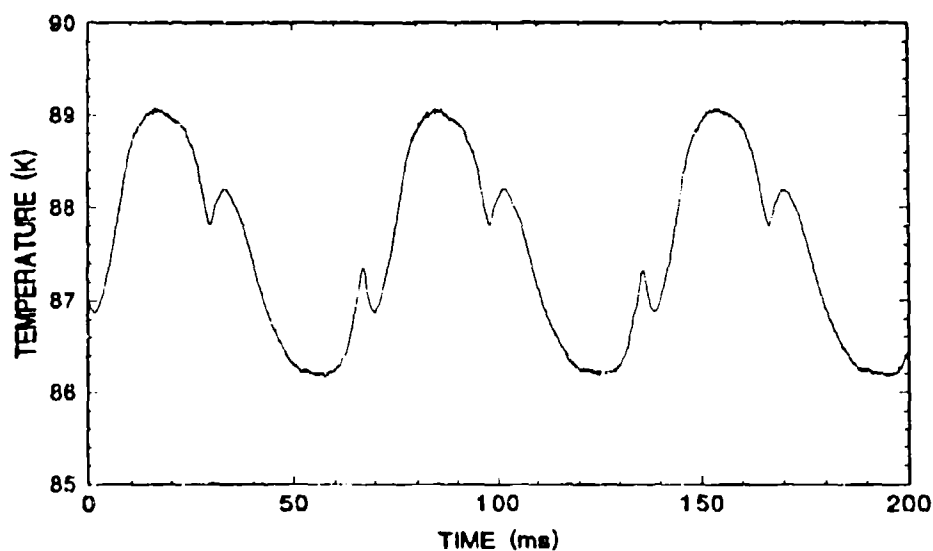


Figure 4 Experimentally determined temperature fluctuations as measured by the RTD at the cold end of the single mesh regenerator with the OPTR operated at 14.61 Hz.

The results of the measurements for the graded and nongraded regenerator are shown in Tables 1 and 2, respectively. The row labeled orifice openings represents the number of full turns the needle valve was opened between the reservoir volume and the warm end of the pulse tube (0 represents a totally closed orifice). The abbreviations REG. and P.T. represent the regenerator and pulse tube, respectively, W.E. and C.E. identify the warm and cold ends, respectively, and the direction of the gas flow is indicated by '-' and '+' representing gas flow towards and away from the compressor, respectively. The ratio P_{MAX}/P_{MIN} is the maximum pressure divided by the minimum pressure measured in the pulse tube, $\langle P \rangle$ the average pressure, and $\langle \Delta P \rangle / \langle P \rangle$ the average pressure drop in the regenerator divided by the average pressure. The total mass flowing past the CTAs in a half cycle is the 1/2 Cycle Mass and $\langle \dot{m} \rangle$ is the average mass flow rate in a half cycle. The nonsinusoidal behavior of the mass flow rates resulted in the average mass flow rates not being equivalent in both flow directions (see Fig. 2). The total mass flowing through the

Table 1 Experimental results for the graded mesh regenerator.

Frequency (Hz)	10.07	15.27	15.00	20.07	24.25
Orifice Openings	2	3.5	3.5	6	6
P_{MAX}/P_{MIN} @ P.T.	1.2113	1.1677	1.1766	1.1344	1.1213
$\langle P \rangle$ (MPa)	2.0765	2.1407	2.1200	2.1501	2.1599
$\% \langle \Delta P \rangle / \langle P \rangle$	1.82	2.80	2.71	3.40	3.58
1/2 Cycle Mass @ W.E. REG. (g)	0.04914	0.04496	0.04475	0.03842	0.03432
1/2 Cycle Mass @ C.E. REG. (g)	0.02455	0.02320	0.02258	0.02033	0.01699
1/2 Cycle Mass @ W.E. P.T. (g)	0.00392	0.00411	0.00349	0.00430	0.00366
$-\langle \dot{m} \rangle$ @ W.E. REG. (g/s)	-0.96131	-1.27431	-1.24645	-1.40587	-1.49859
$\langle \dot{m} \rangle$ @ W.E. REG. (g/s)	1.04545	1.49044	1.45599	1.70758	1.85058
$-\langle \dot{m} \rangle$ @ C.E. REG. (g/s)	-0.45582	-0.63843	-0.61151	-0.73504	-0.74298
$\langle \dot{m} \rangle$ @ C.E. REG. (g/s)	0.54005	0.79576	0.75840	0.91748	0.92501
$\langle T \rangle$ @ W.E. REG.: CTA off (K)	296.77	298.92	298.16	301.46	304.07
T_{code} @ C.E. P.T. (K)	90.92	88.53	89.26	92.83	95.20
$\langle T \rangle$ @ C.E. REG.: CTA off (K)	91.32	89.02	88.89	93.67	95.96
\dot{Q}_{reg} (W)	2.8336	3.9082	3.8165	4.4575	4.5537
λ	0.01093	0.01038	0.01060	0.01050	0.01073

Table 2 Experimental results for the single mesh regenerator.

Frequency (Hz)	9.93	10.12	14.61	19.36	24.47
Orifice Openings	2	2	3.5	6	6
P_{MAX}/P_{MIN} @ P.T.	1.2080	1.2076	1.1601	1.1241	1.1149
$\langle P \rangle$ (MPa)	2.0385	2.0943	2.0917	2.0432	2.0577
$\% \langle \Delta P \rangle / \langle P \rangle$	1.88	1.99	2.91	3.71	3.91
1/2 Cycle Mass @ W.E. REG. (g)	0.04789	0.04785	0.04340	0.03523	0.03014
1/2 Cycle Mass @ C.E. REG. (g)	0.02332	0.02394	0.02290	0.01968	0.01513
1/2 Cycle Mass @ W.E. P.T. (g)	0.00361	0.00367	0.00438	0.00472	0.00352
$-\langle \dot{m} \rangle$ @ W.E. REG. (g/s)	-0.90588	-0.92266	-1.17856	-1.24184	-1.33577
$\langle \dot{m} \rangle$ @ W.E. REG. (g/s)	1.00469	1.02423	1.38112	1.151121	1.65368
$-\langle \dot{m} \rangle$ @ C.E. REG. (g/s)	-0.42580	-0.44730	-0.60229	-0.68802	-0.66638
$\langle \dot{m} \rangle$ @ C.E. REG. (g/s)	0.50297	0.52911	0.75277	0.85410	0.83286
$\langle T \rangle$ @ W.E. REG.: CTA off (K)	296.86	296.79	298.69	301.41	304.26
T_{DIODE} @ C.E. P.T. (K)	90.56	89.99	88.45	94.74	98.50
$\langle T \rangle$ @ C.E. REG.: CTA off (K)	89.37	89.31	87.54	93.72	97.98
\dot{Q}_{reg} (W)	2.3520	2.3619	3.2446	3.4428	3.5092
λ	0.00980	0.00935	0.00923	0.00885	0.00947

cold end of the regenerator for each half cycle though balanced within 1.0% and 1.6% for the graded and nongraded mesh regenerators, respectively, calculated from the experimental data utilizing the CTA and RTD at the cold end of the regenerator. Thus, it is believed that the accuracy of the mass flow measurements is better than 2%. T_{DIODE} is an average temperature as measured by a diode thermometer and $\langle T \rangle$ is the RTD measured temperature averaged over one complete cycle. The time-averaged enthalpy flux measured at the cold end of the regenerator is \dot{Q}_{reg} while λ is the regenerator ineffectiveness calculated using Eq. (3).

Figures 5 and 6 compare the experimentally determined ineffectiveness and enthalpy flux of the single and graded mesh regenerators as a function of the average mass flow rate at the cold end of the regenerator for flow in the positive direction (this is defined as flow leaving the cold end of the regenerator). It appears that in both regenerators the

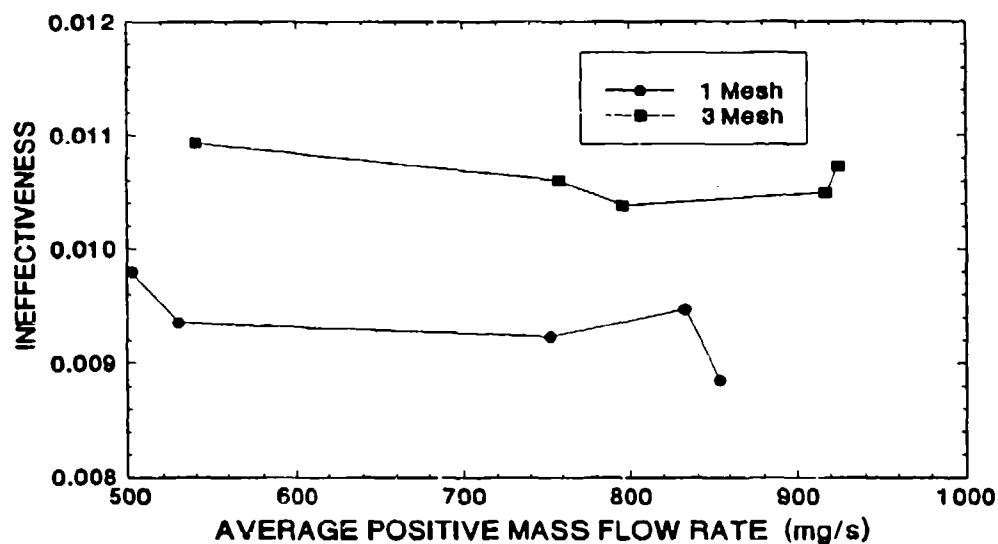


Figure 5 Comparison of the experimentally determined ineffectiveness as a function of the average mass flow rate at the cold end of the regenerator for the two regenerators.

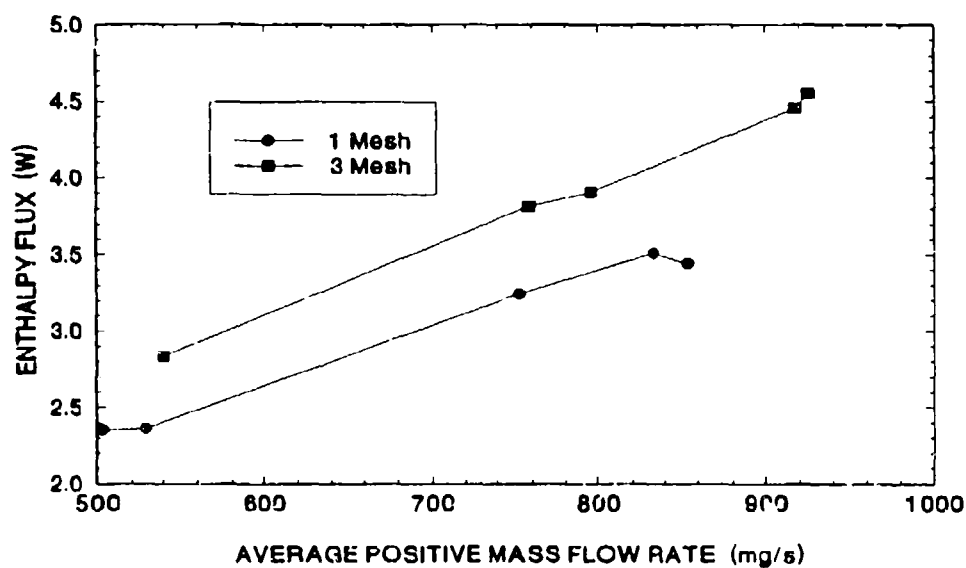


Figure 6 Comparison of the experimentally determined enthalpy flux as a function of the average mass flow rate at the cold end of the regenerator.

ineffectiveness remains approximately constant; therefore, regenerator performance did not show signs of degradation. The average values of the ineffectiveness in the graded and single mesh regenerators were 0.010 63 and 0.009 34, respectively, with standard deviations of 0.000 189 and 0.000 310, respectively. The difference of the experimentally measured ineffectivenesses of the two regenerators is statistically significant, therefore, experimentally, the performance of the single mesh regenerator was approximately 12% better than the graded regenerator.

The average pressure drop in the regenerator divided by the average pressure in the OPTR is plotted in Fig. 7 as a function of the average mass flow rate in the positive direction at the cold end of the regenerator. The experimental results show that this ratio was less for the graded mesh regenerator than for the single mesh regenerator. This resulted in higher pressure ratios in the pulse tube for the OPTR using the graded mesh regenerator as shown in Fig. 8. Higher pressure ratios in the pulse tube should theoretically increase the refrigeration power of the refrigerator. Except for the experimental run at 24.47 Hz, the average temperatures in Tables 1 and 2, as measured by the diode thermometer at the cold end of the pulse tube, are approximately equal for both regenerators. It would appear that any potential gains in refrigeration power were reduced by the additional heat losses in the graded regenerator due to the larger regenerator ineffectiveness.

At 24.47 Hz the temperature at the cold end of the pulse tube is significantly higher for the single mesh regenerator. This possibly indicates that there may be a cross-over point in the optimal choice between the two regenerators for an OPTR. When the average positive mass flow rates at 19.36 and 24.47 Hz are compared for the single mesh regenerator, the mass flow rate at the warm end is greater at 24.47 Hz, as expected. At the cold end of the regenerator though, the reverse is unexpectedly true. The graded mesh regenerator demonstrates the expected trends for the mass flow rate at both ends of the regenerator. For the single mesh regenerator the increase in the ratio of the average pressure drop in the regenerator to the average pressure in the OPTR results in a decrease in the pressure ratio in the pulse tube. It appears that at approximately 25 Hz the pressure drop in the regenerator becomes large enough to decrease refrigerator performance due to the resulting lower pressure ratios in the pulse tube. The 0.33% increase in the pressure drop in the single mesh regenerator over the graded regenerator may appear insignificant until the relative pressure amplitudes (defined as the pressure amplitude in the pulse tube divided by the average pressure) are compared. These relative pressure amplitudes for the

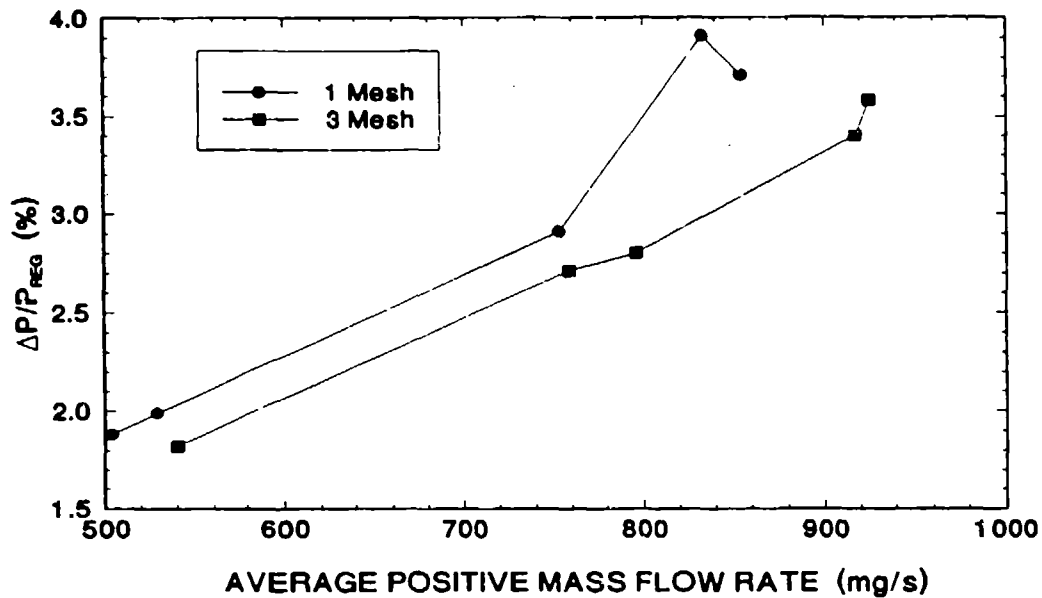


Figure 7 Comparison of the experimentally determined pressure drop as functions of the average mass flow rate at the cold end of the regenerator.

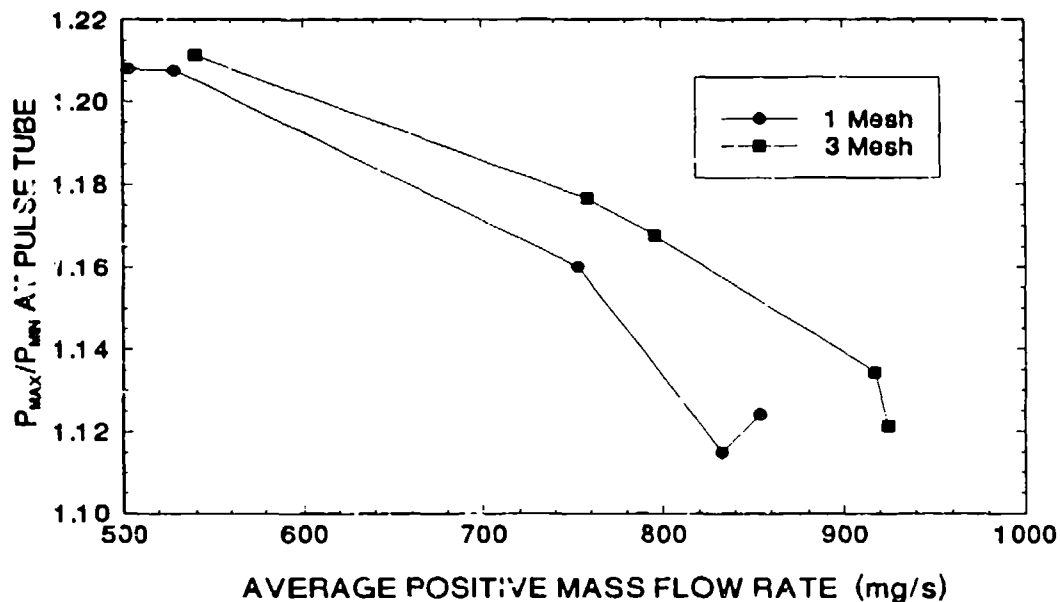


Figure 8 Comparison of the experimentally determined pressure ratio as functions of the average mass flow rate at the cold end of the regenerator.

25 Hz experimental runs were only 5.7% and 5.4% in the graded and nongraded regenerators, respectively, thus, the 0.33% increase in the pressure drop represents a significant percentage of the available pressure amplitude at these low pressure ratios. With higher pressure ratios the pressure drop would become less significant and have less effect on refrigerator performance. Therefore, at higher frequencies and low pressure ratios, the graded mesh regenerator yields a higher refrigerator performance in spite of having a larger ineffectiveness value. In the single mesh regenerator the pressure drop could be decreased by making the regenerator shorter, but this would increase the ineffectiveness and conduction losses of the regenerator.

CONCLUSIONS

It appears that any advantages gained by the lower pressure drops obtained in the graded mesh regenerator are decreased by the 12% higher ineffectiveness of this regenerator when compared with the single mesh regenerator. However, at least for low pressure ratios, there appears to be a cross-over point between the two regenerators where the graded mesh regenerator provides an improved overall refrigerator performance. The numerical model indicates no significant differences between the two regenerators at all frequencies. The numerical model also underestimates the regenerator ineffectiveness by about 40%. This is due to several factors: the mass flow rate not being sinusoidal, possible inaccuracies in the correlations used for calculating heat transfer and pressure drops, and the phase relationships between the pressure and mass flow rate oscillations used in the model. The newly developed method for measuring instantaneous gas temperature and mass flow rates will help in developing a better numerical model since for the first time actual mass flow rates and temperatures in an oscillating system can be measured with reasonable certainty.

REFERENCES

1. Rawlins, W. and Radebaugh, R., "An Apparatus for the Measurement of Regenerator Performance in Pulse Tube Refrigerators," Adv. in Cryo. Eng., Vol 35, Plenum Press, New York, 1990, p. 1213.
2. Radebaugh, R., Linenberger, D. and Voth, R.D., "Methods for the Measurement of Regenerator Ineffectiveness," Refrigeration for Cryogenic Sensors and Electronics

Systems, NBS special publication 607, 1981, p. 70.

3. Nomaguchi, T. et. al., "Determination of the Regenerator Effectiveness of an Actual Stirling Engine," Proc. ASME-JSME Thermal Eng. Conf., 1983, p. 193.
4. Rawlins, W., Measurement and Modeling of Regenerator Performance in an Orifice Pulse Tube Refrigerator, PhD. Thesis, University of Colorado, Dept. of Chem. Eng., 1992.
5. Gary, J. and Radebaugh, R., "A Computational Model for a Regenerator," NBS Special Publication 698, 1985, p. 199.
6. Perry, A. E., Hot Wire Anemometry, Clarendon Press Oxford, 1982.

**SPECIFIC HEAT DESIGN AND PROPOSAL OF
A NEW CUBIC TYPE MAGNETIC MATERIAL
FOR A REGENERATOR MATRIX**

Yoichi Tokai, Akiko Takahashi and Masashi Sahashi
Toshiba R&D Center
1 Komukai-Toshiba, Saiwai, Kawasaki 210, Japan

Takasu Hashimoto
Department of Applied Physics
Tokyo Institute of Technology
2-12-1 Oh-okayama, Meguro, Tokyo 152, Japan

ABSTRACT

The specific heats of three types of Er-Ni compounds, Er_3Ni , ErNi , and ErNi_2 , were analyzed to establish guiding principle of specific heat design. The energy difference between of the ground state and of first excited state, and the ratio of the energy difference to exchange interaction were found to be very important factor for specific heat design in cryogenic temperature, in addition to magnetic ion density, weak exchange interaction and high fold-degeneracy of ground state of magnetic ion.

Regenerator efficiencies were calculated for three combined matrix of one of model materials and Er_3Ni , as a function of the ratio of the model material to the regenerator matrix. The ordering temperatures of the model materials were 3K, 4.5K and 6K, respectively. The model material of 4.5K showed the highest efficiency in the calculation.

A new cubic type magnetic material of rare-earth aluminum carbon compound R_3AlC system is proposed as cascade type regenerator matrix. The magnetic ordering temperature is in proportion to de Gennes factor. Very low magnetic ordering temperature of 3K was observed in Er_3AlC .

INTRODUCTION

The demand for small, highly efficient, and economical refrigerators has become greater in a recent cryogenic engineering. Large specific heat materials are required in order to improve the refrigeration capacity of these refrigerators.

The authors have already proposed rare-earth transition metal compounds, such as Er_3Ni and ErNi , as a regenerator matrix which have a larger specific heat than lead below 15 K.¹⁾ Refrigeration capacity was remarkably improved by replacing Pb with Er_3Ni .²⁾ The 3 K lowest temperature and the 0.28 W refrigeration capacity at 4.2 K were achieved in a two-stage GM refrigerator.³⁾

Cryogenic system needs larger refrigeration capacity at 4K. However, the specific heat of Er_3Ni and ErNi is still smaller than compressed helium below 6 K to obtain larger refrigeration capacity. A GM refrigerator needs larger specific heat for regenerator matrix at 4 K.

The authors have investigated the specific heats of Er-Ni compounds in detail to establish the way to find such a material.

In this paper, important factors to specific heat design for regenerator material with large specific heat and new materials, Er_3AlC and Ho_3AlC are proposed.

SPECIFIC HEAT ANALYSIS FOR Er-Ni COMPOUNDS

At the start of investigating regenerator materials, the authors paid attention to a weak exchange interaction for a lower magnetic ordering temperature below 15 K, a higher rare-earth ion density for a large magnetic specific heat, and a larger magnetic quantum number of the rare-earth for a large magnetic entropy, to realize a large specific heat than Pb in the temperature range below 15 K.

Figure 1 shows the specific heats of Er-Ni compounds. A higher Er density increases the specific heat in the high temperature range ($> 15\text{K}$), and a weak interaction is the

cause of low ordering temperatures same as or below 10 K.

To clarify the origin of magnetic specific heat, the lattice part of the specific heats were estimated from specific heat data of non magnetic rare-earth transition compounds.

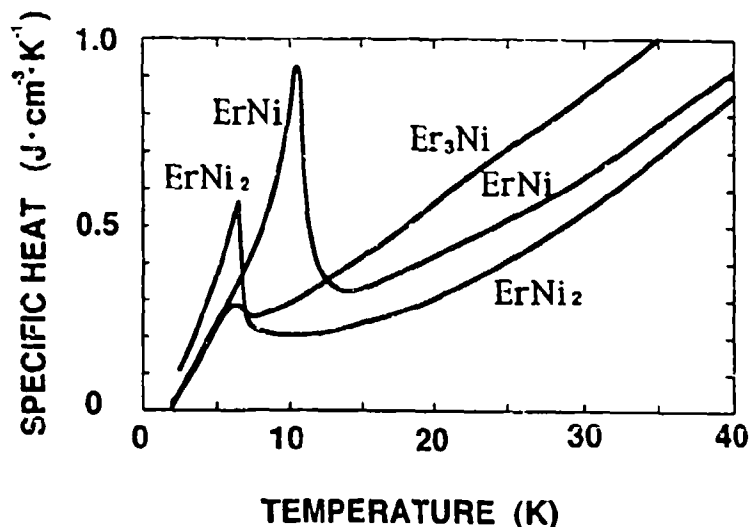


Fig.1 Specific heats of Er_3Ni , ErNi and ErNi_2

Figure 2 shows the specific heat of Er_3Ni and the lattice part of specific heat. Er_3Ni has the largest lattice specific heat due to the low Debye temperature near 150 K and a largest magnetic specific heat in high temperature range among Er-Ni compounds.⁴⁾

Figure 3 shows the magnetic part of specific heat and a calculated Schottky anomaly in 2 level approximation, comparing Er_3Ni ⁴⁾ with ErNi_2 ⁵⁾. The magnetic specific heat at lower temperatures than the ordering temperature is due to magnetic ordering, and that at higher temperature is due to Schottky anomaly.

Er_3Ni has a larger magnetic specific heat and Schottky anomaly than ErNi_2 above 7 K. This corresponds mainly to the 40 % larger value of Er density and a larger energy difference between two energy levels than ErNi_2 .

Below 7 K, however, Er_3Ni has a smaller magnetic ordering

specific heat. It is considered that the fold-degeneracy number of the 4f electron ground state is 2 for Er_3Ni and 4 for ErNi_2 . Er_3Ni has a smaller fold-degeneracy number than ErNi_2 .

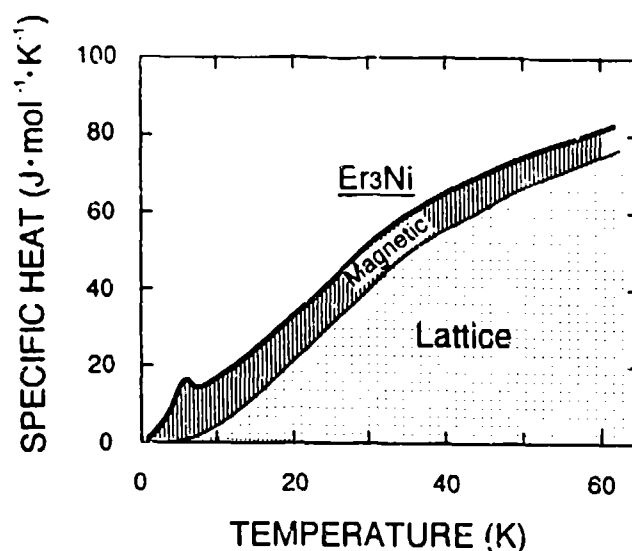


Fig.2 Specific heats of Er_3Ni and its lattice heat

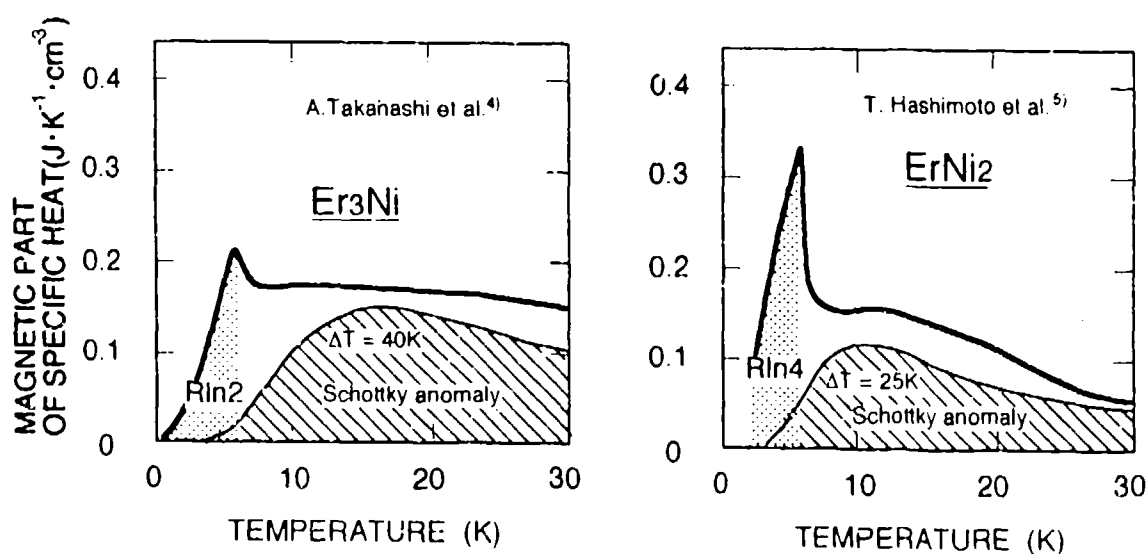


Fig.3 Magnetic part of specific heat and Schottky anomaly

Figure 4 shows the entropy of ErNi. ErNi has an orthorhombic symmetry, the same as Er_2Ni . The ground state should be a 2-fold ground state in this compound, but the entropy of ErNi showed a 4-fold ground state in magnitude.

To explain the result, it is considered that ErNi had a 2-fold ground state close to a 2-fold 1st excited state and the energy gap was as small as the exchange interaction so that the appearance degeneracy was 4-fold.

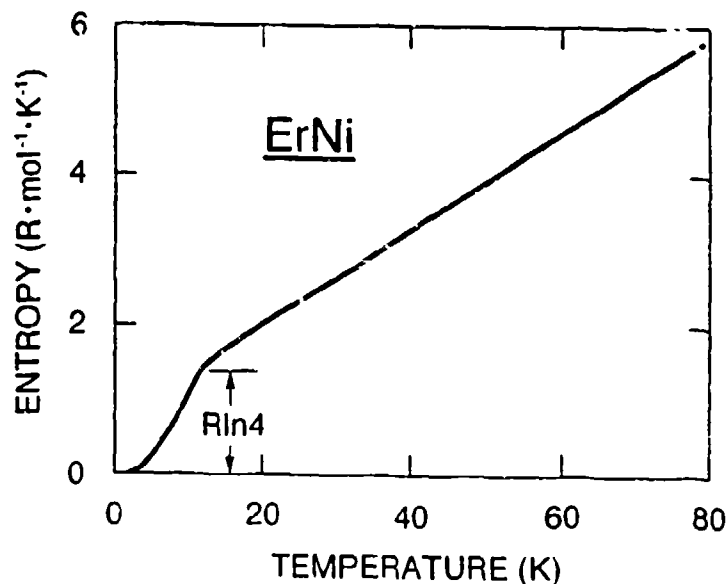


Fig.4 Entropy of ErNi

These results show that the energy difference between a ground state and 1st excited state and the ratio of the energy difference to exchange interaction are important factors to obtain large magnetic specific heat, in addition to magnetic ion density, weak exchange interaction and high fold-degeneracy of ground state for magnetic ion.

REGENERATOR SIMULATION

The effects of combining a magnetic material with λ type specific heat with Er_2Ni on obtaining higher regenerator

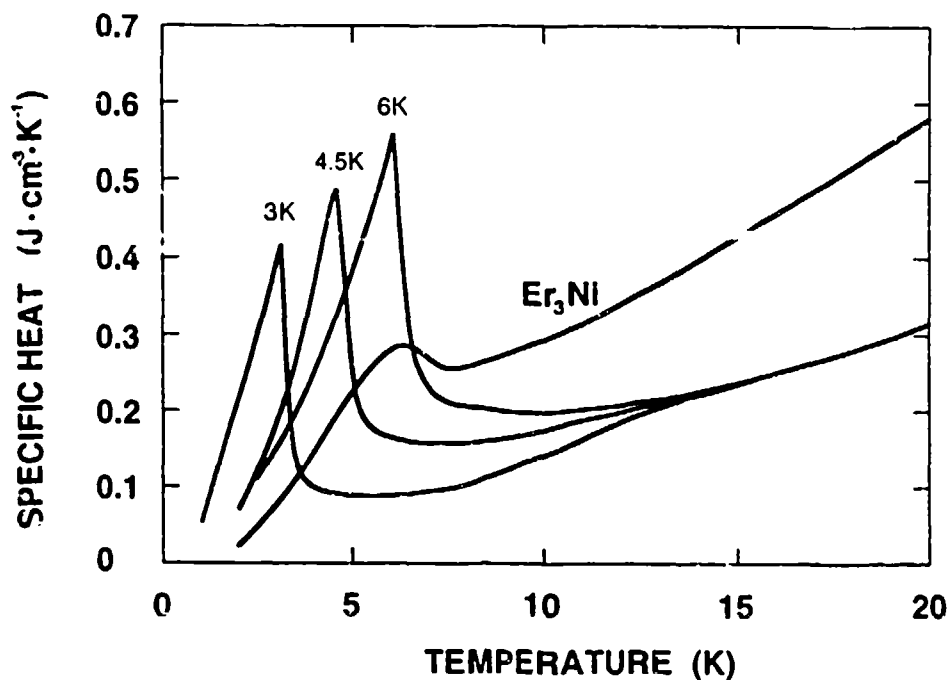


Fig.5 Specific heats of model materials for simulation

efficiency has been shown by Seshake and Hashimoto et al., in a simulation using RNi_2 data.⁶⁾

The authors carried out a simulation, in the same way, using model materials which have λ type specific heats, as shown in figure 5, with ordering temperatures 3 K, 4.5 K, and 6 K, respectively.

Figure 6 shows the simulation conditions. The regenerator efficiencies (η) were obtained as a function of the volume ratio (k) of the model material to the regenerator matrix.

Figure 7 shows the result of the simulation for 4 K refrigeration. The material with the 4.5 K ordering temperature gave the largest efficiency.

This result suggests that we should employ a material with the ordering temperature close to the cooling temperature, in combination with Er_3Ni .

Regenerator simulation

Regenerator efficiency (η)

$$\eta = \frac{\Delta H_{\text{real}}}{\Delta H_{\text{ideal}}}$$

Governing equations

$$\frac{\partial H_g}{\partial x} = \frac{hA_w}{m} (T_s - T_g)$$

$$\frac{\partial H_s}{\partial t} = \frac{hA_w L \tau}{V_s} (T_g - T_s)$$

derived by Rios and Smith

T_g : gas temperature

T_s : regenerator matrix temperature

H_g : gas enthalpy

H_s : volumetric matrix enthalpy

h : heat transfer coefficient

A_w : heat transfer area per unit length

V_s : regenerator matrix volume 52.3 cm³

L : regenerator length 85 mm

m : mass flow rate for gas 1.6 g/s

τ : half-cycle period 0.5 s

x : distance from regenerator inlet point

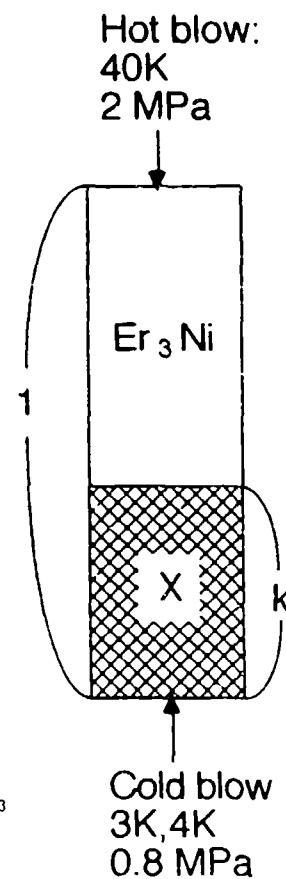


Fig.6 Simulation conditions

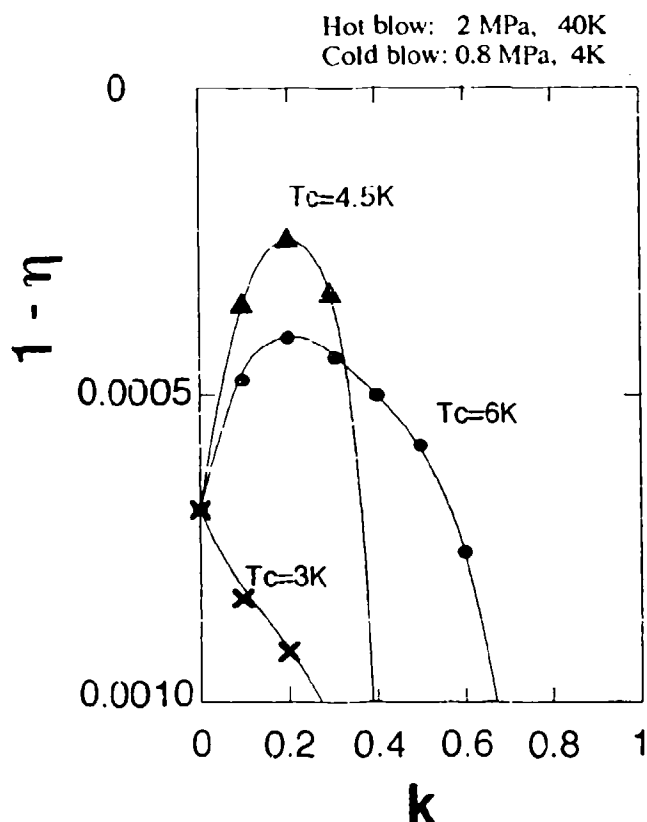


Fig.7 Calculated regenerator efficiency(η) dependance on volume ratio(k) of model material to regenerator matrix

NEW CUBIC TYPE MAGNETIC MATERIAL R_3AlC

The authors investigated high rare-earth density cubic compounds with perovskite structure⁷⁾ in which high magnetic ion density and high fold degeneracy are expected.

The samples of Er_3AlC , Ho_3AlC , and Dy_3AlC were made from 99.9% Er, Ho, Dy, and 99.999% Aluminum and Carbon by arc-melting in Ar gas. They were annealed at 970 K for 1 week. Susceptibilities were measured under alternative magnetic field, 10 Oe, 80 Hz. Specific heats were measured in pulse heating calorimeter.

Figure 8 shows the relation between magnetic ordering temperature and de Gennes factor. Er_3AlC shows a very low magnetic ordering temperature of 3 K.

Figure 9 shows specific heat of Er_3AlC , Ho_3AlC , Er_3Ni and Pb. Er_3AlC had a large specific heat of $0.4 \text{ J} \cdot \text{K}^{-1} \cdot \text{cm}^{-3}$ at 2.8 K.

The temperature was too low to obtain large cooling power at 4 K. A 4.5K magnetic ordering temperature, however, could be obtained in the solid solution of Er_3AlC and Ho_3AlC .

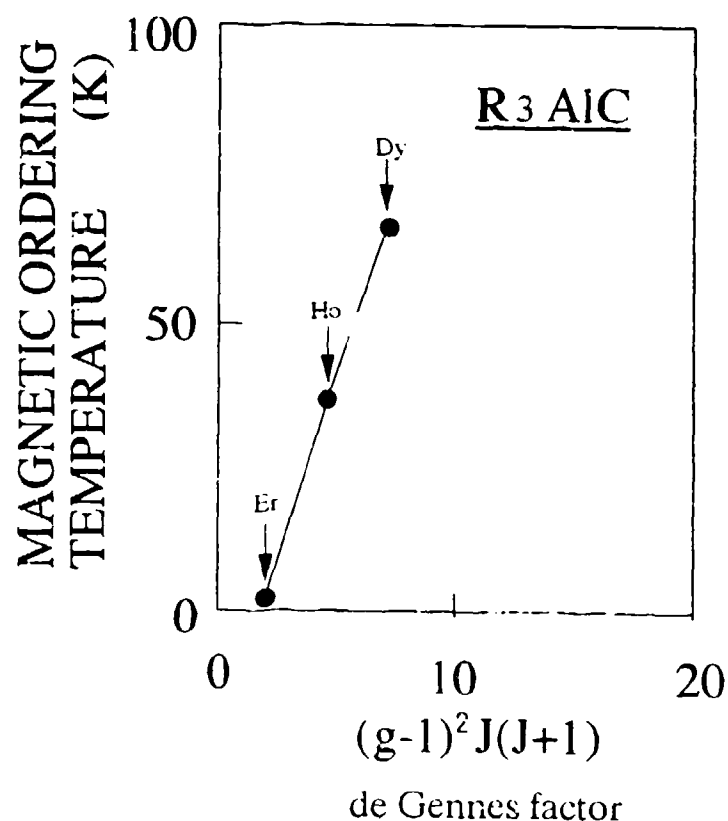


Fig.8. De Gennes factor - magnetic ordering temperature dependence

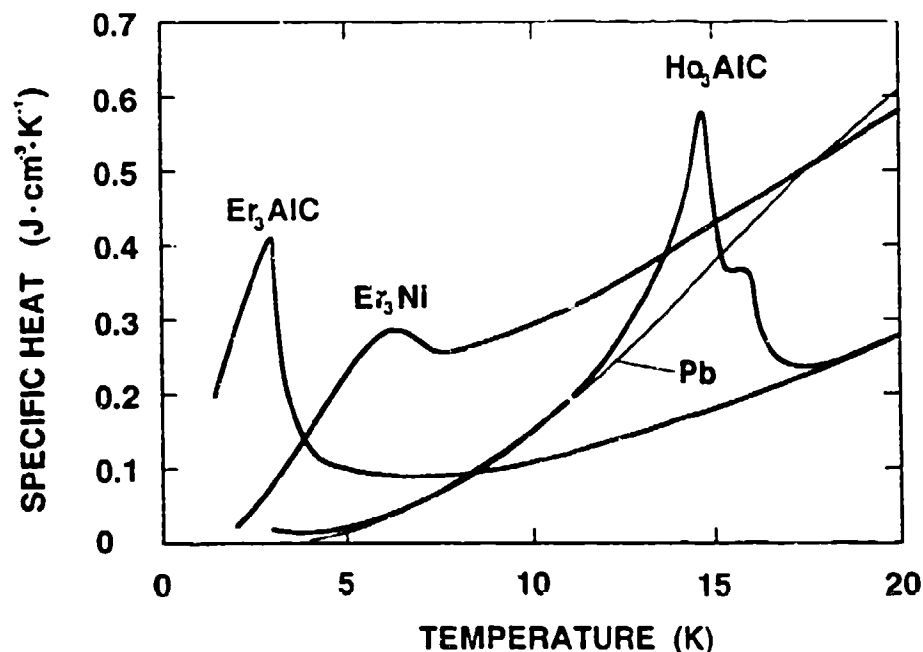


Fig.9. Specific heats of Er_3AlC , Ho_3AlC , Er_3Ni , and Pb

CONCLUSION

The energy difference between ground state and 1st excited state and the ratio between the energy difference and exchange interaction are important factors to obtain large magnetic specific heat, in addition to magnetic ion density, weak exchange interaction and high fold-degeneracy of ground state of magnetic ion.

When we used a magnetic material with λ type specific heat in combination with Er_3Ni , we should employ one with ordering temperature close to cooling temperature.

R_3AlC was found as a hopeful regenerator material for refrigeration at 4K.

Table 1 Properties of Er-Ni compounds

	Er ₃ Ni	ErNi	ErNi ₂
Er ₃ density (mol / l)	49.9	42.6	36.7
Magnetic ordering temperature	6K	12K	6K
Ground state	2-fold	2-fold	4-fold
1st excited state	2-fold	2-fold	4-fold
Energy difference between the states : ΔT	40 K	—	25 K
Magnetic ordering entropy	Rln2	Rln4	Rln4

REFERENCES

- 1) M.Sahashi, Y. Tokai, T. Kuriyama, H. Nakagome, R. Li, M. Ogawa and T. Hashimoto: Adv. Cryog. Eng. 35 (1989) 1175.
- 2) T. Kuriyama, R. Hakamada, H. Nakagome, Y. Tokai, M. Sahashi, R. Li, O. Yoshida, K. Matsumoto and T. Hashimoto: Adv. Cryog. Eng. 35 (1989) 1261.
- 3) T. Kuriyama, M. Takahashi, H. Nakagome, H. Seshake, T. Eda and T. Hashimoto: Proc. 6th Cryocoolers Conf. 1990 (David Taylor Research Center, Bethesda, 1991) 3.
- 4) A. Takahashi, Y. Tokai, M.Sahashi and T. Hashimoto: Japanese Journal of Applied Physics (1993) (to be published).
- 5) T. Hashimoto, M. Ogawa, A. Hayashi, M. Makino, R. Li and K. Aoki: Adv. Cryog. Eng. 37 (1992) 859.
- 6) H. Seshake, T. Eda, K. Matsumoto, T. Hashimoto, T Kuriyama and H. Nakagome: Adv. Cryog. Eng. 37 (1992) 995.
- 7) K. H. J. Buschow and J. H. N. van Vucht: Philips Res. Repts 22 (1967) 233.

A COMPACT 150 GHz SIS RECEIVER COOLED BY 4 K GM REFRIGERATOR

Masahiko Takahashi, Hideo Hatakeyama,
Toru Kuriyama and Hideki Nakagome
Energy and Mechanical Research Laboratories
Toshiba Research and Development Center
Utsunomiya, Kawasaki, Japan

Ryohel Kawabe, Hiroyuki Iwashita, Gerrard McCulloch,
Katsunori Shibata, and Shinji Ukita
Nobeyama Radio Observatory
National Astronomical Observatory
Nobeyama, Nagano, Japan

ABSTRACT

An SIS (Superconductor Insulator Superconductor) mixer is used for the astronomical millimeter radio observation because of its high sensitivity. The SIS mixer, however, must be cooled at the 4 K level, and either liquid helium or a GM+JT refrigerator has been used for a long time.

This paper describes the construction and experimental results of a compact SIS receiver, 720 mm in height, 260 mm in length, 260 mm in width, and 35 kg in weight. The technical point of the receiver was to adopt a 4 K GM (Gifford-McMahon) refrigerator which used Er_3Ni as a regenerator material to cool the SIS mixer.

The cooling temperature of 3.4 K was achieved for the SIS mixer and the cool down time from the room temperature to the 4 K level was 4.5 hours. The power consumption for the compressor unit was 3.3 kW.

This SIS receiver has been installed on the 45 meter antenna at Nobeyama Radio Observatory and used for astronomical observation for more than 3000 hours.

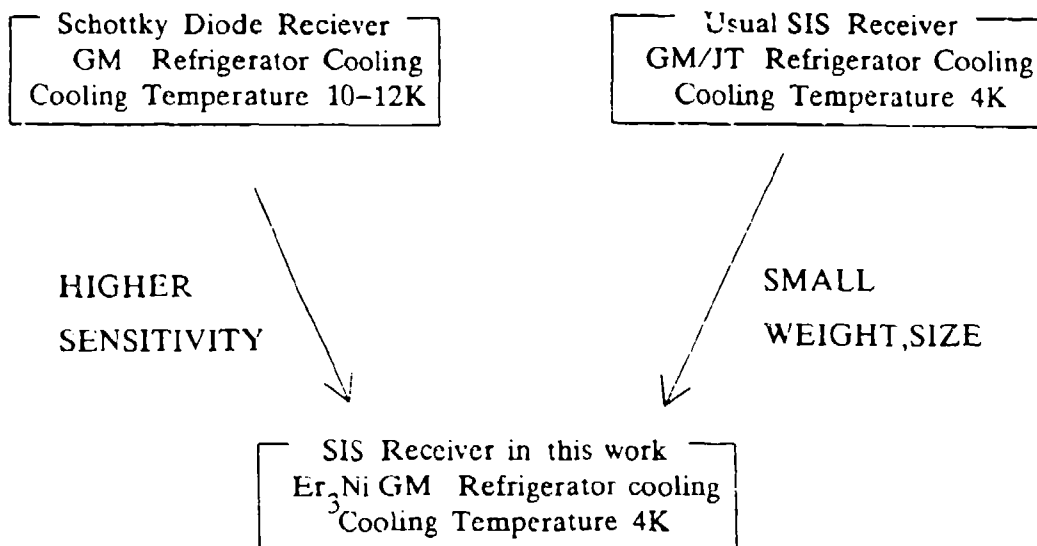
INTRODUCTION

A GM refrigerator has a high reliability because of its simple structure, and reaches a minimum temperature of the 10 K level. It is commercially used as a thermal radiation shield cooler for a magnetic resonance imaging system or as a cryopanel cooler for a cryopump. The cooling temperature of 10 K, however, is not low enough to cool superconducting magnets or devices directly.

In 1989, Kuriyama et al. ⁽¹⁾⁽²⁾ developed the GM refrigerator using Er_3Ni as a regenerator material, which achieved a cooling temperature of the 4 K level. Since then, many experimental results of the GM refrigerator with Er_3Ni or other rare earth regenerator material have been reported (3)-(6).

Meanwhile, in heterodyne receivers for the millimeter wave radio astronomical observation, mixers are cooled to the cryogenic temperature. Two types of non-linear devices are currently the basis of mixers used in heterodyne receivers as shown in Table 1. One is the Schottky diode and the other is the SIS tunnel junction device.

Table 1 Usual millimeter wave receivers and the SIS receiver in this work



Schottky diode mixers are usually cooled at about 20 K by usual GM refrigerators. On the other hand, SIS mixers must be cooled at the 4 K level, and either liquid helium or a GM+JT refrigerator is used. The SIS receiver has higher sensitivity than the Schottky diode receiver, but is usually much larger and heavier.

In this work, the SIS mixer was cooled at the 4 K level by the GM refrigerator with Er_3Ni . It resulted in the SIS receiver which was almost the same size and weight as the usual Schottky diode receiver as shown in Table 1.

CONSTRUCTION

SIS Receiver

Figure 1 shows a schematic diagram at the 4 K stage of the SIS receiver. The 4 K stage consisted of a corrugated feed horn, a crossguide coupler, an SIS mixer, an isolator and an IF (Intermediate frequency) amplifier. The signal from the antenna was focused into the corrugated feed horn. In the crossguide coupler, the local oscillator

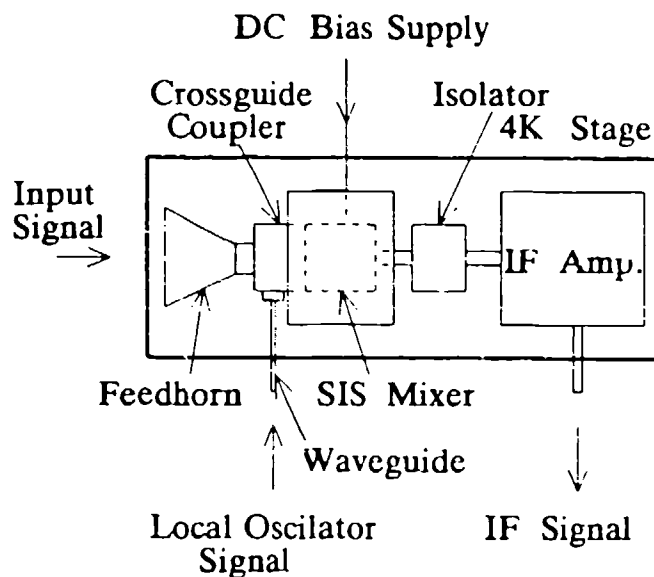


Figure 1 Schematic diagram at the 4 K stage of the SIS receiver

signal and the astronomical signal from the feed horn were coupled into the same piece of waveguide. This waveguide carried these two signals to the SIS mixer, where they were electrically mixed together. The resultant IF output signal was then amplified 1000 times by the IF amplifier.

In this receiver, a tunerless SIS mixer system has been used for ease of operation. Instead of an adjustable backshort tuner, the SIS mixer system used a fixed backshort cavity, designed to work in the radio frequency range of 150 GHz. This tunerless structure also made a lower heat load compared with a usual mixer system.

System Specification

Figure 2 shows the construction of the SIS receiver, and Fig. 3 is a photograph of the completed receiver. The completed SIS receiver is 720 mm in height, 260 mm in length and 260 mm in width, and the total

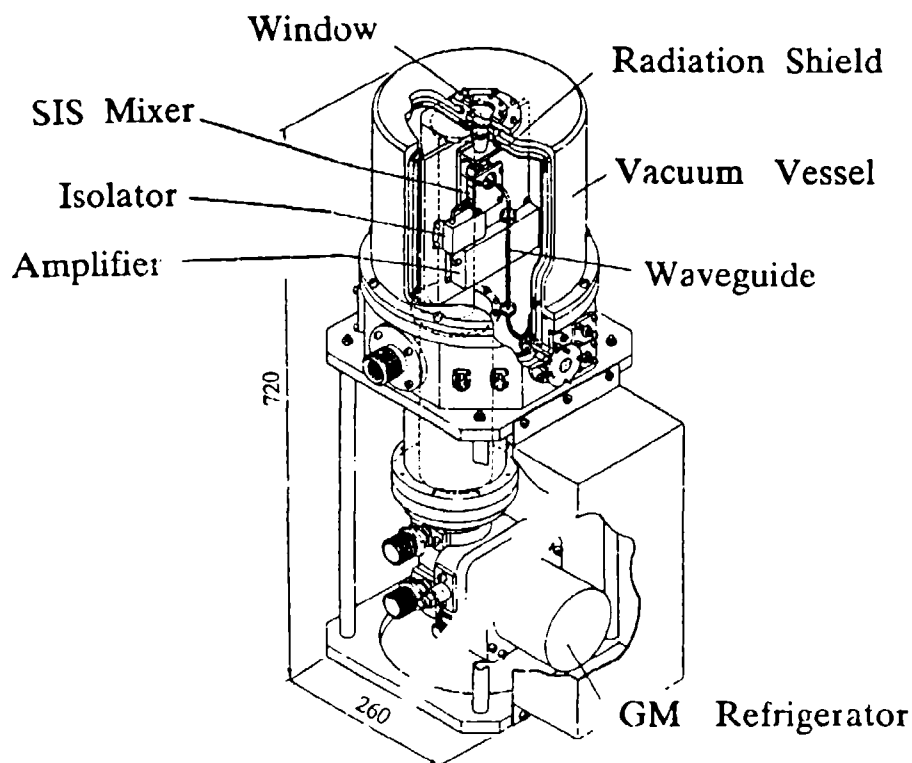


Figure 2 Construction of the SIS receiver

weight is 35 kg. This size and weight are about one-third of that for a usual SIS receiver using a GM+JT refrigerator.

The cryogenic part of the receiver consisted of a two-stage GM refrigerator with Er_3Ni and a 4 K stage mounted on the second stage of the GM refrigerator. Figure 4 is a photograph of the 4 K stage. The SIS mixer was placed in a copper block and the copper block was clamped between a copper plate and the 4 K stage, which, in turn, was mounted on the second stage of the GM refrigerator. Indium seats, 0.2 mm in thickness, were inserted between each pair of contacting surface to ensure good thermal contact between the SIS mixer block and the second stage of the GM refrigerator.

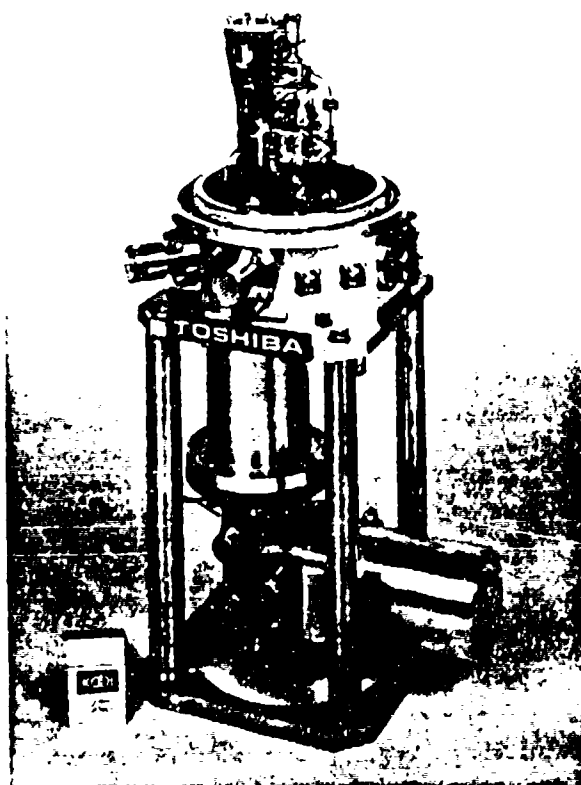


Figure 3 Photograph of the
SIS receiver

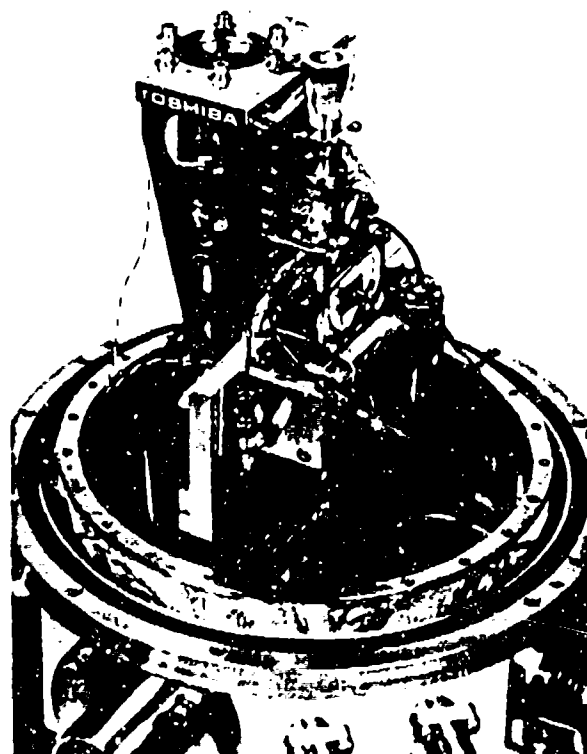


Figure 4 Photograph of the
4 K stage

Thermal Design

The heat loads at the first and second stages of the GM refrigerator were calculated by the thermal conduction, the thermal radiation and the Joule heating of the IF amplifier. The local oscillator waveguide was made of cupronickel. Usually, a waveguide would be internally gold plated to reduce its signal loss, but in this work, gold was not plated to prevent from increasing the conduction heat load. With the tunerless mixer system used here, the thermal conduction from a backshort driving mechanism has been completely removed.

Table 2 shows the calculated heat loads for the first and second stages, where the first and second stage temperatures were assumed 35 K and 4.2 K, respectively. The total heat loads were about 1.4 W for the first stage and about 220 mW for the second stage. These values were sufficiently smaller than the refrigeration capacities of the GM refrigerator with Er_3Ni .

Table 2 Calculated heat loads for the first and second stages

	2nd stage heat load	1st stage heat load
Thermal conduction		
Waveguide	59.9 mW	0.38 W
Co-axial cable	8.9 mW	0.14 W
Lead wire	0.7 mW	0.02 W
Thermal radiation	0.3 mW	0.88 W
Joule heating of IF amplifier	150.0 mW	0 W
Total	219.8 mW	1.42 W

EXPERIMENTAL RESULTS

Refrigeration Performance of the GM Refrigerator

Before installing the receiver components, the refrigeration performance of the GM refrigerator with Er_3Ni was investigated. The compressor unit used for the GM refrigerator was a Dalkin model U108AW, whose power consumption was 3.3 kW. Figure 5 shows the second stage refrigeration capacities obtained at the 30 rpm reciprocating speed without the first stage heat load and with the first stage heat load of 5 W. The refrigeration capacity at 4.2 K was 580 mW without the first stage heat load, and 430 mW with the first stage heat load of 5 W.

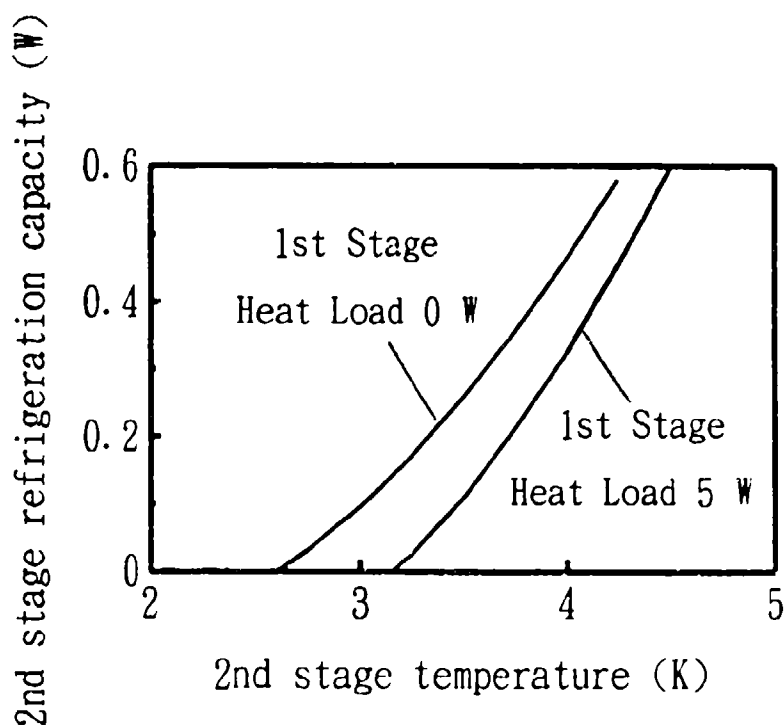


Figure 5 Second stage refrigeration capacities at the 30 rpm reciprocating speed obtained with the first stage heat load and without the first stage heat load

Performance of the SIS Receiver

The cooling performance of the SIS receiver had also been investigated. Figure 6 shows the cool down characteristics of the second stage temperature at the 30 rpm reciprocating speed. The cool down time from the room temperature to the 4 K level was about 4.5 hours. The lowest temperature of 3.0 K was achieved at the second stage without the IF amplifier heat load as shown in Table 3.

Normal operating power was then supplied to the IF amplifier, and the operating temperatures measured again. The first and second stage temperatures rose to 30.9 K and 3.4 K, respectively. They are also shown in Table 3. Both temperatures were lower than the thermal designed values. The SIS mixer block temperature was 3.4 K in this case. The temperature difference between the second stage of the GM refrigerator and the SIS mixer block was in the order of the measuring error.

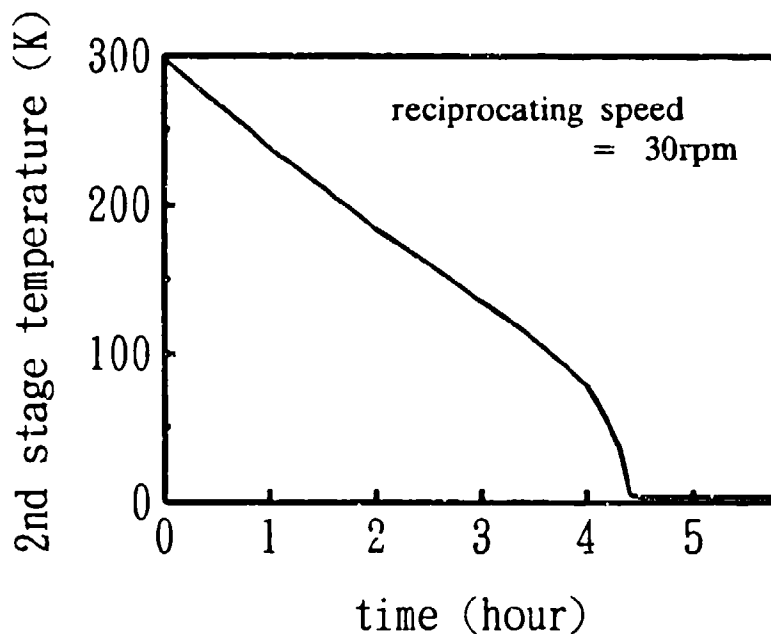


Figure 6 Cool down characteristics of the second stage temperature

Table 3 Temperatures of the first and second stages and the SIS mixer at the 30 rpm reciprocating speed

	without amp. input	with amp. input
SIS mixer temperature	3. 0 K	3. 4 K
1st stage temperature	30. 7 K	30. 9 K
2nd stage temperature	3. 0 K	3. 4 K

Sensitivity of the SIS Receiver

The DSB (double sideband) noise temperature of the SIS receiver was measured using the Y-factor method. Figure 7 shows the DSB noise temperature as a function of frequency. The average DSB noise figure was 55 K between 134 GHz and 148 GHz. This value is the lowest published receiver noise figure in the 150 GHz band.

Astronomical Observation

This SIS receiver has been installed on the 45 meter antenna at Nobeyama Radio Observatory, Nagano, Japan, where it has been used for radio astronomical observations. Figure 8 shows a photograph of the 45 meter antenna. On the 45 meter antenna, the compressor unit used for the GM refrigerator was either a CTI model 1020R or a Sumitomo Heavy Industry model CWS. The cooling performance with either compressor was almost the same as mentioned previously. Figure 9 shows an example of the astronomical observation results. During more than 3000 hours operation on the telescope, the SIS mixer temperature was always less than 4 K.

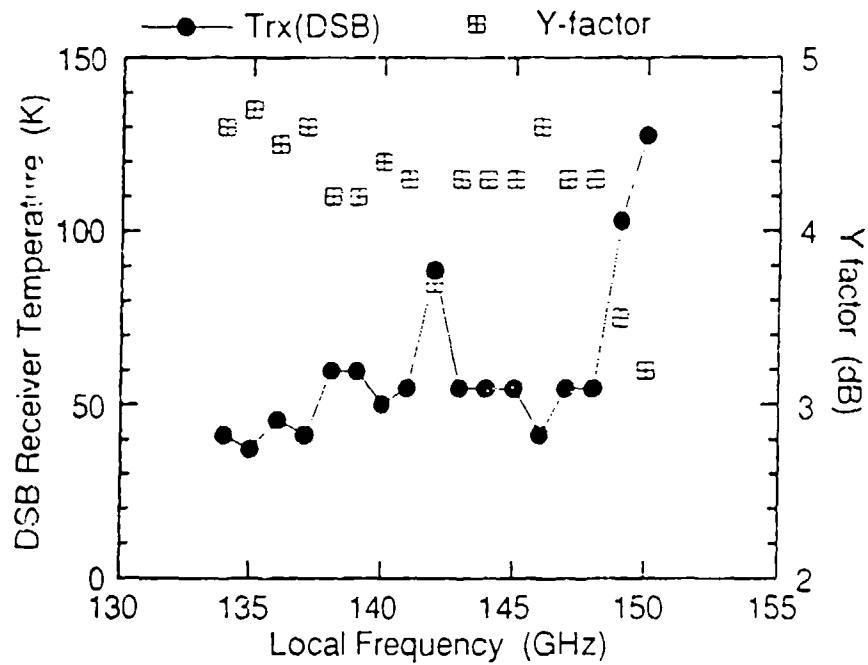


Figure 7 DSB noise temperature as a function of frequency

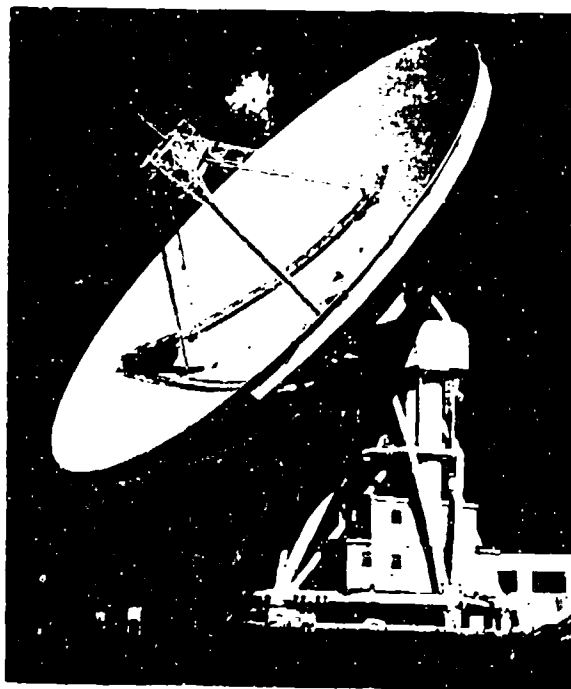


Figure 8 Photograph of the 45 meter antenna



Figure 9 Example of the astronomical observation results

CONCLUSIONS

A compact SIS receiver using a 4 K GM refrigerator has been developed, and the following conclusions have been drawn from the experimental results.

- (1) A compact SIS receiver, 720 mm in height, 60 mm in length, 260 mm in width, and 35 kg in weight, was developed by using the GM refrigerator with the Er_3Ni regenerator material.
- (2) The cool down time from the room temperature to the 4 K level was about 4.5 hours. The cooling temperature for the SIS mixer block was 3.4 K under operation.
- (3) The double sideband noise temperature of the SIS receiver was 55 K between 134 GHz and 148 GHz.
- (4) The SIS receiver has been operating on the 45 meter antenna at Nobeyama Radio Observatory for more than 3000 hours, and has been used for astronomical observations.

REFERENCES

- (1) T. Kuriyama, R. Hakamada, H. Nakagome, Y. Tokai, M. Sahashi, O. Horigami, R. Li, O. Yoshida, K. Matsumoto, and T. Hashimoto "Development of a 5 K refrigerator using rare earth compounds as a regenerator matrix", Proc. Intl. Conf. on Cryogenics and Refrigeration, Hangzhou, China, (1989), pp.91-96.
- (2) M. Sahashi, Y. Tokai, R. Li, M. Ogawa, and T. Hashimoto, "Regenerative material R_sT system with extremely large heat capacities between 4 K and room temperature", Proc. Intl. Conf. on Cryogenic and Refrigeration, Hangzhou, China, (1989), pp.131-136.
- (3) T. Kuriyama, R. Hakamada, H. Nakagome, Y. Tokai, M. Sahashi, R. Li, O. Yoshida, K. Matsumoto, and T. Hashimoto, "High efficient two-stage GM refrigerator with magnetic material in the liquid helium temperature region", Adv. Cryog. Eng. vol. 35B, (1990), pp. 1261-1269.
- (4) M. Nagao, T. Inaguchi, H. Yoshimura, T. Yamada, and M. Iwamoto, "Helium liquefaction by a Gifford-McMahon cycle cryocooler", Adv. Cryog. Eng. vol. 35B, (1990), pp. 1251-1260.
- (5) T. Kuriyama, M. Takahashi, and H. Nakagome, "Two-stage GM refrigerator with $Er_{0.9}Ni$ regenerator for helium liquefaction", Proc. Int. Cryocooler Conf. 6, Volume II, (1991), pp.3-14.
- (6) H. Nakagome, R. Hakamada, M. Takahashi, and T. Kuriyama, "High efficient 4 K refrigerator (GM refrigerator with JT circuit)", Proc. Int. Cryocooler Conf. 6, Volume II, (1991), pp.15-24.
- (7) T. Inaguchi, M. Nagao, and H. Yoshimura, "Two-stage Gifford-McMahon cycle cryocooler operating at about 2K", Proc. Int. Cryocooler Conf. 6, Volume II, (1991), pp.25-36.
- (8) M. Nagao, T. Inaguchi, H. Yoshimura, S. Nakamura, T. Yamada, and M. Iwamoto, "Generation of superfluid helium by Gifford-McMahon

PL-CP--93-1001

cycle cryocooler", Proc. Int. Cryocooler Conf. 6, Volume II, (1991),
pp.37-50.

DEVELOPMENT OF A PRECISION, SIX-AXIS LABORATORY DYNAMOMETER

P. J. Champagne,* S. A. Cordova,* M. S. Jacoby,* and K. R. Lorell*

ABSTRACT

This paper describes the design, fabrication, test, and operation of a unique six-axis force/torque dynamometer developed at the Lockheed Palo Alto Research Laboratory. The specimen table used to hold components under test is supported in a full six-axis kinematic mount. Support struts fabricated from high-strength steel with special integral two-axis flexures link the specimen table to the load cell transducers. Realtime force/torque coordinate transform, rms calculation and data averaging, and color six-axis display with controllable scaling are provided by a specially programmed desktop computer. The extensive structural analysis and design optimization required to obtain a stiff, well-damped, lightweight structure is described in detail. Geometric optimization of the kinematic mount and fabrication details of the struts are also described.

INTRODUCTION

Miniaturized linear-drive Stirling cycle cryocoolers designed with noncontacting parts are ideal for long-life cryogenic cooling onboard a wide range of spacecraft. They consume little power, have an almost indefinite operational life, and require no expensive ground handling equipment or procedures. A major problem in using these cryocoolers with sensitive focal plane instruments is the vibration induced by the reciprocating motion of internal motor/suspension components in both the compressor and expander. The development of a Stirling cryocooler system optimized for minimal residual vibration has been a major goal at the Lockheed Palo Alto Research Laboratory.

Instrumentation capable of measuring a wide spectrum of vibration sources associated with Stirling cryocooler operation had to be developed as part of this program. Requirements for this vibration measurement system included the ability to measure six degrees of freedom simultaneously, resolution to better than 0.004 N (0.001 lb) with a dynamic range of at least 10^4 , continuous monitoring and display of root mean square (rms) forces and torques, structural stiffness so that vibration modes in excess of 300 Hz could be measured, and a load-carrying capacity sized to hold a complete cryocooler (approximately 7 kg). In addition, the measurement device had to have substantial seismic isolation from the laboratory environment so that millipound level forces would not be overwhelmed by background noise.

Description of Stirling Cryocoolers

A split-cycle Stirling cryocooler consists of three main components: a compressor which provides a pressure pulse to the helium working fluid, a regenerator/cold finger in which heat is exchanged between the actual device being cooled and the cooler working fluid, and an electronic control system which provides the drive signals to the compressor and regenerator. Figure 1, a cutaway drawing of the refrigerator mechanical components, shows the linear drive motors used to power the compressor and regenerator, as well as details of the cold finger and transfer tube which connects the two units. The schematic of a refrigerator system in Figure 2 shows all three components connected.

* Lockheed Palo Alto Research Laboratory

The Problem of Vibration

The compressor and expander operate using reciprocating motions of their internal components: the piston in the case of the compressor and the stack of gauze screens inside the cold finger in the case of the expander. Inertial forces generated by the motion of these masses can be as large as 60–70 N in the compressor and about an order of magnitude lower in the expander.

Cancellation of induced vibration requires that the sum of the inertial forces generated by the motion of the reciprocating masses in the compressor and expander be as close to zero as possible. In typical cryocooler systems currently under development at Lockheed, the inertial forces are cancelled by using dual mechanisms mounted so that the motions of their moving components oppose each other. Compressors are mounted back-to-back; expanders are either mounted back-to-back (in a dual refrigerator system), or a single expander has an integrally mounted active balancer. The motions of the moving components are precisely controlled using a custom electronic control system developed at Lockheed to minimize induced vibration (Ref. 1).

Need for a Dynamometer

The residual vibration levels achieved using Lockheed's electronic cryocooler control system combined with the mechanical arrangement described above are extremely small. Typical levels for back-to-back compressors operating with a 4-mm stroke are below 0.02 N at the drive frequency (usually about 50 Hz). Harmonics of the drive frequency, often as high as 1.5 kHz, may still have small amounts of energy, and thus are important to observe and measure. In addition, as part of the baseline measurement for a force cancellation control system, it is important to know the uncompensated forces being generated by a single compressor or expander. These forces may be as high as 60 or 70 N.

The electronic force cancellation techniques only apply to the axial forces generated by the cryocooler. Lateral forces and torques are also of interest, especially since the only means of controlling them is through the careful balancing and alignment of the two opposing coolers. Should two compressors, for example, be either noncoaxial or noncoaligned, the resulting forces and torques could easily exceed the residual achieved for the actively controlled axial forces.

In order to effectively measure the performance of the active force cancellation system as well as ascertain how well the system has been aligned and balanced, some type of realtime multiaxis force measuring system must be used. This system must have sufficient dynamic range to measure both the compensated and uncompensated force levels, and must have an unimpaired frequency response sufficient to observe harmonics out to at least 300 Hz, and, ideally, as high as 1.5 kHz. The instrument developed for this purpose is a precision six-axis dynamometer utilizing special mechanical and electronic hardware, as well as software custom-developed to measure and display the forces and torques generated by cryocoolers.

REQUIREMENTS

Approach

The two common approaches to characterizing the vibration forces produced by oscillating machinery are indirect, using accelerometers, and direct, with force transducers.

The *indirect approach* is to measure the accelerations that are a result of internally generated forces. This is done with accelerometers and requires that the specimen be suspended without mechanical restraints. The unrestrained suspension is usually approximated by mounting the specimen on soft springs and providing generous service loops for the connecting cables. This approach requires minimal fixturing and excels in higher-frequency measurements where all structures appear relatively flexible. However, it is indirect, and requires the mathematical transformation

$$F = M * A$$

to convert the measured acceleration values to the desired force values. This transformation depends not only on the accuracy of the acceleration value, but also the mass—which is another measured value. In addition, the correct mass value to measure is obscured by the fact that in complex machinery portions of the total mass are in relative motion during operation.

The *direct approach*, called a dynamometer, directly measures the reaction forces produced. This approach uses load cells and requires a rigid suspension of the specimen. Since in reality no structure or force measuring transducer is perfectly rigid, this approach is limited to measuring relatively lower frequencies. It has the advantage, however, of measuring the desired value directly and is not dependent on a theoretical transformation or the measurement of any other variable.

For the purposes of accurately characterizing cryocoolers, the direct, dynamometer approach was deemed best. This is due to the relatively low operating frequency of the reciprocating mechanisms, the requirement for connecting cables and pipes, and the ambiguity in the determination of the exact effective mass.

Design Goals

The basis of a dynamometer, simply put, is to rigidly suspend the specimen from an immovable mass base and then measure the forces induced in the connecting structure during operation. Even minute motions of either the specimen or the base invalidate the measurement since some of the vibrational energy will be absorbed by the acceleration of the masses instead of being transmitted by the structure. Of course, in the real world no mass is truly immovable, and no structure is truly rigid. The design goal of the dynamometer is to approximate this ideal closely enough for the desired measurements to be valid.

In order to obtain true simultaneous/independent six-axis measurements, six separate single-axis transducers are used. Each transducer has to be incorporated in such a way that it is subjected to a unique and purely axial load. This requires a true kinematic (statically determinate) structure. Transverse and torsional loads on the transducer would corrupt the measurements by producing unpredictable results, since single-axis transducers are calibrated to pure axial loads.

These requirements led to the basis of the dynamometer design. This design features a test specimen mounted on a platform or table, which is suspended from a large mass via six struts resting on six load cells.

SYSTEM DESCRIPTION

Mechanics

Architecture. Once the determination was made to develop a six-strut dynamometer, the next step was to determine the architecture of the structure. The objective was to achieve the highest possible structural rigidity.

Several configurations of six-strut geometries were considered. Conventional orthogonal, radial, and tangential geometries (see Figure 3) have been used in similar systems, such as the cryocooler dynamometer built by JPL (Ref. 2). Each of these has its advantages and all are capable of full six-axis measurements. However, experience has shown that system structural rigidity with no natural vibration modes below 600 Hz is difficult to achieve. This is because most structural components, while relatively stiff in axial loading, are weaker in bending. The conventional structures studied support the specimen table above the base on three primary vertical struts, with the remaining three struts oriented horizontally in various arrangements. This results in the need for some kind of vertical structure on which to anchor the horizontal struts. The horizontal loading of this vertical structure results in bending loads—and bending loads compromise the rigidity of the system.

To overcome this problem, a new approach was sought. The unique hexapod architecture of the Lockheed dynamometer is the result of this search. The hexapod architecture (Figure 4) supports a triangular specimen table at three points. Each support point has a set of struts at matching angles to the base and approximately perpendicular to each other. Each strut terminates in an axial transducer at its base. The hardware design resulting from this architecture is shown in Figure 5.

While this hexapod design uses the same six struts as in convention designs, it has them oriented in an axisymmetric arrangement in which each strut is a straight load path from the specimen table directly to the seismic mass base. With this configuration, there is no vertical structure and therefore none of the inherent bending and flexibility associated with it.

Although not as readily obvious as the conventional geometries, the hexapod configuration is a true stable kinematic structure in which there are no indeterminate load paths. Therefore the outputs of the six load cells represent six independent degrees of freedom. As a by-product of this fact, there are no adjustments necessary during assembly (other than the inherent minor pivoting of the strut joints) to allow for tolerance variations in the components.

Because the hexapod struts are not in a conventional arrangement, they do not directly read forces and torques in a conventional (orthogonal or polar) coordinate system. Vibration force and torque requirements and specifications are usually stated with reference to an orthogonal coordinate system. Some means of coordinate transformation is necessary in order for the hexapod-based measurements to be readily understood. The solution chosen is to perform this transformation electronically on the transducer signals before they are viewed or analyzed. The analog electronics designed into the system are capable of transforming the load cell outputs, in real time, into the conventional orthogonal force and torque vectors. In this way a superior mechanical design is obtained while maintaining simplicity in the available output data.

Seismic Mass. The base on which the hexapod is mounted must be stable and have a mass large enough that any reaction to the vibrational forces of the test specimen is negligible. Granite was chosen as the material for this base because of its density, inherent stability, and freedom from magnetic interactions, as well as its availability and relatively low cost. The size of the granite block was set to obtain an effective weight of approximately 1400 kg (3000 lb) and yet be able to fit through standard door openings. The proportions are close enough to square that flexibility of the block itself is not an issue.

The block is supported on pneumatic mounts to isolate it from ambient vibrations transmitted through the floor. The mounting system has a very low natural frequency (approximately 1 Hz) and thus effectively eliminates the introduction of background noise into the measurements. The suspension system has been included as an integral part of a wheeled cart which allows for ease of installation and relocation.

Transducer. The selection of the single-axis transducers was driven by the requirement for high sensitivity and high rigidity. Strain-gage-type transducers in the high sensitivity ranges were found to require relatively large amounts of axial motion and were quickly eliminated as viable choices. Piezo-electric transducers are quite rigid, even in the high sensitivity ranges, and were the obvious choice. The fact that they are based on a capacitive effect, and thus not capable of true static measurements, was not a problem since frequencies below 1 Hz were not of interest.

Because load cells in the highest sensitivity range are susceptible to damage from shock overloads, an alternate support structure was included in the design. This structure can support the specimen table independent of the load cells and thus protect them from such excessive loads as might occur during installation and setup of large test specimens. To use this feature, the specimen table is unbolted from the three strut yokes and lowered onto the three hard stop brackets shown in Figure 6. Alignment holes and removeable pins are provided at each yoke for ease of reassembly when testing is to begin.

Strut. Besides elevating the specimen table to a height which can accommodate the intended specimen at its approximate center of mass, the purpose of the struts is to transmit pure axial loads to the single-axis transducers. The struts must be perfectly rigid and yet function as if connected by a frictionless ball joint at each end. Such struts may exist in theory, but in reality only functional approximations can be achieved. In this case, a specialized form flexure-ended struts was devised.

The joints at the end of the struts turned out to be one of the most critical areas of the entire design. The joint must be free to rotate, as would a ball-joint connection, at the same time it cannot have any of the friction or play associated with typical hardware. It also cannot possess any of the minor irregularities of an antifriction bearing (such as sleeve or ball bearings). Fortunately, in a rigid dynamometer application the range of actual rotation required of the joint is extremely small. This leads to the selection of a flexure-type joint. Flexures are inherently free of irregularities of motion and, because of the small motions required, can be designed to be flexible enough to limit the amount of moment transmitted by the strut.

The flexures implemented in the Lockheed dynamometer are a specialized form of integral, cross-linked, single-axis bending elements. Each end of each strut rod is relieved by a narrow slit from both sides until only a small neck-downed portion of the rod remains. This is done at two closely spaced locations such that the bending elements are mutually perpendicular and close to the strut ends (see Figure 7). Each bending element acts as a flex point in

a single axis. The combination of both elements approximates the two-axis motions of a universal or ball joint. The fact that the bending element is an integral part of the strut rod eliminates the need for extra parts and connections.

The technique used to form the flexure area has been devised to give maximum axial stiffness while maintaining close control over flexural stiffness and material stresses. The very short bending element allows the flexures to be located close to the strut ends and limits the inherent reduction in axial stiffness to a small area. In addition, the geometry of the relief is carefully selected to act as an integral stop to limit motions of the flexure so that the yield strength of the material is never exceeded (see Figure 8).

Specimen Table. The goal of the specimen table design is to connect the specimen to the struts with minimum flexibility. The table was shaped to accommodate the mounting of a typical cryocooler component. It has a large hole in the center to allow location of the specimen at the apex of the struts and to provide easy access from both top and bottom for connecting cables. The table structure is analogous to a triangular bridge between three support points. In order to achieve the performance goals of the dynamometer, the material and design of the table were selected to optimize stiffness and reduce weight. This was accomplished through the use of extensive computer modeling and resulted in a one-piece design, deeply pocketed to form the intricate triangulated rib structure shown in Figure 9.

Electronics

The electronics for the dynamometer are shown schematically in Figure 10. The six load cells are connected to charge amplifiers whose outputs are then fed to both the analog electronics and the analog-to-digital converters in the PC. The electronics have a dual function. First, they enable the direct measurement of the load cell outputs and provide an analog coordinate transform so that high bandwidth force/torque measurements may be made using monitor points on the front panel. Second, the electronics provide an interface for the PC used to compute and display the forces and torques. In addition, the PC has, as part of its software, a realtime coordinate transform algorithm, so it could be used independently to determine the six forces and torques. However, because of limitations inherent in the PC's ability to sample analog signals and rapidly compute the coordinate transformation, do the correct scaling, and generate the display, the bandwidth of the PC data is limited to below 300 Hz, and therefore the software transform is generally not used.

Software

Analog voltages from the six load cells are converted to digital signals for processing and display as force and moment values. A flexible data processing scheme is implemented via a CRT display and user interface.

The load cells at each of the six legs of the dynamometer produce output voltages which are proportional to the loads measured. These signals are digitized through an analog-to-digital converter built into the computer. Since each load cell has its own scale factor (volts output per Newton input), the input signals must be normalized before further computation. The normalization may be done by using an analog circuit or by enabling the normalization option in the software. Once this is done, the numbers exist as an input vector of forces in the dynamometer coordinate frame, and must be transformed into a vector of forces and torques in an orthogonal frame whose origin is located along the axis of symmetry of the unit(s) being tested. The transformation requires a matrix multiplication of the 6×6 coordinate transform matrix by the 6×1 input vector of forces. The result is the desired 6×1

output vector containing the forces and torques. Processing continues with a digitally implemented notch filter used to minimize structural resonance in the dynamometer. The rms of the data is calculated, and a running data average is performed with a user-specifiable number of data points to average. The rms and data averaging computations provide a smoothed output signal appropriate for display. Data processing options are independent of each other and may be performed in any combination.

The timer chip on the analog-to-digital converter board is used to implement the timing scheme of the software. Since the bandwidth of the computed data is a direct function of how fast these functions can be executed, it is critical that the computer be able to at least sample the data and perform the rms computation at approximately 1 kHz. At this sample rate, the effective bandwidth of the data is between 300 and 500 Hz. In order to accommodate the relatively slow computational speed of the 80386DX microprocessor, the data is taken in a lump, with 20 ms allocated for this task. The actual time required for this task is determined in the software after the user decides on a desired sample frequency. Twenty ms is more than enough time to accomplish the data acquisition. Note that raw data could be displayed real time using the 80386DX. However, the 6x6 matrix multiplication for the coordinate transformation is the main contributor to the speed limitation of the data processing portion of the software. Thus, the data processing is done independently of the data acquisition. For example, 250 data points are currently being acquired at a 1-kHz sample rate and stored in the computer's far memory. The software starts processing the stored data 20 ms after it first began the data acquisition. Data processing occurs at whatever speed the 80386DX can accommodate. The processed data is then displayed on the screen at two different rates.

Figure 11 is a black-and-white version of the color display screen. The force and moment values are displayed on their respective orthogonal coordinate axes at a speed which is microprocessor limited. The tabulated force and moment data is displayed at a slower rate of 1 Hz to enable the user to easily read the constantly changing values. When 100 ms has elapsed from the initial start of data acquisition, another chunk of data is acquired at the user-specified sample frequency. Raw data, which is constantly being stored in the computer's far memory, is dumped to a file on user command. Data storage is the only program mode that inhibits the display of the data. All other switches between program modes are done without affecting the validity of the incoming data or the constantly updated display.

STRUCTURAL OPTIMIZATION

The dynamometer is intended to measure cryocooler residual vibration levels not only at its operating frequency, but also through the higher harmonic frequencies. In order to measure these harmonics with confidence, vibrations in the dynamometer itself must interfere as little as possible with the residual vibrations generated by the specimen cryocooler. This means that the lowest vibration mode of the dynamometer should occur at the highest possible frequency. This is accomplished by optimizing support strut geometry, maximizing the bending and torsional stiffnesses of the specimen table while minimizing the specimen table weight, and maximizing the axial stiffness of the support struts.

Geometry

Structural design analysis started with the overall dynamometer geometry. To help determine the optimal design, Lockheed's DEWAR design code (Ref. 3) was utilized. DEWAR is an existing software program originally developed for the analysis of stored cryogen-type coolers. It performs automated thermal optimization of cryogenic support

systems that use discrete supports with *pinned ends* and have specific structural performance goals, such as frequency, clearance, support system material allowables, etc. These structures typically use axisymmetric shell structures in conjunction with stiffening rings to hold large amounts of cryogenic fluids or solids, which provide the required cooling to instruments or optics. These large shell structures are in turn supported within a vacuum shell by struts or straps. The structural analyzer within the DEWAR code uses analytical descriptions of shell behavior and simplified numerical procedures describing ring-shell interactions to determine the structural performance of a given design. Thermal optimization is achieved by changing various structural design parameters, such as support thicknesses and winding angles (in the case of struts constructed of composite materials), strut attachment points on the dewar and vacuum shell, etc., until minimum thermal conductance of the overall support system is obtained.

For the dynamometer, thermal conductance of the support system is not a design consideration. However, by fixing the strut thickness (and strut *unit* axial stiffness) in conjunction with a specified minimum frequency, DEWAR can be forced to optimize support system geometry parameters only.

The lowest natural frequency of the dynamometer will occur during testing of the largest supported mass and/or configuration mass moments of inertia. For purposes of this analysis the supported mass includes struts, specimen table and associated bracketry, and the specimen itself. Accordingly, estimates of mass properties corresponding to the testing of a cryocooler compressor pair (approximately 7 kg) oriented vertically with respect to the granite base support were used.

After using DEWAR to experiment with various geometry variables, the optimal ascension angle of the struts, γ , was determined to be 35° . Accounting for clearance and assembly constraints, the final azimuthal angle θ is 90° . At the specimen table, this combination of geometric parameters places the center of the strut pairs at the center of mass of the supported specimen (see Figure 12), eliminating the component of force associated with moments about the horizontal axes.

Once the geometry was optimized, it was left to optimize the stiffness of the various components of the structure. This was accomplished through the use of finite-element modeling.

Finite-Element Model

In order to maximize the bending and torsional stiffnesses of the specimen table, a detailed finite-element model of the entire dynamometer hexapod structure was constructed, including a specimen mass equivalent to a cryocooler compressor pair. In the physical case, the struts are rigidly attached to the specimen table yokes and to stainless steel fixtures at the granite base. Since the struts contain integral flexures designed to reduce the bending stiffness of the struts, they were approximated in the model as simple bars with an axial stiffness (EA) of 4.45×10^6 N and pinned ends. The specimen table yokes are ribbed to reduce weight and to provide access to the strut attachment fasteners. For simplicity these were approximated in the model as solid structures of reduced density. This approximation in the model leads to predicted system frequencies slightly higher than those measured due to the neglect of the softer bending stiffnesses associated with the ribbed structure.

The compressors were modeled as cylindrical solids having the correct mass and moments of inertia and were attached to the specimen table through extremely thick shell

elements. These approximations may artificially stiffen the specimen table somewhat. As a consequence of these approximations, the model overpredicts system frequencies. However, the intent of the model is to assess the impact of detailed design and material alternatives on the bending and torsional stiffnesses of the specimen table. Therefore, it is the *difference* in predicted system frequencies between design alternatives that is important in the specimen table optimization.

The finite-element model is shown in Figure 13. Examples of the nodes of vibration that were predicted are shown in Figure 13a-d. Lockheed's **DIAL** finite-element analysis package was used, and was run on a Digital Equipment Corporation DEC 5000/200 workstation. The finite elements chosen had quadratic displacement functions; 8-node shell, 3-node bar, and 20-node solid elements were used. The model contained 240 shell elements, 6 bar elements, and 60 solid elements, for a total of 4503 degrees-of-freedom.

Specimen Table and Strut Yokes. Material and thickness alternatives for the specimen table and yokes were assessed by computing the primary natural frequencies of the whole system. Candidate materials for the specimen table were stainless steel and magnesium. Both materials have approximately the same ratio of elastic modulus to density ($E/\rho = 10^8$), but magnesium has a lower density; therefore a magnesium specimen table would result in a smaller system mass. Magnesium is commonly used in vibration testing fixtures for its low mass and excellent bulk damping characteristics. These considerations led to the selection of magnesium for the specimen table.

Table 1 describes some of the parameter optimization iterations that were performed during the design process. The initial conditions assumed that all components were magnesium and that all ribs were 8 mm thick. Through this optimization process, the predicted first-mode frequency was raised over 70 Hz.

Struts. Since the dynamometer derives its ability to measure and resolve the vibration forces generated by the cryocoolers through static determinacy, the struts must be pinned, or simply-supported, at the strut ends. The integral flexures used to approximate this condition act to greatly reduce the overall bending stiffness of the struts. However, the strut, including the flexures, must provide a high axial stiffness to maximize system frequencies while still providing the minimum bending stiffness to approximate the end conditions required for static determinacy. The flexure design must achieve a compromise between these two competing requirements.

With respect to overall axial stiffness, the struts behave as several springs in series. The total axial stiffness of the struts is maximized by increasing the strut diameter to the maximum extent possible, by reducing the overall strut length, and by maximizing the thickness of the integral flexures. The overall stiffness of the strut is driven by the "softest" axial spring within the strut, which in this case is the flexure. However, increasing the thickness of the flexures will increase their bending stiffness and therefore undermine the static determinacy of the system. Dynamometer assembly and disassembly requirements set the minimum angular rotation which the flexures must withstand without yielding the strut material. The actual design of the flexures and struts was accomplished through the use of beam theory for an element subject to a bending moment (in this case, the bending moment resulting from the required angular displacement).

The overall axial stiffness of the strut was then computed by first computing the extensional stiffness of each strut component (flexures and shaft), EA_i/L_i , and then summing these component stiffnesses according to the springs-in-series model. However, it was con-

sidered that the axial stiffness of the strut would be overestimated by this approach. Due to the extreme difference in the cross-sectional area between shaft and flexure, not all of the shaft area will contribute stiffness in the regions adjacent to the flexures. To test this hypothesis, a simplified finite-element model of a generic strut with two flexures was constructed. This model, with its boundary conditions, is shown in Figure 14. The axial stiffness of this strut was first calculated with the springs-in-series approach. Using this approach, the predicted total axial stiffness is 7.8×10^5 N/mm. The finite-element model predicts an axial stiffness of 5.1×10^5 N/mm, thus confirming the hypothesis that the simplified springs-in-series model is not adequate in this case. The apparent explanation is that not all of the cross-sectional area acts to resist axial forces in the regions adjacent to flexures. To confirm this, the axial stiffness of the generic strut was recalculated assuming that only an area equal to the profile area of a flexure was acting in the shaft between the two flexures. This assumption, used in a springs-in-series model, yielded a total axial stiffness of 3.9×10^5 N/mm, in substantial agreement with the axial stiffness predicted by the finite-element model.

The goal of the dynamometer strut, designed using the original springs-in-series model, was to provide an axial stiffness of 1.7×10^5 N/mm. It is clear from the above discussion that the actual axial stiffness of the struts is less than the design goal. This explains, in large part, the frequency difference between the predicted modes and the observed structural resonances.

EXPERIMENTAL RESULTS

Calibration

To ensure the accuracy of the dynamometer measurements, calibration of the output was required. This was done to verify the coordinate transformation as well as the operation of the load cells.

Since piezoelectric transducers are not capable of true static measurements, the straightforward method of using dead weights for calibration was not applicable. At the same time, the dynamic response to the *addition* of weights made data acquisition difficult. However, it was possible to use the *removal* of weight for this purpose. In this method, an accurately measured weight was placed on the specimen table and the output from the load cells was allowed to decay over time. After this reading returned to the null point, the weight was suddenly, but carefully removed from the table. The display computer was set to monitor the output and capture the peak reading.

Due to the axisymmetry of the hexapod structure, a single weight will load all six transducers. All transducers and all elements of the transformation electronics are used to convert this load into a single Z-axis force. Therefore, it was possible to verify the operation of the transducers and the design and operation of the transformation electronics by observing the results of this one calibrated weight. Since the absolute accuracy of this verification test is limited, the factory calibration factors for each individual load cell were assumed to be accurate and were entered into the computer unchanged.

Measurements of Cryocooler Vibrations

The Lockheed six-axis dynamometer was used for the first time to make measurements as part of the Advanced Infrared Sounder (AIRS) cryocooler development program (Ref. 4). One of the goals of this development program was to make accurate performance measurements of the Lockheed vibration cancellation system. The dynamometer was expected to achieve these high-accuracy results.

Two back-to-back compressors driven by the Lockheed electronic control system were mounted on the dynamometer. Dynamometer outputs were observed on both the PC screen and using a Hewlett-Packard 3562A dynamic signal analyzer connected to the analog-transformed monitor points. A photograph of the two compressors mounted on the dynamometer can be seen in Figure 15. Also seen in the figure is the computer display generated by the dynamometer PC. Figure 16 is an output from the dynamic signal analyzer. This spectrum is remarkable in that it shows dynamometer data out to 1.562 kHz. In addition, the resolution of the dynamometer output is below 0.01 N. This indicates not only how sensitive the instrument is, but also how well the seismic isolation system works.

An important element in Figure 16 is the dynamometer resonances which occur just below 400 Hz. Initially, these resonances interacted with the electronic control system and limited its performance because the control system gain had to be reduced substantially in order not to become unstable. However, with the addition of a simple passive damper used to absorb the energy of this extremely high Q mode, the dynamometer structural dynamics were no longer interactive with the control system and the gains could be increased to extremely high levels with no adverse effects.

REFERENCES

- 1 Aubrun, J-N., R. R. Clappier, K. R. Lorell, and T. C. Nast: A High Performance Force Cancellation Control System for Linear-Drive Split-Cycle Stirling Cryocoolers, *Proceedings of the Cryogenic Engineering Conference*, NASA Marshall Spaceflight Center, Huntsville, AL, June, 1991.
- 2 Larson, C., A. Mauritz, D. Moore: *Development and Application of a Sensitive Six Axis Dynamometer*, JPL D-6611, NASA/Jet Propulsion Laboratory, October 23, 1989.
- 3 Bushnell, D.: Improved Optimum Design of Dewar Supports, *Computers and Structures*, Vol. 29, No. 1, 1988.
- 4 Nast, T. C., R. R. Clappier, D. O. Murray, and B. Hocking: *Final Report for the AIRS Cooler Development Program*, LMSC-P000132, Lockheed Missiles and Space Company, Inc., November 18, 1991.

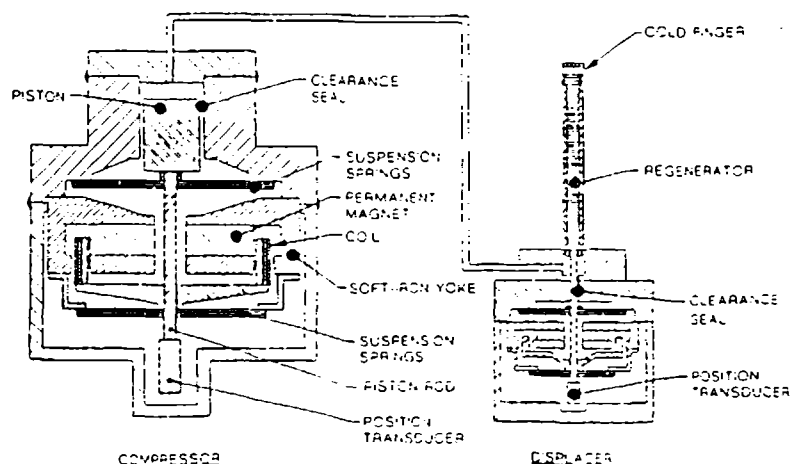


Figure 1 Split Stirling Cooler Schematic

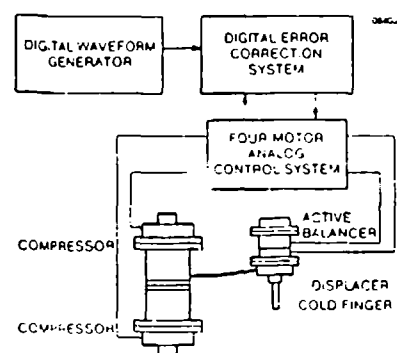
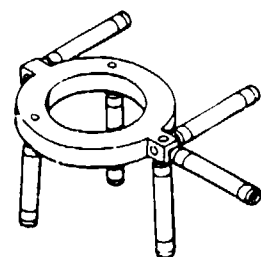
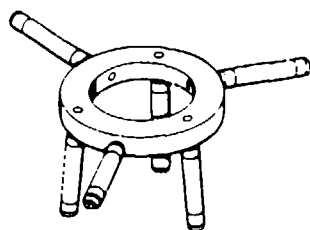


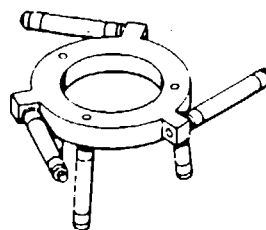
Figure 2 Cryocooler System Block Diagram



ORTHOGONAL CONFIGURATION



RADIAL CONFIGURATION



TANGENTIAL CONFIGURATION

Figure 3 Conventional Geometries: Orthogonal, Radial, and Tangential

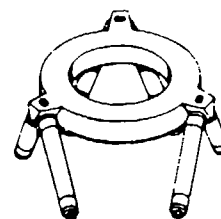


Figure 4 Hexapod Geometry

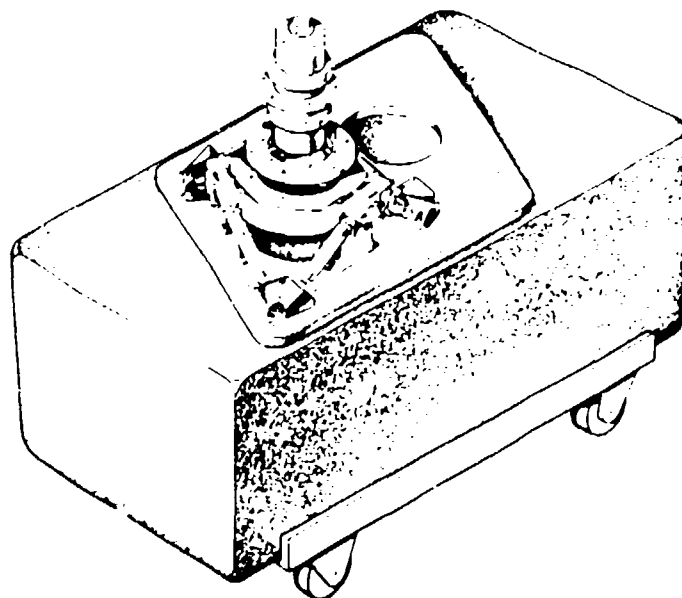


Figure 5 Lockheed Six-Axis Dynamometer

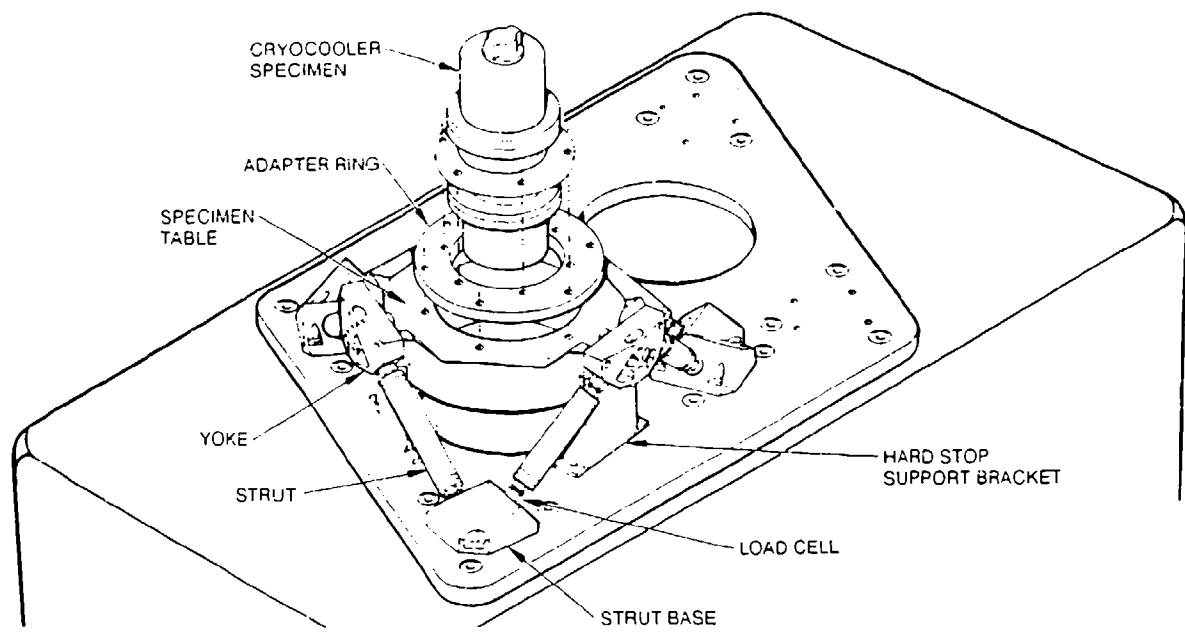


Figure 6 Dynamometer Components

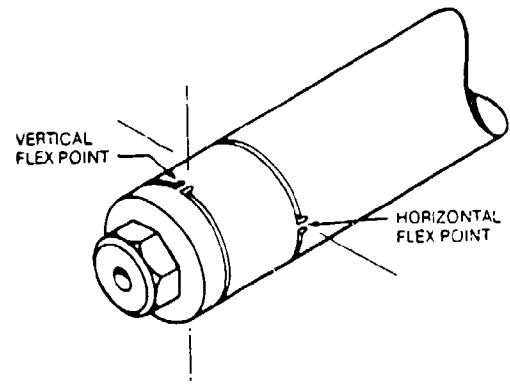


Figure 7 Strut Design With Integral Crossed Flexures

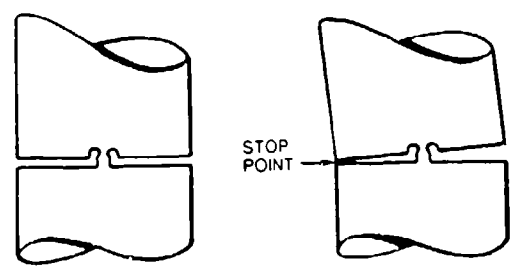


Figure 8 Flexure Design With Integral Stops

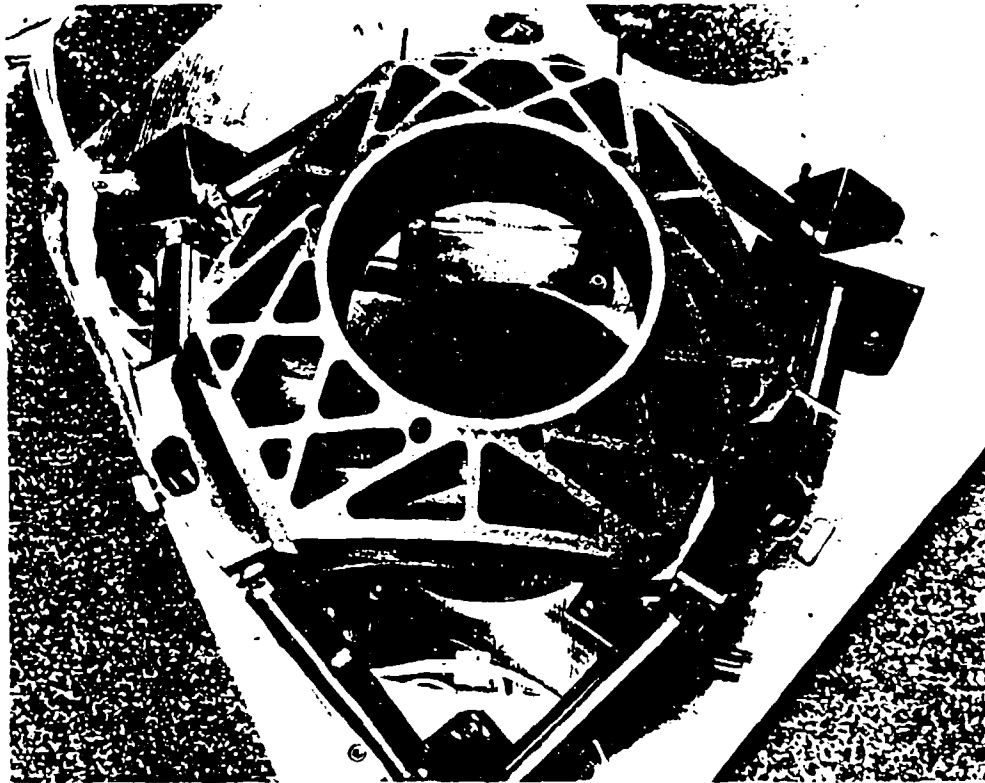


Figure 9 Specimen Table Rib Structure

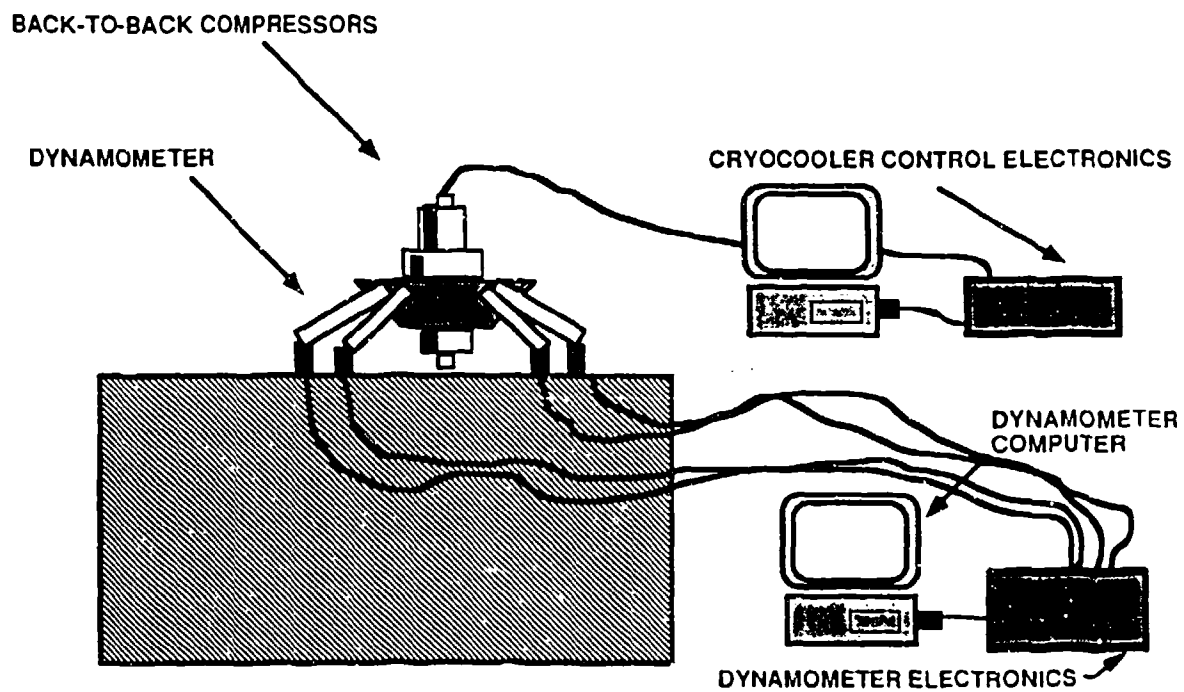


Figure 10 Dynamometer Test Setup

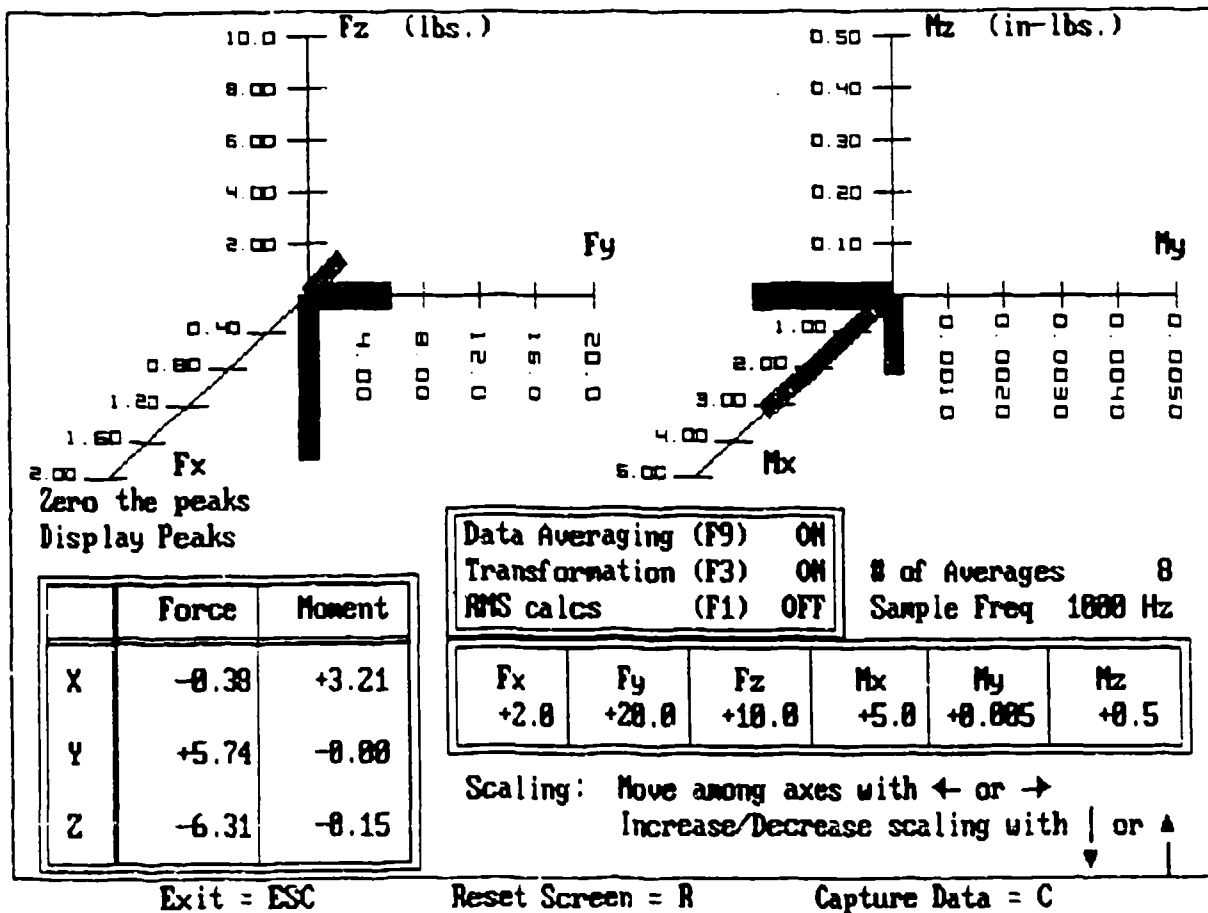


Figure 11 Display Screen Graphics

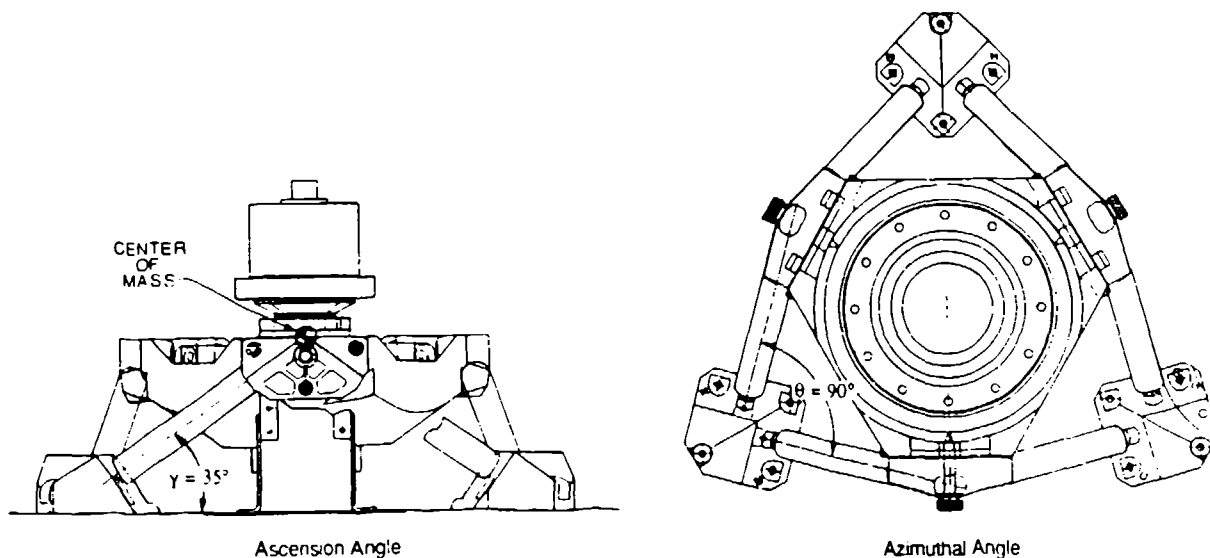


Figure 12 Optimized Hexapod Geometry

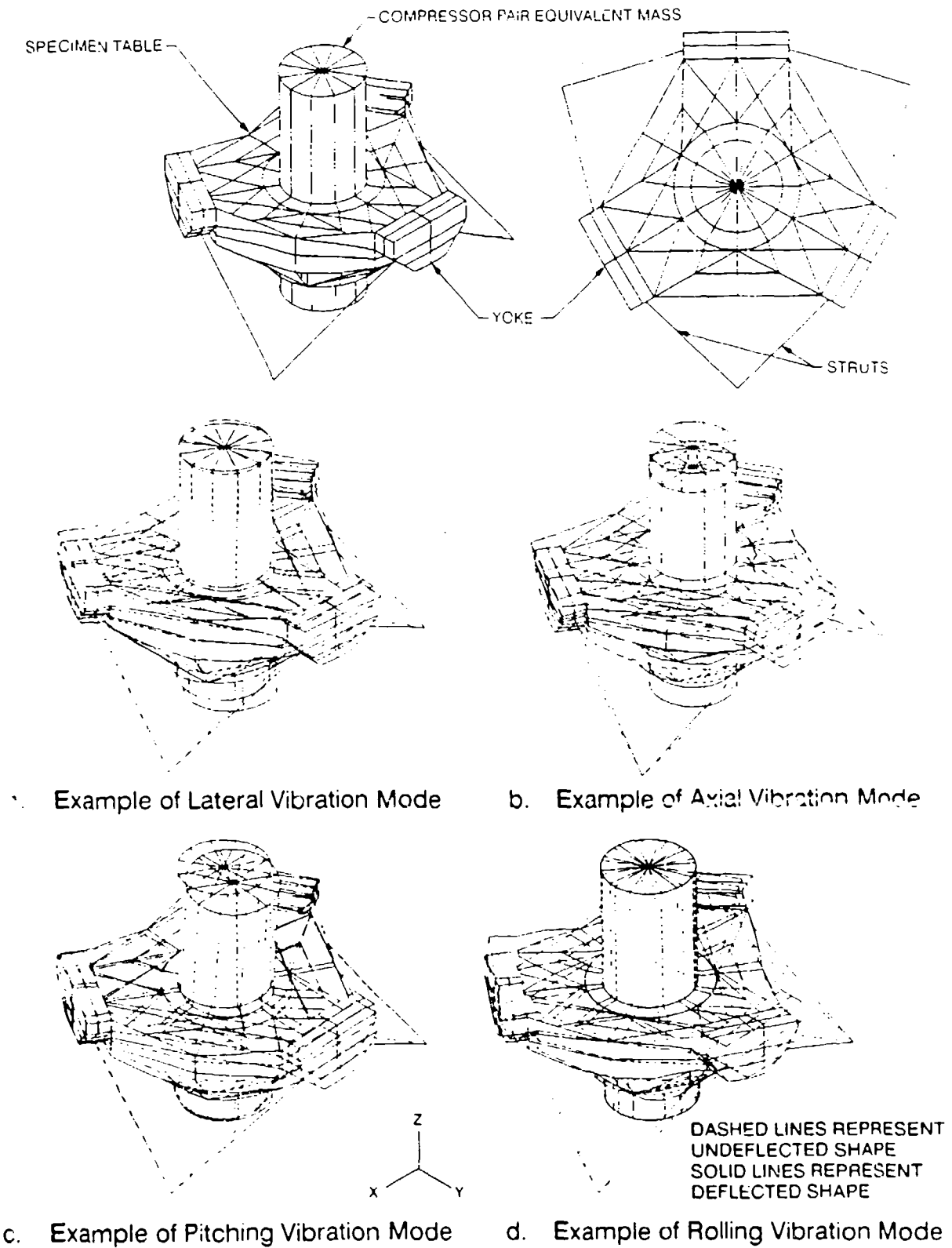


Figure 13 Finite Element Model of Hexapod

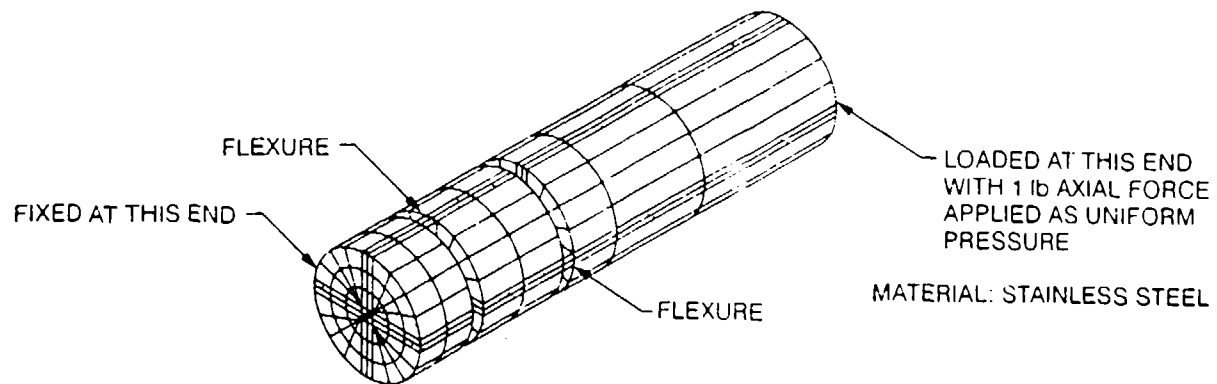


Figure 14 Finite Element Model of Generic Strut

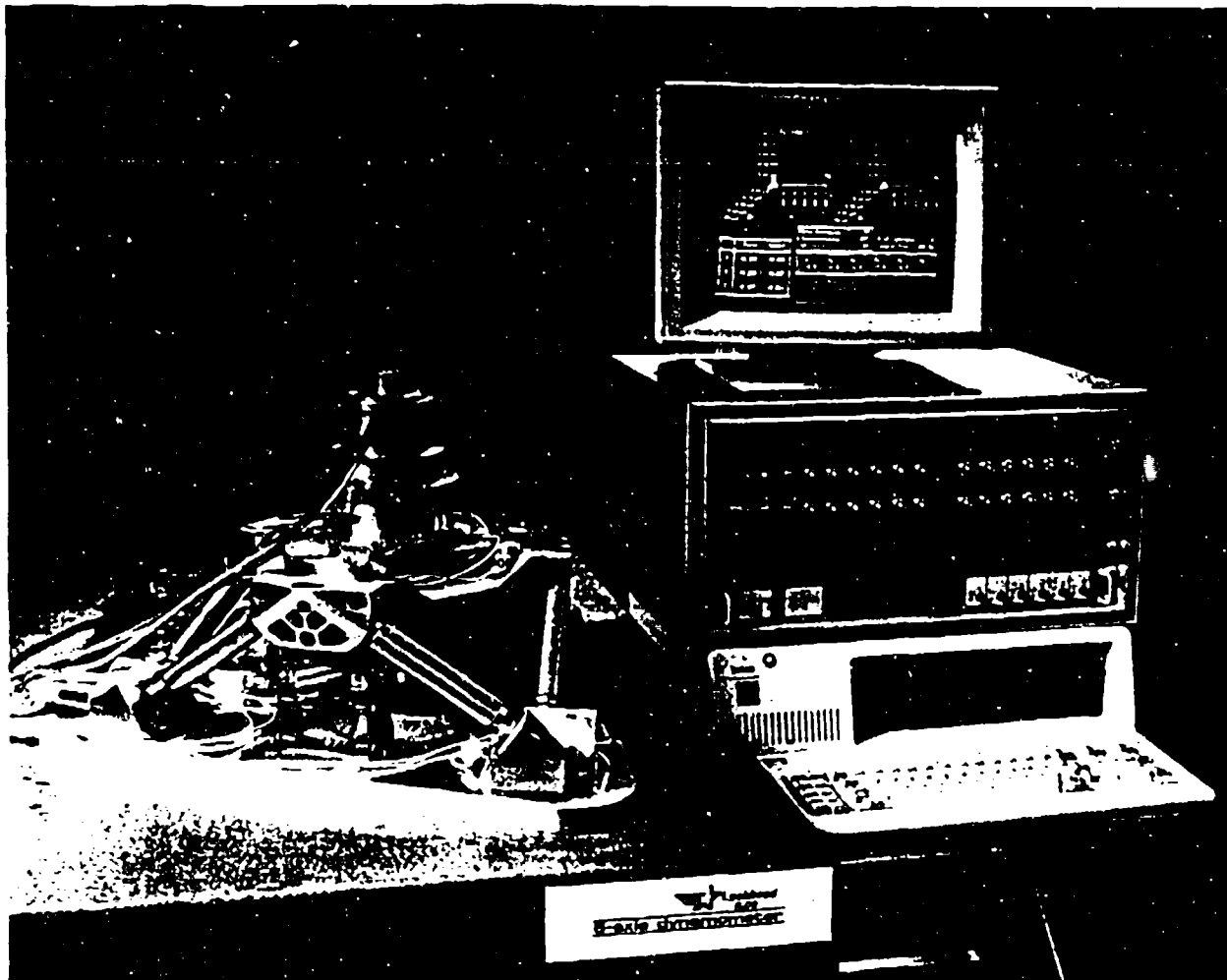


Figure 15 Dynamometer Testing of a Cryocooler

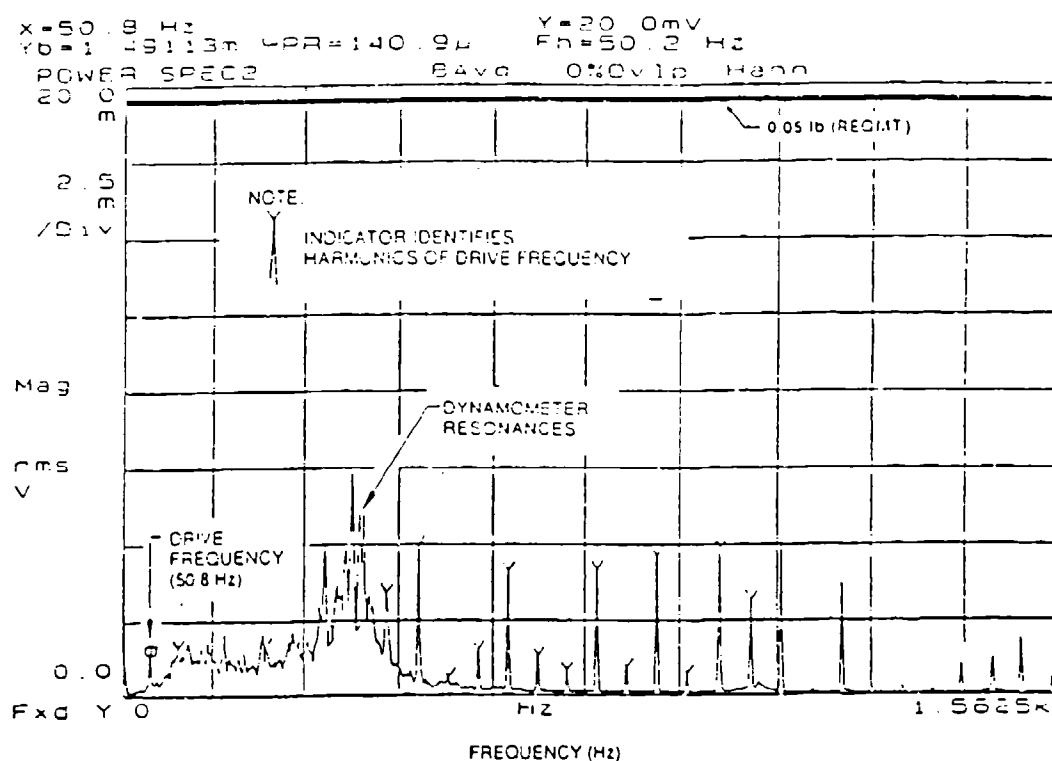


Figure 16 Frequency Spectrum of Cryocooler Vibrations

Table 1 DEVELOPMENT OF A PRECISION SIX-AXIS DYNAMOMETER

Case	Design Parameter	Calculated First Mode Frequency (Hz)	Selected?
1	Optimize specimen table top plate thickness		
2	t = 6 mm (initial condition)	504.9	No
3	t = 8 mm	516.9	No
	t = 10 mm	526.2	Yes
4	Optimize specimen table outer web thicknesses		
	t (short side) = 8 mm	529.0	No
	t (long side) = 6 mm		
5	t (short side) = 8 mm (initial condition)	530.5	No
	t (long side) = 8 mm (initial condition)		
6	t (short side) = 12.5 mm	530.9	Yes
	t (long side) = 8 mm		
7	Reduce specimen table spoke rib thickness from 8 mm to 6 mm, all ribs	531.5	Yes
8	Change material for strut yokes to stainless steel	553.4	Yes
9	Reoptimize specimen table top plate thickness by increasing to 12.5 mm	576.7	Yes

DEVELOPMENT AND DEMONSTRATION OF AN ELECTRONIC CONTROLLER
FOR A DOUBLE-ACTING DIAPHRAGM CRYOCOOLER

C. Konkell, T. Gibbeney, L. Van Allen and K. Ha
Electrical Engineering Section
Washington Technical Support Center
Fairchild Space
Greenbelt, MD 20770

R. Boyle
Cryogenics Technology Section
NASA/Goddard Spaceflight Center
Greenbelt, Maryland 20771

INTRODUCTION

A six-month conceptual design phase of a 30K cryogenic cooler resulted in the development of a system model and governing equations for control of double-acting diaphragms using Linear Oscillating Motors (LOMs). The potential reduction in vibration and power using a combination of sinusoidal feedforward drive signals was analyzed. Using a dynamic simulation and validating results against actual laboratory test data, a variety of feedforward control techniques were evaluated including commutated and non-commutated versions of both current-driven and voltage-driven waveforms. A voltage-driven stimulus based on two sinusoidal drive signals at the desired 30Hz diaphragm operating frequency with an added DC bias exhibited the best vibration and power performance and was selected for implementation. A test apparatus was used to operate typical compressor diaphragm mechanisms. Stable control of diaphragm stroke along with active vibration compensation using a harmonic cancellation technique was demonstrated.

OVERVIEW

The Fairchild Space Division of the Fairchild Space and Defense Corporation under contract to the NASA Goddard Spaceflight Center is actively pursuing the development of a reliable, low power electronic controller to operate a space-based cryocooler in the 30K temperature range. Various control techniques for operating cryocoolers based on unique double-acting diaphragms instead of reciprocating pistons have been evaluated. A control technique is described that demonstrated low mechanical

vibration (<0.2 Newtons) and stable operation over the operating range while minimizing power consumption.

The electromechanical drive method selected for the 30K compressor diaphragm is based on a Linear Oscillating Motor (LOM) as shown in Figure 1. This type of motor was chosen for its relatively high force capability while minimizing radial or tilt components. This motor has been built and extensively tested for both the 65 K Standard Spacecraft Cryocooler (SSC) and 30K cryocooler and has been well characterized. Its primary characteristic is a highly non-linear relationship between magnetic force and LOM current.

First a system model for the unique drive motors and diaphragms will be developed. Analytical estimates of power dissipation and harmonic generation for various drive waveforms will be derived based on simplifying assumptions. Simulation and test results are evaluated and a preferred approach for further development is described.

SYSTEM MODEL

In this section, the development of a non-linear model of the LOM and diaphragm used in the 30K cryocooler compressor is discussed. This model is based on simplifying assumptions for several important components of the system: the dynamics of the diaphragm, the generation of force in the air gap by the induced magnetic field, the effect of the air gap on the description of the LOM circuit, and the relation between the time-varying current generated by the LOM circuit and the induced magnetic field. These assumptions simplify the system considerably and have been verified extensively with actual data obtained from a prototype hardware model.

In terms of LOM operation, the desired electrical current is the current needed to produce the necessary magnetic force capable of generating the proper motion at the diaphragm, which in turn creates the desired pressure waveform. The prerequisite efforts thus are basically to identify:

- The magnetic force $F(t)$ required to produce $X(t)$.
- The electrical current $I(t)$ or Voltage $V(t)$ required to give $F(t)$.
- The control hardware capable of generating $I(t)$ or $V(t)$.

The mappings $X(t)$ to $F(t)$, and $F(t)$ to $I(t)$ or $V(t)$ can be expressed in terms of the functions $F(X(t))$, and $I(F(t))$ or $V(F(t))$. They have been derived using both analysis and simulation. The composite mappings

$I(F(X(t)))$ or $V(F(X(t)))$ are important in the design of the control algorithm that uses sensors measuring either $X(t)$ or $F(t)$.

The first simplifying assumption is that the diaphragm motion can be described by a second-order response along the vibrating direction with total mass (M), stiffness (K), and damping (D). This one-dimensional model is deemed appropriate because the diaphragm is rigidly fixed to a primary structure and can only produce motion in that direction. With $X(t)$ defined to be the diaphragm's displacement, the following equation describing the diaphragm's motion can be given:

$$F(X(t)) = M \ddot{x} + D \dot{x} + Kx$$

With the assumptions that the magnetization throughout the magnetic material is tangentially uniform, that no magnetic volume density exists inside the material, and that magnetic surface density exists on the sides of the LOM stator bars and the armatures in the air gaps, then the components of the magnetic flux density (B) and field intensity (H) inside the inner core of the material and inside the air gaps are tangential. Thus, the B fields induced by the LOM current and magnetic poles near the center line threading through the stators, armatures and air gaps is assumed to have the following characteristics:

$$B(x, y, z, t) = B_t(t)$$

for all (x, y, z) points within the bars and the air gaps, i.e., B is a spatially independent quantity and B is dominantly tangential, i.e., B is normal to all cross sections along the bars. Therefore, B is continuous across the gaps.

From Ampere's circuital law:

$$\oint_c H dl = \int_c (H_m + H_a) dl = 2NI$$

one obtains:

$$\frac{B}{\mu_0} \left(\frac{\mu_0}{\mu} l_o + 4g \right) = 2NI$$

in which the closed loop path threading through all four bars and gaps has length $l = (l_o + 4g)$, and

l_o = total length of four armature/stator elements

g = gap size

μ = permeability in magnetic material

μ_o = permeability in air

H_m = magnetic field intensity in magnetic material

H_A = magnetic field intensity in air

Therefore,

$$B = \frac{\mu_o 2NI}{4 \left(\frac{\mu_o l_o}{\mu} + g \right)} \quad (1)$$

Define

$$l_o' = \frac{l_o \mu_o}{4 \mu}$$

as the average effective length inside each magnetic element.

As shown in (1), $B_t(t)$ changes not only with current I but also with gap g . This implies that the inductance L of the LOM is a time-varying quantity.

We know:

$$L \equiv \frac{2N\Phi}{I}$$

where

L = inductance

N = Number of turns in coil

$\Phi = \int_A B da$ magnetic flux

I = coil current

The flux Φ through a cross section A can simply be expressed as:

$$\Phi = BA$$

From (1)

$$\Phi = \frac{\mu_o 2NI}{4(l_o' + g)} A$$

then

$$L = \frac{\mu_o (2N)^2 IA}{4(l_o' + g)} = \frac{\mu_o N^2 A}{(l_o' + g)} \quad (2)$$

From the general relation between V_{in} and I in an LR circuit:

$$IR + L \frac{dI}{dt} = V_{in}$$

the LOM circuit then becomes:

$$IR + \left\langle \frac{\mu_o N^2 A}{l_o' + g} \right\rangle \frac{dI}{dt} = V_{in} \quad (3)$$

where resistance R is due to the LOM electrical coil. From the above results, it is not likely that a closed form expression describing the LOM current can be obtained since the time-varying gap causes the system to be nonlinear. Assuming that the current profile is obtainable, the relationship between the induced magnetic force in the gap and the LOM current can be derived from the following simple consideration of the magnetic potential energy in the gap:

$$\begin{aligned} F_{mag} &= \frac{dU}{dg} = \frac{du\Delta V}{dg} = \frac{1}{2} \frac{B^2}{\mu_o} \frac{d(4Ag)}{dg} \\ &= \frac{1}{2} \frac{B^2}{\mu_o} 4A = 2 \frac{A}{\mu_o} \left\langle \frac{\mu_o 2NI}{4(l_o' + g)} \right\rangle^2 \\ &= \mu_o \frac{A}{2} N^2 \frac{I^2}{(l_o' + g)^2} \end{aligned}$$

where U = magnetic potential energy
 u = magnetic energy density = B^2 / μ_0
 ΔV = volume in gaps - $4 = Ag$
 F_{mag} = resultant magnetic force

It can be seen that LOM magnetic force is proportional to current squared and inversely proportional to gap squared.

The LOM stator and armature motion relationship in simplified form is shown in Figure 2. Here, g_0 represents the gap between the LOM stator and armature when at rest and x represents excursions from rest.

The resultant force that causes the diaphragm to oscillate is

$$F_{mag} = F_{LOM1} - F_{LOM2}$$

Thus,

$$F_{mag} = \mu_0 \frac{A}{2} N^2 \left\langle \frac{I_{LOM1}^2}{(l_0' + g_0 - x)^2} - \frac{I_{LOM2}^2}{(l_0' + g_0 + x)^2} \right\rangle = M \ddot{x} + D \dot{x} + Kx \quad (4)$$

assuming both LOMs have the same N, A, μ_0 and l_0' .

Also, from (3):

$$I_{LOM1} R_{LOM1} + \left(\frac{\mu_0 N^2 A}{l_0' + g_0 - x} \right) \frac{dI_{LOM1}}{dt} = V_{LOM1} \quad (5)$$

$$I_{LOM2} R_{LOM2} + \left(\frac{\mu_0 N^2 A}{l_0' + g_0 + x} \right) \frac{dI_{LOM2}}{dt} = V_{LOM2} \quad (6)$$

(4), (5) and (6) are the set of governing equations for the system to be analyzed.

The function $F(t)$ that generates the desired $X(t)$ is assumed to be sinusoidal. By assuming also that the diaphragm possesses a second-order response as in (4), the resultant (net) magnetic force produced by the LOMS to generate $X(t)$ must be sinusoidal. That is,

$$M\ddot{x} + D\dot{x} + Kx = F_o \sin(\omega t + \phi) = F_{mag}$$

(Note that individual LOM forces will follow a non-negative sine-squared profile due to the I^2 term in (4). The physical basis for this occurrence can be appreciated intuitively by realizing that the LOM responds unidirectionally to a bidirectional current.)

The mapping of current $I(t)$ to $F(t)$ from (4) will result in a feedforward current drive technique that can take advantage of straightforward commutation techniques to alternately stimulate opposite LOM coils. The analysis will then be carried out to include a mapping of voltage $V(t)$ to position $F(t)$ and it will be shown that this voltage drive technique essentially removes the variation in gap from the feedforward equation and greatly simplifies LOM electronics.

COMMUTATED CURRENT DRIVE TECHNIQUE

Figure 3 is a block diagram of this drive technique. From (4), and assuming that the desired force and resultant position varies sinusoidally,

$$\begin{aligned} F_{mag} &= F_o \sin(\omega t + \phi) \\ &= \frac{AN^2\mu_o}{2} \frac{I_{LOM1}^2}{(l_o + g_o - x)^2} - \frac{AN^2\mu_o}{2} \frac{I_{LOM2}^2}{(l_o + g_o + x)^2} \end{aligned}$$

Since $I(0) = 0$ (the onset of diaphragm motion), F_{mag} can be separated into two forces, F_{LOM1} and F_{LOM2} applied to LOM_1 and LOM_2 respectively. This current can be alternately turned on and off and switched (commutated) to opposite LOMs to cause symmetric motion as shown in Figure 4.

$$F_{mag} = F_{LOM1} - F_{LOM2} = F_o \sin(\omega t + \phi)$$

where

$$F_o = X_o \sqrt{(K - M\omega^2) + D^2\omega^2}$$

Commutation can be incorporated using the following expression:

$$\sin(\omega t + \phi) = \frac{1}{2} \left[|\sin(\omega t + \phi)| + \sin(\omega t + \phi) \right] - \frac{1}{2} \left[|\sin(\omega t + \phi)| - \sin(\omega t + \phi) \right]$$

F_{mag} is then expanded to include two separate components:

$$F_{LOM1} = F_o \frac{1}{2} \left[|\sin(\omega t + \phi)| + \sin(\omega t + \phi) \right] = \frac{AN^2 \mu_o}{2} \frac{I^2_{LOM1}}{(l_o' + g_o - \frac{1}{2} X_o [|\sin \omega t| + \sin \omega t])^2}$$

$$F_{LOM2} = F_o \frac{1}{2} \left[|\sin(\omega t + \phi)| - \sin(\omega t + \phi) \right] = \frac{AN^2 \mu_o}{2} \frac{I^2_{LOM2}}{(l_o' + g_o + \frac{1}{2} X_o [|\sin \omega t| + \sin \omega t])^2}$$

Solving for current I yields:

$$I_{LOM1} = \sqrt{\frac{F_o}{C} \frac{1}{2} \left[|\sin(\omega t + \phi)| + \sin(\omega t + \phi) \right] \left[l_o' + g_o - \frac{1}{2} X_o [|\sin \omega t| + \sin \omega t] \right]}$$

$$I_{LOM2} = \sqrt{\frac{F_o}{C} \frac{1}{2} \left[|\sin(\omega t + \phi)| - \sin(\omega t + \phi) \right] \left[l_o' + g_o + \frac{1}{2} X_o [|\sin \omega t| + \sin \omega t] \right]}$$

where

$$C = \frac{AN^2 \mu_o}{2}$$

This expression describes the current waveform for the "commutated current" mode of operation. It can be seen that the feedforward drive current profile must include a varying gap term in addition to constants equal to LOM electromechanical parameters (M, K and D).

Average power can be approximated using the standard relationship between peak current I_o and rms current I_{rms} for a sinusoidal input:

$$I_{rms} = \frac{I_o}{\sqrt{2}}$$

In general, assuming all power is resistive,

$$P_{avg} = I_{rms}^2 R = \frac{I_o^2 R}{2}$$

90° VOLTAGE DRIVE TECHNIQUE

Figure 5 is a block diagram of this drive technique. Using (3) and (4), the set of governing equations in terms of current and voltage for LOM1 and LOM2 are as shown previously in (5) and (6).

The following analysis is based on a first order approximation of the inductance in terms of gap. From (2) the inductance can be rewritten as:

$$L(g) = \frac{\mu_o N^2 A}{l_o'} \left\langle \frac{1}{1 + \frac{g}{l_o'}} \right\rangle$$

Expanding $L(g)$ about $g = 0$ results in:

$$L(g) = \sum_{n=0}^{\infty} \frac{L^{(n)}(0)}{n!} g^n = \frac{\mu_o N^2 A}{l_o'} \sum_{n=0}^{\infty} a_n \left\langle \frac{g}{l_o'} \right\rangle^n$$

For g and $g_o \ll l_o'$ assume all terms containing $\frac{g}{l_o'}$ are negligible. Then, since $a_0 = 1$,

$$L \sim \frac{\mu_o N^2 A}{l_o'}$$

This is the first order approximation of L .

The system equations become:

$$\mu_o \frac{AN^2}{2l_o'^2} (I_{LOM1}^2 - I_{LOM2}^2) = M \ddot{x} + D \dot{x} + Kx \quad (7)$$

$$I_{LOM1}R + \frac{\mu N^2 A}{l_o'} \frac{dI}{dt} = V_{in1} \quad (8)$$

$$I_{LOM2}R + \frac{\mu N^2 A}{l_o'} \frac{dI}{dt} = V_{in2} \quad (9)$$

assuming

$$R_{LOM1} = R_{LOM2} = R.$$

Solutions of (8) and (9) have the same following form:

$$I(t) = e^{-\frac{R}{L}t} \int_0^t e^{\frac{R}{L}\tau} V_{in}(\tau) d\tau$$

where

$$I(0) = 0$$

$$L = \frac{\mu_0 N^2 A}{l_0}$$

Taking advantage of the unique unidirectional force property of the LOM in response to bidirectional current, the following trigonometric relationship can be applied:

$$\cos(\omega t + \phi) = \cos^2 \frac{1}{2}(\omega t + \phi) - \sin^2 \frac{1}{2}(\omega t + \phi)$$

This relationship suggests that the application of two sinusoidal waveforms to opposite LOMs at one-half the operating frequency and 90° out of phase from one another will result in sinusoidal motion.

Define these stimulus voltages as follows:

$$V_{in1} = V_o \sin \omega_o t$$

$$V_{in2} = V_o \cos \omega_o t$$

where ω_o = operating frequency.

The LOM currents become:

$$I_{LOM1} = \frac{V_o}{\sqrt{R^2 + L^2 \omega_o^2}} (\sin(\omega_o t + \phi) - \sin \phi e^{-\frac{R}{L}t})$$

$$I_{LOM2} = \frac{V_o}{\sqrt{R^2 + L^2 \omega_o^2}} (\cos(\omega_o t + \phi) - \cos \phi e^{-\frac{R}{L}t})$$

where

$$\tan \phi = \frac{L\omega_0}{R}$$

The second term in each of the above equations can be ignored since it is a transient responses and will dissipate as $t \gg \frac{L}{R}$.

The steady state solution is therefore:

$$I_{LOM1} = \frac{V_o}{\sqrt{R^2 + L^2\omega_0^2}} \sin(\omega_0 t + \phi)$$

$$I_{LOM2} = \frac{V_o}{\sqrt{R^2 + L^2\omega_0^2}} \cos(\omega_0 t + \phi)$$

It can be seen that the voltage stimulus can be essentially independent of gap or LOM physical parameters K, D and M.

Let

$$F_{mag} = F_o \cos(\Omega t + \gamma)$$

and assume that F_o and Ω are known. ($\Omega = 30\text{Hz}$, F_o is computed from K, D, M). Then,

$$\begin{aligned} I_{LOM1}^2 - I_{LOM2}^2 &= I_o^2 (\cos^2(\omega_0 t + \phi) - \sin^2(\omega_0 t + \phi)) \\ &= F_o \cos(\Omega t + \gamma) \end{aligned}$$

This implies:

$$I_o^2 = F_o$$

$$\omega_0 = \frac{\Omega}{2}$$

$$\phi = \frac{\gamma}{2}$$

Letting

$$F_{LOM1} = F_o \cos^2 \frac{1}{2}(\omega t + \phi)$$

$$F_{LOM2} = F_o \sin^2 \frac{1}{2}(\omega t + \phi)$$

results in the net force shown in figure 6.

The power consumption in this case is simply:

$$P = R(I_{LOM1}^2 + I_{LOM2}^2) = RI_o^2 = RF_o$$

which is time dependent.

If a harmonic term ω_1 is introduced into both LOMs in this 90° case in order to cancel vibration, and ignoring phase shift, the result can be shown as follows:

$$\begin{aligned} F_{net} &= (I_o \sin \omega_o t + I_1 \sin \omega_1 t)^2 - (I_o \cos \omega_o t + I_1 \cos \omega_1 t)^2 \\ &= I_o^2 \sin^2 \omega_o t + I_o^2 \sin^2 \omega_1 t + 2I_o I_1 \sin \omega_o t \sin \omega_1 t \\ &\quad - I_o^2 \cos^2 \omega_o t - I_1^2 \cos^2 \omega_1 t - 2I_o I_1 \cos \omega_o t \cos \omega_1 t \\ &= -I_o^2 \cos 2\omega_o t - I_1^2 \cos 2\omega_1 t - 2I_o I_1 \cos(\omega_1 + \omega_o)t \end{aligned}$$

If the purpose is only to cancel components at twice the fundamental frequency ($= 2\omega_1$) then there will be an unwanted harmonic term at $(\omega_1 + \omega_o)$.

0° VOLTAGE DRIVE TECHNIQUE

Figure 7 is a block diagram of this drive technique. This drive method uses a sinusoidal voltage stimulus at the desired operating frequency applied to both LOMs. A DC bias voltage is added to one LOM and

subtracted from the other to form a fractional sine wave with a resultant nulling of alternating peaks. In this case, define the following voltages:

$$V_{in1} = V_o \sin \omega_o t + V_b$$

$$V_{in2} = V_o \sin \omega_o t - V_b$$

where V_b = bias voltage.

The LOM currents in this case are:

$$I_{LOM1} = \frac{V_b}{R} (1 - e^{-\frac{R}{L}t}) + \frac{V_o}{\sqrt{R^2 + L^2 \omega^2}} (\sin(\omega_o t + \phi) - \sin \phi e^{-\frac{R}{L}t})$$

$$I_{LOM2} = -\frac{V_b}{R} (1 - e^{-\frac{R}{L}t}) + \frac{V_o}{\sqrt{R^2 + L^2 \omega^2}} (\sin(\omega_o t + \phi) - \sin \phi e^{-\frac{R}{L}t})$$

Again the $e^{-\frac{R}{L}t}$ term can be ignored. Then the steady state solutions are:

$$I_{LOM1} = \frac{V_b}{R} + \frac{V_o}{\sqrt{R^2 + L^2 \omega^2}} \sin(\omega_o t + \phi)$$

$$I_{LOM2} = -\frac{V_b}{R} + \frac{V_o}{\sqrt{R^2 + L^2 \omega^2}} \sin(\omega_o t + \phi)$$

Define

$$I_b = \frac{V_b}{R} \text{ and } I_o = \frac{V_o}{\sqrt{R^2 + L^2 \omega^2}}$$

Then,

$$F_o \cos(\Omega + \gamma) = (I_b + I_o \cos(\omega_o t + \phi))^2 - (-I_b + I_o \cos(\omega_o t + \phi))^2$$

$$= 4I_b I_o \cos(\omega_o t + \phi)$$

This implies:

$$F_o = 4I_B I_o$$

$$\omega = \Omega$$

$$\phi = \gamma$$

Letting

$$F_{LOM1} = F_o \cos(\omega_o t + \phi)$$

$$F_{LOM2} = F_o \cos(\omega_o t + \phi)$$

results in the net force shown in Figure 8.

The power dissipated by the LOM can be shown to be:

$$P = R(I_{LOM1}^2 + I_{LOM2}^2) = R(2I_B^2 + 2I_o^2 \cos^2(\omega_o t + \phi))$$

Consider the average power in this case:

$$P_{avg} = R(2I_B^2 + I_o^2)$$

By minimizing the average power with the single constraint : $F_o = 4I_B I_o$:

$$\frac{\partial}{\partial I_B, I_o} P_{avg} = \frac{\partial}{\partial I_B, I_o} (R(2I_B^2 + I_o^2) - \lambda(4I_B I_o - F_o))$$

Taking the partial derivatives of this expression with respect to I_B and I_o and solving for λ results in:

$$I_o = \sqrt{2} I_B$$

then,

$$I_B = \sqrt{\frac{F_o}{4\sqrt{2}}}$$

$$I_o = \sqrt{2} \sqrt{\frac{F_o}{4\sqrt{2}}}$$

Therefore,

$$P_{avg} = \frac{RF_o}{\sqrt{2}}$$

Compared to the previous result for the 90° voltage drive case there is a reduction in power consumption. Also, in terms of input voltage:

$$I_o = \frac{V_o}{\sqrt{R^2 + L^2 \omega^2}} = \sqrt{2} \frac{V_B}{R} = \sqrt{2} I_B$$

Therefore, the bias voltage for minimum power dissipation is:

$$V_B = V_o \frac{R}{\sqrt{2(R^2 + L^2 \omega^2)}}$$

By introducing a harmonic term into both LOMs as before, (and ignoring phase shift),

$$\begin{aligned} F_{mag} &= (I_B + I_o \cos \omega_o t + I_o \cos \omega_1 t)^2 - (-I_B + I_o \cos \omega_o t + I_1 \cos \omega_1 t)^2 \\ &= 4I_B I_o \cos \omega_o t + 4I_B I_1 \cos \omega_1 t \end{aligned}$$

If the goal is cancellation of only the component at ω_1 , then this 0° approach is valid with correct selection of I_1 .

SIMULATION

Prior to hardware fabrication, a dynamic simulation was developed for the LOM. This simulation included a second order differential equation for LOM magnetic force:

$$F_{mag} = M \ddot{x} + D \dot{x} + Kx$$

It also included the electrical relationships between voltage, current, inductance and resistance:

$$I_{LOM} R_{LOM} + L \frac{dI_{LOM}}{dt} = V_{in}$$

Results for two cases are shown in Figures 9 and 10. Figure 9 shows drive current, LOM power dissipation, armature (diaphragm) position and force for the commutated current case using 30K cryocooler parameters. It can be seen that power dissipation per LOM is relatively low (~2W). Armature position is not a pure sinusoid, however, as can be seen by the accompanying FFT. The force profile contains significant higher harmonics due to the "on/off" nature of the commutated drive signal as seen in the top two traces.

Figure 10 illustrates the same variables for the 90° "continuous", one-half frequency drive approach. Here, LOM current is continuously flowing without interruption. Armature position is sinusoidal as can be seen from the FFT. Force is also monotonic. However, power dissipation is several times higher for this case.

TEST

Test data was obtained for all four drive techniques. In this case, a special configuration consisting of two compressor motors (each with two LOMs) mounted "back-to-back" was used as a test bed. The two compressor motors in this "vibration apparatus" were mounted in such a way as to cancel axial forces when operated together. Note that this configuration does not incorporate gas force; results for such a case can be extrapolated using proportional masses and damping factors, however.

Figure 11 shows the acceleration results for a single LOM driven by a 90° "continuous" drive signal. Back-to-back operation using the second motor as an active counter balance is shown in Figure 12. Peak force is reduced by a factor of 5. Harmonic amplitudes are reduced significantly; the fundamental (30Hz) is reduced by a factor of 60 (to 0.012 Newtons) while no component exceeds 0.07 Newtons. (The GSFC Specification requires <0.2 Newtons).

ACTIVE HARMONIC CANCELLATION

An acceleration feedback vibration minimization method was developed and tested using the vibration apparatus and National Instruments LabView software on a Macintosh computer.

This acceleration (force) feedback method enabled the operator to monitor the FFT of the accelerometer signal and introduce harmonic frequencies into the drive signal which resulted in a reduction of that harmonic.

Figure 13 is a block diagram used within LabView to generate the drive signal array. The various harmonics are summed with the fundamental drive frequency to develop the final LOM drive signal. The feedback loop is "closed" through the operator. The operator views the FFT of the accelerometer signal and inputs amplitude and phase to cancel each harmonic. In this experiment "anti-harmonics" out to the 7th were added to the fundamental drive frequency. The previous Figure 14 illustrates the FFT of the accelerometer signal when both vibration apparatus motors (all 4 LOMs) are operating normally. In this experiment all drive signals were in phase (0° Drive) with a 35% DC bias which resulted in approximately 12 mil peak to peak motion for each of the diaphragms. The Y axis is in Newtons and that the top line (0.2224 Newtons or 0.05 lbs) represents the GSFC specification limit for the vibration level of the 30K system. Figure 15 depicts the results of adding harmonics to the drive signals of a pair of LOMs (one motor). It can be seen that the 30Hz - 210 Hz frequency components have been reduced significantly. Figure 6 illustrates the reduction by modifying the Y axis scale. It is clear that the 30Hz - 210 Hz frequency components are below the 0.005 Newton Level. This is less than 1/45 of the specification level. It is concluded that vibration harmonics can be controlled by inserting appropriate harmonic frequencies of specific amplitude and phase into the 0° voltage drive signals.

CONCLUSION

A summary of test results is shown in Table I. A comparison of column 1 for the four test cases shows the commutated current approach dissipates the least power as predicted by analysis and simulation. However, peak vibration force is the highest amongst all candidates as also predicted.

Column 2 compares the peak vibration force values for dual back-to-back compressors using the vibration apparatus. The feedforward technique using two 90° sinusoids at one-half the fundamental frequency provides minimal vibration. However, as described earlier, use of an anti-harmonic cancellation technique with this approach resulted in the generation of multiple unwanted harmonics. The 0° voltage drive technique with DC bias provides slightly higher vibration levels (about 3X) but lends itself to active harmonic cancellation without appearance of unwanted harmonics.

The 30K Cryocooler Electronics Module is presently being designed to allow the incorporation of both control techniques for maximum flexibility.

REFERENCES:

1. Van Valkenburg, M. E., Network Analysis, 2nd Edition, 1964.

2. D'Azzo, John J., Houpis, Constantine H., Linear Control System Analysis and Design, 2nd Edition, 1981.
3. Kraus, John D., Electromagnetics, 1953.

TABLE I. COMPARISON OF FOUR CONTROL CIRCUITS

Control Circuit	Dual Compressor Power Dissipation (Watts)	Dual Compressor Peak Vibration (Newtons)
Feed Forward Using Commutated Current	7.9	0.59 (7th)
Feed Forward Using 90° Sinusoids	21.3	0.04 (4th)
Feed Forward Using 0° Sinusoids	11.6	0.11 (2nd)
Feed Forward Using 0° Sinusoids with vibration compensation	11.6	0.005 (2nd)

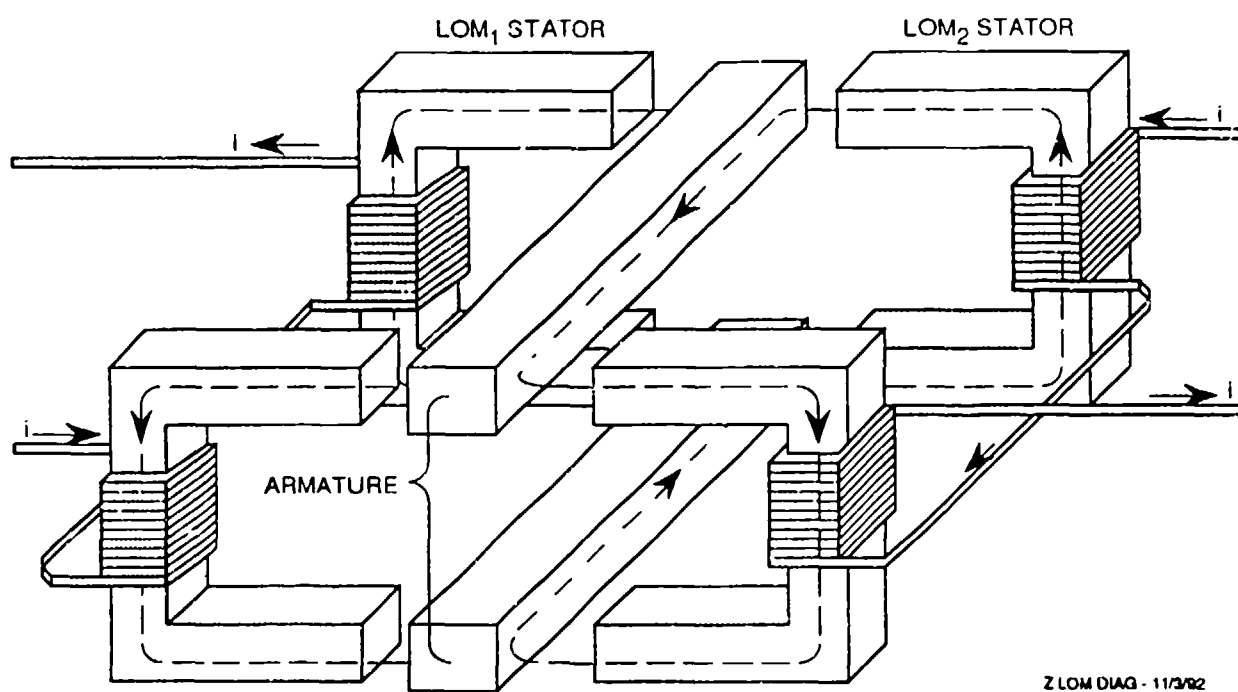


Figure 1. LINEAR OSCILLATING MOTOR (LOM)
CONFIGURATION

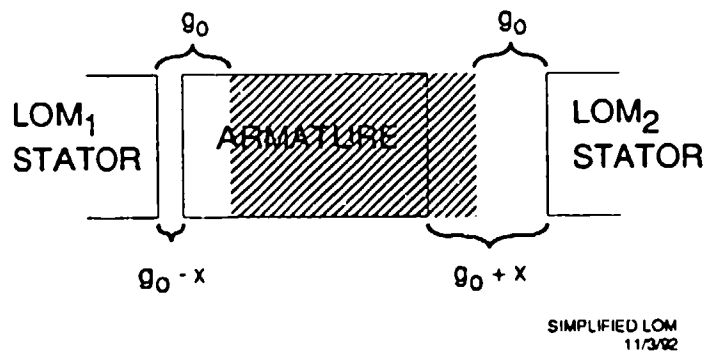


Figure 2. SIMPLIFIED LOM MOTION

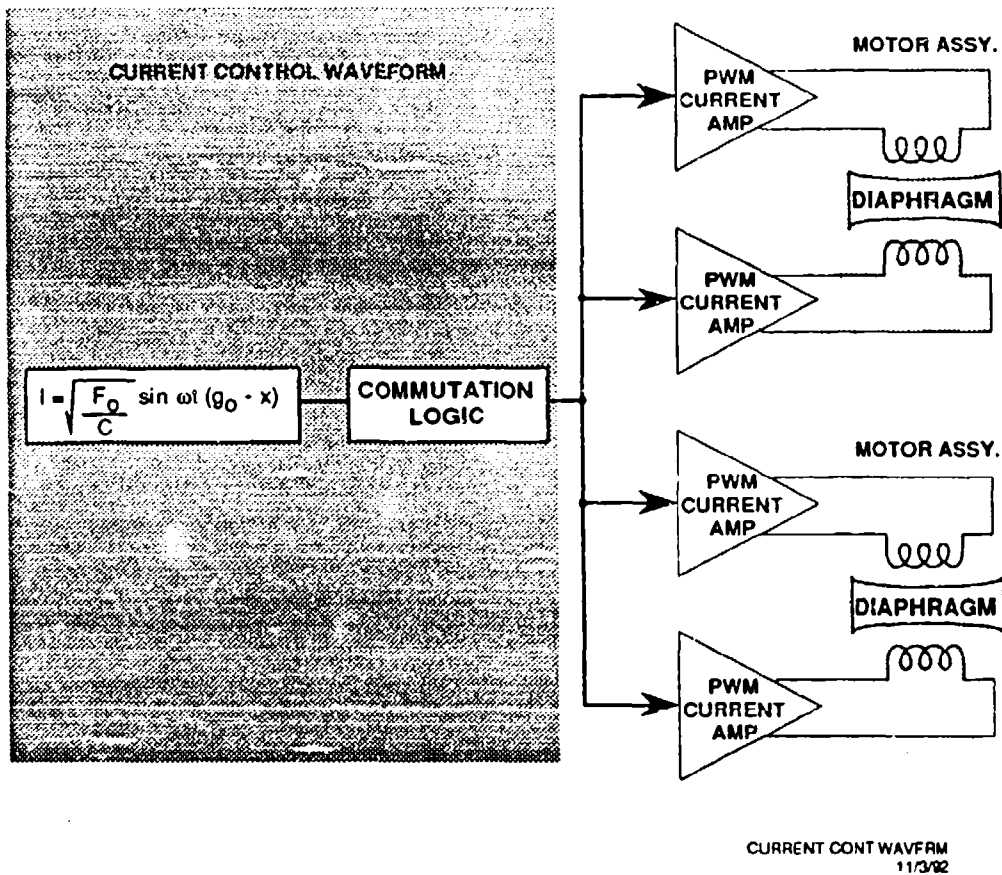


Figure 3. FEEDFORWARD CONTROL USING COMMUTATED CURRENT MODE

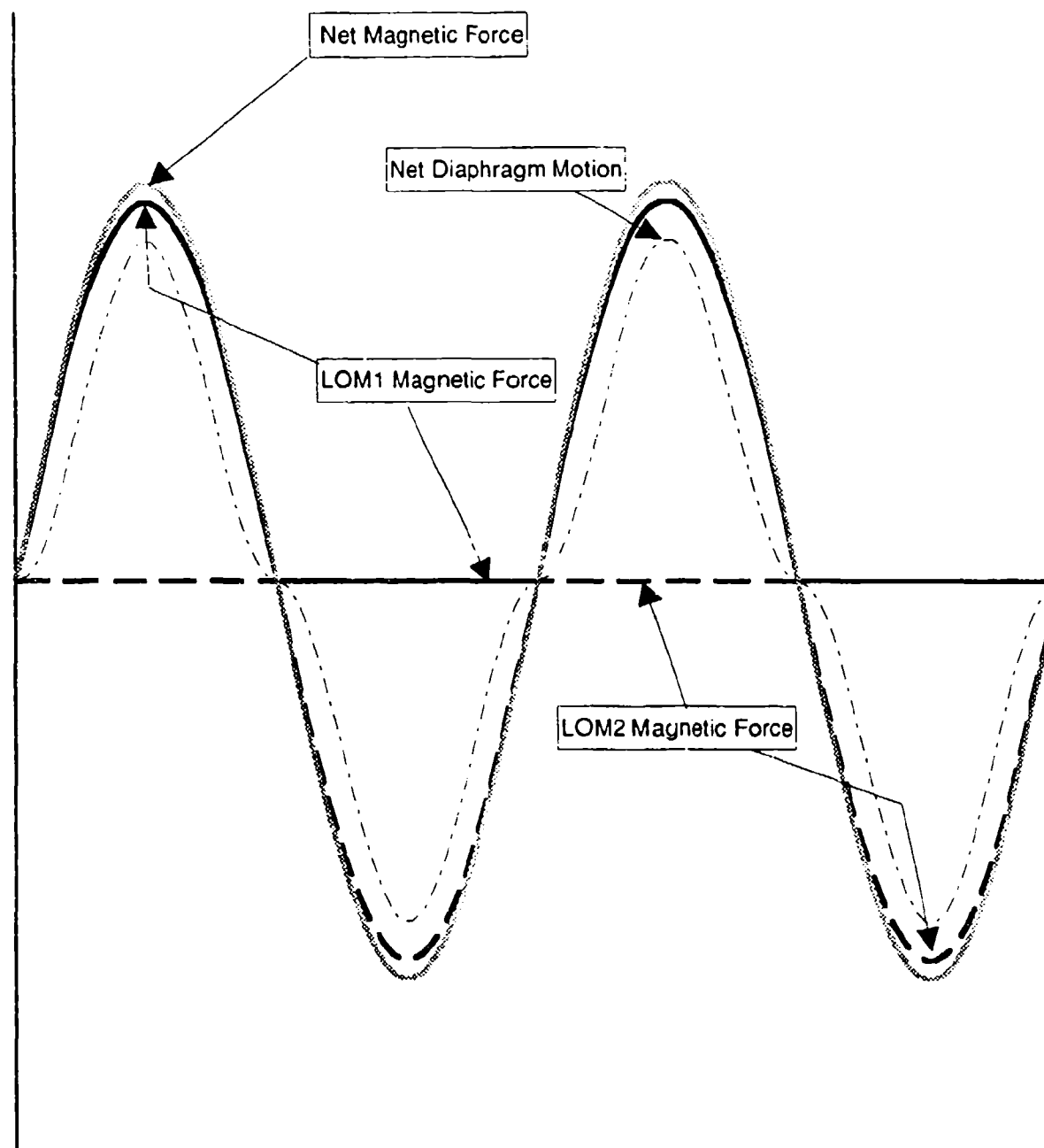
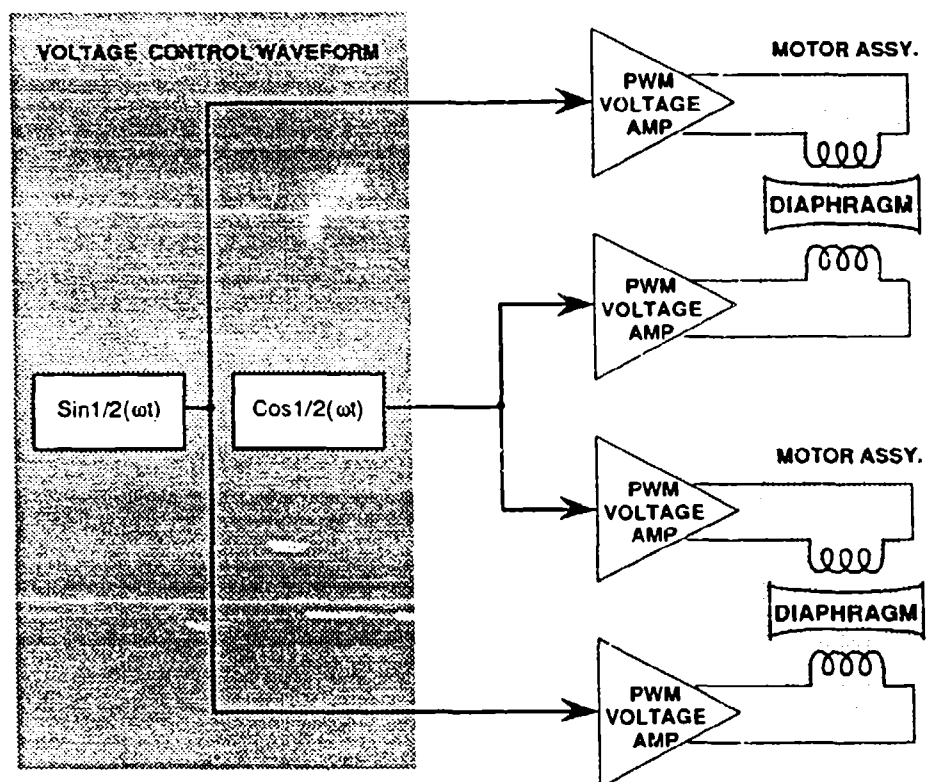


Figure 4. COMMUTATED CURRENT COMPONENT WAVEFORMS



IICAL CONT WAVEFORM
11/3/92

Figure 5. FEEDFORWARD CONTROL USING 90°
VOLTAGE MODE

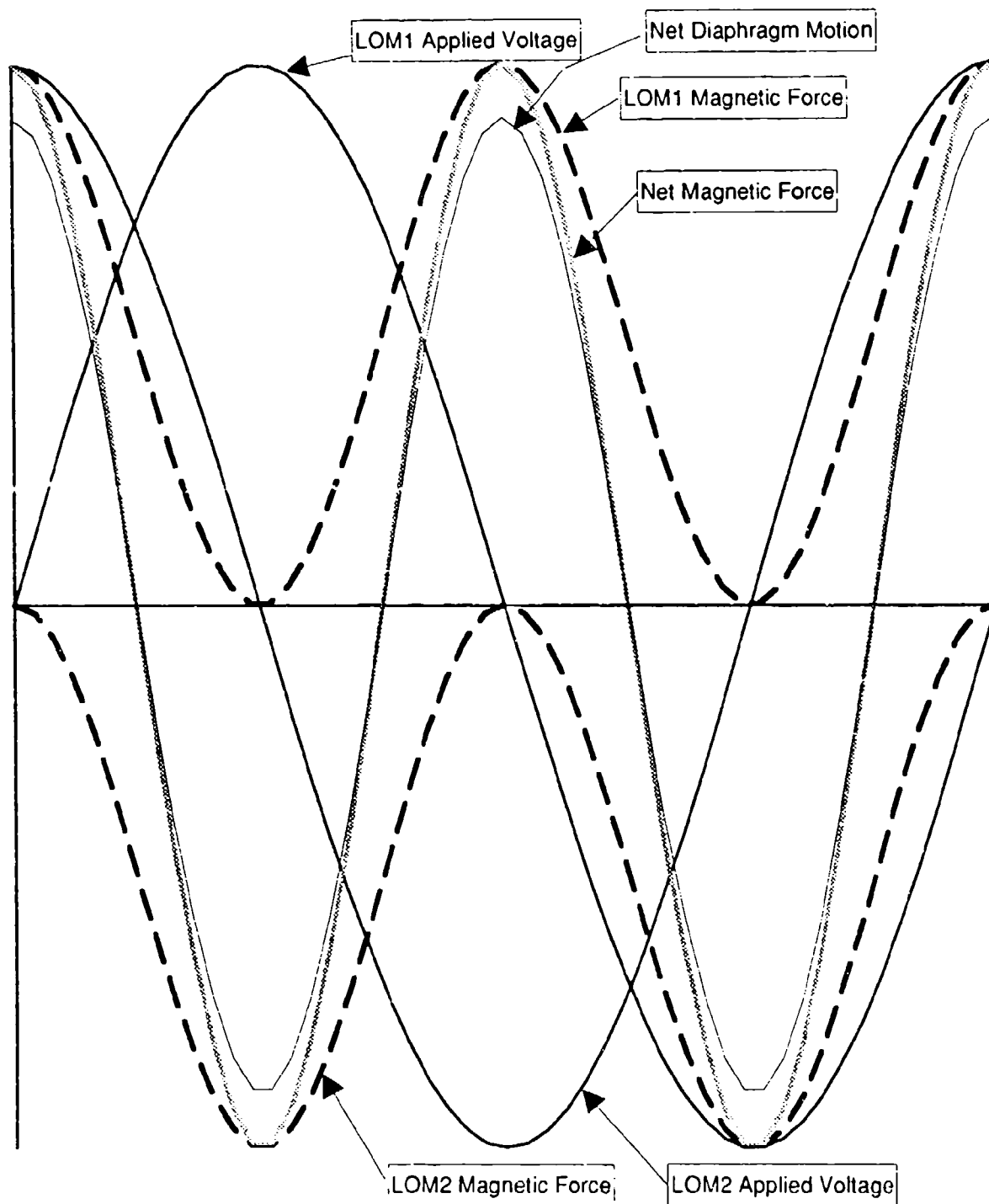
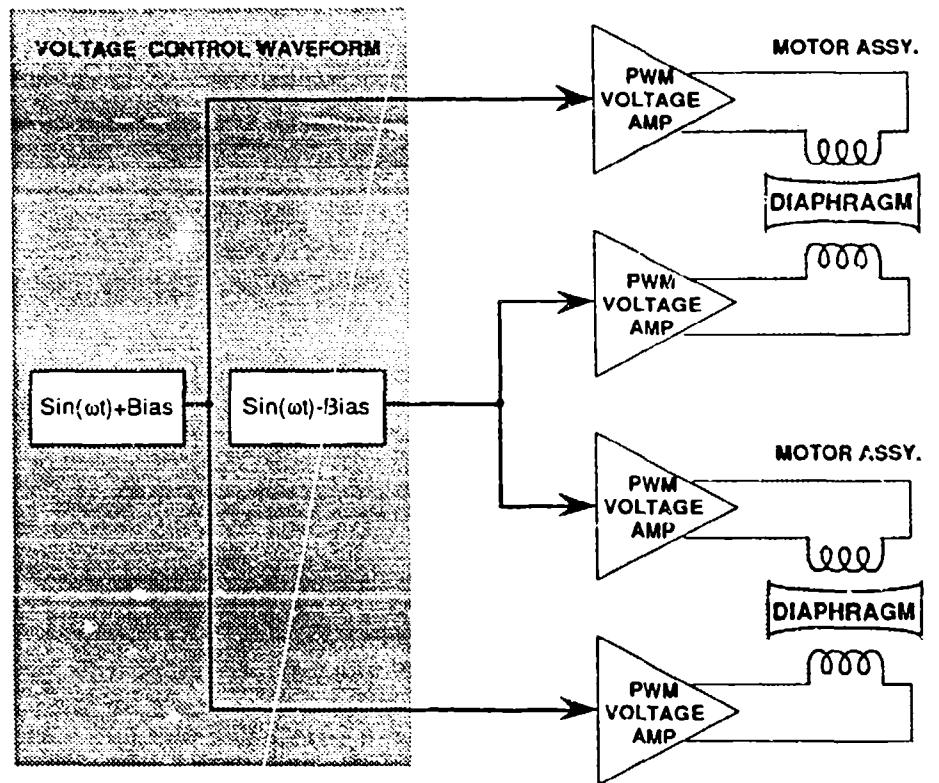


Figure 6. 90 DEGREE VOLTAGE DRIVE COMPONENT WAVEFORMS



CALCULATED CONT WAVRM
11/3/92

Figure 7. FEEDFORWARD CONTROL USING 0° VOLTAGE MODE WITH DC BIAS

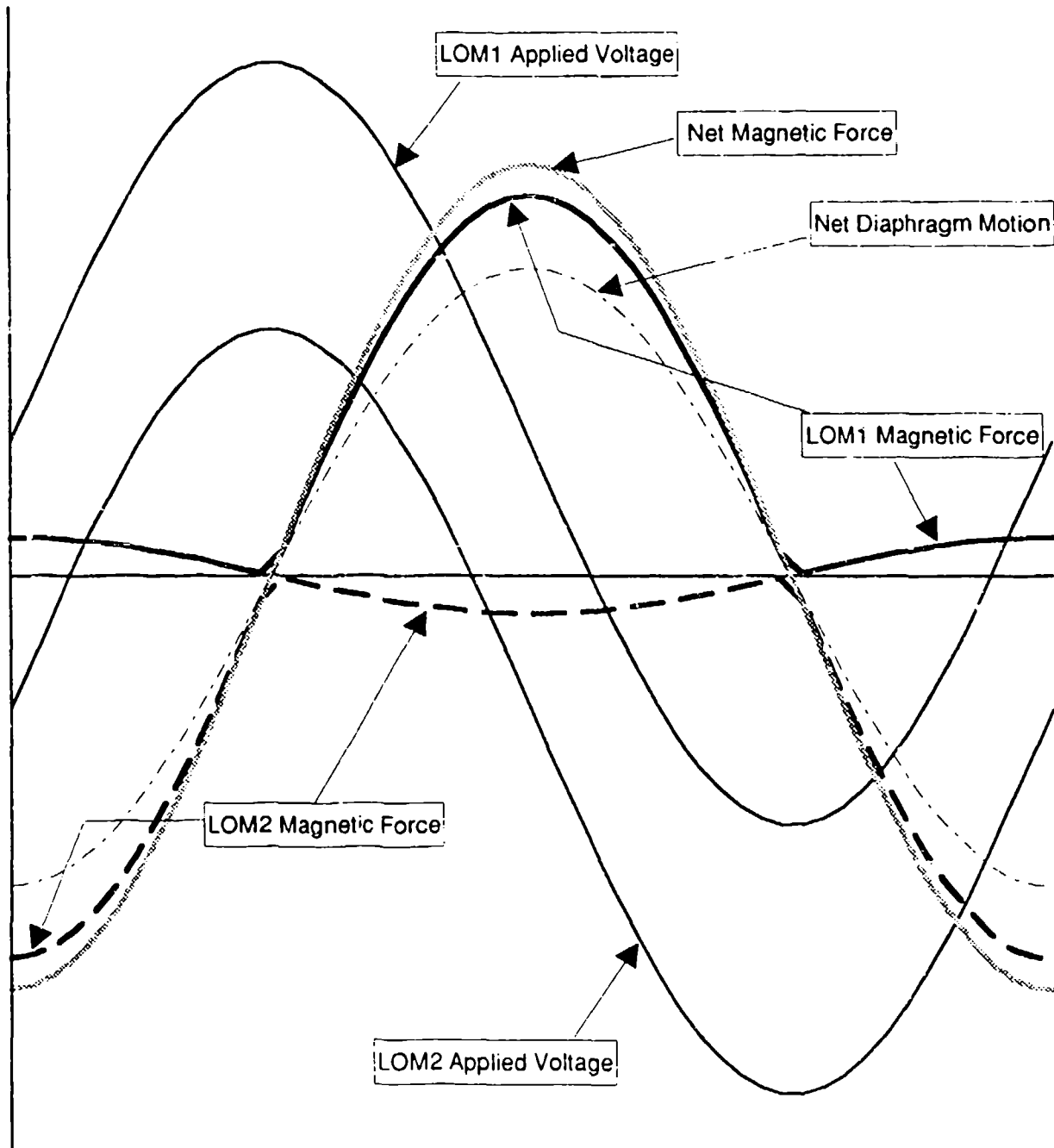


Figure 8. 0 DEGREE VOLTAGE DRIVE COMPONENT WAVEFORMS

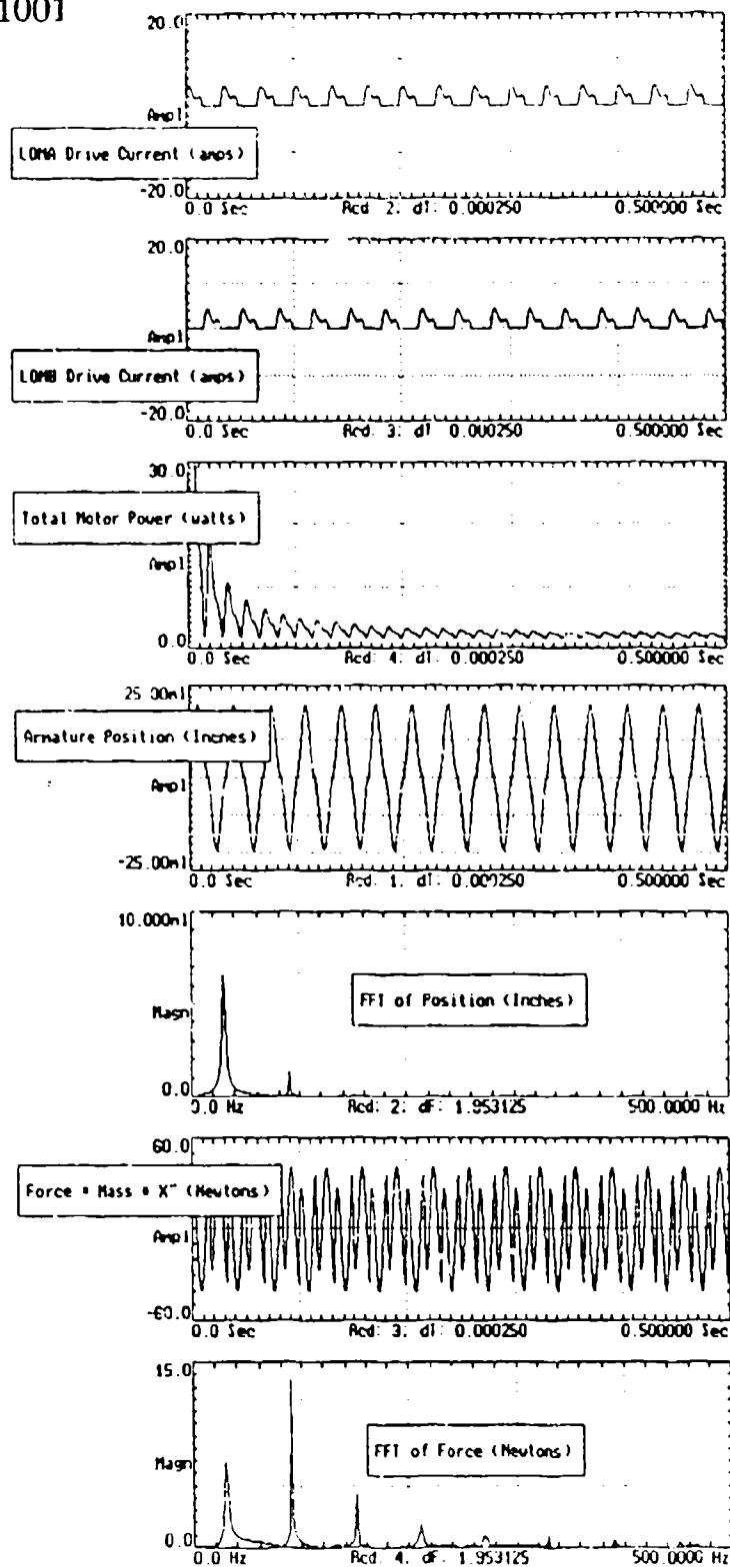


Figure 9. SIMULATION RESULTS FOR COMMUTATED CURRENT DRIVE TECHNIQUE

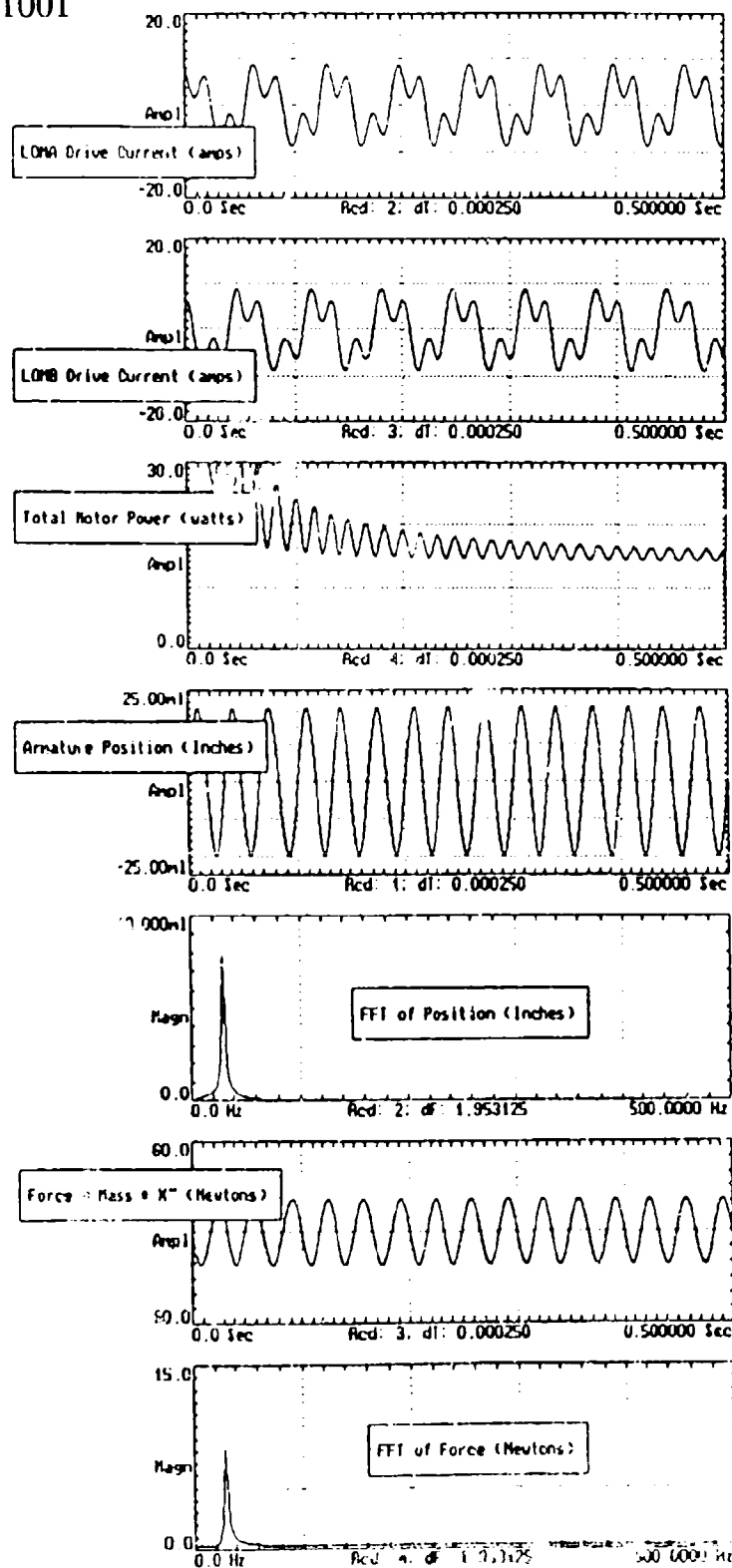


Figure 10. SIMULATION RESULTS FOR 90-DEGREE DRIVE TECHNIQUE

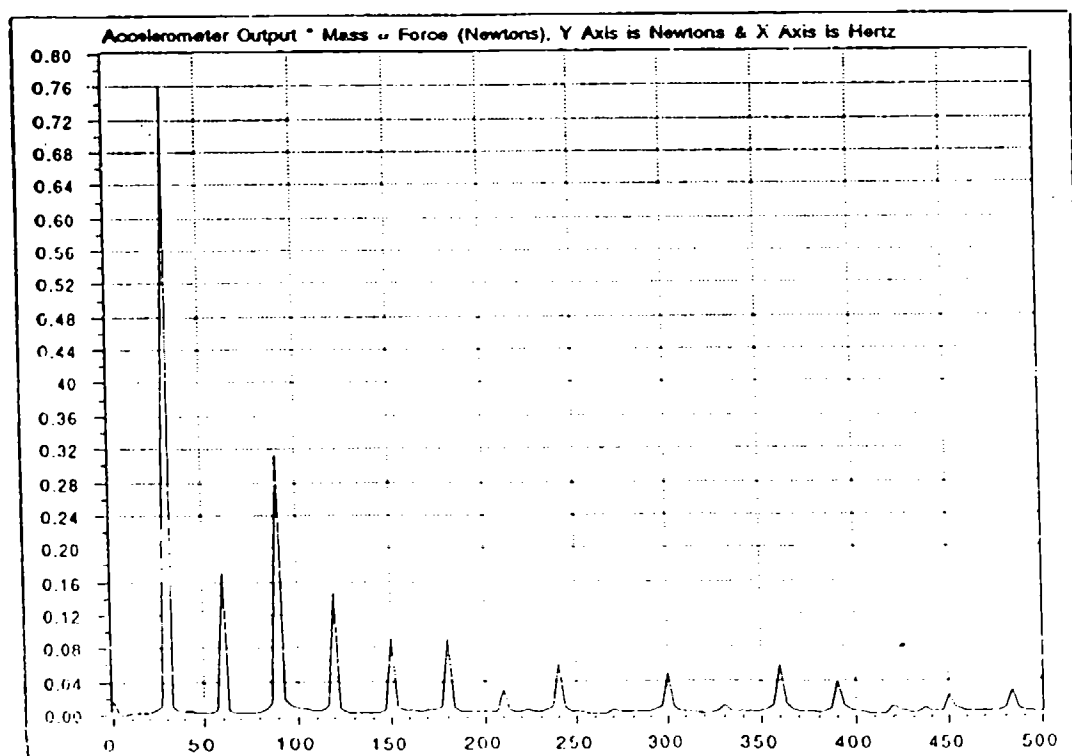
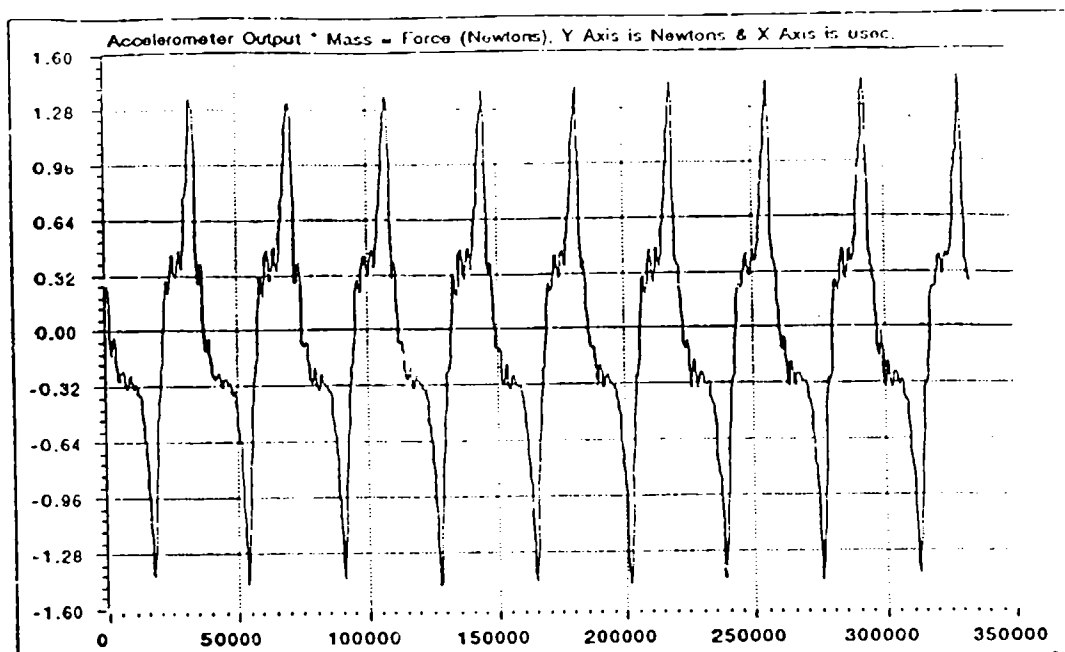


Figure 11. FORCE (ACCELERATION) RESULTS FOR SINGLE MOTOR
(TWO LOMS)

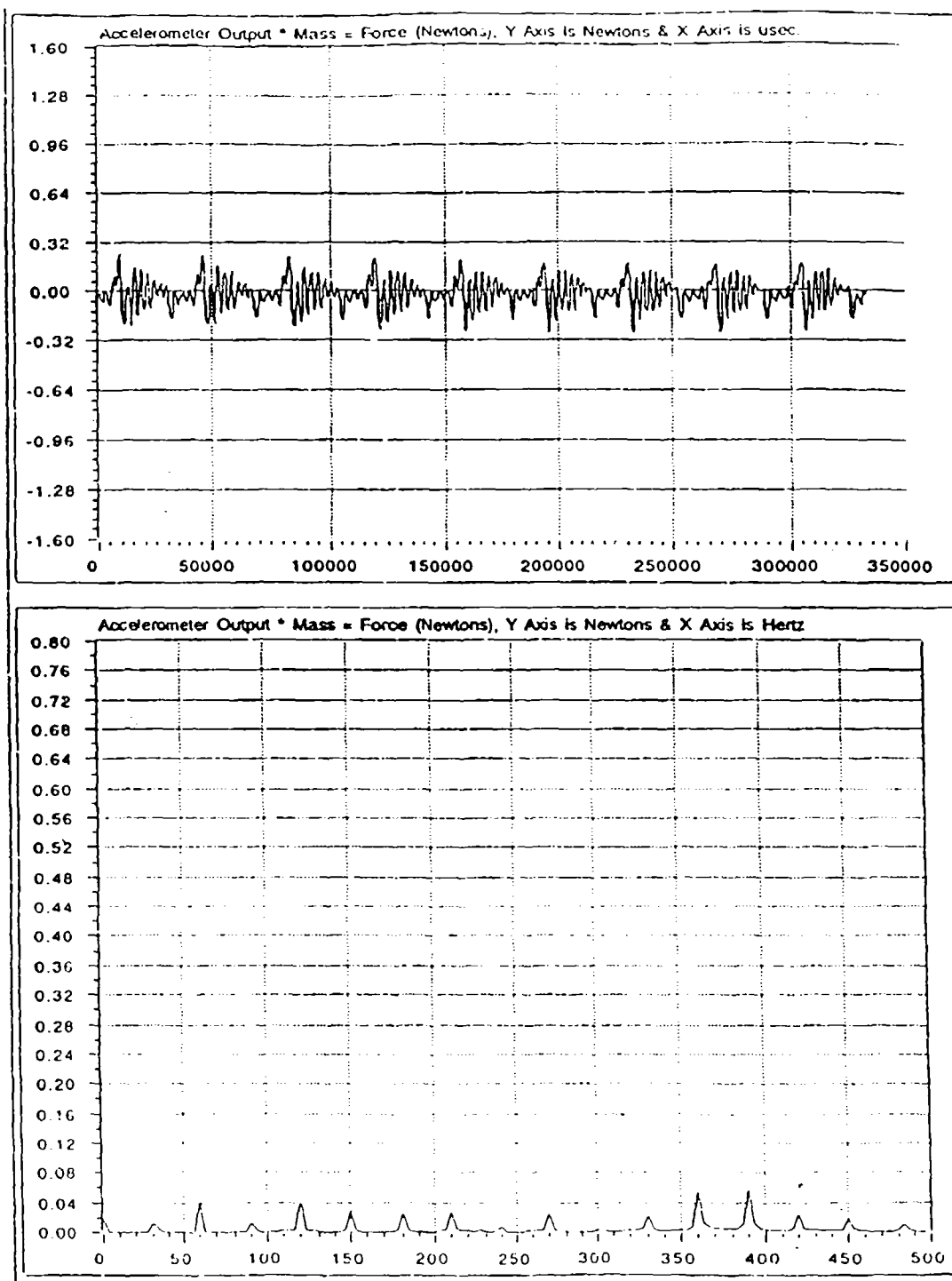


Figure 12. FORCE (ACCELERATION) RESULTS FOR DUAL OPPOSING MOTORS SHOWING HARMONIC REDUCTION

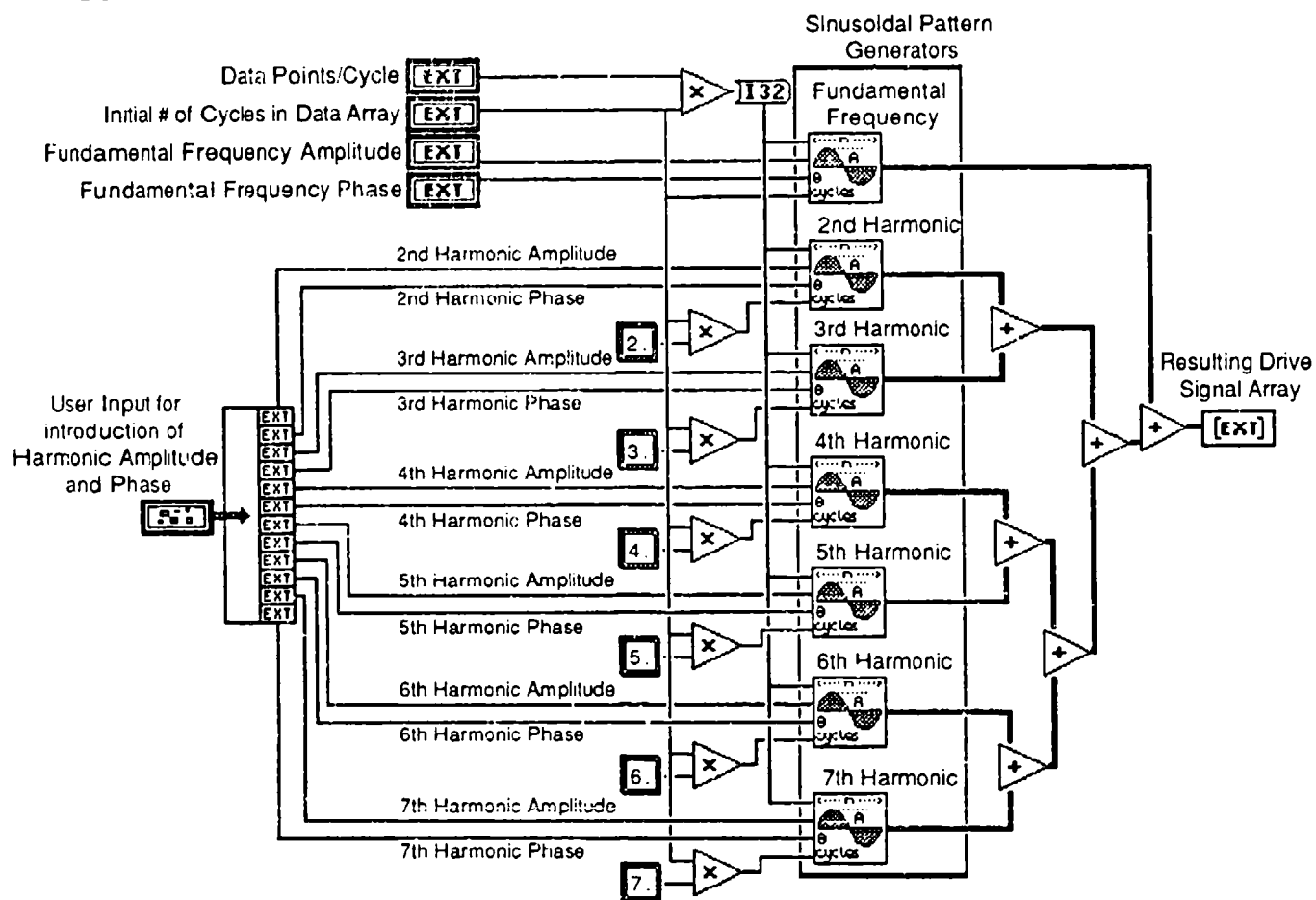


Figure 13. VIBRATION CANCELLATION ALGORITHM UTILIZING MANUAL INPUTS FROM THE USER

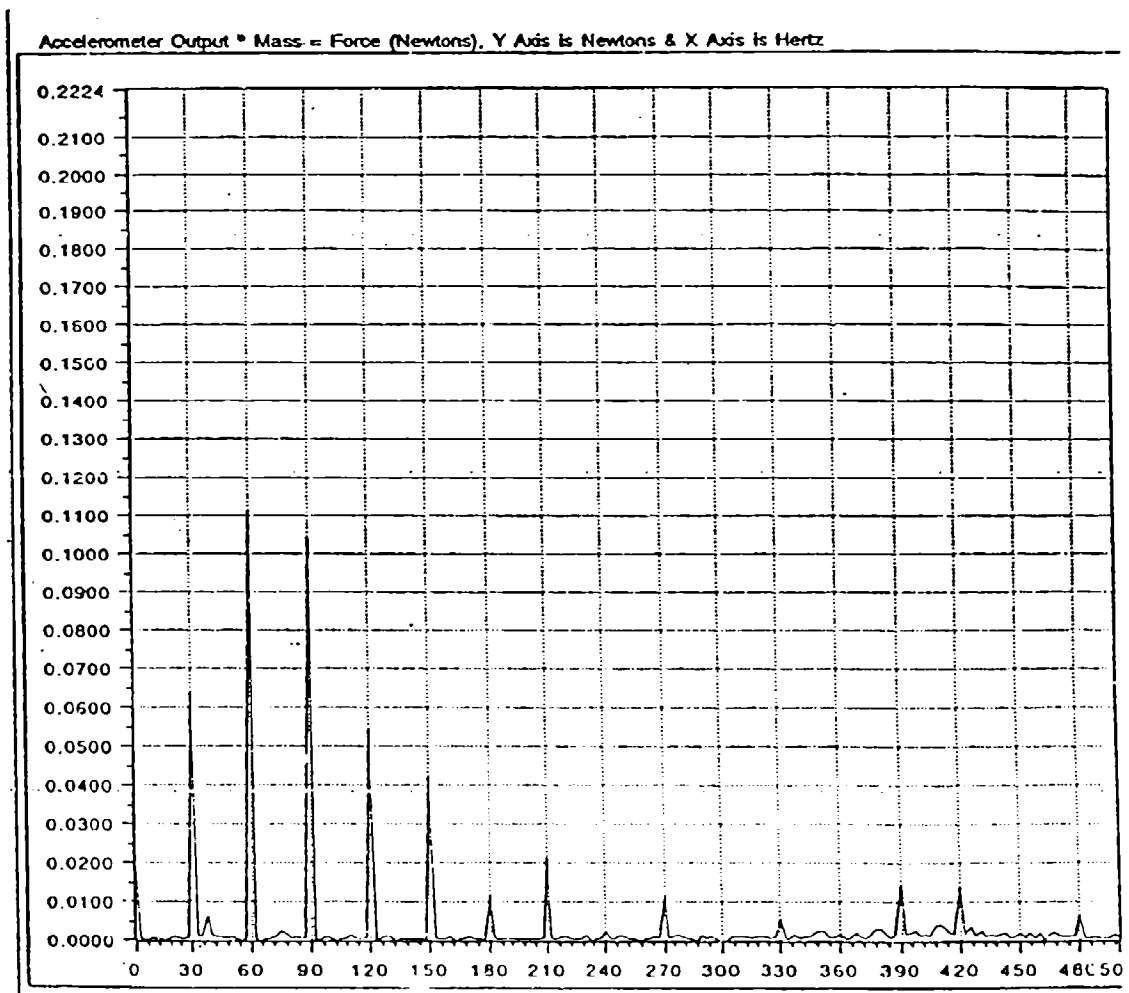


Figure 14. FFT OF ACCELERATION SIGNAL WITHOUT HARMONICS ADDED

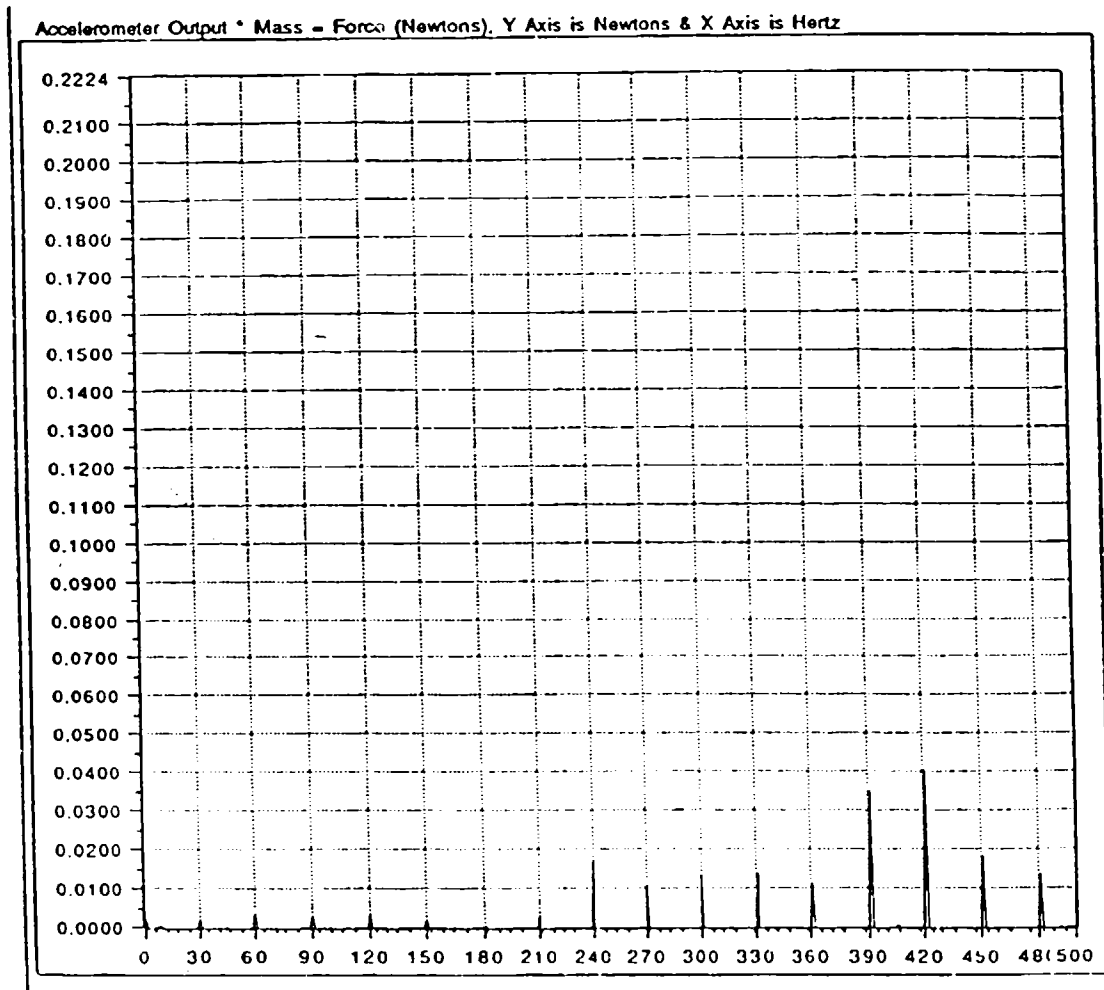


Figure 15. FFT OF ACCELERATION SIGNAL WITH HARMONICS ADDED

MAGNETIC NOISE PRODUCED BY GM CRYOCOOLERS

S. Fujimoto, H. Ogata, and H. Kado
Superconducting Sensor Laboratory
2-1200 Muzaigakuendai, Inzai
Chiba 270-13, JAPAN

ABSTRACT

Magnetic noise produced by the operation of a Gifford-McMahon (GM) cryocooler is measured. The tested GM cryocooler has two cooling stages and the valve motor (VM) can be separated from the expander to reduce the electromagnetic VM noise. A magnetic regenerative material, Er_3Ni (Erbium-3 Nickel), is used in the second-stage regenerator in order to liquefy helium without using a Joule-Thomson circuit. This material becomes magnetized under an environmental magnetic field, which causes oscillation of the magnetic field due to the reciprocal movement of the regenerator. Experimental results show that the field oscillation amplitude decreases as the distance between the center of the regenerator and the measuring point increases and that the amplitude of field oscillation at a point 0.3 meters from the regenerator is less than 10^{-5} of the environmental field. A suitable design will provide a highly sensitive SQUID magnetometer cooled by a GM cryocooler if it is used in a magnetically-shielded room.

INTRODUCTION

A key requirement for cryocoolers used in SQUID magnetometers is the reduction of mechanical vibration and electromagnetic noise. At present, most cryocoolers used for SQUIDs are Gifford-McMahon (GM) /Joule-Thomson (JT) cryocoolers. [1][2] These cryocoolers are usually rather large and complex due to JT circuits, but when a rare-earth regenerative material is used in the GM cryocooler expander,

liquid helium temperatures can be attained without the JT circuit.[3] Using this type of GM cryocooler therefore results in cooling systems that are smaller, lighter, simpler, and more reliable, in spite of their lower cooling efficiency. The rare-earth material used in the regenerator is usually ferro-magnetic or antiferro-magnetic, and thus produces magnetic noise due to reciprocal movement. This paper describes the magnetic noise of a GM cryocooler using magnetic regenerative material, and presents an example of its application to a SQUID cooling system.

EXPERIMENTAL APPARATUS

The tested GM cryocooler has two cooling stages. Its specifications are summarized in Table 1. The expander is pneumatically driven [4] and the valve motor (VM) can be separated from the expander to reduce the electromagnetic VM noise. [5] As shown in Figure 1, we placed the VM 1.8 meters from the expander and connected them with a plastic tube. Almost all of the magnetic materials used in the expander (such as the backup spring for the second displacer gas seal and the pin in the connecting rod between the first and the second displacer) were replaced with non-magnetic materials (such as a phosphor bronze spring and a titanium pin).

Table 1. Specifications of the tested cryocooler.

displacer stroke	11.2 mm
inside dia. of first cylinder	50.8 mm
inside dia. of second cylinder	25.4 mm
operating frequency	2.0 Hz

We first measured the axial magnetic noise produced by a conventional expander in an environmental magnetic field. We then replaced the lead material in the second displacer with Er_3Ni (Erbium-3 Nickel) and measured the magnetic noise again. The mean temperature of the second cooling stage was about 4.5

K. The axis of the expander was horizontally-oriented parallel to the earth's magnetic field.

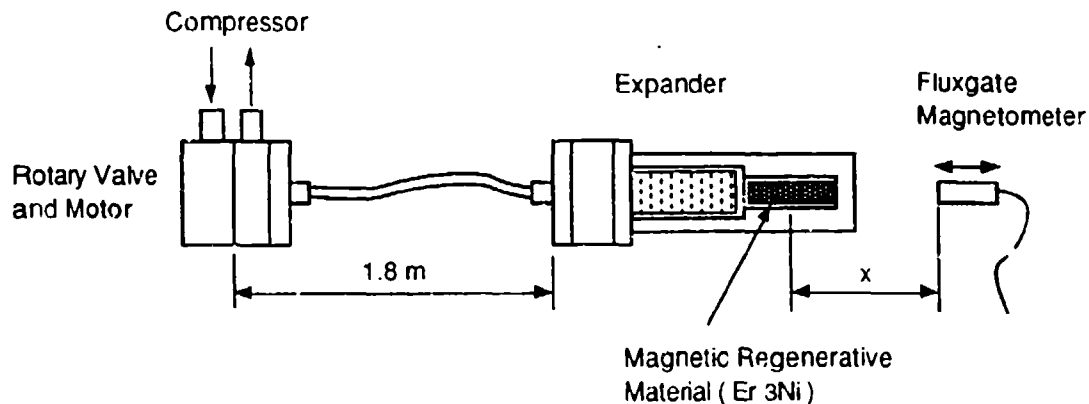


Figure 1. Schematic of experimental apparatus.

EXPERIMENTAL RESULTS

A typical magnetic noise pattern produced by a GM cryocooler using magnetic regenerative material is shown in Figure 2, where ΔB is the amplitude of the field oscillation. The phase of the oscillation is synchronized with the movement of the displacer. Figure 3 shows the 0.5 - 10 Hz magnetic noise spectrum. At a fundamental frequency of 2.0 Hz and its harmonics, there is noise due to the displacer movement, but VM operation frequency (1.0 Hz) noise is not seen. Figure 4 shows that the amplitude of 2.0-Hz noise decreases according to $x^{-2.5}$, where x is the distance between the center of the regenerator and the measuring point. The noise produced by the magnetic regenerative material is about six or seven times that produced by a cryocooler using non-magnetic material (lead).

If an expander could be constructed without any magnetic materials, the noise level should be zero. This tested expander, however, includes a few magnetic materials (such as a welded stainless-steel cylinder) which vibrate due to the movement of the displacer and gas in the expander. Noise may also result from the non-magnetic materials due to induced

electrical current in the regenerator materials such as lead and phosphor bronze, moving in the uniform earth magnetic field. This noise factor has not yet been clarified. The experimental results for Er_3Ni should closely approximate the actual noise produced by magnetic regenerative material, however, since the noise level for lead is relatively low.

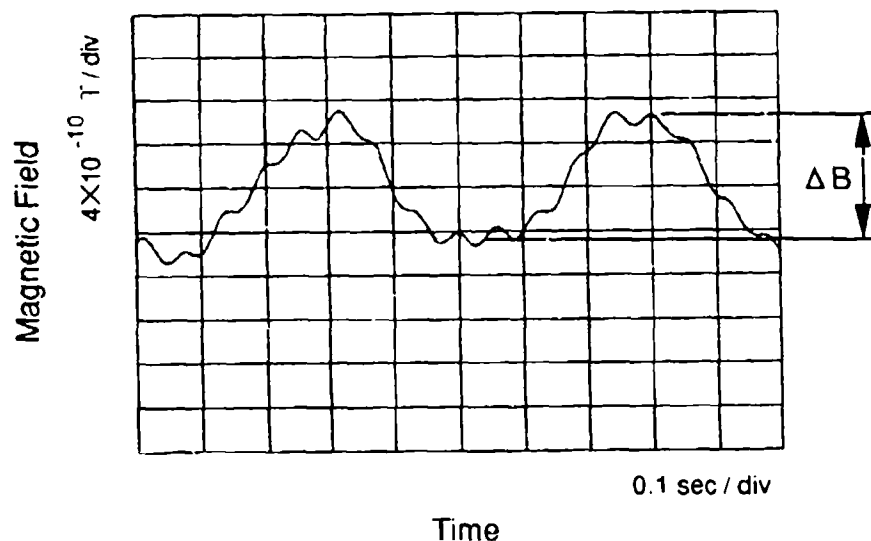


Figure 2. Typical magnetic noise pattern.

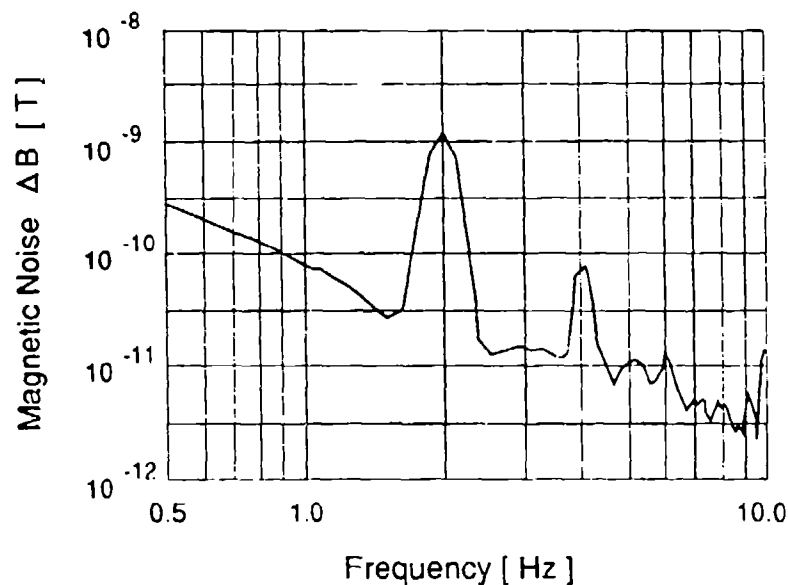


Figure 3. 0.5-10 Hz noise spectrum.

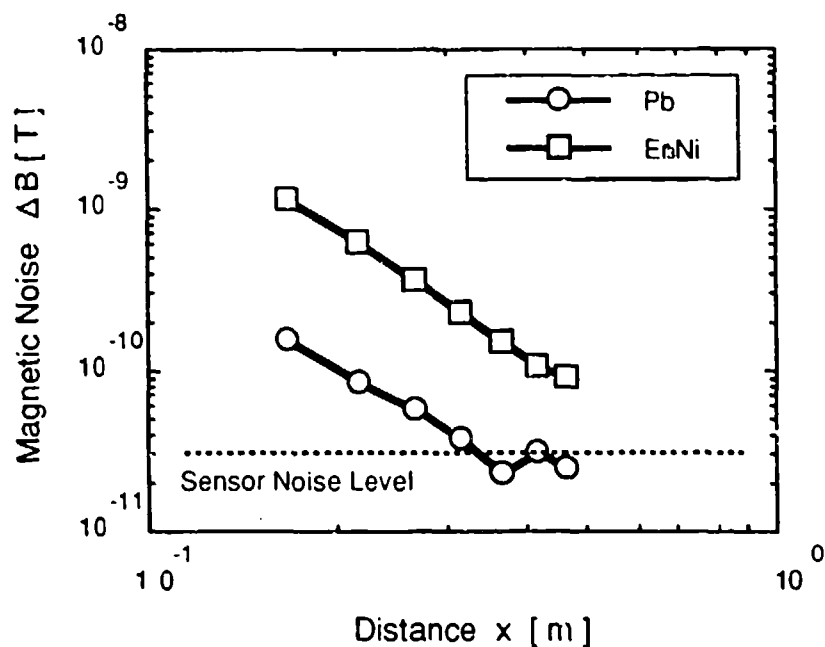


Figure 4. Relation between distance and magnetic noise.

CALCULATION AND COMPARISON WITH EXPERIMENTAL RESULTS

We estimated the oscillation of the magnetic field due to reciprocal regenerator movement by using integral computational analysis of magnetic fields. The model dimensions are shown in Table 2; they are equal to those of the tested cryocooler.

Table 2. Numerical analysis model dimensions.

Outside Dia. of Regenerator	19.05 mm
Length of Regenerator	78.0 mm
Magnetic Susceptibility of Matrix	0.28

In this analysis, the regenerator was assumed to be a cylindrical ingot and static in the environmental field, B_0 , that is the same as the experimental conditions. We calculated the field around the regenerator, $B(x)$, and obtained ΔB as $B(x-S/2) - B(x+S/2)$, where S is the displacer stroke. We found that magnetic regenerative material produces magnetic noise only along its axial direction. In Figure 5, the

calculated results are compared with the experimental results. The magnetic noise ratio is expressed as the magnetic noise to the environmental field, $\Delta B/B_0$. The results show relatively good agreement.

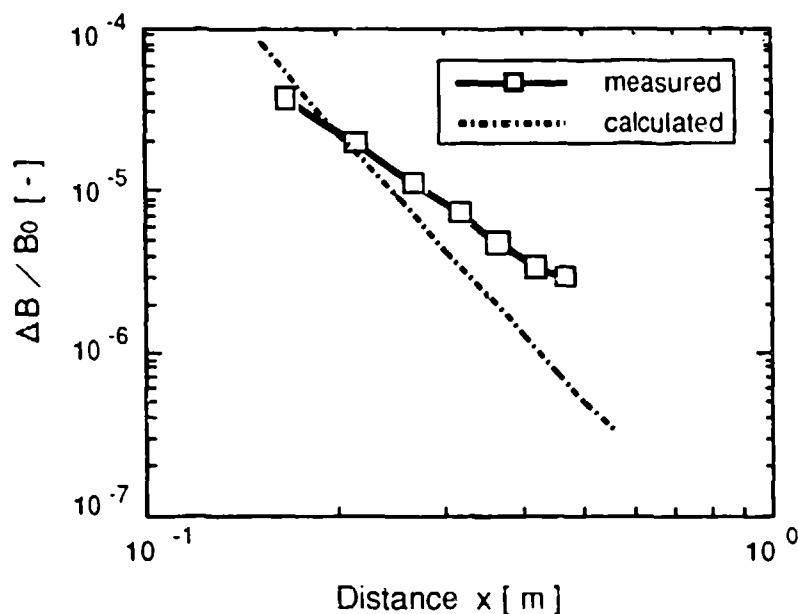


Figure 5. Measured vs. calculated results of field oscillation due to magnetic materials.

DISCUSSION

From Figure 5, the noise produced by the magnetic regenerative material is 10^{-5} of the environmental magnetic field at a point 0.3 meters from the center of the regenerator. If this expander were operated in a magnetically-shielded room in which the dc shielding factor was larger than 10^3 , the noise level at the operating frequency might be less than 10^{-12} T. As shown in Figure 6, this noise level is smaller than the magnetic signal level from the human heart.

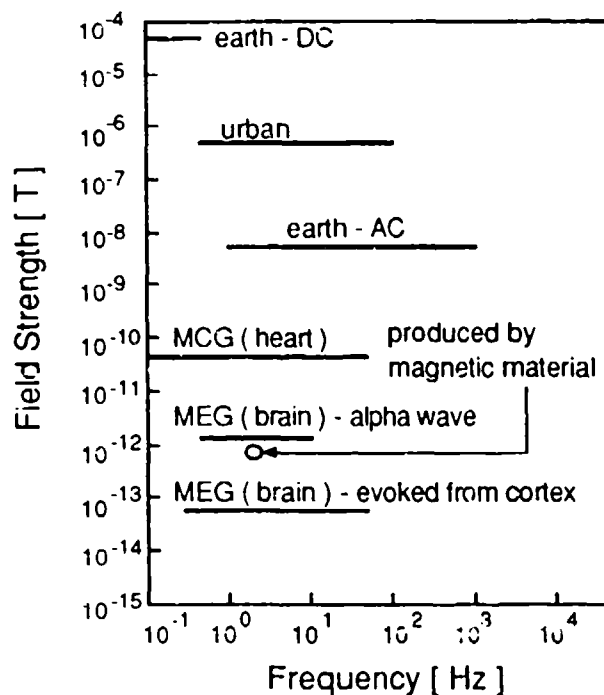


Figure 6. Magnetic noise strength compared with magnetic signals from the human body.

MCG : Magnetocardiogram

MEG : Magnetoencephalogram

APPLICATION

Figure 7 shows an example of a GM cryocooler system used for cooling a SQUID magnetometer. A SQUID and a pickup coil are placed at the bottom of a liquid helium bath in a vacuum chamber. The liquid helium bath and the vacuum chamber are almost vibration-isolated from the expander by the use of a bellows and rubber bumpers. The first cooling stage of the expander and the liquid helium bath are thermally connected by many cooling fins, but are not connected mechanically. When a single-channel SQUID is cooled by using this system, the heat load of the first and second cooling stages are estimated to be 2.8 watts at 50 K and 26 milli-watts at 4.5 K, respectively.

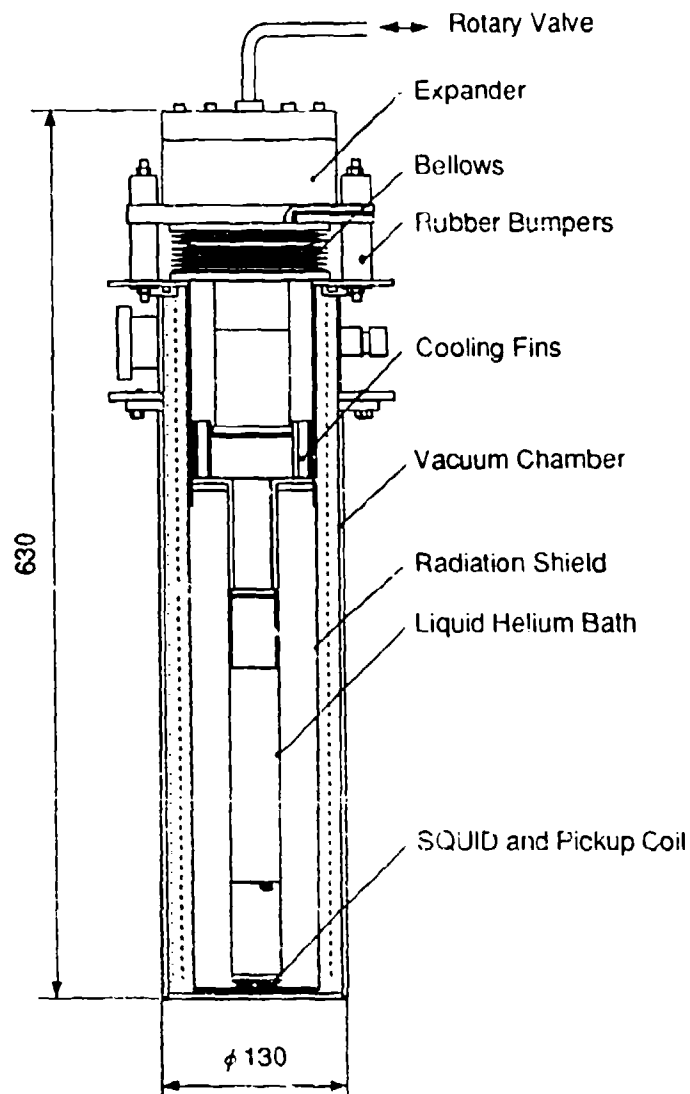


Figure 7. Schematic of a SQUID cooling system using a GM cryocooler.

CONCLUSION

A GM cryocooler using a magnetic regenerative material, Er_3Ni , was found to produce large field oscillation due to the movement of the regenerator. The magnitude of the field oscillation (magnetic noise) was 10^{-3} of the environmental field at 0.3 meters from the center of the regenerator. The calculated magnetic noise agrees well with the experimental

results. The feasibility of a SQUID cooling system using a GM cryocooler with Er_3Ni was demonstrated.

REFERENCES

1. D.S. Buchanan, D.N. Paulson, G.A. Klemic, and S.J. Williamson, "Development of a Hybrid Gifford-McMahon Joule-Thomson Based Neuromagnetometer CryoSQUID", Proc.CRYOCOOLERS 5 (1988) pp. 35-46.
2. Y.M. Kang, T. Ogura, S. Uosaki, K. Sakitani, S. Sochi, S. Fujimoto, K. Sata, and N. Fukui, "4K GM/JT Cryocooler for Cryogenic Sensors", Proc.CRYOCOOLERS 6, vol. 1(1990) pp. 17-25.
3. T. Kuriyama, R. Hakamada, H. Nakagome, Y. Tokai, M. Sahashi, R. Li, O. Yoshida, K. Matsumoto, T. Hashimoto, "High Efficient Two-Stage GM Refrigerator with Magnetic Material in the Liquid Helium Temperature Region", Adv. Cryog. Eng., vol. 35(1990) pp. 1261-1269.
4. R.C. Longworth, "A Modified Solvay-Cycle Cryogenic Refrigerator", Adv. Cryog. Eng., vol. 16(1971) pp. 195-204.
5. R.C. Longworth, "Interfacing Small Closed-Cycle Refrigerators to Liquid Helium Cryostats", Cryogenics, vol. 24, no. 4(1984) pp. 175-178.

**REGENERATOR TWO-PHASE "SINGLE-BLOW" FOR PERFORMANCE
EVALUATION AT SMALL VELOCITIES:
ORIENTATION INFLUENCE AT "1g"**

K.V. Ravikumar, R. M. Carandang, T.H.K. Frederking
Chem. E. SEAS, UCLA, LA 90024 CA

and

Robert Confair* , Winn Hong*, Faiz Sherman*, Cristina Toribio*

ABSTRACT

The "single blow" transient technique has been used mostly for single-phase fluid flow, e.g. gas flow^{1,2}. We have extended the blow test (BT) to two-phase (gas-liquid) fluid flow at small velocities in order to evaluate the performance of screen regenerator stacks. As the BT - velocity is reduced, our screen stack results show a deterioration in regenerator performance starting at an "onset" flow speed. After undergoing a transition, a plateau-like reduced rate of heat transfer is observed. We have extended our studies to include the influence of stack axis orientation with respect to the gravitational buoyancy direction at "1g". Various screen and perforated plate systems have been used. Some configurations, such as plates, show directional sensitivity, while screen-like stacks do not exhibit a significant orientation influence.

INTRODUCTION

Cryocoolers with reliability, compactness and efficient operation require extension of hydrodynamic and thermal equilibration processes to small velocities. We focus attention on the regenerator performance at relatively high density differences. They arise in conjunction with a recently proposed two-phase "single blow" protocol. In the present investigation we supplement previous work looking at gravitational driving forces at "1g" (g = gravitational acceleration) with the goal of a better understanding of compact structures, such as screens and perforated plates.

The transient methods for cryocooler regenerator performance evaluation include the "single blow" test. In our modified version of the test, there is the advantage of

*) Undergraduate research participants including SRP students, UCLA.

short blow test times. However there is a need to understand thoroughly the response of thermodynamic parameters in various flow regimes, such as stagnant fluid conditions, fluctuation influences and various convection modes. In the present paper we investigate the angular dependence of regenerator performance in a modified BT version using the gravity - related buoyancy force as the BT "driver". In these runs, the sample stack's axis is varied with respect to the "g" direction. The early phase of this work has been presented by Luna et al. (ref. 3 and related references). We address first a two-phase reference case in order to assess the influence of transport processes occurring at the peak flux of nucleate boiling in cryogenic liquids. This mode of transport has been probed by many investigators. After a discussion of the "peak" orientation influence, we examine the experiments conducted with various regenerator stack systems, discuss the results and present conclusions.

ORIENTATION REFERENCE CASE: "1g" results for plates and ducts

The reference case selected is the "peak flux" of nucleate boiling known to be sensitive to orientation with respect to gravitational buoyancy. The first case selected is the flat plate of a pure metal with the heat flowing up from a horizontal setup to an angle ϕ of about 60 degrees; ϕ is the angle between the gravitational buoyancy direction and the normal to the surface. The second case is an open-ended duct rejecting heat at the side of the rectangular cross section.

Flat plate. The simplified equation for the first case is given as (average) angle-dependent vapor velocity.

$$v_v = q_p / [\rho_v \lambda] = 0.16 [(g \cos \phi) \sigma \Delta \rho]^{1/4} / \rho_v^{1/2} \quad (1)$$

[v_v , vapor velocity ; q_p , peak heat flux density; λ , latent heat of vaporization; ρ_v , density of saturated vapor; $\Delta \rho$, density difference between the saturated vapor density and the saturated liquid density; σ , surface tension; g , gravitational acceleration). Figure 1 shows the vapor velocity prediction for He I and experimental He I data⁴. The configuration is shown schematically in the inset of figure 1. It is seen that there is agreement in a ϕ - range from zero (horizontal plate) up to about 45 degrees.

Vertical duct with rectangular cross section. The duct axis is inclined at the angle ϕ with respect to the gravitational buoyancy. A simplified model of Lehongre et al.⁵ and its modification by Sato and Ogata⁶ for He I data takes into account the duct axis orientation. We make use of a simplified version of the model. The average vapor velocity of continuum flow conditions is expressed by the following equation.

$$v_v = v_{ref} [\cos \phi] \quad (2)$$

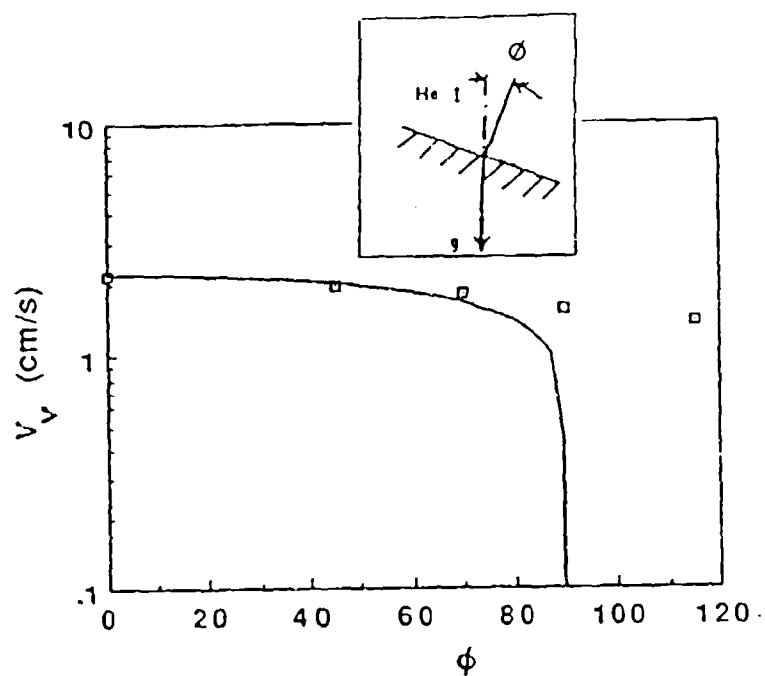


Fig. 1. Orientation influence: average "peak" vapor velocity (calorimetric velocity) versus the angle of orientation ϕ ; (the calorimetric velocity is the ratio of the heat flux density divided by the latent heat per unit volume of vapor).

Data points, ref. 4 ; --- $v_0 [\cos \phi]^{1/4}$; v_0 = value for $\phi=0$; inset: configuration.

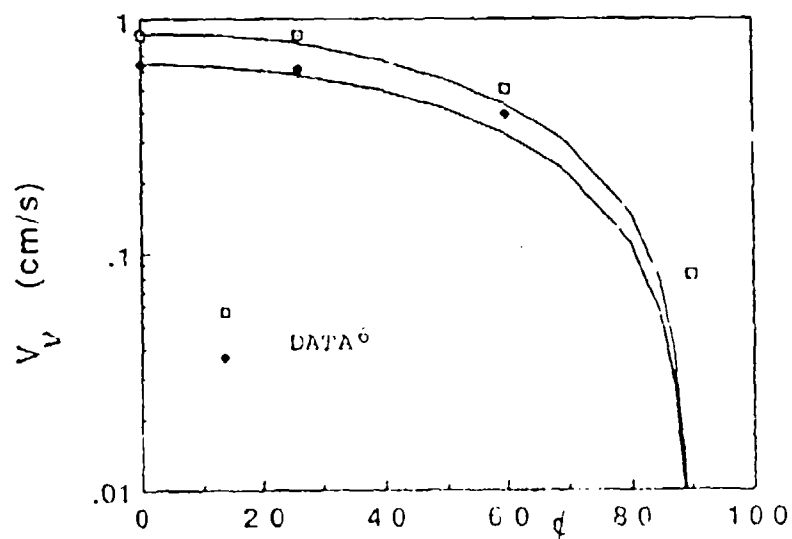


Fig. 2. Orientation influence: average "peak" vapor velocity (= calorimetric continuum velocity) versus angle of orientation (ϕ); data of ref. 6; -- $v_0 [\cos \phi]$

The reference value is the highest velocity for the duct with vertical axis [$\cos \phi = 1$]. To first order, within data scatter, the experimental results in figure 2 appear to agree with equation (2) in the range from ϕ equal to 0 to about 40 degrees. However, other side wall heating conditions for the duct with rectangular cross section show maximum velocities not at $\phi = 0$, but for finite ϕ - values where the duct axis is inclined.

GEOMETRY OF REGENERATOR SAMPLES

We have used three types of regenerator stacks. These are fine wire mesh screens, partially perforated plates containing a hexagonal flow geometry, and perforated plates with circular holes arranged within hexagonal "macro-cells".

Screen stacks. 500 mesh stainless steel has been used. The wire diameter is nominally 1 mil. Figure 3a shows a single screen stack with a thermocouple in the middle. This stack has a overall height of about 1 in. The outer diameter of the screens is 1/2 in. There is a surrounding sleeve of thin stainless steel tubing machined to a wall thickness of less than 10 mil. A layer of masking tape has been used around the outer tube. Several samples of this kind have been used. This early phase of the work has been reported in reference 3 and related papers.

Figure 3b presents the two-section sample used in our runs concerning the orientation influence. There is an inner screen stack, and an outer annular screen system serving as guard section. The inner section is a screen stack with 80 screens of (1/2) in. diameter. The outer guard section has an outer diameter of (nominally) 1 in., measured as 0.958 in. The number of screens in the annulus is 60 (also 500 mesh stainless steel). Between the two screen sections, there is a thin stainless steel (1/2 in. diameter) tube of the type used for the single-stack sample (figure 3a). The height of the sample is 0.67 in. All samples have a lower and an upper end brass screen (40 mesh).

Hexagonal disks. The plate, made of copper, has an inner solid copper core. The shape of the core is a rounded hexagon, about 0.35 in. diameter. The plate thickness is 52.5 mil (= 0.133 cm). The outer diameter of the plate is 0.715 in. The hexagon pattern is shown schematically in figure 4. The total plate area is 2.63 cm², the "active" hexagon area is 2.01 cm². The system investigated has a thermocouple in the center of a stack of 8 plates. Again, stainless steel tubing machined to a thickness below 10 mil has been used.

Perforated plates. The plates (fig. 5a) have been described by Nilles et al⁷. The plate is a copper disk with an outer diameter of 6.137 cm and a height of 0.1397 cm. The hole pattern is a triangular "mini - unit cell" within a "macro-cell" of hexagonal

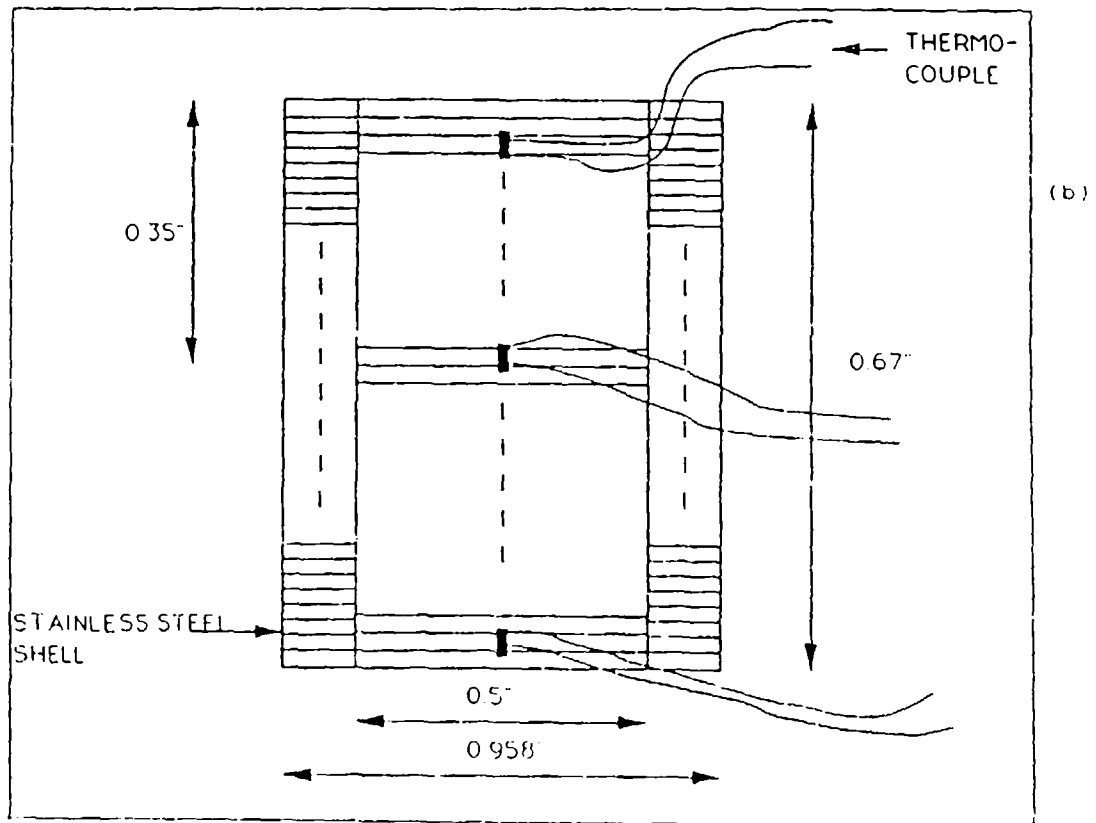
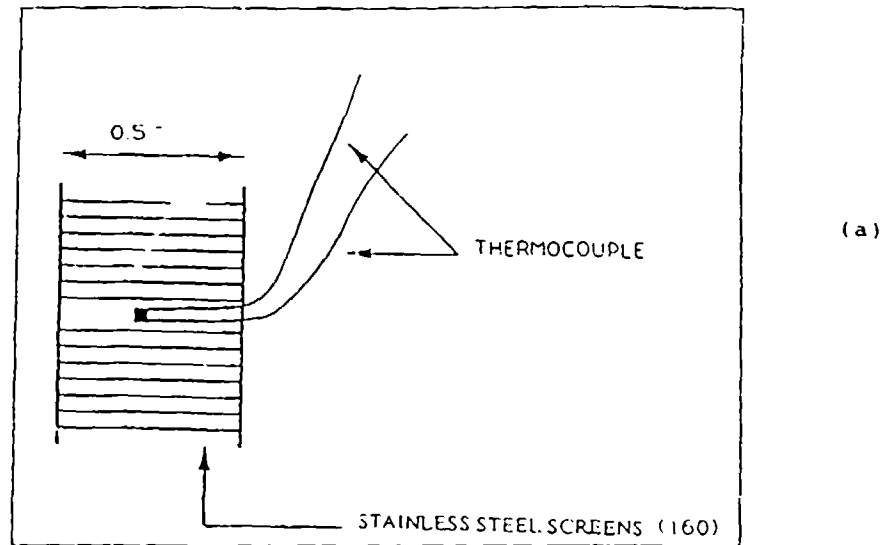
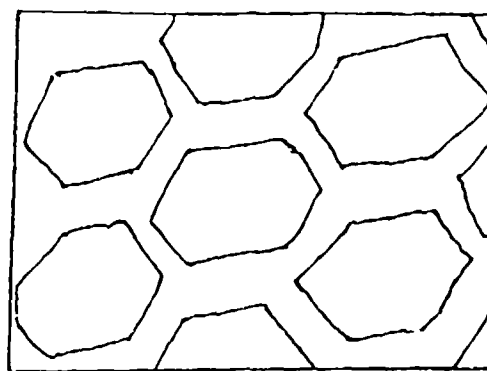


Fig. 3 Screen system schematically;
a. single stack ; b. stack of 80 screens with annular guard (60 screens).



100 μm

Fig. 4. Hexagonal plate system: geometry (schematically) as shown on SEM record.

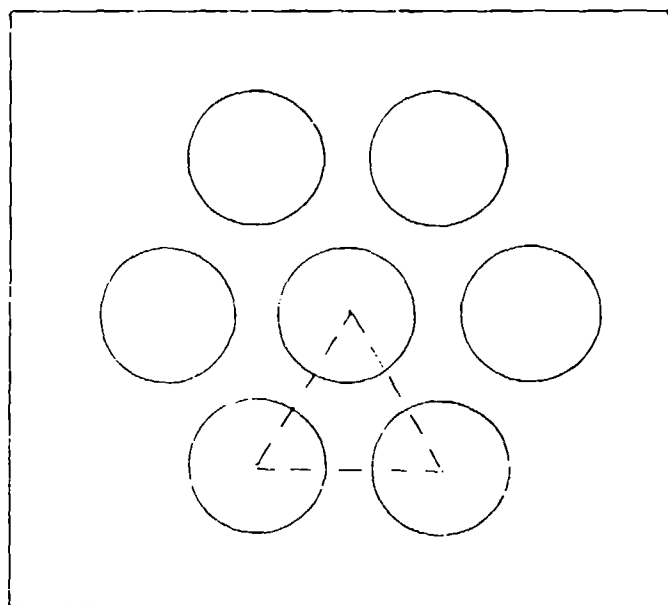


Fig. 5a. Perforated plate system ; a. geometry with triangular "mini" unit cell .

shape. The circular holes have a diameter of about 300 micrometers. Two types of thermometers have been used, thermocouple sensors, and electrical resistance thermometry. There are several parameters of influence for each type of thermometer. Examples are the location of the wire pair (outer rim or plate interior), and the method of wire attachment in the resistance thermometry.

THERMOGRAMS

Several types of thermograms have been encountered. The temperature-time function is either close to exponential decay conditions, with decreasing absolute (dT/dt) during most of the single blow process, or with increasing absolute (dT/dt).

Initial BT-runs have been conducted using a stack of 6 perforated Cu-plates. The liquid is LIN at atmospheric pressure (77 K). This stack has been mounted in a 5 mm thick non-conducting sleeve (material: cardboard) leaving thermocouples between various plates (figure 5b). The thermocouples are insulated 3 mil diameter constantan-chromel (type E) wire pairs. Temperature sensor T_1 is below plate number 1 (fig. 6); temperature sensor T_3 is between plate number 2 and 3; temperature sensor T_4 is between plate number 3 and number 4; temperature sensor T_7 is on top of the system, i.e. above the 6th plate. The T_1 trace is a typical response of the stack system at the "upstream" location. The time constant is less than 0.5 seconds. T_3 shows a monotonically decreasing function of time. Temperatures T_4 and T_7 display a delayed cooldown with a subsequent temporary increase in temperature. Thus, fig. 6 shows a modified "single blow" of considerable duration for the upper portion of the stack. These records indicate additional thermal energy removal from the non-conducting sleeve, and cooldown is not completed yet at 22 seconds.

The initial runs with perforated plates suggest that three major transport regions exist: first, a regime with efficient rates of heat transfer from the Cu-plates to the gas; second, a regime of very small heat transfer rates caused by stagnating fluid inside the stack assembly; third, a transition between the two transport regimes. The first efficient regime has the characteristic properties of a convection-dominated regime. The second inefficient regime has the typical properties of a Fourier conduction-dominated transport scenario. The third transition regime is important for the choice of optimum parameters which ought to be above the limit corresponding to a deterioration of regenerator performance. After these initial runs, the emphasis has been on stacks with a relatively small number of plates.

Figure 7 is another set of thermograms for the hexagonal disk assembly at various orientations. The cooldown behavior is consistent with other runs. It is seen that there is an influence of the axis orientation on the dT/dt derivative.

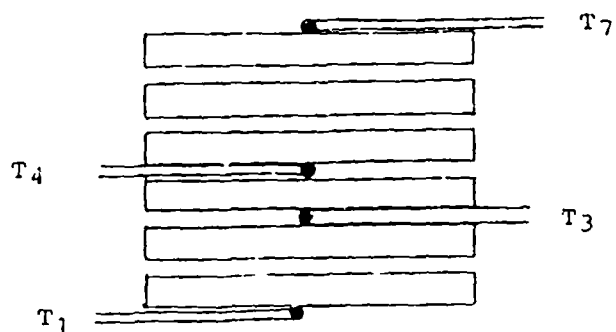


Fig. 5b. Perforated plate system; b. assembly of 6 plates with thermocouple location, schematically.

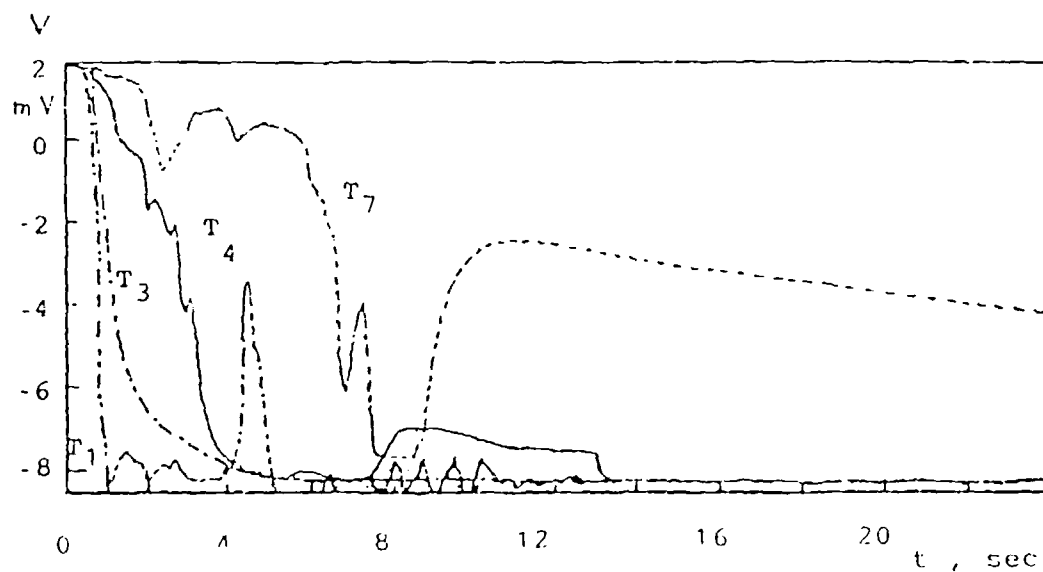


Fig. 6. Perforated plate assembly: thermocouple voltages of blow test; T_j - values in thermogram denote thermocouple number, as indicated schematically in fig. 5b.

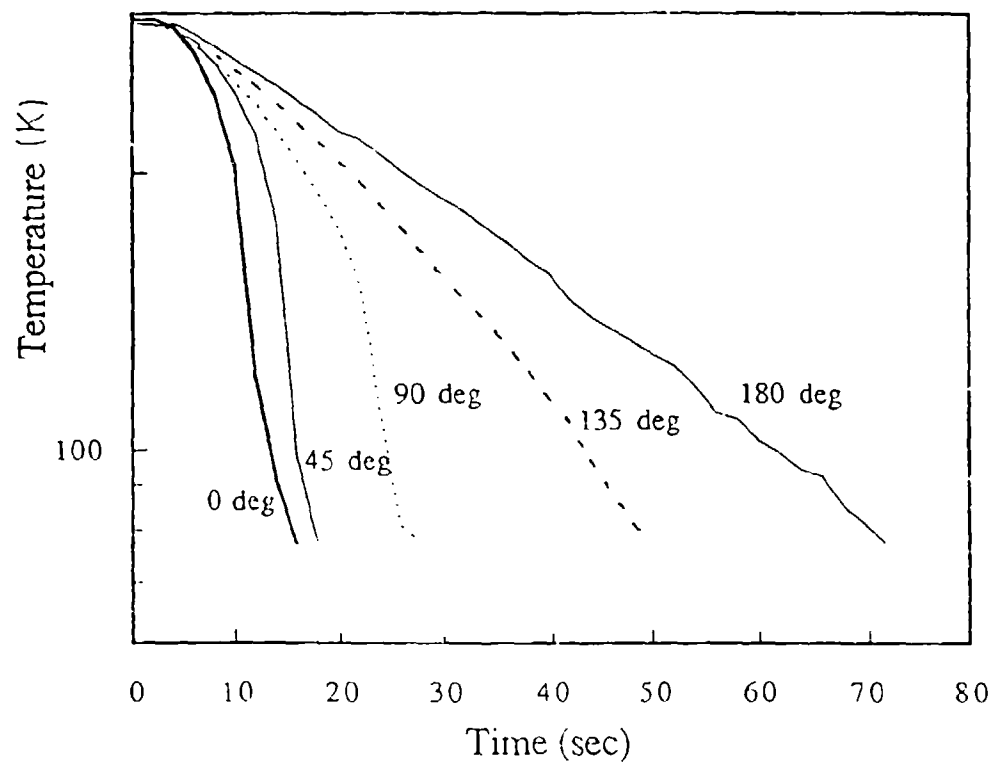


Fig. 7. Thermograms of the hexagonal disk assembly; parameter: angle (ϕ) of stack axis inclination with respect to the gravitational buoyancy direction; plate number : 8; mass : 11.9405 g ; spacer rings between plates: mass 0.0605 g ; stainless steel tube : 2.7134 g.

ORIENTATION EXPERIMENTS.

The influence of the angle ϕ is exhibited in figures 8 to 10. Figure 8 is for the screen sample with the guard section (figure 3b). Figure 9 is a plot of hexagonal disk stack results, and figure 10 presents the plate results.

Figure 8 is a plot of the times needed to reach specified temperatures in the range from 250 K down to 150 K. At the highest temperature of 250 K, only 4 to 5 seconds are needed. At the lowest temperature of 150 K, we see a time of about 30 seconds all the way up to an angle of about 140 degrees. Subsequently there is a noticeable rise in the time toward a maximum value at 180 degrees. For the range from 90 to 180 degrees, a cover has been placed on top of the sample to approximate, as closely as possible, the inverted configuration for angles above 90 degrees. For intermediate temperatures similar results have been obtained, as shown also in figure 8.

Figure 9 is a plot of the total cooldown times versus the angle of orientation for the hexagonal stack. It is seen that the range from 0 to 90 degrees is not strongly affected by the angle. When the angle exceeds 90 degrees, a significant increase of the test time occurs. The function $(t_c)/[\cos \phi]$ is included in the figure for a comparison. The data do not agree with this simple function noting that at 90 degrees the fluid convection prevents a BT - slowdown toward very large times.

Figure 10 plots the total time ratio for the perforated plate runs. The data show a certain scatter. Aside from this uncertainty, we see a clear change of the time ratio in approximate agreement with a $[\cos \phi]^{-1}$ variation. The theoretical function is included in the figure. Since in all previous cases, $[\cos \phi]$ -related functions have meaning only in a rather narrow angular range, we expect the departure from the theoretical function to become pronounced at 90 degrees.

CONCLUDING REMARKS

The present studies show the following results. There is a very weak influence of the angle of orientation for the present screens. This indicates that the high porosity of our screen runs favors a gas flow which is relatively unimpeded by the gravitational buoyancy component over a large angular range. The gas/vapor can easily find a least-resistance path. The exception is the angle near 180 degrees.

The hexagonal disks and, in particular, the perforated plates exhibit a clear influence of the angle of orientation. The influence is weak up to the 90 degree range for the hexagon geometry. The perforated plates show a distinct ϕ - influence in the range

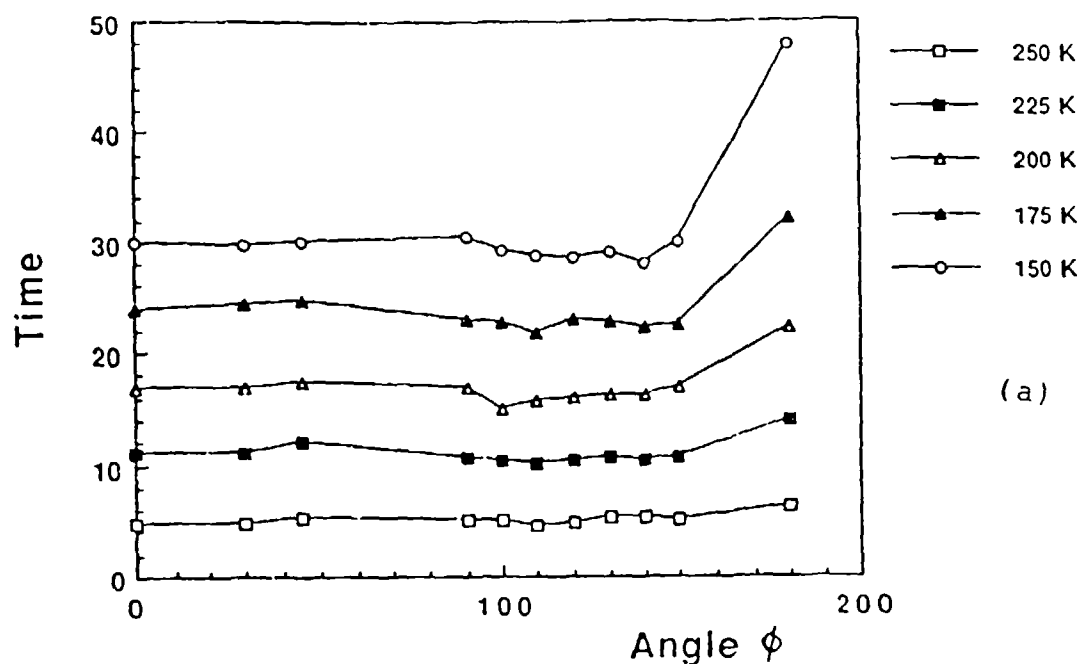


Fig. 8. Stack orientation influence: screen system times at different temperatures during blow test.

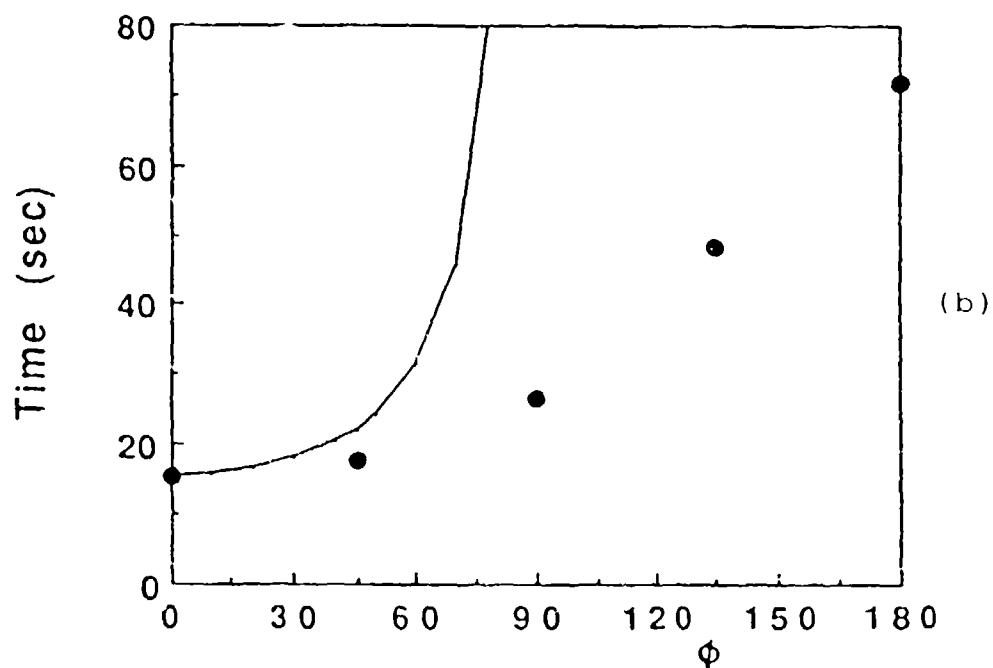


Fig. 9. Orientation influence on the duration of the blow test: hexagonal disk system; the theoretical function is $t = t_0 / [\cos \phi]$; t_0 = time for $\phi = 0$.

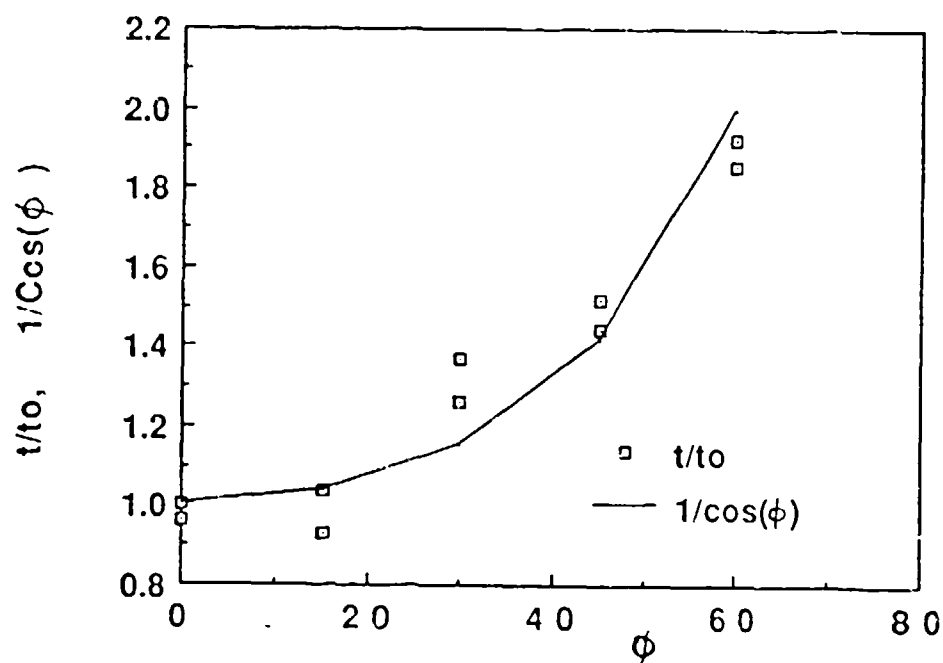


Fig. 10. Time ratio versus inclination angle of plate axis (single perforated plate); the theoretical function is $t = t_0 / [\cos \phi]$; t_0 = time for $\phi = 0$.

covered in our runs. This confirms the expectation based on a constant driving force at "1g" involving the gravitational buoyancy component "seen" by the individual channel within the plate.

The modified "single blow" has been found to be a fast tool which requires additional information for full understanding of thermograms. For the present case of orientation effects, we note that the single perforated plates show good agreement with the time constant prediction that τ is inversely proportional to the thermal conductance (h), and that in addition, h is proportional to v . The latter assumption is not a "classical" case. In continuum fluid mechanics, the dimensionless heat transfer number (Nusselt number) has been said to be constant at small v , i. e. independent of velocity. This is at variance with our results.

In contrast to screens, the perforated plates exhibit a distinct influence of the angle ϕ up to about 60 degrees. Despite these differences between screens and plates, An "S-shaped" function of the Nusselt number (Nu) versus Reynolds number (Re) appears to be a *general* feature⁸. The $Nu(Re)$ function reflects the three regimes outlined above. There is additional evidence that plates behave similar to screens as far the S-shape of the three regimes is concerned. Upon an increase in Re , Nu starts at a "plateau", undergoes the transition, and arrives finally in the "classical" heat exchanger regime.

Further details of vapor flow kinematics have been presented in reference 9, and the Appendix sections [A, B] illustrate vapor velocity variations.

ACKNOWLEDGEMENTS. The initial phase of the work has been supported by ACE-DOE (DE-FG05 -90 - ER80865), and we acknowledge the interest and encouragement of Dr. John Hendricks. In the subsequent phase our student research participation group helped significantly, in particular Christian Shull.

REFERENCES

1. J.I.Rodriguez, Ph.D. thesis, UCLA 1991.
2. R. H. Hubble and C. L. Cain, Adv. Cryog. Eng. 33 (1987) 383.
3. Jack Luna et al., paper 53a, ICS-8, 8th Intersociety Cryog. Sympos., AIChE, Houston Meeting, April 1991.
4. D. N. Lyon, Int. Adv. Cryog. Eng. 10 (1965) 371.
5. S. Lehongre et al, Proc. ICEC-2, 1968, 274.

6. S. Sato and H. Ogata, Proc. Commission I Meeting, Tokyo, Refrig. Sci. Technol. Annexe to Bull. IIR 1970-2, p. 119.
7. M. J. Nilles, M. E. Calkins, M. L. Dingus and J.B. Hendricks, First Intern. Conf. on Aerospace Heat Exchanger Technology, Palo Alto, Febr. 15-17, 1993, paper 6.1.
8. John Hendricks et al., paper presented at 1992 Space Cryogenics Workshop, Munich, June 1991.
9. K. V. Ravikumar et al., LTEC-92, Low Temp. Engng. and Cryogenics Conf. Southampton, UK 1992, paper 6-2.

APPENDIX A : Relative Order of Magnitude of the Average Vapor Velocity at the Flat Plate

Consider the simplest case of a gravitational potential energy ($g B$) where B is the characteristic vapor bubble size [Laplace length ; $B = \{\sigma/[g (\Delta\rho)]\}^{1/2}$]. The kinetic energy is ($v^2/2$). Matching of these two energy terms, by order of magnitude, leads to the following velocity

$$v_B = [2 g B]^{1/2} \quad (A.1)$$

The velocity is shown in fig. A.1 versus the normal boiling point (NBP) for cryoliquids and several high boiling liquids.

Figure A.1 includes the "peak" vapor velocity for the special orientation of the horizontal plate (e.g. ref. 4 for He I) with heat flow up . The vapor velocity for this simple case is

$$v_v = 0.16 [g B \Delta\rho/\rho_v]^{1/2} \quad (A.2)$$

Details concerning the kinematics have been given in ref. 9.

APPENDIX B : Average Vapor Velocity in Open-Ended Duct with Heated Side Wall

The Lehongre et al.⁵ - Sato/Ogata model⁶ is considered. The related reciprocal heat flux density is a simple function of parameters for the vertical axis orientation. There are two peak heat flux densities corresponding to two average vapor velocity terms $v_j = q/[\rho_v \lambda]$; ($j = c$ designates the critical ("peak") value varying with geometry; j

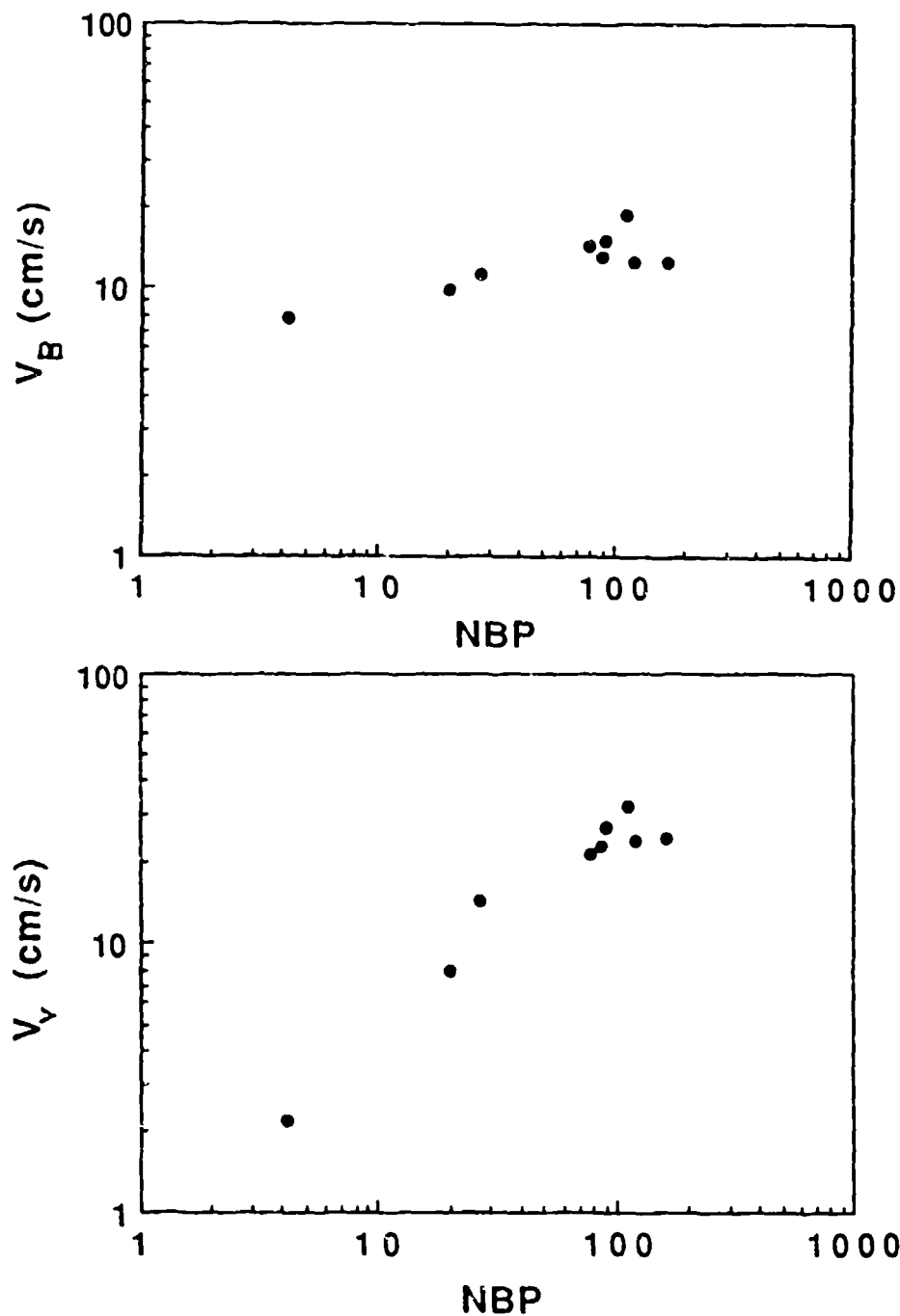


Fig. A.1. Velocity of rising vapor versus normal boiling point (NBP);
 a. characteristic velocity $(2 g B)^{1/2}$, based on an order of magnitude assessment;
 b. calorimetric "Kutateladse - Zuber continuum velocity" for the vapor removed by gravitational buoyancy; geometry: smooth horizontal plate with smooth surface and high conductivity ($\phi = 0$).

= o designates a reference value). Because of the presence of liquid, the average vapor velocity is considerably smaller than the actual rise velocity (u) of the vapor bubbles. The velocity is given by the following function.

$$1/v = 1/v_o + (x/d_e) 4 / u \quad (\text{A.3})$$

The model assumes vapor bubbles rise at constant velocity (u) along the channel. Figure A.2 indicates that this condition is realized, to first order, in the data range covered in the He I runs. The related reciprocal heat flux density of the model is expressed in the following equation

$$1/q_c = 1/q_o + (x/d_e) 4 / q_{\text{conv}} \quad (\text{A.4})$$

(The subscripts [$j = c, o$] denote the same conditions as in equation (3)). The convective q -value represents the following term: $q_{\text{conv}} = u \rho_v \lambda$. The reciprocal heat flux density of equation (4) is shown in figure A.3 versus the dimensionless distance (x/d_e); d_e is the equivalent duct diameter $d_e = 4 A_d/C_c$; A_d is the cross section of the duct; C_c is the heated circumference of the duct. Figure A.4 plots the bubble rise velocity (u) of the model as documented in the data range. A comparison with figure 2 provides additional insight into the continuum aspects of the vapor bubble kinematics.

The angle of inclination, in general, causes a complex function $v(\phi)$. However for side wall heating of a rectangular duct⁶, there is a simple angular dependence. The constant reference term in equation (A.3) is relatively small. The $[\cos \phi]$ - relation is a rough (first order) approximation.

$$1/v_c = 1/v_o + 4 (x/d_e)/[(\cos \phi) u] \quad (\text{A.5})$$

This function simplifies to a "cosine relation" if the $(1/v_o)$ - term in equation (A.4) is negligible. Thus, a first order result is written as follows:

$$v_v = v_{\text{ref}} [\cos \phi] \quad (\text{A.6})$$

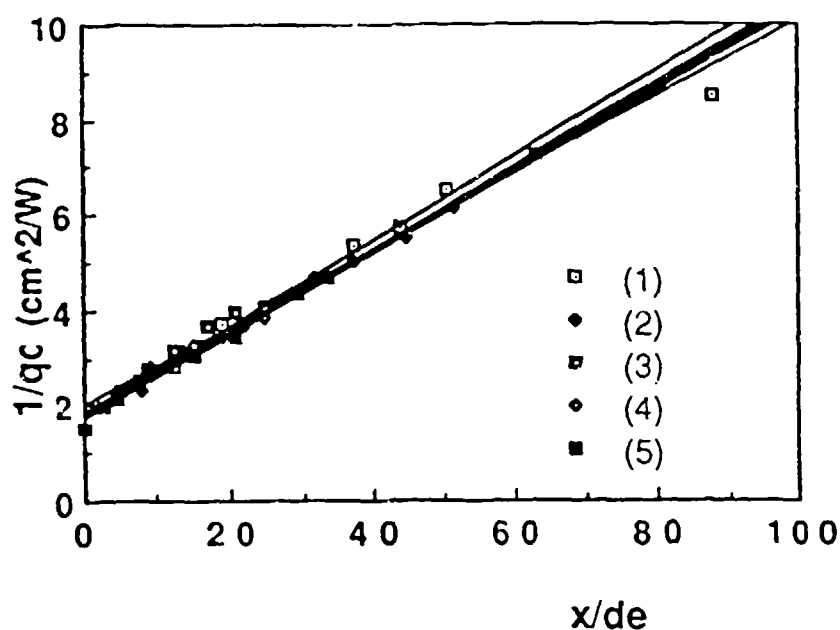


Fig. A.2. Reciprocal "critical" heat flux density (q_c) of a vertical open-ended duct versus distance ratio; x = spatial coordinate along duct axis ; de = equivalent channel diameter ($= 4 \times [\text{cross section}] / \text{circumference}$).

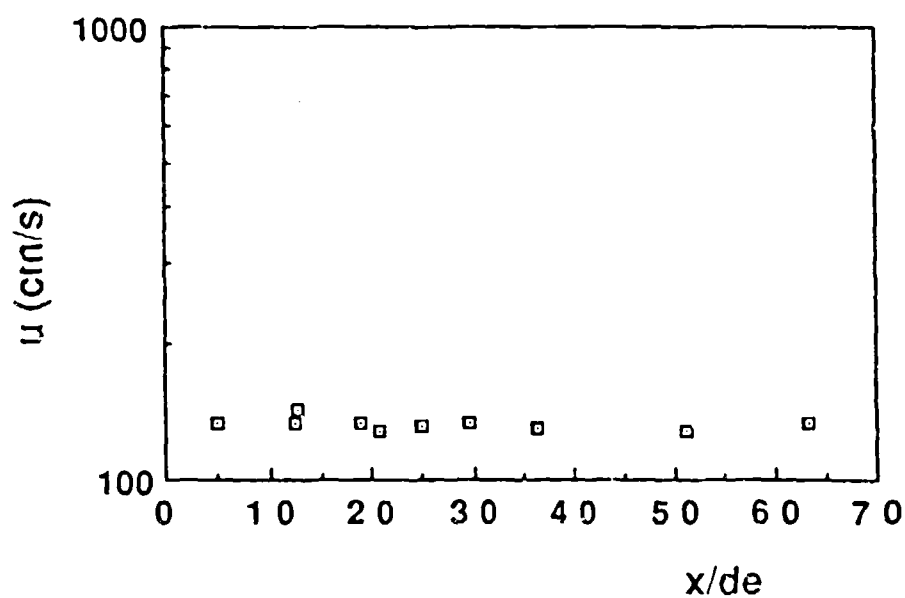


Fig. A.3. Velocity of duct data of figure A.2.

OPTIMIZATION ANALYSIS ON A TWO-STAGE AMR HYDROGEN LIQUEFIER

Li Zhang
Mechanical Engineering Department
University of Miami
Coral Gables, FL 33124

Anthony J. DeGregoria
Astronautics Corporation of America
Astronautics Technology Center
Madison, WI 53716

S.A. Sherif
Department of Mechanical Engineering
University of Florida
Gainesville, FL 32611

T.N. Veziroglu
Clean Energy Research Institute
University of Miami
Coral Gables, FL 33124

ABSTRACT

Optimization studies of a detailed magnetic hydrogen liquefier model are described. The liquefier utilizes an Active Magnetic Regenerator cycle. The device is proposed for the industrial liquid hydrogen market. Overall efficiency is the primary performance measure. Operating variables such as particle size, bed length, and interstage temperature are varied. Efficiency comparable to much larger gas cycle plants is predicted. The device may be modified, in a simple manner, to become a two-stage magnetic refrigerator operating between 77 K and 20 K with a high efficiency.

INTRODUCTION

For engineering systems, it is often expensive, time-consuming or risky to use a real system

to carry out performance studies. Models are typically used in engineering design because they offer an inexpensive and fast way of studying the effects of changes in design variables on system's performance. A time-dependent one-dimensional model of the Active Magnetic Regenerator (AMR) has been developed to evaluate AMR magnetic refrigerator performance and to aid in the design of AMR magnetic refrigerators (DeGregoria, 1991). The model assumes that the heat capacity of the pore fluid in the regenerator is negligible compared to the magnetic material and uses measured material properties provided by Zimm et al. (1991). The model includes axial conduction and axial dispersion effects in the regenerator. The numerical results of the model were validated with experimental data. Based on this model, a two-stage AMR hydrogen liquefier operating between 77 K and 20 K was designed. A detailed design of the liquefier is described in Janda et al. (1991).

The time-dependent one-dimensional AMR model (DeGregoria, 1991) was used to evaluate the performance of the liquefier. The estimated liquefier efficiency is found to be comparable to gas-cycle liquefiers. The design however, is a point design. No optimization was performed. The maximum efficiency of the liquefier system should be determined through an optimization analysis, optimizing the configuration parameters and operating variables for maximum efficiency.

Optimization methods generally can determine the best operating point of an engineering system without testing all possible combinations of design variables since they use a modest level of mathematics and clearly defined logical algorithms in iterative numerical calculations. For engineering systems, optimization methodology can be used to predict improved choices of the independent variables values. This paper describes an optimization method applied to the design of the two-stage AMR hydrogen liquefier and the associated results.

MODELING

To apply an optimization process to the engineering design of the liquefier system, we need

to formulate the problem. The objective function is identified as the liquefier system's liquefaction efficiency which should be maximized vis-a-vis the independent variables and external factor dependent variables.

The design schematic of the two-stage AMR hydrogen liquefier is shown in Fig. 1. The upper stage operating temperature range is 39 - 77 K while that of low stage is 19 -39 K. Each stage consists of two material beds with a moving magnet. Seven Tesla and 5 Tesla magnetic fields are provided for the high and low stages, respectively. Material bed volumes are fixed for each stage. A 2-second period for the AMR cycle operates on packed particle beds of GdNi_2 and GdPd for the high and low stages, respectively. With a total operating period of 2 seconds, the cycle is divided into 0.5 seconds for magnet motion separated by 0.5 seconds for helium flow through the beds. A liquid nitrogen bath connected to the high stage provides the precooling. The gaseous hydrogen feedstock is supplied at 40 atm and 41.5% para-hydrogen concentration. Helium pressure within the hydrogen-helium magnetic refrigerators of both stages is 20 atm. With a specification of the counterflow heat exchanger and demanded production of hydrogen liquefaction, the cold helium mass flow to the heat exchanger is determined. Therefore, there is a flow imbalance, with some of the cold helium that is emerging from the cold end being diverted to the heat exchanger. Over a cycle, more helium flows from the hot end to the cold end than from the cold end to the hot end of the regenerator for both stages.

By analyzing the design of the two-stage liquefier and the time-independent one-dimensional model of the AMR developed by DeGregoria (1991), the Davidon-Fletcher-Powell (DFP) algorithm is used (Reklaitis et al., 1983 and Wilmert, 1988). This algorithm is quadratically convergent for non-linear engineering problems. Two models are developed here which enable the parametric studies of liquefier performance and the optimization of the operating variables of the liquefier.

For the parametric study of the liquefier's performance model, the DFP code is employed for both stages. For the low stage, the objective function is the residual cooling capacity

whose value should be zero with the independent variable being the unbalanced mass flow rate. For the high stage, the objective function is the helium outlet temperature from the cold end which should match the hot inlet temperature of the low-stage with the independent variable of the unbalanced mass flow rate. With the given input data for each stage, the liquefaction efficiency is obtained. For the optimization study model, the DFP code is employed again to maximize the liquefier efficiency with respect to feasible, changeable variables.

The liquefaction efficiency is based on the ideal work required to cool normal hydrogen from 300 K and 40 atm to para-hydrogen at 20 K and 40 atm. This ideal work is divided by the real work required by the hydrogen liquefier. This includes the work required at the liquid nitrogen plant which is assumed to have an efficiency of 45%. The total real input work is the sum of the input work at the liquid nitrogen plant, the input work to each stage, and the input work for the circulator pump.

RESULTS AND DISCUSSION

The parametric study model is used to determine the performance of the hydrogen liquefier with specified two stage operating parameters. The model was verified by the point design data. Changing mass flow rates of the two stages changes the operating temperature ranges of the two stages, and hence, changes the liquefier's efficiency. With all the design liquefier parameters, the parametric study model gave results for the liquefier efficiency over the interstage temperature from 35 K to 43 K. Figure 2 shows the effect of interstage temperature on the liquefier efficiency. From Fig. 2 we see that the designed interstage temperature 39 K falls within the optimized range.

The optimization study model is used to maximize the liquefaction efficiency with the changeable variables. The magnetic material bed plays an important role in the liquefier system's performance, thus a careful choice of parameter values is required. With the constraints of using the materials GdNi_2 and GdPd and the limits on material bed volumes,

particle sizes and bed length can be changed with the objective of improving the liquefier efficiency. Figure 3 shows the efficiency contours with respect to two stage particle sizes. From Fig. 3 we can see that the high stage particle size has a larger effect on the system's efficiency. These results suggest that the high-stage particle size should not be less than 0.1 mm in diameter and the low-stage particle size should be less than the high-stage particle size. This is primarily because the denser low-stage bed can improve the liquefier efficiency without contributing to increasing pump work (due to the smaller volume of the low-stage). Figure 3 shows a maximum efficiency point of 26.2% corresponding to a low-and high-stage particle size of 0.035 mm and 0.136 mm, respectively.

An optimization study of the low-stage bed structure was also carried out. Figure 4 shows efficiency contours in terms of the particle size and bed length of the low stage. From Fig. 4 we see that the design bed length is in the optimized range, while the particle size is not. With the design high-stage parameters, the best combination of the low-stage particle size and bed length is 0.063 mm with a relative bed length of 5.6.

The performance of the liquefier is sensitive to the thermodynamic properties of the magnetic materials. The "ideal" material properties were derived by DeGregoria (1991) as:

$$\Delta t_{ad} = f(B) \frac{m_c}{m_h} t_{bc} - t_{bc}$$

for both the unbalanced flow and the balanced flow. With the unbalanced flows obtained with a low-stage particle size of 0.063 mm and a relative bed length of 5.6, the "ideal" adiabatic temperature change is shown in Fig. 5 compared to GdPd at 5 T and GdNi₂ at 7 T. The "ideal" material properties shown in Fig. 5 are the ones employed in Fig. 2 to obtain the "ideal" material efficiency. "Ideal" materials can significantly improve liquefier efficiency.

CONCLUSIONS

Parametric and optimization study models of a two-stage AMR hydrogen liquefier were developed. Studies maximizing liquefier efficiency with respect to changeable variables were performed. Results show that key design parameters fall within the optimized range. It is suggested that the low-stage particle size be reduced. Significant improvements are possible if materials can be found which approximate "ideal" materials.

ACKNOWLEDGEMENT

This work is partially based on research supported by a grant from the U.S. Department of Energy to the Astronautics Corporation of America under contract number DE-AC02-90CE40895. Support from the Department of Mechanical Engineering and the Clean Energy Research Institute at the University of Miami is also gratefully acknowledged. The third author would like to acknowledge the help of Mrs. Alice Jempson.

REFERENCES

DeGregoria, A.J., 1991, "Modeling the Active Magnetic Regenerator," Advances in Cryogenic Engineering, Vol. 37, Plenum Press, NY, pp. 867-873.

Janda, D., DeGregoria, T., Johnson, J., and Kral, S., 1991, "Design of an Active Magnetic Regenerative Hydrogen Liquefier," Advances in Cryogenic Engineering, Vol. 37, Plenum Press, NY, pp. 891-898.

Reklaitis, G.V., Ravindran, A., and Ragsdell, K.M., 1983, "Engineering Optimization, Methods and Applications," John Wiley & Sons, Inc.

Wilmert, K.D., 1988, "An Optimization Program to Solve Non-Linear Problems by DFP Algorithm," Mechanical Engineering Department, Clarkson University, Potsdam, NY.

Zimm, C.B., Ludeman, E.M., Severson, M.C., and Henning, T.A., 1991, "Materials for

Regenerative Magnetic Cooling Spanning 20 K to 80 K," Advances in Cryogenic Engineering, Vol. 37, Plenum Press, NY, pp. 883-890.

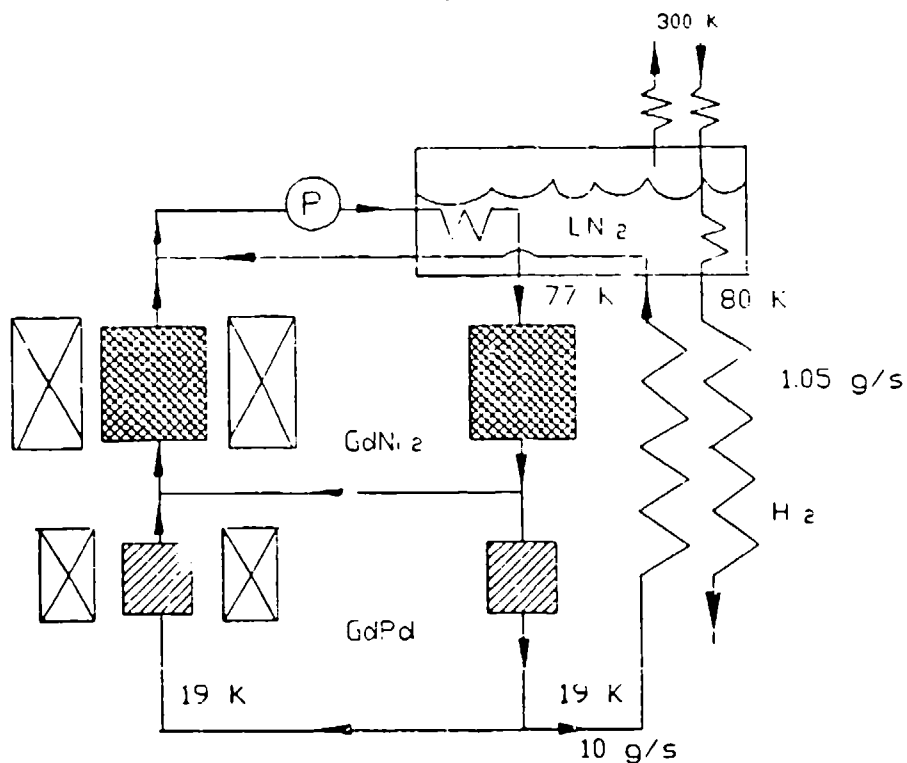


Fig. 1. Schematic of the two-stage AMR hydrogen liquefier

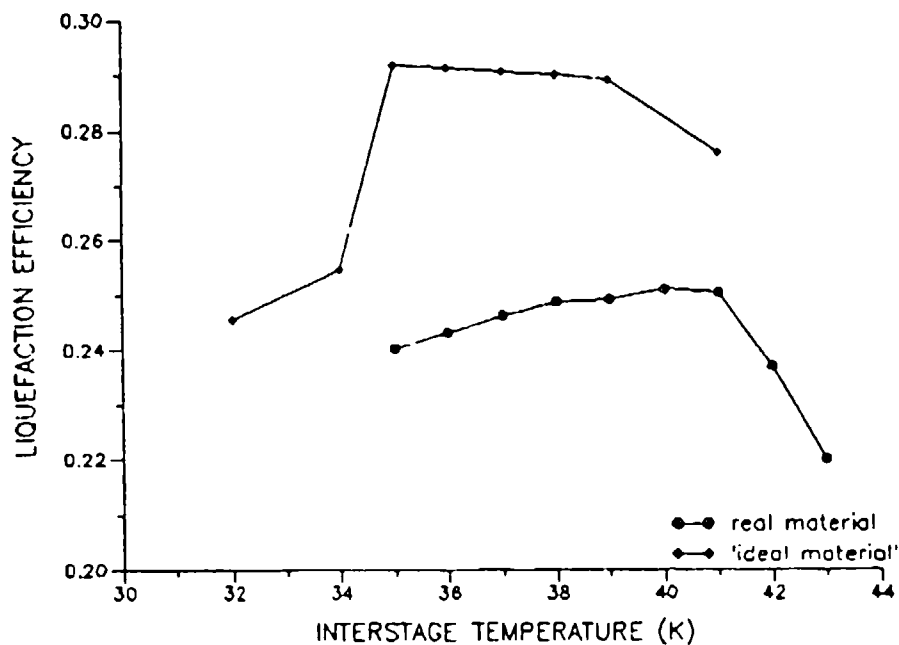


Fig. 2. Efficiency comparison using the "ideal" and real materials

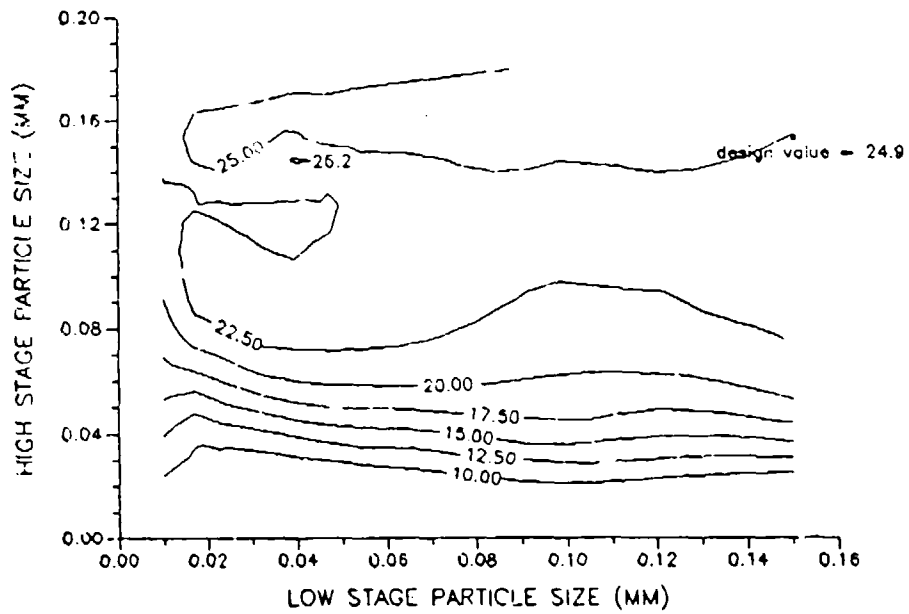


Fig. 3. Efficiency contours of two stage particle size

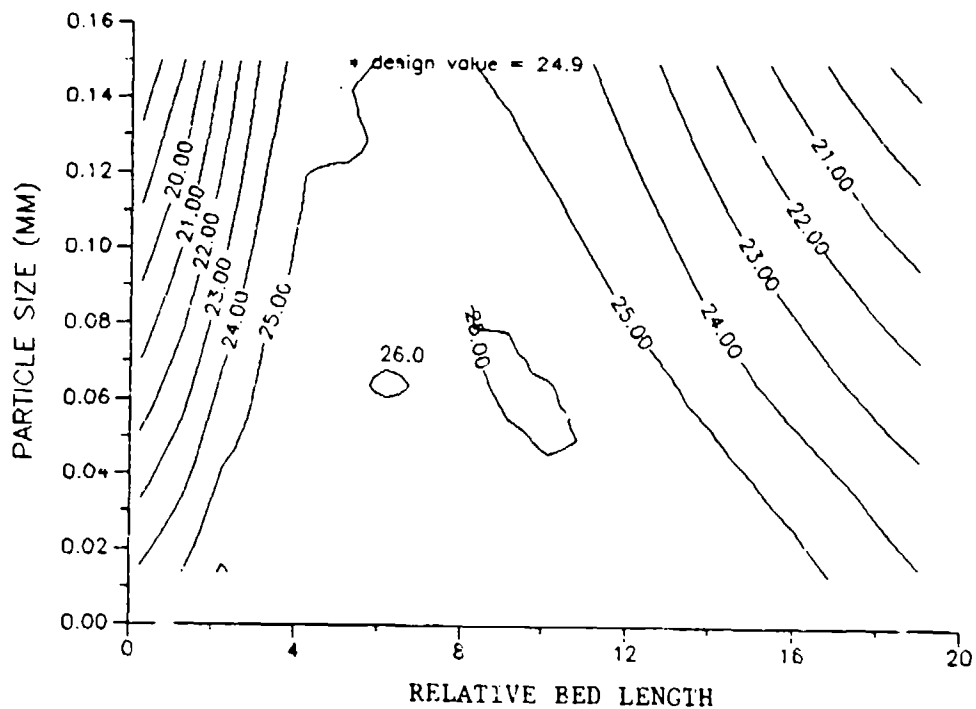


Fig. 4. Efficiency contours of low stage particle size and bed length

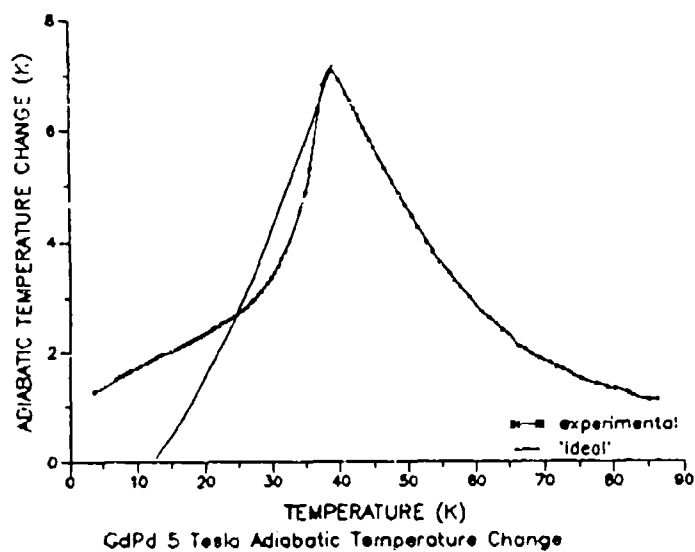
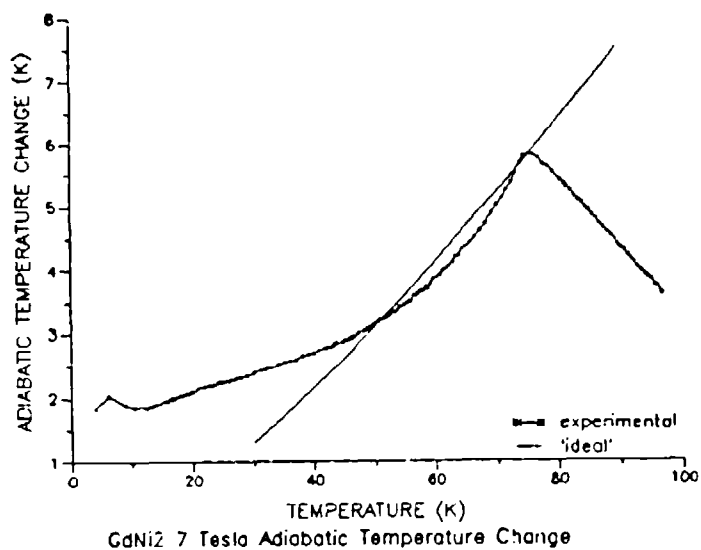


Fig. 5. Adiabatic temperature change for "ideal" materials